

Experimental Advances in Electrode Kinetics

A thesis submitted for the degree of Doctor of Philosophy

in Physical and Theoretical Chemistry

Danu Suwatchara

St. John's College

June 2013

Abstract

At the present, numerous kinetic theories are available to electrochemists in describing chemical reactions at the electrode. These exist in varying degree of complexity, ranging from simplistic empirical formulae to more rigorous models that account for microscopic physical phenomena pertaining to the reactive species and their environment. However, experimental work documented in support of the validity and comparison between these theories is scarce. This is largely due to difficulty in attaining and controlling the experimental conditions where applicability of the theories break down. As such, the current work utilizes state-of-the-art electrochemical experimental techniques in order to test some of the most prominent electrode kinetics theories via comparison to simulations. This is done with the aim of identifying their limitations and providing new insight into fundamental mechanistic processes that occur during an electrochemical reaction.

Part 1 of this thesis describes the preliminary topics of electrode reactions and electrochemical techniques. Fundamentals of electrode processes (Chapter 1) and an overview of kinetics theories involved (Chapter 2) are presented along with the detail of instrumentation used (Chapter 3).

Part 2 reports the comparison between the use of Butler-Volmer (BV) and Marcus-Hush-Chidsey (MH) formalisms in the simulation of voltammetric responses of model processes, namely: the oxidation of 9,10-Diphynylanthracene and reduction of 2-Nitropropane at the High-Speed Channel Microband Electrode (Chapter 4), and the reduction of Cyclooctatetraene at the hemispherical mercury electrode (Chapter 5). It was found that both formalisms yields excellent fits for the 9,10-Diphenylanthracene system which involves relatively fast kinetics. However, for the 2-Nitropropane and

Cyclooctatetraene systems which involve much slower kinetics, the MH formalism yields inferior quality of fittings as a result of its inherent assumption of equal reorganization energies for oxidation and reduction.

Part 3 demonstrates the ability of the asymmetric form of the Marcus-Hush-Chidsey (aMH) model, a formalism developed in-house which extends on the Marcus-Hush-Chidsey formalism, allowing it to account for asymmetry between the oxidative and reductive processes. When tetraphenylethylene was used as the model experimental system (Chapter 6), the aMH model was found to yield excellent quality of fittings comparable to that of the BV formalism while the MH model displays an inferior quality of fittings. Further comparisons between the MH and aMH models in fitting experimental systems of 2-Methyl-2-Nitropropane, Cyclooctatetraene and Europium (III) (Chapter 7) reveals the correlation between the transfer coefficient used within the BV formalism and the asymmetric parameter of the aMH model. This gives physical insight to the BV transfer coefficient as the indicator of the differences between the force constants of the oxidized and reduced species.

Part 4 concerns further developments of physical insights into microscopic processes of heterogeneous electron transfer based on the aMH model. In particular, cyclic voltammetry carried out at variable temperature has been applied to 1-Nitropentane (Chapter 8) and 3-Nitrophenolate (Chapter 9) as a method for the appraisal of the value of reorganization energy of the reactive species. Furthermore, the ability of the model to correlate the variation of electron transfer rate to the degree of adiabaticity was also evaluated using 3-Nitrophenolate as the reagent (Chapter 10). In this experiment, a varying degree of adiabaticity was achieved by changing the distance of approach between the reagent and the electrode through the use of supporting electrolyte cations of differing size. Chapter 11 extends the study on adiabaticity to a

system with a lesser degree of adiabaticity, namely 2-Nitropropane. Here, the potential energy curve model developed by Waldeck and Mishra was also used to rationalize the adiabaticity behavior of the experimental system.

Acknowledgements

I would like to thank the following for their support and involvement through the course of my research and production of this thesis.

My supervisor, Prof. R. G. Compton, for his supervision and guidance throughout the course of my D.Phil.

Dr. N. V. Rees for imparting his expertise in hydrodynamic electrochemistry, fast-scan voltammetry and electrode fabrication techniques.

St. John's College, Oxford, for funding through the Kendrew Scholarship.

The members of the Compton Group (2010-2013) for their support and friendship.

Finally, to my parents and younger brother for their love and support that made this D.Phil. possible.

Contents

PART I ***Preliminary Topics*** ***1***

Chapter 1: Fundamental Concepts in Electrochemistry…….. 2

1.1 Equilibrium Electrochemistry……. 2

1.2 Dynamic Electrochemistry…….. 4

1.2.1 Faradaic and Non-faradaic Processes……. 5

1.2.2 Electrical Double Layer…….. 6

1.3 Mass Transport…… 7

1.3.1 Diffusion……. 8

1.3.2 Convection…….. 9

1.3.3 Migration…… 9

1.4 Voltammetric Techniques…… 10

1.4.1 Linear Sweep Voltammetry…… 10

1.4.2 Cyclic Voltammetry……... 12

1.4.3 Square Wave Voltammetry…… 13

1.4.4 Potential Step Chronoamperometry…… 14

1.5 References……... 16

Chapter 2: Theories of Electrode Kinetics……. 17

2.1 Butler-Volmer Kinetics……... 17

2.2 Marcus Theory……. 20

2.3 Marcus-Hush-Chidsey Formalism……... 22

2.4 Asymmetric Marcus-Hush-Chidsey Formalism…….. 24

2.5 Waldeck and Mishra Potential Energy Curve Model…….. 26

2.6 References……... 29

Chapter 3: Instrumentation……. 30

3.1 The High-Speed Channel Electrode…… 30

3.2 Fast Scan Potentiostat…….. 32

3.3 Electrode Fabrication……... 33

3.3.1 Microband Electrodes……. 33

3.3.2 Microdisk Electrodes…….. 34

3.4 References……... 36

PART II Comparative Study of the Marcus-Hush-Chidsey and Butler-Volmer Formalisms 37

Chapter 4: Experimental Comparison of the Marcus-Hush-Chidsey and Butler-Volmer Descriptions of Electrode Kineetics. The One-Electron Oxidation of 9,10-Diphenylanthracene and One-Electron Reduction of 2-Nitropropane Studied at High-Speed Channel Microband Electrodes 38

4.1 Introduction……. 39

4.2 Theory…….. 42

4.3 Experimental…… 46

4.4 Results and Discussion…… 47

4.5 Conclusions……. 56

4.6 References……... 58

Chapter 5: Experimental Comparison of the Butler–Volmer and Marcus-Hush-Chidsey Formalisms of Electrode Kinetics: The Reduction of Cyclooctatetraene at Mercury Hemispherical Electrodes via Cyclic and Square Wave Voltammetries 62

5.1 Introduction……. 63

5.2 Experimental…… 66

5.3 Results and Discussion…… 75

5.4 Conclusions……...…….. 81

5.5 References……... 82

PART III ***Experimental Validation of Asymmetric Marcus-Hush-Chidsey Formalism*** ***86***

Chapter 6: Comparative Evaluation of the Symmetric and Asymmetric Marcus–Hush-Chidsey Formalisms of Electrode Kinetics – The One-Electron Oxidation of Tetraphenylethylene in Dichloromethane on Platinum Microdisk Electrodes **87**

6.1 Introduction……... 88

6.2 Experimental……. 91

6.3 Results and Discussion…….. 93

6.4 Conclusions……... 102

6.5 References……. 103

Chapter 7: Giving Physical Insight to the Butler–Volmer Model of Electrode Kinetics: Application of Asymmetric Marcus–Hush-Chidsey Theory to the Study of the Electro-reductions of 2-Methyl-2-Nitropropane, Cyclooctatetraene and Europium(III) on Mercury Microelectrodes **106**

7.1 Introduction……... 107

7.2 Experimental……. 109

7.3 Results and Discussion……. 113

7.4 Conclusions……... 125

7.5 References……. 126

PART IV Developing Further Physical Insights Based on the Asymmetric Marcus-Hush-Chidsey Model of Electrode Kinetics ***128***

Chapter 8: Molecular Insights into Electron Transfer Processes via Cyclic Voltammetry at Variable Temperature: Application of the Asymmetric Marcus-Hush-Chidsey Model **129**

8.1 Introduction……... 130

8.2 Experimental……. 131

8.3 Theory……... 136

8.4 Results and Discussion…….. 138

8.5 Conclusions……... 153

8.6 References……. 153

Chapter 9: Variable Temperature Study of the Electro-reduction of 3-Nitrophenolate via Cyclic and Square Wave Voltammetry. Molecular Insights into Electron Transfer Processes Based on the Asymmetric Marcus-Hush Model **157**

9.1 Introduction……... 158

9.2 Experimental……. 159

9.3 Results and Discussion…….. 164

9.4 Conclusions……... 176

9.5 References……. 177

Chapter 10: On the Adiabaticity of Electrode Processes: Effect of the Supporting Electrolyte Cation on the Kinetics of Electro-reduction of 3-Nitrophenolate **180**

10.1 Introduction……. 181

10.2 Experimental……... 183

10.3 Results and Discussion…… 187

10.4 Conclusions……. 197

10.5 References……... 198

Chapter 11: Theoretical and Experimental Approach to the Adiabaticity of Diffusional Electron Transfer Processes. Electro-reduction of 2-Nitropropane on Mercury Microelectroelectrodes **200**

11.1 Introduction……. 201

11.2 Experimental……... 202

11.3 Theory……. 208

11.4 Results and Discussion…… 213

11.5 Conclusions……. 223

11.6 References……... 224

Appendix: Fast Scan Potentiostat……. 227

PART I

Preliminary Topics

The work presented in this thesis concerns the study of kinetics of electrochemical reactions in the solution phase occurring at the surface of an electrode. As such, discussions presented in Part I pertain to fundamental concepts of heterogeneous electrochemical reaction and experimental techniques used. Chapter 1 encompasses fundamental concepts of electrochemical reactions at the electrode and related mass transport phenomena. A cursory description of experimental techniques used in the current work is also included. Chapter 2 presents the description of various kinetic theories studied in this work. Detail regarding experimental instrumentation is also outlined in Chapter 3.

Chapter 1

Fundamental Concepts in Electrochemistry

This chapter outlines fundamental concepts in heterogeneous electrode reactions. Discussions presented here cover both thermodynamic and kinetic aspects. Furthermore, electrochemical methods applied to experimental work presented in this thesis are also introduced.

1.1 Equilibrium Electrochemistry

Consider a solution containing species A and B related by the reduction scheme below, existing at equilibrium:

$$A + e \rightleftharpoons B \tag{1.1}$$

If a metallic electrode is inserted into the solution, an interfacial potential exists which may thermodynamically drive the reaction forward, if the electrode acts as an electron source, or backward, if it acts as an electron sink. At equilibrium, the net charge accumulation from the reaction results in a difference in charge concentration between the two phases, hence, an equilibrium potential difference.

It is also required that, at equilibrium, the sum of electrochemical potentials ($\bar{\mu}$) of the reactants is equal to that of the products [1,2]:

$$\bar{\mu}_A + \bar{\mu}_e = \bar{\mu}_B \tag{1.2}$$

For a species, *j*, the electrochemical potential can be given as a function of its chemical potential (μ_j) and electrical energy ($z_j F\phi$) as follows:

$$\bar{\mu}_j = \mu_j + z_j F\phi \tag{1.3}$$

where z_j is the charge of the species *j*, *F* the Faraday's constant (96,485 C·mol^{-1}) and ϕ is the potential of the phase where species *j* is situated.

For the reduction scheme laid out in Equation 1.1, the equality of electrochemical potentials at equilibrium is then given by:

$$(\mu_A + z_A F\phi_s) + (\mu_e - F\phi_M) = (\mu_B + z_B F\phi_s) \tag{1.4}$$

where ϕ_s is the potential at the solution phase, and ϕ_M at the metal electrode. This can be rearranged as:

$$F(\phi_M - \phi_s) = \mu_A + \mu_e - \mu_B \tag{1.5}$$

Since the chemical potentials are given as:

$$\mu_A=\mu_A^0 + RT\ln(a_A) \tag{1.6}$$

$$\mu_B=\mu_B^0 + RT\ln(a_B) \tag{1.7}$$

where R is the universal gas constant (8.314 J mol^{-1} K^{-1}); T is the temperature measured in Kelvin and a is the activity of the species, Equation 1.5 can be rearranged to give the Nernst equation [3,4]:

$$\phi_M - \phi_s = \frac{1}{F}(\mu_A^0 + \mu_e + \mu_B^0) + \frac{RT}{F}\ln\left[\frac{a_A}{a_B}\right] \tag{1.8}$$

The implication of the Nernst equation is profound, as in dynamic electrochemistry, concentrations of species involved are assumed to conform to this relationship at equilibrium.

1.2 Dynamic Electrochemistry

Dynamic electrochemistry is the study of the electron transfer reaction between an electrode and a reagent molecule through the application of controlled electrical potential difference between the electrode and solution [2]. Information about the reaction can then be extracted via monitoring of the induced current as a function of the applied potential.

It is worth noting that, in order to monitor the current through the working electrode where the electrochemical reaction takes place, the 3-electrode electrochemical cell needs to be employed. A second (reference) is needed to complete

the electrical circuit while a third (counter) electrode balances the current passed at the working electrode, allowing the potential at the reference electrode to be held constant [4].

1.2.1 Faradaic and Non-Faradaic Processes

Electrical current measured at the electrode during an electrochemical reaction may be classified under two classes, namely Faradaic and non-Faradaic current [3].

Faradaic current is one which arises from electron transfer across the electrode/solution interface as a result of oxidation or reduction of the electroactive species. For the simple reduction system given in Equation 1.1, the Faradaic current is given by:

$$I = FAj_0 \tag{1.9}$$

where A is the area of the electrode and j_0 is the flux at the electrode surface:

$$j_0 = -k_{red}c_{A,0} + k_{ox}c_{B,0} \tag{1.10}$$

where k_{red} and k_{ox} are the rate constants for reduction and oxidation, respectively and $c_{A,0}$ and $c_{B,0}$ are the concentrations of species A and B, respectively, at the electrode surface.

In general, the amount of Faradaic current is a function of the kinetics of the electrochemical reaction and rate of reagent replenishment at the electrode.

Apart from Faradaic current, however, non-Faradaic current may also traverse the electrode/solution interface. Generally, non-Faradaic current arises due to capacitative charging around the electrode/solution interface which may occur as a result of adsorption/desorption processes, or charging of the electrical double layer. The latter phenomenon is addressed in a greater detail in the following section.

1.2.2 Electrical Double Layer

When a charged electrode is placed within an electrolyte solution, redistribution of charged species and solvent dipoles occurs such that charge neutrality is maintained at the electrode surface. As a result of this, species with opposite charge to the electrode surface is attracted towards the electrode, whereas those of like charge are repelled, giving rise to an electrical field gradient that extends into bulk solution. This region of charge separation is the electrical double layer that gives rise to capacity around the electrode/solution interface.

The simplest and most prevalent model of the electrical double layer is the Helmholtz model [5,6] (see Figure 1.1). According to this model, the electrical double layer consists of the inner and outer Helmholtz planes (IHP and OHP, respectively).

The IHP which exists at distance x_1 is made up of solvent molecules and specifically adsorbed species. Due to the existence of the IHP, solvated ions are impeded from approaching the surface of the electrode. Those solvated ions closest to the electrode, with their centers at distance x_2 from the electrode surface, form the OHP.

The formation of IHP and OHP results in a sharp, linear drop of potential between the electrode surface and the OHP. Collectively, this structure is referred to as the compact layer.

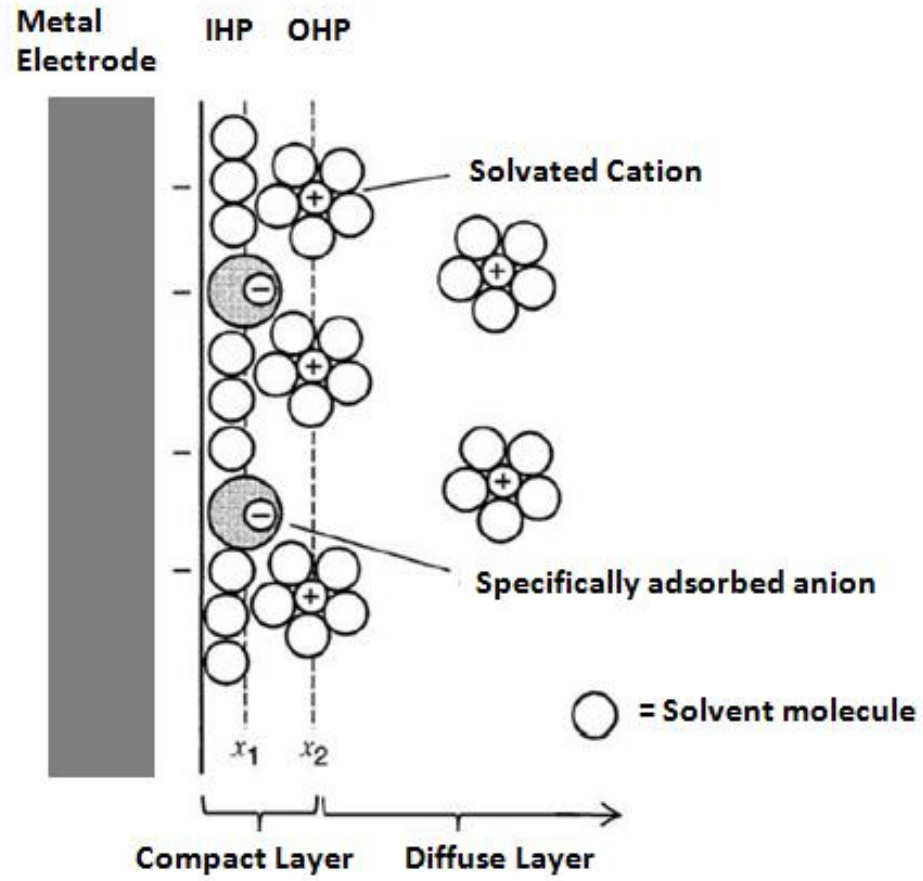


Figure 1.1: *The Helmholtz model of electrical double layer (adapted from [3])*

Beyond the OHP, ions in bulk solution move under the influence of thermal forces. A gradual drop in potential is observed across this diffuse layer whose thickness depends on the total ionic concentration in the solution [3].

1.3 Mass Transport

For an electrochemical reaction occurring at an electrode in solution, 3 modes of mass transport are responsible for sustaining the total flux of fresh reactants to the surface of the electrode, namely diffusion, convection and migration [3,4]. The ability to quantify mass transport to the electrode is important as, given the fact that the kinetics

of the redox reaction normally takes place within a much shorter timescale, the rate at which fresh reagent is replenished at the electrode becomes the limiting factor of the amount of current produced. Each of the 3 modes of mass transport are discussed in more detail below:

1.3.1 Diffusion

Diffusion refers to the spontaneous movement of species under the influence of concentration gradient, from a region of high concentration to that of low concentration. The flux due to diffusion of a species (j_d) can be quantified by Fick's first law (Equation 1.11), and the change of its concentration with time, by Fick's second law (Equation 1.12):

$$j_{d,i} = -D_i \nabla c_i \tag{1.11}$$

$$\frac{\partial c_i}{\partial t} = D_i \nabla^2 c_i \tag{1.12}$$

where D is the diffusion coefficient, c the concentration, ∇ the del operator, ∇^2 the Laplacian operator, and the subscript i denotes the reagent species.

During an electrochemical experiment, a concentration gradient exists between the bulk solution (region of highest reagent concentration) and the electrode surface (region of lowest reagent concentration due to its consumption in the electrode reaction) such that a flux of fresh reagent diffuses towards the electrode due to this concentration gradient. It is important to note that this mode of transport is often the

dominant factor as the others are often mitigated such that their contributions become insignificant under experimental conditions.

1.3.2: Convection

Convection refers to movement of species under the influence of mechanical forces that may arise from natural sources (e.g. thermal gradient or density difference within the solution) or forced in a controlled way (e.g. induced flow under pressure gradient). As the effect of natural convection is usually irreproducible, an experimental setting normally seeks to minimize its effect by limitation of the timescale of the experiment (an upper limit for non-viscous solvent is approximately 30 s [3]) or overriding with quantifiable forced convection.

1.3.3: Migration

Migration refers to the movement of charged species due to potential difference in the electric field. The flux due to migration (j_f) can be expressed as:

$$j_f = -\frac{F}{RT} z_i c_i \nabla \phi \tag{1.12}$$

Since a potential gradient exists around the region of electrode/solution interface, the resulting migratory flux may complicate the interpretation of resulting current measured at the electrode. In order to minimize the effect of migration during an electrochemical experiment, a large excess of inert supporting electrolyte can be added to the solution in order to compress the potential difference to a very short distance rendering mass transport through migration negligible [4].

1.4 Voltammetric Techniques

Experimental work in this thesis makes use of a variety of electrochemical measurements collectively known as voltammetric techniques. In general, these refer to techniques where current is measured in response to the applied potential profile. In particular, 4 different voltammetric techniques are employed in this work, namely, linear sweep voltammetry (LSV), cyclic voltammetry (CV), square wave voltammetry (SWV), and chronoamperometry. Each of the foregoing techniques is described in turn.

1.4.1 Linear Sweep Voltammetry

In linear sweep voltammetry, the potential is swept linearly from a starting potential (E_1) to a final potential (E_2) at a fixed scan rate (υ) at which the potential is varied with time, resulting in a potential profile displayed in Figure 1.2.

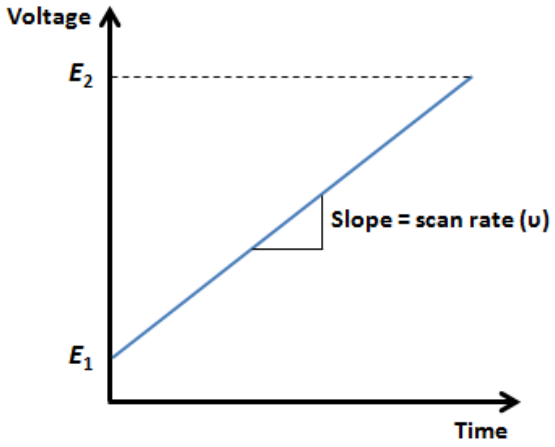


Figure 1.2: *Potential profile for linear sweep voltammetry*

Normally, E_1 is selected such that no reagent is converted to the product, and E_2 such that rapid conversion occurs ($E_2 >> E_f^o$). As a result, for a system where reagent

diffuses freely in solution, the current measured is initially zero and increases after the point where reaction occurs ($E \geq E_f^{\ominus}$). However, as the reaction proceeds, the reagent close to the electrode surface is consumed and the resulting current becomes limited by the rate of its replenishment. As a result, the current passes through a peak and begins to drop. The measured current as a function of applied potential is called a voltammogram, an example of which is shown in Figure 1.3.

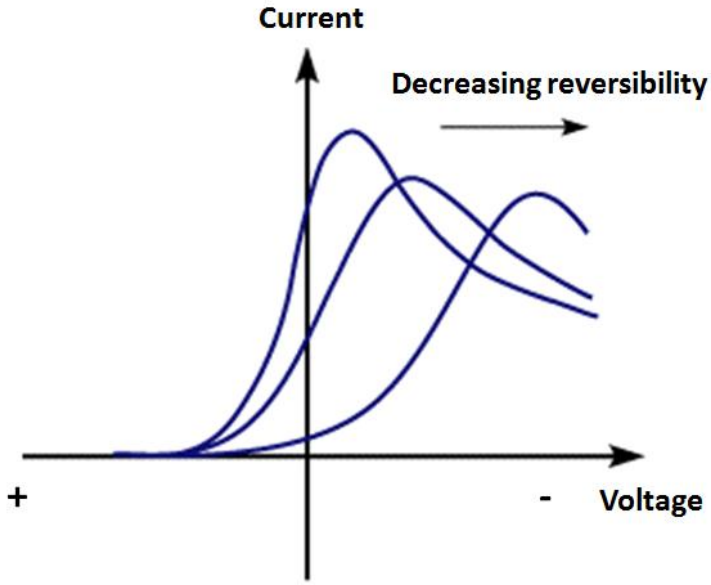


Figure 1.3: *Typical waveshape of linear sweep voltammogram for simple electro-reduction: $A + e \rightarrow B$ (adapted from [7])*

It is noteworthy that, for fast (reversible) electron transfer, the peak of the voltammogram occurs nearer to the formal potential. However, for slow (irreversible) electron transfer, a higher potential is required to drive the reaction sufficiently so that mass transport become the limiting factor, therefore, the peak of the voltammogram occurs at a further potential.

1.4.2 Cyclic Voltammetry

In cyclic voltammetry, potential sweep is done between 2 potential values (E_1 and E_2) at a fixed scan rate, however, once the potential reaches the final value, E_2, the scan is reversed back to E_1. This results in the potential profile shown in Figure 1.4.

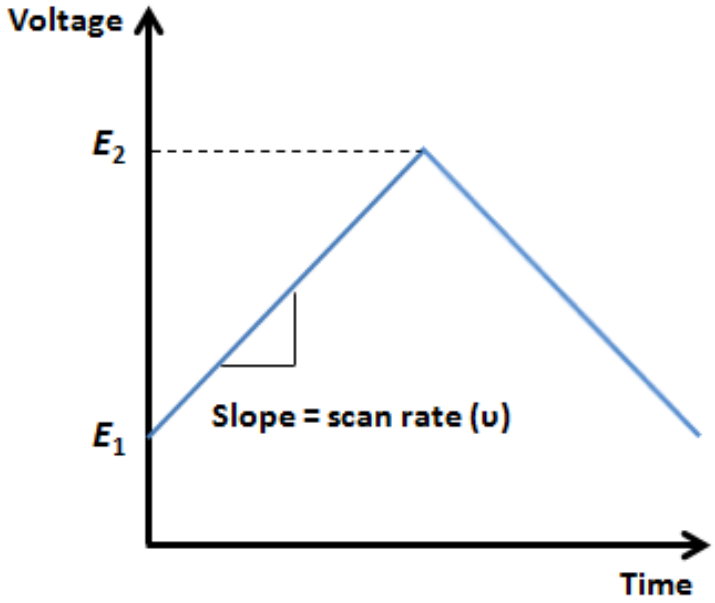


Figure 1.4: *Potential profile for cyclic voltammetry*

For the forward sweep from E_1 to E_2, the characteristic of the current response is identical to that of the linear sweep voltammetry. On the reverse sweep, the product is converted back to the reagent, resulting in a current signal that occurs in the opposite direction of the forward scan. The resulting voltammogram is shown in Figure 1.5.

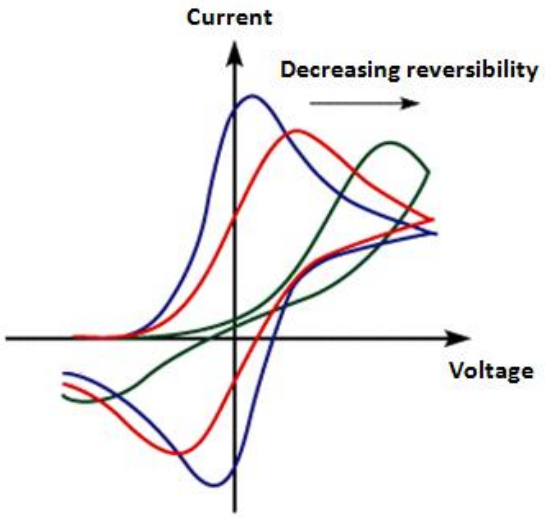


Figure 1.5: *Typical waveshape of cyclic voltammogram(adapted from [7])*

1.4.3 Square Wave Voltammetry

Square wave voltammetry is a pulse voltammetric technique where symmetrical square waves are superimposed on the linear potential sweep voltage profile. The resulting potential profile is shown as follows:

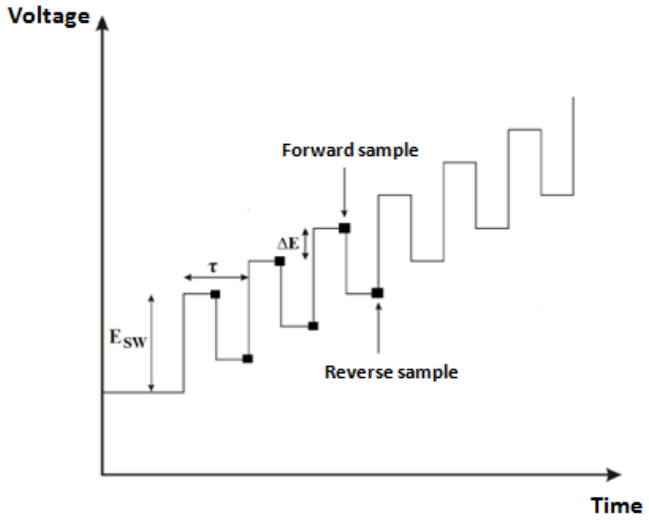


Figure 1.6: *Potential profile for square wave voltammetry characterized by the amplitude (E_{SW}), pulse height (ΔE) and period of one cycle (τ).*

In this technique, the current is sampled twice each cycle (see sample points in Figure 1.6). The resulting voltammogram arises from the subtraction of reverse sample currents from the forward ones. This subtractive nature results in a high level of sensitivity which suppresses the capacitative current from double layer effects.

1.4.4 Potential Step Chronoamperometry

In potential step voltammetry, the voltage is stepped from an initial value E_1 where no electrochemical reaction occurs to a value E_2 where the electrode reaction is fully driven to mass transport limited conditions ($E_2 >> E_f^{\theta}$) and is held for a certain period of time. The resulting potential profile is shown in Figure 1.7.

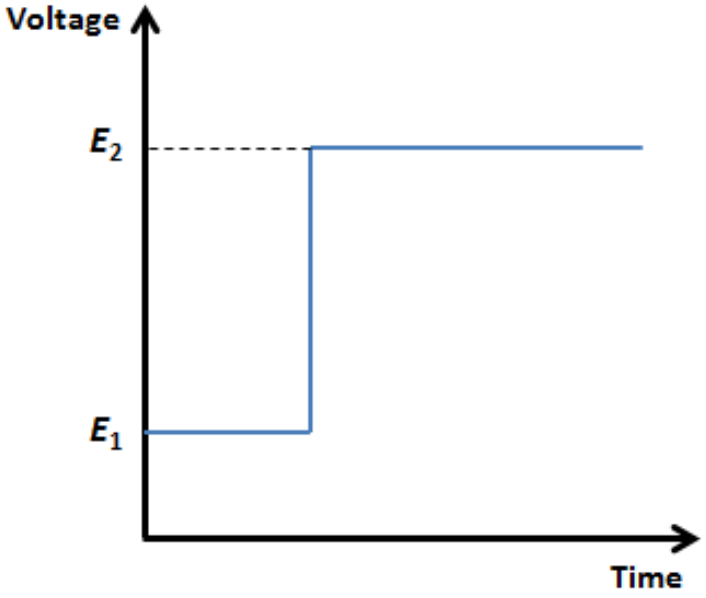


Figure 1.7: *Potential profile for potential step chronoamperometry*

The resulting current is then measured as a function of time. When the potential was first stepped to E_2, the current rises instantaneously as regent is rapidly converted into product. However, as time passes, the reagent becomes depleted and current decays. The resulting current response is presented in Figure 1.8.



Figure 1.8: *Current response of potential step chronoamperometry (adapted from [7])*

For chronoamperometry at a macroelectrode, the current-time dependence is described by the Cottrell equation (Equation 1.13), and at a microdisk electrode, the Shoup and Szabo expression (Equation 1.14).

$$i(t) = \frac{nFAD^{0.5}c^*}{\pi^{0.5}t^{0.5}} \tag{1.13}$$

$$I = \frac{4FADc^*}{\pi r_0}(0.7854 + 0.8862\tau^{-0.5} + 0.2146\exp(-0.7823\tau^{-0.5})) \tag{1.14}$$

where n is the number of electrons transferred, F the Faraday constant, A the electrode surface area, c^* is the concentration of the electroactive species, D the diffusion coefficient of the electroactive species, t the time, $\tau = 4Dt/r_0^2$, and r_0 the disk radius.

1.5 References

1. R. G. Compton and G. H. W. Sanders, *Electrode Potentials*, Oxford University Press, Oxford ; New York, 1996.
2. A. C. Fisher, Electrode Dynamics, Oxford University Press, Oxford ; New York, 1996.
3. A. J. Bard, L. Faulkner, *Electrochemical Methods: Fundamentals and Applications, second ed.*, Wiley & Sons, New York, 2001.
4. R.G. Compton, C.E. Banks, *Understanding Voltammetry, second ed.*, Imperial College Press, London, 2011.
5. H. L. von Helmholtz, *Wied. Ann.*, **7** (1879) 337.
6. G. Lipp, *Journal of the Franklin Institute*, **115** (1883) 310.
7. http://www.cheng.cam.ac.uk/research/groups/electrochem/teaching.html
8. D. Shoup, A. Szabo, *J. Electroanal. Chem.* **237** (1982) 140.

Chapter 2

Theories of Electrode Kinetics

This chapter provides the overview of kinetic theories studied in the current work. The discussion encompasses both the conceptual element and mathematical aspects of these models.

The asymmetric version of Marcus-Hush-Chidsey formalism for heterogeneous electrode kinetics described in Section 2.4 was developed in-house by Dr. E. Laborda and Dr. M. C. Henstridge.

2.1 Butler-Volmer Kinetics

The Butler Volmer model [1,2] of electrode kinetics is a phenomenological model which is most widely used for interpretation of electrochemical reactions due to its simplicity. This model is developed based on the view that, during an electrochemical reaction, the reactant is required to cross an energy barrier and go through a transition state before transforming into the product. Figure 2.1 depicts this behaviour for a reagent, A, being reduced into product, B:

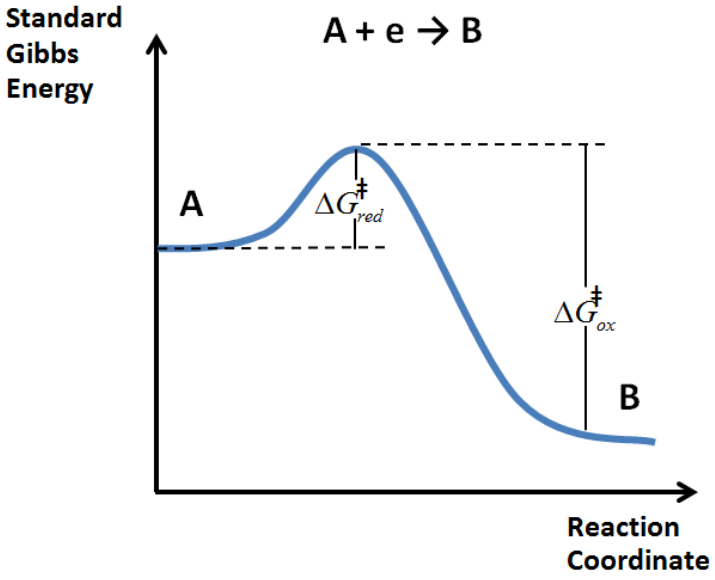


Figure 2.1: *Reaction profile for A/B redox couple at a fixed potential.*

Based on this model, the reaction rate constants (k_{red} for reduction and k_{ox} for oxidation) are given by:

$$k_{red} = Z \exp \frac{-\Delta G^{\ddagger}_{red}}{RT} \tag{2.1}$$

$$k_{ox} = Z \exp \frac{-\Delta G^{\ddagger}_{ox}}{RT} \tag{2.2}$$

where Z is a constant, R the ideal gas constant, T the temperature, $-\Delta G^{\ddagger}_{red}$ Gibbs energy of reduction reaction and $-\Delta G^{\ddagger}_{ox}$ its oxidation counterpart.

However, the reaction profile (hence $\Delta G_{red}^{\ddagger}$ and $\Delta G_{ox}^{\ddagger}$) varies with the applied potential $(\phi_M - \phi_S)$ where ϕ_M is the potential of the metal electrode and ϕ_S the potential of the solution phase. Therefore:

$$\Delta G_{red}^{\ddagger} = \Delta G_{red,0}^{\ddagger} + \alpha F(\phi_M - \phi_S) \tag{2.3}$$

$$\Delta G_{ox}^{\ddagger} = \Delta G_{ox,0}^{\ddagger} - (1 - \alpha) F(\phi_M - \phi_S) \tag{2.4}$$

where α is the transfer coefficient, $\Delta G_{red,0}^{\ddagger}$ the Gibbs energy of reduction with no applied voltage and $\Delta G_{ox,0}^{\ddagger}$ its oxidation counterpart. Substituting $(\phi_M - \phi_S)$ for $(E - E_f^0)$ + constant where E is the potential applied to the working electrode and E_f^0 is the formal potential, we can re-write Equations 2.1 and 2.2 to give the Butler-Volmer formalism:

$$k_{red} = k_0 \exp \frac{-\alpha F\left(E - E_f^0\right)}{RT} \tag{2.5}$$

$$k_{ox} = k_0 \exp \frac{\beta F\left(E - E_f^0\right)}{RT} \tag{2.6}$$

where k_0 is the standard electrochemical rate constant and transfer coefficient β = (1-α).

It is noteworthy that the transfer coefficients α and β correlates to the "position" of the transition state. For most electrochemical reactions, $\alpha = \beta = 0.5$, implying that the transition state behaves mid-way between the reagent and product [3,4]. For a one-electron transfer reaction, it is normally required that $\alpha + \beta = 1$.

2.2 Marcus Theory

The Marcus theory [5,6] is a mechanistic model which considers the microscopic physical processes that takes place during electron transfer. To account for energetic consideration with physical structural changes, the reagent and product are represented as potential energy curves (most conveniently represented by parabolic curves) along a reaction coordinate (Figure 2.2). As the rate of electron transfer is in a much shorter time-scale compared to that of nuclear motions [3,4] (following the Frank-Condon principle), electrons transfer between the reagent and product can only be represented as vertical shift in potential energy. Based on this view, it follows that the most energetically favourable configuration for electron transfer is represented by the point of crossing between the two potential energy curves. Considering a reagent which has been exited to reach the point of crossing, the excited species can remain on the reagent curve or transfer an electron and follows the product curve, effectively transforming into the product. The likelihood of this happening depends on the probability of electron transfer, K, which in turn is a function of the degree of electronic coupling between the two species, H_{AB}. In the adiabatic limit where coupling is strong, $K \sim 1$, while in the non-adiabatic limit where coupling is weak, $K << 1$.

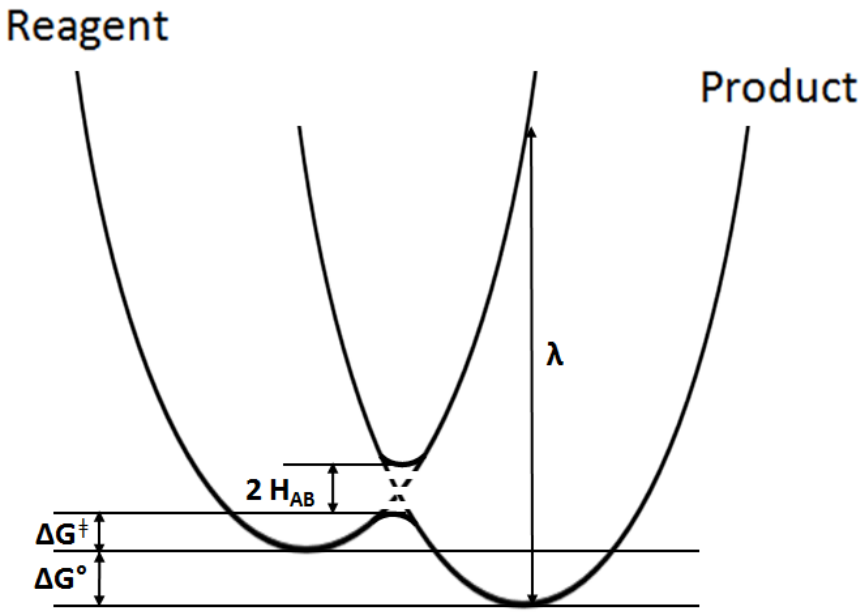


Figure 2.2: *Potential energy cures for the electron transfer process: Reagent = Product + e^-*

Based on this view, other features with significant importance defined by the Marcus theory includes the Gibbs energy of activation, $\Delta G^{\ddagger}$, and the reorganization energy, λ (both shown in Figure 2.2).

The activation energy can be expressed as:

$$\Delta G^{\ddagger} = \frac{\lambda}{4}\left(1 + \frac{\Delta G^{0}}{\lambda}\right)^{2} \tag{2.7}$$

The reorganization energy represents the energy required to change the nuclear configurations of the reactive species (inner-sphere reorganization energy, λ_i) and the

solvation shell around it (outer-sphere reorganization energy, λ_o) into those of the product state, such that the overall reorganization energy can be expressed as:

$$\lambda = \lambda_i + \lambda_o. \tag{2.8}$$

where λ_i can be expressed as the sum of all vibration modes of the species, and λ_o expressed as the change in Born solvation energy [6]:

$$\lambda_i = \frac{1}{2}\sum_j k_j \left(q_{product} - q_{reagent}\right)_j^2 \tag{2.9}$$

$$\lambda_o = \frac{e^2 N_A}{8\pi\varepsilon_0}\left(\frac{1}{r} - \frac{1}{2d}\right)\left(\frac{1}{\varepsilon_{op}} - \frac{1}{\varepsilon_s}\right) \tag{2.10}$$

where k_j are the force constants for each oscillator, q the displacement in normal mode corrdinates, e the elementary charge, ε_0 permittivity of free space, N_A the Avogrado's constant, r the radius of reagent, d the distance from reagent to the electrode surface, and ε_{op} and ε_{op} the optical and static permittivity of the solvent, respectively.

2.3 Marcus-Hush-Chidsey Formalism

The Marcus-Hush-Chidsey formalism is the application of the Marcus theory to electrode processes. Originally, the Marcus theory addresses homogeneous electron transfer only. Hush [7,8] has also contributed to the refinement of this theory. The application of the Marcus theory to electron transfer at the electrode is then developed

by Chidsey [9] who suggested the treatment of the metal electrode as electron source/sink with a continuum of electronic states. As a result of this, the overall rate of electron transfer will be the sum of rate at each electronic state, weighted by the probability of occupancy of that state described by the Fermi-Dirac distribution:

$$k_{red/ox} = \int_{-\infty}^{\infty} A_{red/ox}(\varepsilon) \frac{\exp\{\Delta G^{\ddagger}_{red/ox}(\varepsilon)/k_B T\}}{1 + \exp(\mp e(\varepsilon - E)/k_B T)} \tag{2.11}$$

where k_B the Boltzmann constant $A_{red/ox}(\varepsilon)$ a pre-exponential factor that includes the influence of the electronic coupling between metallic states and electroactive species and the density of electronic levels of the electrode and $\Delta G^{\ddagger}_{red/ox}$ is the activation energy of the reduction/ oxidation process given by:

$$\Delta G^{\ddagger}_{red}(x) = \frac{\Lambda}{4}\left(1 + \frac{\theta + x}{\Lambda}\right)^2 \tag{2.12}$$

$$\Delta G^{\ddagger}_{ox}(x) = \frac{\Lambda}{4}\left(1 - \frac{\theta + x}{\Lambda}\right)^2 \tag{2.13}$$

where $x = F(\varepsilon - E)/RT$, $\theta = F(E - E_f^{\ominus})/RT$ and $\Lambda = F\lambda/RT$.

Considering the pre-exponential factor to be independent of energy ($A(\varepsilon) \approx A$) the rate constants can be written as:

$$k_{red} = k_0 \exp\left[-\frac{\theta}{2}\right]\frac{\mathrm{I}(\Lambda,\theta)}{\mathrm{I}(\Lambda,0)} \tag{2.14}$$

$$k_{ox} = k_0 \exp\left[+\frac{\theta}{2}\right]\frac{\mathrm{I}(\Lambda,\theta)}{\mathrm{I}(\Lambda,0)} \tag{2.15}$$

where the integral $I(\Lambda,\theta)$ is given by:

$$I(\Lambda,\theta) = \int_{-\infty}^{\infty} \frac{\exp\left[\frac{-(\varepsilon-\theta)^2}{4\Lambda}\right]}{2\cosh\left[\frac{\varepsilon}{2}\right]} d\varepsilon \tag{2.16}$$

in which ε is an integration variable, evaluated numerically using the trapezium rule. In the limit of very high reorganization energy (i.e., $\Lambda \rightarrow\infty$), the ratio of integrals in Equations 2.14 and 2.15 tends to unity. Thus in this limit the Marcus-Hush-Chidsey rate constants (Equations 2.14 and 2.15) are reduced to their Butler-Volmer equivalents (Equations 2.5 and 2.6) for the case when α = 0.5.

2.4 Asymmetric Marcus-Hush-Chidsey Formalism

The asymmetric version of Marcus-Hush-Chidsey formalism [10] was developed in-house by Dr. E. Laborda and Dr. M. C. Henstridge. This makes use of the asymmetric version of the Marcus theory (see Appendix IV in reference [11]) which allows the disparity between the curvature of the reagent and product Gibbs energy curves to be accounted for.

Based on this approach, the Gibbs energy of the redox processes, which can be substituted into Equation 2.11 to give the asymmetric Marcus-Hush-Chidsey formalism, can be written as:

$$\Delta G_{red}^{\ddagger}(x) = \frac{\Lambda}{4}\left(1 + \frac{\theta + x}{\Lambda}\right)^2 + \gamma^* \left(\frac{\theta + x}{4\Lambda}\right)\left\{1 - \left(\frac{\theta + x}{\Lambda}\right)^2\right\} + \frac{\gamma^{*2}}{16\Lambda} \tag{2.17}$$

$$\Delta G_{ox}^{\ddagger}(x) = \frac{\Lambda}{4}\left(1 - \frac{\theta + x}{\Lambda}\right)^2 + \gamma^* \left(\frac{\theta + x}{4\Lambda}\right)\left\{1 - \left(\frac{\theta + x}{\Lambda}\right)^2\right\} + \frac{\gamma^{*2}}{16\Lambda} \tag{2.18}$$

where $\gamma^* = F\gamma/RT$ and the parameter γ defined by:

$$\gamma = \lambda_i \langle l_s \rangle = \lambda_i \frac{\sum_s k_s (\Delta q_s^0)^2 l_s}{\sum_s k_s (\Delta q_s^0)^2} \tag{2.19}$$

where Δq_s^0 is the difference of the equilibrium values for the s-th normal mode coordinate of reactants and products, and k_s and l_s symmetric and antisymmetric combinations of the force constants of the s-th mode of reactants and products, f_s^{ox} and f_s^{red} respectively:

$$k_s = \frac{2 f_s^{red} f_s^{ox}}{f_s^{red} + f_s^{ox}} \tag{2.20}$$

$$l_s = \frac{f_s^{ox} - f_s^{red}}{f_s^{ox} + f_s^{red}} \tag{2.21}$$

Based on this, the symmetric MH model can be considered a particular case of this model for which γ = 0. This is because, for the value of γ = 0, the activation Gibbs energy of the system collapses to that of the symmetric MH form.

2.5 Waldeck and Mishra Potential Energy Curve Model

Waldeck and Mishra [12] recently developed a kinetic model for heterogeneous electron transfer through the construction of the potential energy curve at each energy level of the electrode. Through the generalization of the Anderson-Newns model [12-14], the potential energy is given by:

$$G(q,x) = \frac{q^2}{4\lambda} + [\theta + x + \lambda(1-2z) + q]\langle n_r(q)\rangle - zq + \frac{\Delta}{2\pi}\ln[[\theta + x + \lambda(1-2z) + q]^2 + \Delta^2 + C] \tag{2.22}$$

where q is an effective reaction coordinate and C a constant. The parameter Δ is associated with the strength of the electronic interaction between the electrode and reactant electronic states that decays exponentially with the distance from the electrode, r [12-14]:

$$\Delta = \Delta_0 \exp[-\omega(r - r_0)] \tag{2.23}$$

where Δ_0 is the Δ value at the distance of closest approach (r_0), ω the spatial decay constant and $\langle n_r(q) \rangle$ the average occupation probability of the reactant orbital:

$$\langle n_r(q) \rangle = \frac{1}{2} + \frac{1}{\pi} \tan^{-1}\left(-\frac{\theta + x + \lambda(1 - 2z) + q}{\Delta}\right) \tag{2.24}$$

For small Δ values, the curves show two minima corresponding to the reduced and oxidized forms of the electroactive species, and a maximum that relates to the transition state. As the electronic coupling is stronger (that is, as the Δ value increases), there is a lowering of the energy barrier such that the transition region is less defined. In the limit of very large Δ, only one minimum is present signifying a barrierless process. From the difference between the potential energies of the electroactive species and the transition state, the reduction and oxidation activation energies can be determined from the energy curves. Following Mishra and Waldeck's formulation [12], the following relationships are employed for these calculations for the different energy levels, *x*, at a given overpotential:

$$\begin{aligned} &\Delta G^{\ddagger}_{red}(x) = G\left(q_{\dagger}, x\right) - G(q_{ox}, x) \qquad \text{for } x > x^{red}_{cr} \\ &\Delta G^{\ddagger}_{red}(x) = 0 \qquad \text{for } x^{red}_{cr} \geq x \geq -(\lambda + \theta) \\ &\Delta G^{\ddagger}_{red}(x) = \Delta G^{\ddagger}_{red}(-2(\lambda + \theta) - x) \qquad \text{for } x < -(\lambda + \theta) \end{aligned} \tag{2.25}$$

where x_{cr}^{red} is the critical value from which an activationless situation is attained and so the energy curve does not show two minima and a maximum but only one minimum.

The rate constant for reduction can then be calculated from the following expression [15]:

$$k_{red} = \frac{\upsilon_n}{\omega}\int_0^{\infty}\kappa_{el}\int_{-\infty}^{\infty}\frac{\exp\left[-\frac{\Delta G_{red}^{\ddagger}(x,r)}{RT}\right]}{1+\exp(-x^*)}dx^*d\omega(r-r_0) \tag{2.26}$$

where υ_n is the effective nuclear frequency, x^* the integral defined by x^* = F*x*/RT = F(ε-*E*)/RT with *F*ε being the energy of given electronic level and *E* the applied potential and the effect of the degree of adiabaticity on the electronic transmission coefficient (κ_{el}) can be estimated through the Landau-Zener expression [12,15]:

$$\kappa_{el} = \frac{2\left[1-\exp\left(-\frac{\upsilon_{el}}{2\upsilon_n}\right)\right]}{2-\exp\left(-\frac{\upsilon_{el}}{2\upsilon_n}\right)} \tag{2.27}$$

where υ_{el} is the electron tunnelling frequency:

$$\upsilon_{el} = \frac{4\pi^2\rho_M}{h\sqrt{4\pi\frac{\lambda F}{RT}}}H_{AB}^2 \tag{2.28}$$

where ρ_M is the density of electronic levels of the electrode, *h* the Planck's constant and H_{AB} is an effective average of the electronic coupling element at a given electron transfer distance.

Once the rate constant for the reduction process is known, its oxidation counterpart can then be found from the Nernst relationship: $k_{ox} = k_{red} \exp(\theta)$.

2.6 References

1. J. A. V. Butler, *Trans. Faraday Soc.* **28** (1932) 379.
2. T. Erdey-Grúz, M. Z. Volmer. *Phys. Chem.* **150** (1930) 203.
3. R. G. Compton and G. H. W. Sanders, *Electrode Potentials*, Oxford University Press, Oxford ; New York, 1996.
4. A. J. Bard, L. Faulkner, *Electrochemical Methods: Fundamentals and Applications, second ed.*, Wiley & Sons, New York, 2001.
5. R.A. Marcus, *J. Chem Phys.* **24** (1956) 4966.
6. R.A. Marcus, N. Sutin, *Biophys. Chim. Acta* **265** (1985) 811.
7. N.S. Hush, *J. Chem. Phys.* **28** (1958) 962.
8. N.S. Hush, *J. Electroanal. Chem.* **470** (1999) 170.
9. C.E.D. Chidsey, *Science* **215** (1991) 919.
10. E. Laborda, M. C. Henstridge, R. G. Compton, *J. Electroanal. Chem.* **667** (2012) 48.
11. R.A. Marcus, *J. Chem. Phys.* **43** (1965) 679.
12. A. K. Mishra, D.H. Waldeck, *J. Phys. Chem. C* **113** (2009) 17904.
13. W. Schmickler, *J. Electroanal. Chem.* **204** (1986) 31.
14. W. Schmickler, J. Mohr, *J. Chem. Phys.* **117** (2002) 2867.
15. S. W. Feldberg, N. Sutin, *Chem. Phys.* **324** (2006) 216.

Chapter 3

Instrumentation

This chapter presents a summary of instruments used during the research presented in this thesis, particularly those that were fabricated in-house. Fabrication techniques for the various types of electrodes used in this work are also discussed.

3.1 The High-Speed Channel Electrode

The high-speed channel electrode consists of flow channel (Figure 3.1) which houses the microband electrode and a pressurized apparatus (Figure 3.2) that provides a pressure gradient that drives the flow of the electrolyte solution. This system was developed and constructed in-house, and have been described previously [1-3].

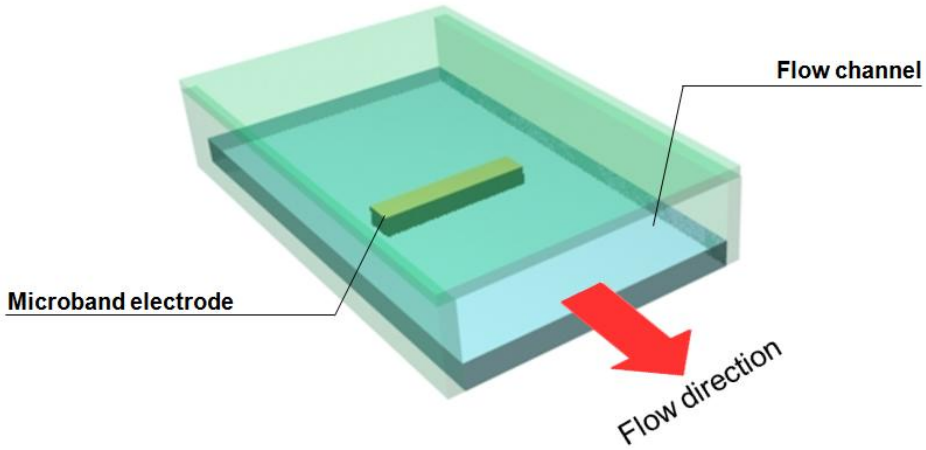


Figure 3.1: *Schematic of the flow channel*

Solution flow is induced across the flow channel by pressurizing a chamber which houses the solution by an argon source (BOC Gases Ltd., UK). The influx from high pressure argon cylinder is controlled by two fast-acting magnetic valves (Clippard Inc., Cinncinnati, Ohio, USA) operated through a computer. The pressure within the chamber is monitored by a silicon diaphragm pressure sensor (Entran Ltd., Watford, UK). Deoxygenation of the electrolyte solution can be achieved by bubbling argon through the solution (effectively pressurizing the chamber) and venting repeatedly.

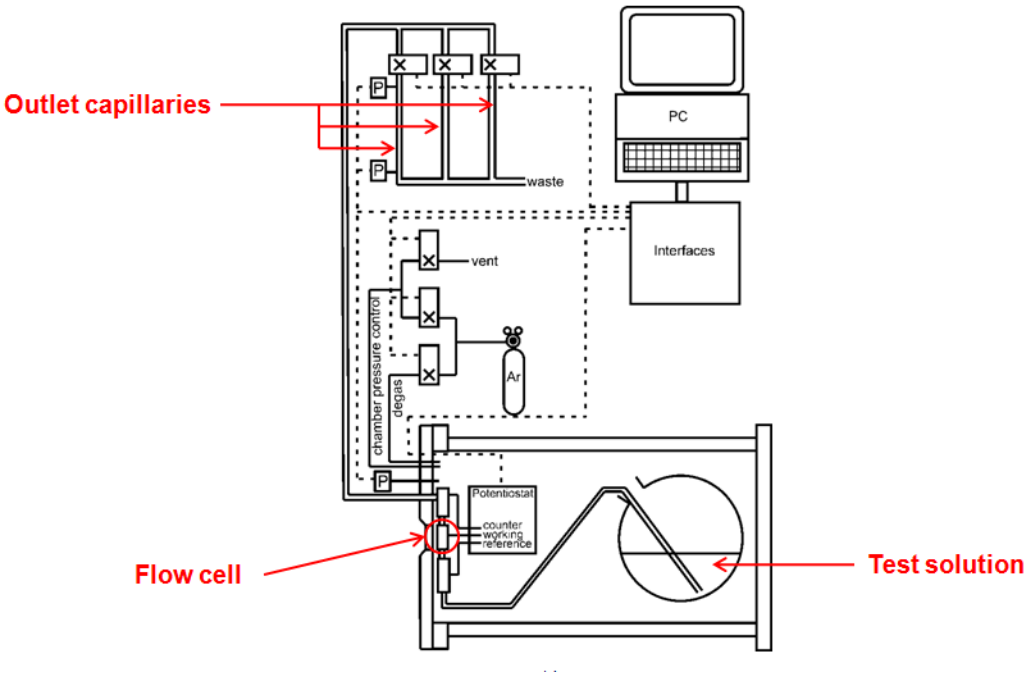


Figure 3.2: *Schematic of the pressurized apparatus*

Flow rates can be controlled by opening one of the three outlet electromagnetic valves (Neptune Research Inc., Maplewood, New Jersey, USA), each fitted to an outlet capillary with different bore size. This, combined with the pressure limit of up to 1.5 atmospheres, allows volume flow rates of between 0.1 and 4 cm^3 s^{-1} to be obtained. This corresponds to linear flow velocities close to the electrode of 0.7 to 20 m s^{-1}.

The flow channel is formed by clamping the flow cell (Figure 3.3) constructed of fused silica blocks (Optiglass Ltd, Hainault, Essex, UK) together with the microband electrode (fabrication described in Section 3.1). In order to prevent leakage, the assembly is sealed with silicone gasket. Due to the small dimensions of the flow channel (height in the order of 0.1 mm) well-defined laminar flow traverses across the electrode for all experimental flow rates employed.

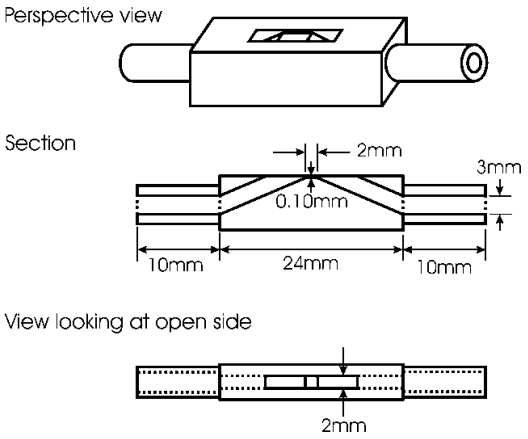


Figure 3.3: *Schematic of the fused silica block flow cell*

3.2 Fast Scan Potentiostat

The fast scan potentiostat used for all fast scan cyclic voltammetry in this work was constructed in-house by Mr. Philip Hurst (Electronics Workshop, PTCL) conforming to schematics provided by Prof. Christian Amatore (ENS, Paris). The potentiostat is capable of providing scan rate of up to 3×10^4 V s^{-1} with a response time of 0.5 μs. A positive feedback circuit included in the design enables on-line compensation of ohmic drop. The applied potential was controlled with a TTi TG1304 function generator (Thurlby Thandar Instruments Ltd, Huntingdon, Cambs, UK). The current response recorded with a Tektronix TDS 3032 oscilloscope and data processing

was carried out through the use of Wavestar software for oscilloscope (Tektronix UK Ltd, Bracknell, UK).

The schematics of the fast scan potentiostat circuit design are presented in Appendix 1.

3.3 Electrode Fabrication

3.3.1 Microband Electrodes

Microband electrodes used in the work described in Chapter 4 are fabricated in-house. The fabrication steps are shown in Figure 3.4 and are described as follows:

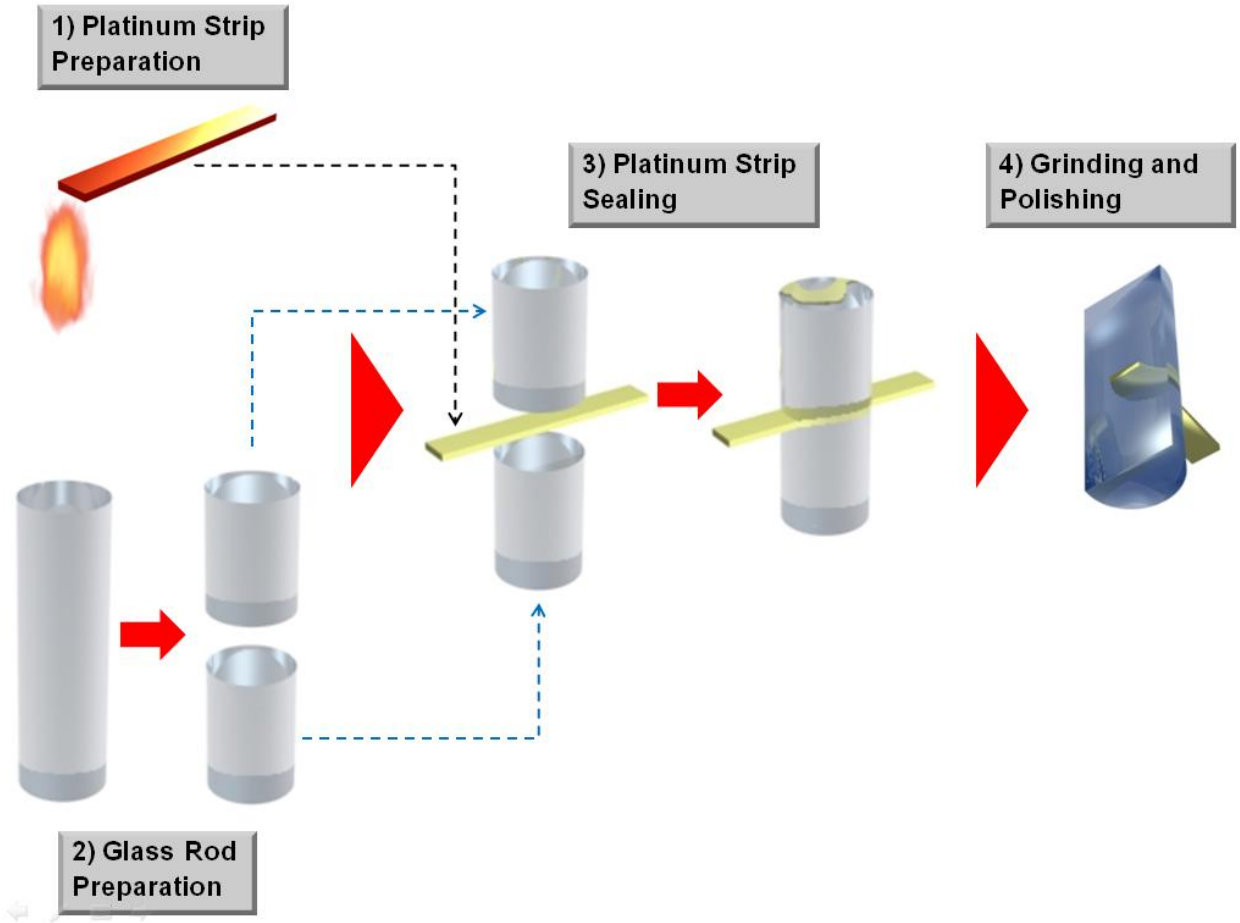


Figure 3.4: *Procedure for microband electrode fabrication.*

Step 1: Platinum strip preparation

A platinum strip of desired dimensions is cut from a platinum foil. The strip is then heated over ethanol flame for cleaning.

Step 2: Glass rod preparation

A soda glass rod is cleaved in the middle with a glass knife.

Step 3: Platinum strip sealing

The platinum strip is placed between the cleaved surfaces of the glass rod. The assembly is then placed within a programmable furnace at a temperature of 935 K for 3.5 hours, fusing the platinum strip into thee soda glass matrix.

Step 4: Grinding and polishing

The fused assembly is then ground using a diamond lapping wheel to expose a cross-section of the platinum strip. The ground surface is then polished to a mirror finish using 1.0, 0.3 and 0.05 μm alumina-water slurry on soft lapping pads (Buehler, Illinois). The protruding section of the platinum strip is connected to a copper strip using silver loaded epoxy resin (RS Components Ltd, Corby, Northants, UK) to provide an electrical contact.

3.3.2 Microdisk Electrodes

Microdisk electrodes used throughout the experimental work in this thesis are fabricated in-house conforming to the procedure described previously [4]. The fabrication steps are laid out as follows:

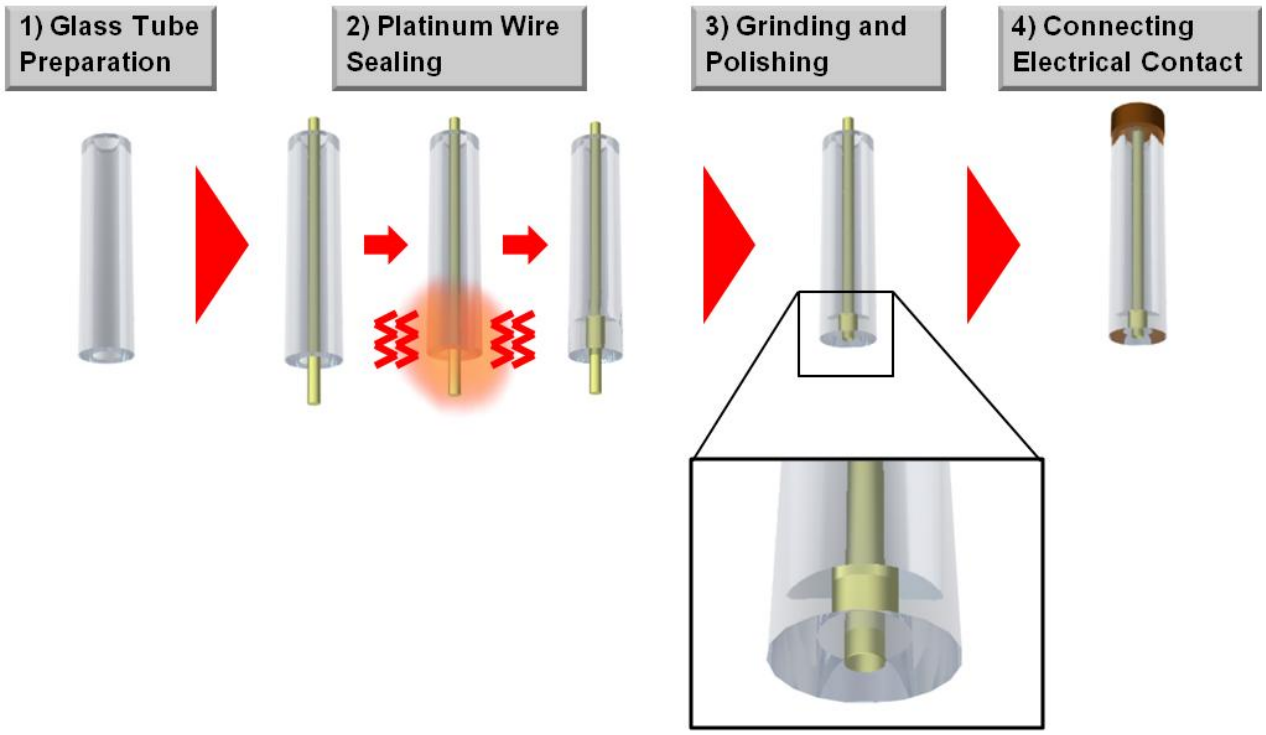


Figure 3.5: *Procedure for microdisk electrode fabrication.*

Step 1: Glass tube preparation

A section of soda glass capillary with desired length is cut with a glass knife.

Step 2: Platinum wire sealing

A microwire with desired dimensions is inserted through the capillary of the glass tube. One end of the assembly is then heated at 935 K in a variac heater, fusing the microwire into the glass matrix. It is also noteworthy that, if the radius of the microwire is very small (< 10 μm), only a short section of the microwire is placed at fused end and a larger connecting wire is used to provide electrical contact to ensure adequate mechnical strength.

Step 3: Grinding and polishing

A section of the fused tip is then ground away using a diamond lapping wheel to expose a cross-section of the platinum wire. The ground surface is then polished to a mirror finish using 1.0, 0.3 and 0.05 μm alumina-water slurry on soft lapping pads (Buehler, Illinois). The exposed platinum disk at the fused tip forms the working surface of the microdisk electrode.

Step 4: Connecting electrical contact

The protruding section of the platinum wire at the open end of the capillary is connected to a copper strip using silver loaded epoxy resin (RS Components Ltd, Corby, Northants, UK) to provide an electrical contact, forming the completed microdisk electrode.

3.4 References

1. N. V. Rees, R. A. W. Dryfe, J. A. Cooper, B. A. Coles, R. G. Compton, S. G. Davies, T. D. McCarthy, *J. Phys. Chem.* **99** (1995) 7096.
2. N. V. Rees, J. A. Alden, R. A. W. Dryfe, B. A. Coles, R. G. Compton, *J. Phys. Chem.* **99** (1995) 14813.
3. N. V. Rees, O. V. Klymenko, B. A. Coles, R. G. Compton, *J. Electroanal. Chem.* **534** (2002) 151.
4. C. Amatore, E. Maisonhaute, G. Simonneau, *J. Electroanal. Chem.* **486** (2000) 141.

PART II

Comparative Study of the Marcus-Hush-Chidsey and Butler-Volmer Formalisms

Part II presents a comparative study between the use of the Marcus-Hush-Chidsey and Butler-Volmer formalisms in the fitting of experimental voltammetric responses. Experimental studies reported include the oxidation of 9,10-diphynylanthracene and reduction of 2-nitropropane at the High-Speed Channel Microband Electrode (Chapter 4), and the reduction of cyclooctatetraene at the hemispherical mercury electrode (Chapter 5). These model processes cover a wide range of electron transfer rates, spanning more than 3 orders of magnitude.

Programs used for cyclic voltammetry simulations were written by Dr. M. C. Henstridge, and for square wave voltammetry, by Dr. E. Laborda.

Chapter 4

Experimental Comparison of the Marcus-Hush-Chidsey and Butler-Volmer Descriptions of Electrode Kinetics. The One-Electron Oxidation of 9,10-Diphenylanthracene and One-Electron Reduction of 2-Nitropropane Studied at High-Speed Channel Microband Electrodes

The work presented in this chapter has been published in

J. Phys. Chem. C **115** (2011) 14876.

In this chapter, an experimental comparative evaluation of the Marcus-Hush-Chidsey (MH) and Butler-Volmer (BV) kinetic formalisms. Numerical simulations using both kinetic models are used to fit experimental voltammetry of the one-electron oxidation of 9,10-diphenylanthracene (DPA) and the one-electron reduction of 2-nitropropane (NP) at a high-speed channel microband electrode. For DPA the Butler-Volmer and Marcus-Hush-Chidsey formalisms yield indistinguishable fits, as expected for a system with fast electrode kinetics. For the BV formalism best fits were obtained with k_0 = 0.83 cm s^{-1} and α = 0.49; for MH the best fit parameters were k_0 = 0.85 cm s^{-1} and λ = 0.58 eV. For NP, neither Butler-Volmer nor Marcus-Hush-Chidsey models are able to obtain very accurate fits to experiment, although it was possible for the Butler-Volmer model to yield more accurate fits if the transfer coefficients, α and β, are not required to sum to unity, which is possibly justifiable due to the very large difference between oxidative and reductive peak potentials. The best fit obtained using MH

kinetics used $k_0 = 7.0 \times 10^{-6}$ cm s^{-1} and $\lambda = 1.0$ eV, while BV kinetics was able to fit using $k_0 = 9.5 \times 10^{-4}$ cm s^{-1} and $\alpha = \beta = 0.24$.

Programs used for simulation work in this chapter were written by Dr. M. C. Henstridge.

4.1 Introduction

The theoretical interpretation of electron transfer at electrodes has developed significantly over the past century, from the purely phenomenological yet well-established Butler-Volmer approach[1,2] through the more physically based work of Marcus [3-8] to more recent stochastic and quantum mechanical models [9-20]. Following the seminal paper by Chidsey [21], Marcus-Hush-Chidsey theory has become increasingly used and has been applied to surface-bound species by several groups [22-29]. Feldberg has recently published some theoretical work concerning electron transfer from the electrode to electroactive species in solution[30], derived the conditions required for equivalence between the BV and MH formalisms at a disk electrode, and suggests that discrepancies between the models should be observable where the diffusion layer approaches 100 nm. However, to date, no experimental studies have been reported.

The Butler-Volmer equation (see Chapter 2.1) relates electron transfer to a standard heterogeneous rate constant, k_0, and two transfer coefficients α and β. This formulation has proved very successful in the analysis and interpretation of electron transfer at electrodes, especially where low overpotentials are involved. The principle of microscopic reversibility as applied to Butler-Volmer theory suggests that the sum of the transfer coefficients α and β is unity. While this will very likely be true for reactions of low overpotential, in the case of extremely slow reactions such that distinct oxidation

and reduction voltammetric waves are seen at very different potentials, this need not necessarily apply since the forward and backward reactions take place under very different conditions, viz, contrasting electrode potentials. Physically, such a difference might arise from the potential dependence of the double-layer and/or solvation of electroactive species.

Marcus theory has steadily developed since the first paper in 1956 [3], covering numerous applications and environments where electron transfer occurs, and many aspects of it have been verified experimentally, including the prediction of the existence of the so-called "inverted region" and the theoretical basis of curved Tafel plots [21,31]. The Marcus theory has been described in more detail in Chapter 2.2. By relating the standard heterogeneous rate constant to a reorganization energy, it has provided a physical model for understanding the energetic control on electron transfer as well as a means of its calculation: outer-sphere(solvent) reorganization energy from the Born-Marcus solvation equation and inner-sphere reorganization energy from calculations (e.g., DFT) of changes in bond lengths, angles, etc. of the molecule. The Marcus-Hush-Chidsey treatment (see also Chapter 2.3) considers the electrode as a continuum of energy levels with the electroactive species represented by the familiar parabolic free energy curve. An early success of the Marcus theory in an approximate form which considered only electron transfer to and from the Fermi level was the modeling of the potential dependence of the apparent transfer coefficient measured for the reduction of t-nitrobutane in dimethylformamide and acetonitrile by Savéant and Tessier[33]. Note that this is a seemingly curious system in that the standard electrochemical rate constant is found to be faster in DMF than MeCN, contrary to the simple expectation for an outer-sphere electron transfer process where the faster relaxation dynamics of MeCN (in

particular the longitudinal dielectric relaxation: 0.2 and 7ps for MeCN and DMF respectively) are normally found to lead to faster electron transfer[32].

In this chapter, a comprehensive experimental comparison of the Marcus-Hush-Chidsey (MH) and Butler-Volmer (BV) formalisms is attempted. We consider the MH and BV formalisms under hydrodynamic conditions, using a high-speed channel electrode system (HSChE). The HSChE has been described previously[34] (see also Chapter 3.1) and consists of a pressurized chamber containing the solution of interest and electrode assembly. The solution flows through a flow-cell containing the working electrode and out through one of three capillaries to the exit at atmospheric pressure. The flowcell is designed to smoothly accelerate the solution flow as it enters the channel, achieving volume flow rates of 4 cm^3 s^{-1} and linear solution velocities of 20 m s^{-1}. This arrangement enables Reynolds' numbers approaching 10^4 to be reached while maintaining a well-defined laminar flow profile. It has been found that the measured E_f^o is independent of scan rate at a given volume flow rate of solution, and the channel electrode is designed such that no distortions due to ohmic losses are observed for fully supported systems [35]. The HSChE was chosen over other hydrodynamic microelectrode arrangements due to its reliable and extensive use in accurately measuring a wide range of electron transfer kinetics [36]. Previous studies using the HSChE have widely utilized the BV formalism for interpretation of experimental data, but it has also been used with particular success to verify results of semi-classical Marcus theory [32,37-39].

As test systems for use in the HSChE, we have selected the one-electron reduction of 2-nitropropane (NP) and the one-electron oxidation of 9,10-diphenylanthracene (DPA). NP was chosen due to its having a potential-dependent value of α, a feature which is predicted of Marcus theory [40]. DPA was chosen to enable

confirmation of the coincidence of the MH and BV models for redox systems with fast electrode kinetics. In addition, substituted anthracenes have been shown to obey the Marcusian relationship between heterogeneous rate constant and reorganization energy[32]. These molecules have literature k_0 values of 10^{-2} and 0.94 cm s^{-1} and α values of 0.4 and 0.5 [32,40]. The literature values for NP were based on measurements at mercury electrodes which, from our preliminary work and a survey of related nitroalkanes in the literature [40,41], are typically greater than those measured at platinum electrodes. Both DPA and NP have the additional benefit of being neutral molecules, thus minimizing any possible double-layer effects.

4.2 Theory

We consider the redox reaction A + e $\rightleftharpoons$ B taking place in a solution flowing over a microband electrode embedded in a channel (Figure 1). We assume in the presence of sufficient supporting electrolyte that migration may be neglected and that the width (w_e) of the electrode is much larger than its length (x_e) in the direction of flow, thus reducing the problem to two spatial dimensions. In addition, we assume the flow to be laminar and the flow velocity to be sufficiently high so that the effects of axial diffusion may be neglected [42].

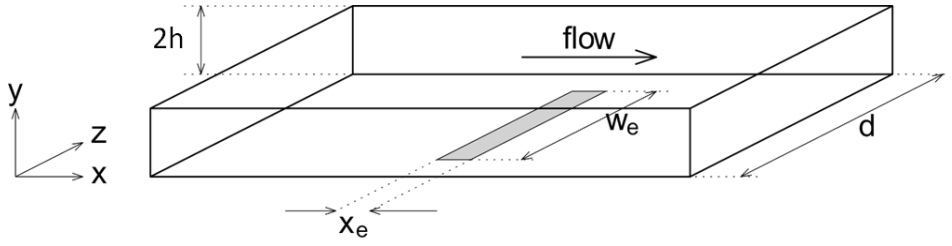


Figure 4.1: *Schematic diagram of the flow cell*

The mass transport equation is therefore

$$\frac{\partial c_i}{\partial t} = D_i \frac{\partial^2 c_i}{\partial y^2} - v_x \frac{\partial c_i}{\partial x} \tag{4.1}$$

where c_i (mol cm^{-3}) and D_i (cm^2 s^{-1}) are respectively the concentration and diffusion coefficient, t (s) is time, x and y (cm) are respectively distance parallel and perpendicular to the direction of flow, and v_x (cm s^{-1}) is the flow velocity profile, given by

$$v_x = v_0 \left[1 - \frac{(h-y)^2}{h^2}\right] \tag{4.2}$$

where v_0 (cm s^{-1}) is the flow velocity in the middle of the channel and h (cm) is the half-height of the channel.

Equation 4.1 is discretized using the space-marching backward implicit method[43], over a regular grid along the x-axis and an expanding grid along the y-axis, subject to the following

$$t = 0 \quad all\ x, y \quad c_A = c_A^*, c_B = 0 \tag{4.3}$$

$$t > 0 \quad x < 0 \quad c_A = c_A^*, c_B = 0 \tag{4.4}$$

$$t > 0 \quad y = 2h \quad \frac{\partial c_A}{\partial y} = 0, \frac{\partial c_B}{\partial y} \tag{4.5}$$

$$t > 0 \quad 0 < x \leq x_e, y = 0 \quad D_A \frac{\partial c_A}{\partial y} = k_{red} c_A - k_{ox} c_B \tag{4.6}$$

where c_A^* (mol cm^{-3}) is the bulk concentration of A and k_{red} and k_{ox} (cm s^{-1}) are the rate constants for reduction and oxidation respectively, which are defined differently within the Butler-Volmer and Marcus-Hush-Chidsey formalisms.

Within the Butler-Volmer model these rate constants are given by

$$k_{red} = k_0 exp[-\alpha\theta] \tag{4.7}$$

$$k_{ox} = k_0 exp[+\beta\theta] \tag{4.8}$$

where k_0 (cm s^{-1}) is the standard electrochemical rate constant, α and β are transfer coefficients, and θ is dimensionless potential, defined thus

$$\theta = \frac{F}{RT}\left(E - E_f^{\ominus}\right) \tag{4.9}$$

where E (V) is potential, $E_f^{\ominus}$ (V) is the formal potential, and F, R and T are, respectively, the Faraday constant, gas constant, and absolute temperature. Within the Marcus-Hush-Chidsey formalism for electron transfer at a metallic electrode [21,30,44] these rate constants are given by

$$k_{red} = k_0 \exp\left[-\frac{\theta}{2}\right]\frac{\mathrm{I}(\Lambda,\theta)}{\mathrm{I}(\Lambda,0)} \tag{4.10}$$

$$k_{ox} = k_0 \exp\left[+\frac{\theta}{2}\right]\frac{\mathrm{I}(\Lambda,\theta)}{\mathrm{I}(\Lambda,0)} \tag{4.11}$$

where Λ is dimensionless reorganization energy, defined thus

$$\Lambda = \frac{F}{RT}\lambda \tag{4.12}$$

in which λ (eV) is reorganization energy and the integral

$$I(\Lambda,\theta) = \int_{-\infty}^{\infty} \frac{\exp\left[\frac{-(\varepsilon-\theta)^2}{4\Lambda}\right]}{2\cosh\left[\frac{\varepsilon}{2}\right]} \tag{4.13}$$

in which ε is an integration variable, evaluated numerically using the trapezium rule. In the limit of very high reorganization energy (i.e., $\Lambda \rightarrow\infty$), the ratio of integrals in Equations 4.10 and 4.11 tends to unity. Thus in this limit the Marcus-Hush-Chidsey rate constants (Equations 4.10 and 4.11) are reduced to their Butler-Volmer equivalents (Equations 4.7 and 4.8) for the case when α = 0.5.

In this work we consider cyclic voltammetry, and thus the potential applied at the electrode varies as a function of time according to

$$E(t) = |E_1 - \sigma t - E_2| + E_2 \tag{4.14}$$

where E_1 and E_2 (V) are the starting and vertex potentials respectively and σ (V s^{-1}) is the scan rate.

The resulting set of simultaneous equations, which forms a diagonal matrix, is then solved using the Thomas algorithm [45].

Both the Butler-Volmer and Marcus-Hush-Chidsey program variants were written in C++ and run on a desktop PC. Due to the inherent extra calculation required in numerically evaluating the integral in Equation 4.13 when calculating the rate

constants for the Marcus-Hush-Chidsey model, these simulations were slightly slower than those for the Butler-Volmer model. However for both programs typical simulation times were below 10 s.

4.3 Experimental

Tetra-n-butylammonium perchlorate (TBAP, Fluka puriss grade), 9,10-diphenylanthracene (DPA, 98% Aldrich), 2-nitropropane (NP, 99% Aldrich), and acetonitrile (HPLC grade, Fisher Scientific) were all used as received without further purification. All solutions contained 0.1M of TBAP as supporting electrolyte to ensure that the voltammetry was fully supported [46]. Microband working electrodes of lengths (x_e) 12.5 and 40.5 μm and widths (w_e) 0.87 and 0.96 mm, respectively, were fabricated in-house by sealing Pt foil (Goodfellow Cambridge Ltd., U.K.) into soda glass according to a published method [34]. The 12.5 and 40.5 μm electrodes were used for the DPA and NP investigations respectively. A silver quasi-reference and large surface area platinum coil counter electrode completed the three-electrode arrangement. The high-speed channel apparatus has been described previously, and the solution flow within it fully characterized and shown to be laminar under the conditions used within this study[32,34,37-39,42,43,47,48].The fast-scan potentiostat, capable of ohmic drop compensation by means of an internal positive feedback circuit, was constructed in-house according to a design from Amatore et al. [49] and was operated in conjunction with the flow apparatus as described previously [48].

4.4 Results and Discussion

Quantifying Quality of Fit

In order to quantify agreement between simulation and experiment, mean-scaled absolute deviation (MSAD) was calculated [47], which is defined by

$$\%MSAD = \frac{1}{n}\sum_{n}\left|\frac{i_{exp} - i_{sim}}{i_{exp}}\right| \times 100 \tag{4.15}$$

where i_{exp} and i_{sim} are experimental and simulated current respectively and n is the number of data points. Since the points of the simulated voltammetry are not necessarily aligned at the same potential values as those of the experimental voltammetry, spline interpolation was used to calculate i_{sim} at the potentials of the experimental points. Additionally a narrow strip of the experimental voltammetry near $i = 0$ was omitted from the MSAD calculations because dividing by a very small value of i_{exp} yields a very large value of MSAD even if $i_{exp} - i_{sim}$ is small. In particular, for the forward scan, i_{exp} smaller than 10% of the peak reductive current are disregarded. For the reverse scan, an analogous procedure is carried out after translating the reverse voltammogram along the current axis so that the vertex (starting point of the reverse scan) begins at $i = 0$. The MSAD values at each point considered are then averaged to yield a final value of average MSAD per point.

Oxidation of 9,10-Diphenylanthracene

The first system of study was chosen to be the one-electron oxidation of DPA [32]. Linear sweep and cyclic voltammetries (LSV and CV) were performed on solutions containing 0.67 mM DPA and 0.1 M TBAP in acetonitrile at a range of volume flow

rates and voltage scan rates. The scan rates used ranged from 200 mV s^{-1} to 2 kV s^{-1} and encompassed steady-state to transient voltammetry.

In order to rigorously compare simulation to experiment for the MH and BV approaches, we first measured the diffusion coefficients of both DPA and $DPA^{\bullet+}$ via double-potential step chronoamperometry at a platinum microdisk (radius 10 μm). The direct use of a simulation model using finite electrode kinetics was not practical, since both k_0 and D are unknown, and so the following procedure was adopted.

First, the double-potential step transients were simultaneously fitted for both diffusion coefficients and concentration using a previously reported program [50], based on the Shoup and Szabo expression (and therefore assuming infinite electrode kinetics)[51]. The diffusion coefficients of both neutral and radical cation species were found to be equal taking the value of 1.40×10^{-5} cm^2 s^{-1}. These diffusion coefficients were then used in conjunction with the MH and BV cyclic voltammetry programs outlined above, to model full cyclic voltammograms (CVs) over the full range of voltage scan rates: fitting the peak position thereby fixing both the formal potential ($E_f^{\ominus}$) and standard heterogeneous electron transfer rate constant (k_0).

Having derived a value for the heterogeneous rate constant (for MH and BV), this was used to verify the diffusion coefficients by repeating the simulation of the double-potential step chronoamperograms using a program based on finite electrode kinetics [52]. Again, the diffusion coefficients of both neutral and radical cation species were found to be effectively equal with the value of 1.40×10^{-5} cm^2 s^{-1}, in excellent agreement with both the value derived assuming infinite electrode kinetics and the literature [32].

These diffusion coefficients were then used with the MH and BV programs outlined above to model full CVs over the full range of voltage scan rates. An example of the simulation results is shown in Figure 4.2.

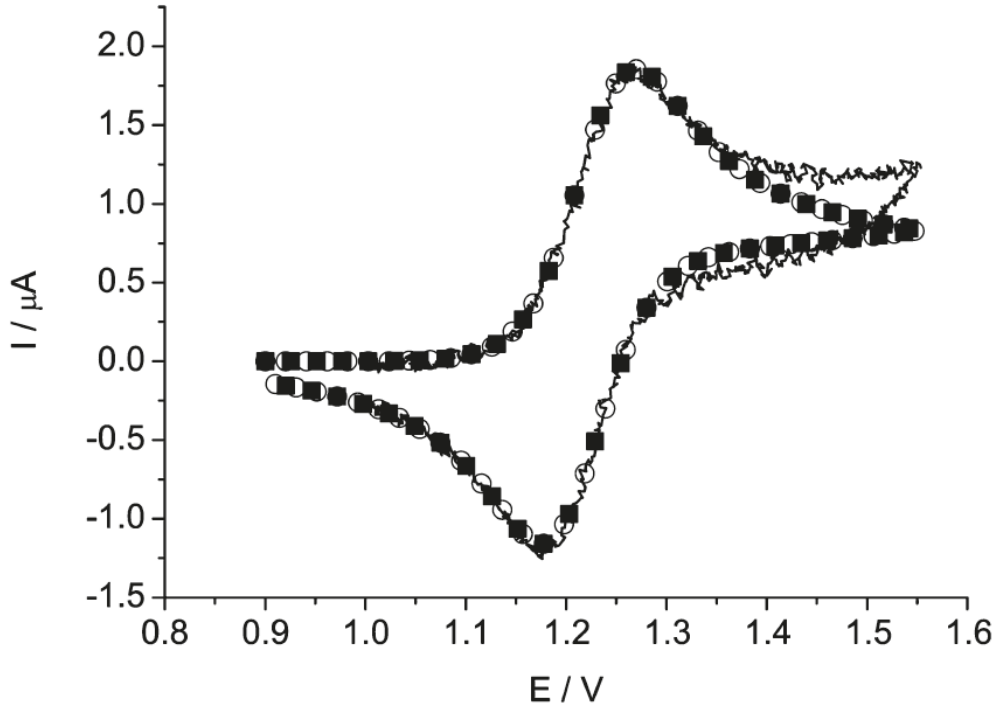


Figure 4.2: *Cyclic voltammetry of DPA oxidation (background subtracted) measured at a volume flow rate of 0.14 cm^3 s^{-1} and voltage scan rate of 1 kV s^{-1}, including simulations using Butler-Volmer (solid squares) and Marcus-Hush-Chidsey (open circles). Simulation parameters are given in Table 1. The high currents at E > 1.4 V are due to the influence of the nearby second oxidation wave.*

Finally, the MH and BV programs were used to systematically simulate voltammograms across all scan rates, to find a common set of parameters that provided a "best fit" of theory to experiment. Table 4.1 lists the parameters thus obtained, along with the MSADs. These results show that under the BV formalism, k_0 = 0.83 ± 0.15 cm s^{-1} and α = 0.49 ± 0.02 (comparing well with literature values of k_0 = 0.94 ± 0.16 cm s^{-1} and α = 0.53 ± 0.02 respectively [32]), and under the MH approach k_0 = 0.85 ± 0.17 cm s^{-1} and λ = 0.58 ± 0.08 eV. The value of the reorganization energy agrees well with the outer-sphere reorganization energy of 0.50 eV calculated from

$$\lambda_{os} = \frac{N_A e^2}{8\pi\varepsilon_0 r}\left(\frac{1}{\varepsilon_{op}} - \frac{1}{\varepsilon_s}\right) \tag{4.16}$$

via the spherical approximation of the Stokes-Einstein equation [32,37-39]

$$r = \frac{k_B T}{6\pi\eta D} \tag{4.17}$$

where r is the molecular radius here treated as the solvodynamic radius according to Clegg et al. [32], ε_0 is the permittivity of free space, ε_{op} and ε_s are the optical and static frequency components of the dielectric permittivity of the solvent, η is the solvent viscosity, and D is the diffusion coefficient. N_A, e, k_B and T have their usual meanings.

Table 4.1: *Best fit simulations parameters for DPA*

	Butler-Volmer	**Marcus-Hush-Chidsey**
k_0 (cm s^{-1})	0.83 ± 0.15	0.85 ± 0.17
α	0.49 ± 0.02	-
λ (eV)	-	0.58 ± 0.08
E_f^{Θ} (V)	1.18 ± 0.3	1.18 ± 0.3
% MSAD	3.1 ± 0.8	3.0 ± 0.7

Examination of the MSAD values in Table 4.1 illustrates that for this system, there is no discernible difference between the abilities of the MH and BV formalisms to simulate the experimental data. Figure 4.3 illustrates the equivalence of MH and BV best fits to the experimental voltammetry.

Reduction of 2-Nitropropane

Analogous experiments and procedures were followed for the one-electron reduction of NP, using solutions of 2.65 mM NP in 0.1 M TBAP and acetonitrile. Double-potential step chronoamperometry at a microdisk electrode was conducted to determine the diffusion coefficients of the neutral and radical anion species at 3.1×10^{-5} and 2.7×10^{-5} cm^2 s^{-1} respectively, having carried out the same procedure and verifications on simulation programs as described above for DPA (no literature values exist for NP species, but the related t-nitropropane was reported to be 3×10^{-5} cm^2 s^{-1} [40,53]). Cyclic and linear-sweep voltammograms were then recorded under solution flow for voltage scan rates ranging from 0.2 to 2000 V s^{-1}. Due to the high rates of mass transport, combined with the highly irreversible nature of the $NP/NP^{\bullet-}$ redox couple, the

anodic peak was only clearly observable in the CV for scan rates exceeding 1 kV s^{-1}: attempts to simulate these high scan rate data to determine values for E_f^{Θ} and k_0 revealed two limiting cases for each of the Butler-Volmer and Marcus-Hush-Chidsey approaches, illustrated in Figures 4.4 and 4.5 and parametrized in Table 4.2. There was no observed systematic variation of either E_f^{Θ} or k_0 with varying flow rate or varying scan rate; thus, ohmic drop does not distort the voltammetry.

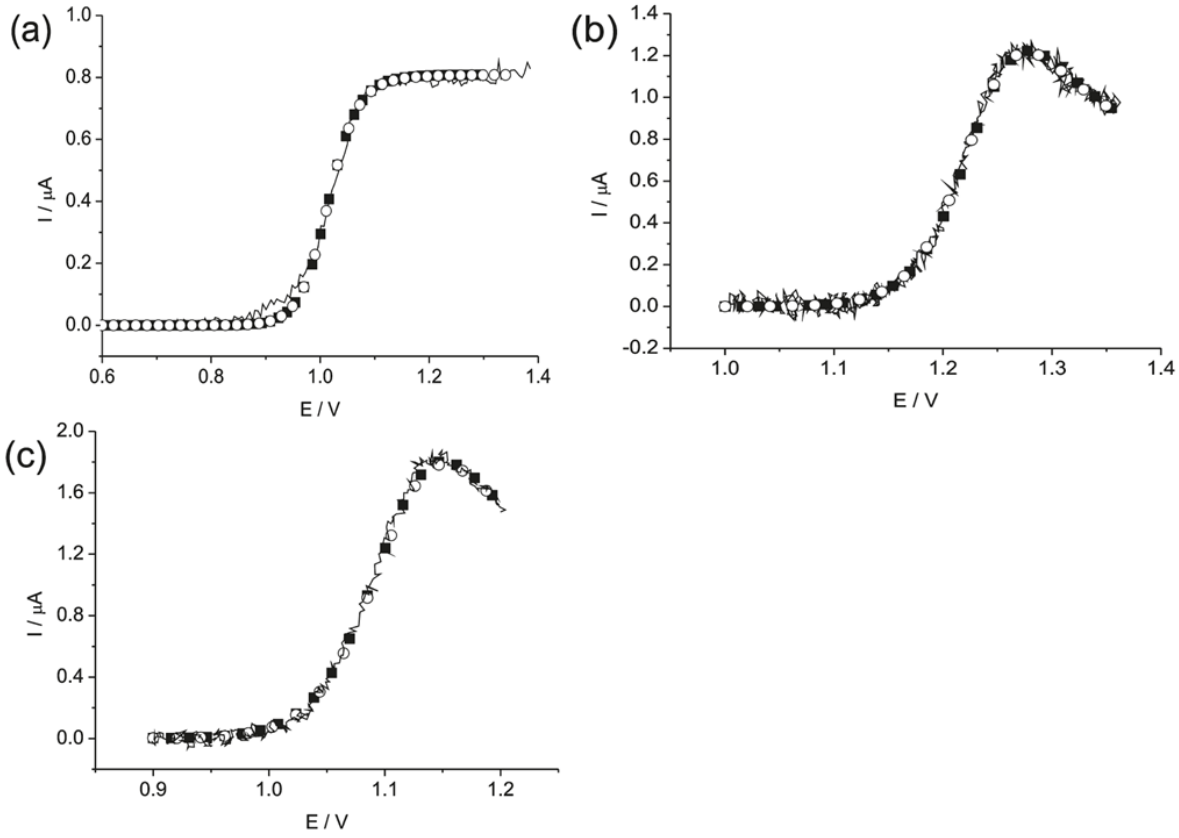


Figure 4.3: *Experimental linear sweep voltammetry of DPA oxidation (solid line) compared to Butler-Volmer (solid squares) and Marcus-Hush-Chidsey (open circles) theoretical results for a volume flow rate of 0.14 cm^3 s^{-1} and voltage scan rates of (a) 1, (b) 250, and (c) 1000 V s^{-1}.*

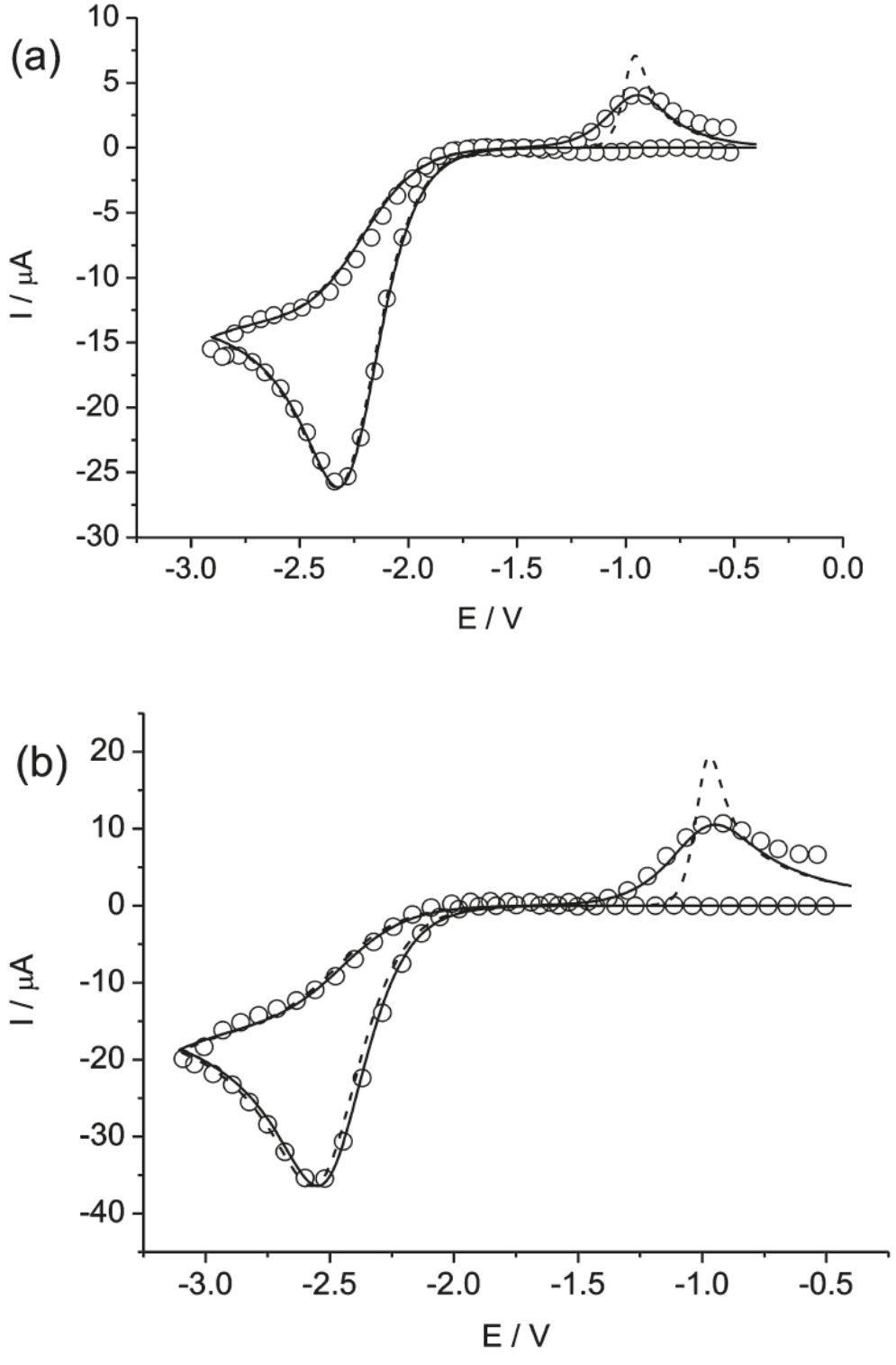


Figure 4.4: *Experimental cyclic voltammetry of NP reduction (open circles) compared to Butler-Volmer cases I (dotted line) and II (solid line) for scan rates of (a) 1000 and (b) 2000 V s^{-1} at a volume flow rate of 0.14 cm^3 s^{-1}.*

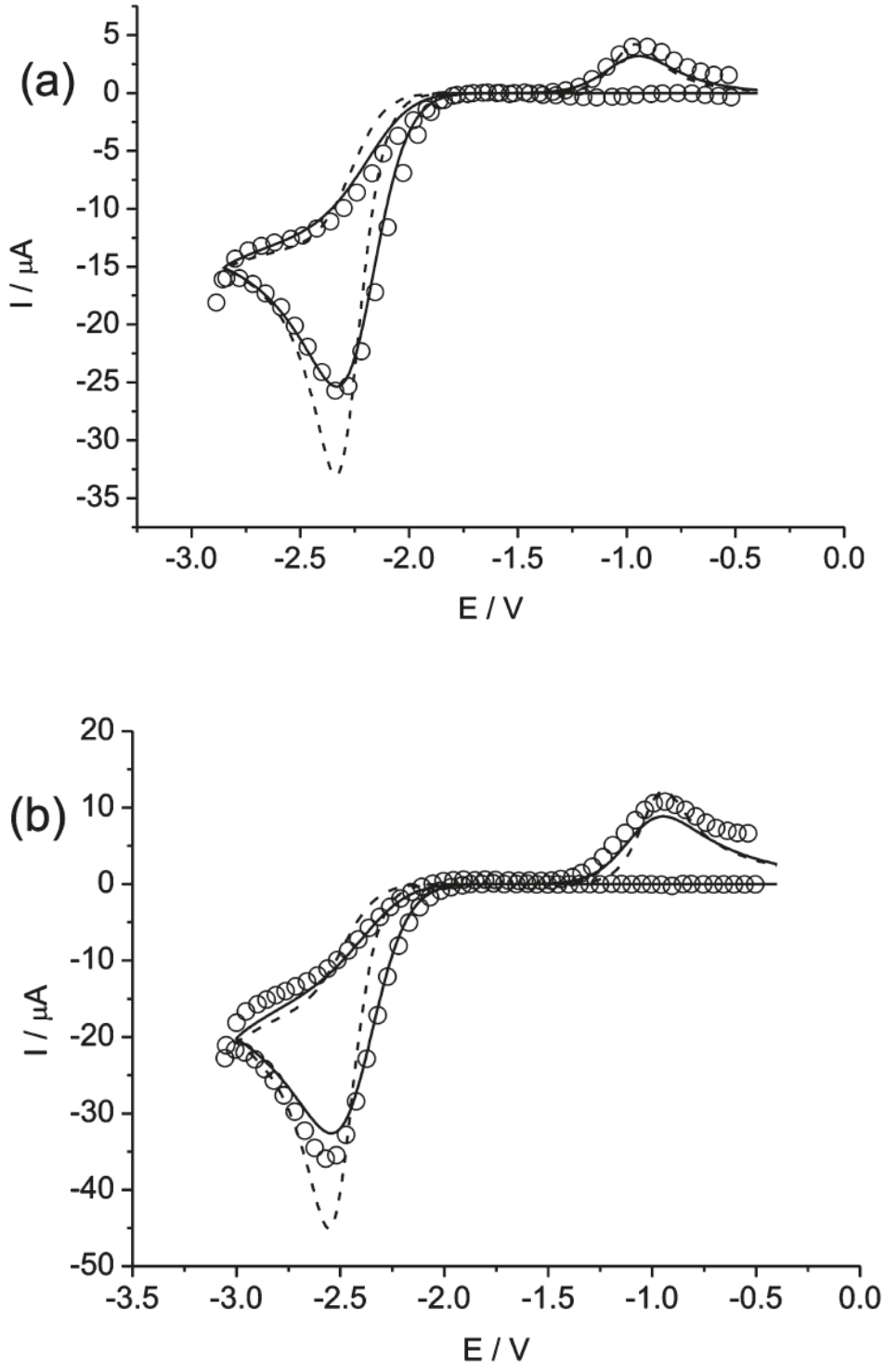


Figure 4.5: *Experimental cyclic voltammetry of NP reduction (open circles) compared to Marcus-Hush-Chidsey cases III (dotted line) and IV (solid line) for scan rates of (a) 1000 and (b) 2000 V* s^{-1} *at a volume flow rate of 0.14* cm^3 s^{-1}.

Table 4.2: *Simulation Results for NP*

	BV (Case I)	**BV (Case II)**	**MH (Case III)**	**MH (Case IV)**
k_0 (cm s^{-1})	$(7.0\pm3.0) \times 10^{-5}$	$(9.5\pm1.5) \times 10^{-4}$	$(7.0\pm3.0) \times 10^{-6}$	$(5.0\pm1.0) \times 10^{-5}$
α	0.24 ± 0.02	0.24 ± 0.02	-	-
β	0.76 ± 0.02	0.24 ± 0.02	-	-
λ (eV)	-	-	2.5 ± 0.1	1.0 ± 0.1
$E_f^{\ominus}$ (V)	-1.32 ± 0.04	-1.66 ± 0.05	-1.68 ± 0.06	-1.64 ± 0.08
% MSAD	19.0 ± 4.9	7.1 ± 0.5	22.1 ± 3.2	10.1 ± 2.1

In the case of the Butler-Volmer simulations, Figure 4.4 clearly shows that although the cathodic wave can be adequately fitted with a value of the (cathodic) transfer coefficient α = 0.24, this low value confers a significant asymmetry between the two peaks, leading to a very poor fit of the anodic wave if the usual relationship of α + β = 1 is assumed to hold (case I). However, according to Evans and Corrigan [40], the measured dα/dE is equal to 0.4 for the reduction of the related molecule t-nitrobutane at Pt electrodes in acetonitrile. In addition, the peak-to-peak separation of more than 1.5 V makes it highly probable that the energetic environment is quite different at the reduction and oxidation potentials; thus, the requirement of α + β = 1 can be relaxed without contravening the principle of microscopic reversibility (case II). Indeed, the relationship of α + β = 1 only rigorously holds for measurements at the same potential, which is clearly not the case here [54]. If, then, α + β ≠ 1, excellent fits can be obtained between Butler-Volmer simulations and the experimental data (see Figure 4.4).

Figure 4.5 illustrates the same CV data fitted by the Marcus-Hush-Chidsey simulations. The value of the reorganization energy has been calculated to lie within the range 2.2-2.8 eV, comprised of outer-sphere (1.4-2.0 eV according to Equations 4.16 and 4.17 above) and inner-sphere (0.8 eV according to the DFT calculations reported in Kraiya et al. [41]) components. Taking a mean value of 2.5 eV (case III) results in very poor agreement to experiment in the cathodic wave, although there is better agreement in the oxidative wave. However, best fits can be obtained of the reductive wave by reducing the value of the reorganization energy to 1.0 eV (case IV). However, unlike the case I/II dichotomy outlined above for Butler-Volmer, there can be no obvious justification or physical interpretation for lowering λ to 1.0 eV, a value significantly lower than the solvent reorganization energy alone, especially when a significant contribution of inner-sphere reorganization has been long established for the nitroalkanes [41]. Even in the limit of case IV, however, the MSAD values indicate that the fit of simulation to theory does not match that of case II (Butler-Volmer—this can be seen in comparison of Figure 4.4 and Figure 4.5, by examination of the reductive peak. The variation in MSAD values is further demonstrated in Figure 4.6, which compares Butler-Volmer and case III (Marcus-Hush-Chidsey) simulations to experimental LSVs for a range of scan rates (for reductive scan alone, cases I and II are equivalent).

4.5 Conclusions

The BV and MH approaches for modeling the heterogeneous electron transfer kinetics under high-mass transport conditions have been compared and the quality of the fits to experimental data quantified. In the case of DPA, no significant measurable

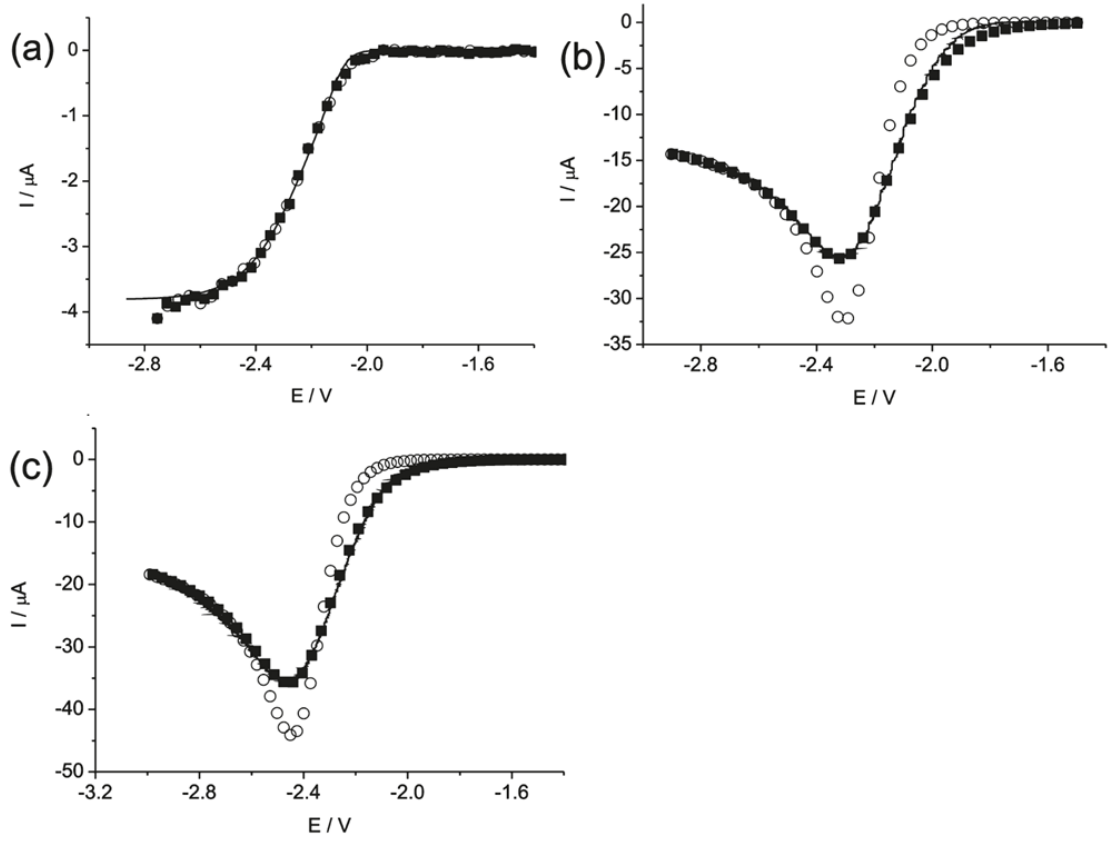


Figure 4.6: *Experimental linear sweep voltammetry of NP reduction (solid line) compared to Butler-Volmer (solid squares) and Marcus-Hush-Chidsey Case III (open circles) simulations for scan rates of (a) 1000 and (b) 2000 V* s^{-1} *at a volume flow rate of 0.14* cm^3 s^{-1}.

differences were found between the two models and excellent fits to cyclic and linear sweep voltammetry experiments were found. For NP, there was a clearly better agreement with experiment for the BV model. Although MH theory may provide a superior physical insight into the molecular processes occurring, on the basis of the systems considered here, the BV formalism may remain the preferred model for the parametrization, if nothing more, of experimental data.

4.6 References

1. J. A. V. Butler, *Trans. Faraday Soc.* **28** (1932) 379.
2. T. Erdey-Gruz, M. Z. Volmer, *Phys. Chem.* **150** (1930) 203.
3. R. A. Marcus, *J. Chem. Phys.* **24** (1956) 966.
4. R. A. Marcus, *J. Chem. Phys.* **24** (1956) 979.
5. R. A. Marcus, *J. Chem. Phys.* **26** (1957) 867.
6. R. A. Marcus, *J. Chem. Phys.* **26** (1957) 872.
7. R. A. Marcus, *J. Phys. Chem.* **67** (1963) 853.
8. R. A. Marcus, *J. Chem. Phys.* **43** (1965) 679.
9. H. J. Kim, J. T. Hynes, *J. Phys. Chem.* **94** (1990) 2736.
10. D. F. Calef, P. G. Wolynes, *J. Chem. Phys.* **78** (1983) 470.
11. D. F. Calef, P. G. Wolynes, *J. Phys. Chem.* **87** (1983) 3387.
12. W. R. Fawcett, *Electrochim. Acta* **42** (1997) 833.
13. C. Hartnig, M. T. M. Koper, *J. Chem. Phys.* **115** (2001) 8540.
14. M. Hilczer, M. Tachiya, *J. Mol. Liq.* **64** (1995) 113.
15. V. B. P. Leite, *J. Chem. Phys.* **110** (1999) 10067.
16. V. B. P. Leite, J. N. Onuchic, *J. Phys. Chem.* **100** (1996) 7680.
17. D. M. Mohilner, *J. Phys. Chem.* **73** (1969) 2652.
18. A. Samanta, S. K. Ghosh, *Chem. Phys.* **214** (1997) 61.
19. B. B. Smith, J. T. Hynes, *J. Chem. Phys.* **99** (1993) 6517.
20. M. Tachiya, *Radiat. Phys. Chem.* **47** (1996) 43.
21. C. E. D. Chidsey, *Science* **251** (1991) 919.
22. J. F. Smalley, M. D. Newton, S. W. Feldberg, *J. Electroanal. Chem.* **589** (2006)
    1.

23. H. O. Finklea, L. Liu, M. S. Ravenscroft, S. Punturi, *J. Phys. Chem.* **100** (1996) 18852.

24. Q. Chi, J. Zhang, J. E. T. Andersen, J. Ulstrup, *J. Phys. Chem. B* **105** (2001) 4669.

25. J. Yan, S. Dong, J. Li, W. Chen, *J. Electrochem. Soc.* **144** (1997) 3858.

26. J. Hirst, F. A. Armstrong, *Anal. Chem.* **70** (1998) 5062.

27. H. Finklea, D. Hanshew, *J. Am. Chem. Soc.* **114** (1992) 3173.

28. M. Ravenscroft, H. Finklea, *J. Phys. Chem.* **98** (1994) 3843.

29. P. Fristrup, M. Grubb, J. Zhang, H. Christensen, A. Hansen, J. Ulstrup, *J. Electroanal. Chem.* **511** (2001) 128.

30. S. W. Feldberg, *Anal. Chem.* **82** (2010) 5176.

31. J. R. Miller, L. T. Calcaterra, G. L. Closs, *J. Am. Chem. Soc.* **106** (1984) 3047.

32. A. D. Clegg, N. V. Rees, O. V. Klymenko, B. A. Coles, R. G. Compton, *J. Am. Chem. Soc.* **126** (2004) 6185.

33. J. Savéant, D. Tessier, *Faraday Discuss. Chem. Soc.* **74** (1982) 57.

34. N. V. Rees, R. A. W. Dryfe, J. A. Cooper, B. A. Coles, R. G. Compton, S. G. Davies, T. D. McCarthy, *J. Phys. Chem.* **99** (1995) 7096.

35. B. Coles, R. Compton, J. Larsen, R. Spackman, *Electroanalysis* **8** (1996) 913.

36. N. Rees, R. Compton, *Russ. J. Electrochem.* **44** (2008) 368.

37. A. D. Clegg, N. V. Rees, O. V. Klymenko, B. A. Coles, R. G. Compton, *J. Electroanal. Chem.* **580** (2005) 78.

38. A. D. Clegg, N. V. Rees, O. V. Klymenko, B. A. Coles, R. G. Compton, *ChemPhysChem* **5** (2004) 1234.
39. N. V. Rees, A. D. Clegg, O. V. Klymenko, B. A. Coles, R. G. Compton, *J. Phys. Chem. B* **108** (2004) 13047.
40. D. A. Corrigan, D. H. Evans, *J. Electroanal. Chem.* **106** (1980) 287.
41. C. Kraiya, P. Singh, D. H. Evans, *J. Electroanal. Chem.* **563** (2004) 203.
42. J. A. Alden, R. G. Compton, *J. Electroanal. Chem.* **404** (1996) 27.
43. R. G. Compton, M. B. G. Pilkington, G. M. Stearn, *J. Chem. Soc., Faraday Trans. 1* **84** (1988) 2155.
44. K. B. Oldham, J. C. Myland, *J. Electroanal. Chem.* **655** (2011) 65.
45. L. Lapidus, G. F. Pinder, *Numerical solution of partial differential equations in science and engineering;* Wiley: New York, 1982.
46. E. J. F. Dickinson, J. G. Limon-Petersen, N. V. Rees, R. G. Compton, *J. Phys. Chem. C* **113** (2009) 11157.
47. N. V. Rees, O. V. Klymenko, B. A. Coles, R. G. Compton, *J. Electroanal. Chem.* **534** (2002) 151.
48. N. V. Rees, O. V. Klymenko, E. Maisonhaute, B. A. Coles, R. G. Compton, *J. Electroanal. Chem.* **542** (2003) 23.
49. C. Amatore, C. Lefrou, F. Pfluger, *J. Electroanal. Chem.* **270** (1989) 43.
50. O. V. Klymenko, R. G. Evans, C. Hardacre, I. B. Svir, R. G. Compton, *J. Electroanal. Chem.* **571** (2004) 211.
51. R. G. Compton, C. E. Banks, *Understanding voltammetry*, 2nd ed.; Imperial College Press: London, 2010.

52. S. R. Belding, E. I. Rogers, R. G. Compton, *J. Phys. Chem. C* **113** (2009) 4202.

53. J. Savéant, D. Tessier, *J. Electroanal. Chem.* **65** (1975) 57.

54. W. J. Albery, *Electrode kinetics*; Clarendon Press: Oxford, U.K., 1975.

Chapter 5

Experimental Comparison of the Butler–Volmer and Marcus-Hush-Chidsey Formalisms of Electrode Kinetics: The Reduction of Cyclooctatetraene at Mercury Hemispherical Electrodes via Cyclic and Square Wave Voltammetries

The work presented in this chapter has been published in

J. Electroanal. Chem. **665** (2012) 38.

This chapter describes the critical analysis of the Butler–Volmer and Marcus–Hush–Chidsey kinetic models carried out through the study of the first one-electron reduction of cyclooctatetraene in DMSO at mercury hemispherical microelectrodes. This is an atypically slow process due to the conformational distortion taking place from the tub-shaped neutral species to the planar radical anion.

Cyclic and square wave voltammetries are employed with the aim of examining the consistency of the results extracted from each model. Whereas the experimental results in cyclic voltammetry are adequately fitted by both models, the fit of square wave voltammograms at high frequency are not satisfactory when the Marcus–Hush–Chidsey formalism is employed.

Programs used for cyclic voltammetry simulations were written by Dr. M. C. Henstridge, and for square wave voltammetry, by Dr. E. Laborda.

5.1 Introduction

The electrochemical behavior of the reduction of cyclooctatetraene (COT) and its derivatives in aprotic solvents has been often studied [1-7] with the primary aim of explaining the unusual slowness of the first reduction of the neutral species to yield the corresponding radical anion:

$$COT + e^- \rightleftharpoons COT^{\bullet -} \quad (5.1)$$

The radical anion can undergo a further reduction to form the dianion, which can be followed by homogeneous reactions including protonation [3]:

$$COT^{\bullet -} + e^- \rightleftharpoons COT^{2-} \rightarrow \ldots. \quad (5.2)$$

This chapter therefore focuses on the study of the first reduction of COT in order to avoid complications derived from considering processes coupled to the electron transfer.

The first electron-transfer process (5.1) is atypically sluggish in comparison with other neutral hydrocarbon molecules in aprotic media. The most widely-accepted explanation of this behavior is based on the significant conformational distortion taking place as the tub-shaped neutral species reorganizes to form the planar radical anion (see Figure. 5.1). Consequently, the inner-sphere reorganization energy is quite significant (ca. 1.7 eV according to DFT calculations [8]), which gives rise to a large Gibbs energy of activation and slow electron transfer. Analogous considerations can also account for the extremely slow reduction of 2-methoxyazocines [9].

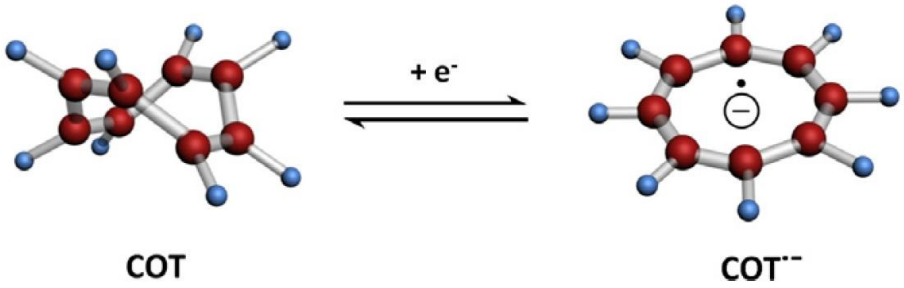


Figure 5.1: *Conformation of neutral COT and radical $COT^{\bullet -}$ anion molecules*

The small value of the transfer coefficient reported for COT (ca. $\alpha = 0.4$ [3,6]) has been shown [3] to be associated with a ‘‘late’’ transition state with relatively planar structure. This aspect is consistent with the observed decrease of the value of the heterogeneous rate constants when the electroactive molecule is more hindered [3]. Therefore, this redox system is an excellent example of the effect on the electrode kinetics of a significant difference in the molecular geometry between the oxidized and reduced species.

The Butler–Volmer (BV) and Marcus–Hush–Chidsey (MH) models are the most commonly employed for studying electrode kinetics [10,11]. The BV model [12,13] is an empirical treatment that relates the reductive and oxidative rate constants (k_{red}, k_{ox}) as functions of the standards heterogeneous rate constant (k_0), the transfer coefficient (α) and the formal potential (E_f^{Θ}). This leads to good parameterization of many electrochemical systems but offers limited physical insights. Therefore, this approach is still the preferred choice due to its simplicity and the large body of data available in the literature. Consequently, the alternative microscopic MH approach [14–18] has been increasingly used, particularly for the case of surface-bound redox couples where numerous systems have been successfully described [19-23]. According to this formalism, the rate constants are also functions of three parameters, the standard heterogeneous

rate constant (k_0), the formal potential ($E_f^{\ominus}$) and the reorganization energy (λ) [24]. Mathematical treatment of the BV and MH models have been described in Chapter 2.

Based on findings described in the previous chapter and other recent work [25-29], the MH model was found to display an inferior quality of fit when applied to systems where rate of electron transfer is slow and those with BV transfer coefficient significantly different from 0.5. In the context of exploring the generality of these findings, this chapter reports the assessment of the MH model with the one-electron reduction of COT in DMSO. This is known to be a quasireversible process with small value of the transfer coefficient, α, and purely diffusional behavior [1–7]. The reduction of COT at mercury electrodes has been previously studied in dimethylformamide (DMF) [3] and acetonitrile [6] solvents (see Table 5.1). The relative rates of the electron transfer for the first and second reduction waves are traditionally explained from Marcus-type arguments related to the relative reorganization energies of COT (tub-shaped) to $COT^{\bullet-}$ (planar), and subsequently to COT^{2-} (planar).

Table 5.1: *Kinetic parameters for the first reduction of COT at mercury electrode reported in the literature.*

Solvent	Supporting Electrolyte	k_0 (cm s^{-1})	α	T(°C)	Refs.
DMF	0.1 M TBAP	$(2.0\pm0.5) \times 10^{-3}$	0.40±0.03	25±0.2	3
		$(2.5\pm0.5) \times 10^{-3}$	0.40±0.03	35±0.2	3
MeCN	0.1 M TEAP	$(2.3\pm0.2) \times 10^{-2}$	0.43±0.02	20±0.2	6
	0.1 M TH_pAP	$(2.3\pm0.2) \times 10^{-4}$	0.43±0.02	20±0.2	6

DMF: dimethylformamide; MeCN: acetonitrile; TBAP: tetra-n-butylammonium perchlorate; TEAP: tetraethylammonium perchlorate; THpAP: tetra-n-heptylammonium perchlorate.

First, the reduction of COT in different organic solvent/background electrolyte combinations is studied in order to achieve a maximum separation between the first and second reduction processes. Hence, the study of the first reduction process can be performed with negligible interference of the second electron transfer.

Next, the kinetics of the first reduction of COT at mercury hemispherical microelectrodes is examined through the most commonly used voltammetric techniques, namely, cyclic and square wave voltammetries. The use of microelectrodes is very advantageous in comparison with the utilization of macroelectrodes [1–6] since it has enabled us to reduce undesirable ohmic-drop and capacitative effects. Moreover, due to its one dimensional symmetry, simulation of the electrochemical response at spherical electrodes is simpler, faster and more accurate than at the more conventional microdisks. Hence, the inference of ohmic-drop effects can be easily evaluated in order to discard their influence in the experimental results [30–32].

For the fitting of experimental data, simulations considering the BV and MH formalisms are developed and the quality of the fittings compared in order to check the suitability of each approach and to extract the kinetic parameters.

5.2 Experimental

Chemical Reagents

Cyclooctatetraene (COT, Aldrich, 98%), mercury(I) nitrate dehydrate ($Hg_2(NO_3)_2 \cdot 2H_2O$, Aldrich, >97%), nitric acid (HNO_3, Fisher scientific, 70%), ferrocene ($Fe(C_5H_5)_2$, Aldrich, 98%), cobalt(III) sepulchrate trichloride ($[CoSep]Cl_3$, Aldrich, 95%), potassium nitrate (KNO_3, Aldrich, >99%), acetonitrile (MeCN, Fisher Scientific, HPLC grade), N,N-dimethylformamide (DMF, Aldrich, anhydrous grade)

and dimethylsulfoxide (DMSO, Alfa Aesar, >99%) were all used as received without further purification. Background electrolytes including tetraethylammonium perchlorate (TEAP, Fluka, Puriss grade), tetraethylammonium bromide (TEABr, BDH Chemicals, 98%), tetrabutylammonium perchlorate (TBAP, Fluka, Puriss grade) and tetrabutylammonium iodide (TBAI, Aldrich, >98%) were recrystallized from ethanol and dried in a dessicator for 48 h prior to use in order to remove adsorbed moisture and trace electroactive species.

Instrumentation

All electrochemical measurements were carried out employing a computer-controlled Autolab PGSTAT12 (Metrohm-Autolab BV, Utrecht, Netherlands). Microdisk working electrodes of radii 5.5 and 50 μm were fabricated in-house by sealing Pt wire (Goodfellow Cambridge Ltd., UK) into soda glass capillary according to published method [33] (see also Chapter 3.3). The platinum disk was polished prior to hemisphere deposition using 1.0, 0.3 and 0.05 μm alumina-water slurry on soft lapping pads (Buehler, Illinois). The disk size was calibrated by numerical fitting of the chronoamperometric response of the 1 mM ferrocene solution in acetonitrile supported by 0.1 M TBAP using the Shoup and Szabo expression [10,11,34]:

$$I = \frac{4FADc^*}{\pi r_0}(0.7854 + 0.8862\tau^{-0.5} + 0.2146\exp(-0.7823\tau^{-0.5})) \quad (5.3)$$

where $\tau = 4Dt/r_0^2$, A is the area of the disk (cm^2), D the diffusion coefficient of the electroactive species ($cm^2\ s^{-1}$), c^* its bulk concentration (mol cm^{-3}) and r_0 the disk

radius (cm). A widely adopted literature diffusion coefficient for ferrocene of $D = 2.3 \times 10^{-9}$ m^2 s^{-1} at 25 ºC [35] was employed for the calculations.

A mercury hemisphere was then electrochemically deposited onto each microdisk from a 50 mM $Hg_2(NO_3)_2$ solution containing 0.1 M KNO_3 and acidified to 0.5% with HNO_3 following the method laid out by Bard et al. [36]. For deposition, the potential was stepped to -0.25 V vs. Ag wire. The size of the hemispherical drop was controlled by the amount of charge passed.

A platinum foil counter electrode was employed for all measurements while a silver wire was used as the reference electrode.

Stringent thermal control of the electrochemical cell was achieved through the use of an air heater-controller system fabricated in-house. With this system, all measurements were carried out at 25 ± 0.2 ºC.

Characterization of the Electrodeposited Mercury Hemispheres

The size and shape of the mercury deposits were characterized by optical and electrochemical methods.

Visual measurement of the hemispheres was obtained through the use of a JVC digital video camera TK-C921EG. To allow the appraisal of size and shape of the hemisphere in the environment of the reagent solution, the working electrode was submerged in the solution sealed within a UV/vis cuvette, and visual images taken. In all cases, it was found that the mercury droplet formed a hemisphere which adopted the radius of its respective microdisk. An image of the 50 μm hemisphere is shown in Figure 5.2.

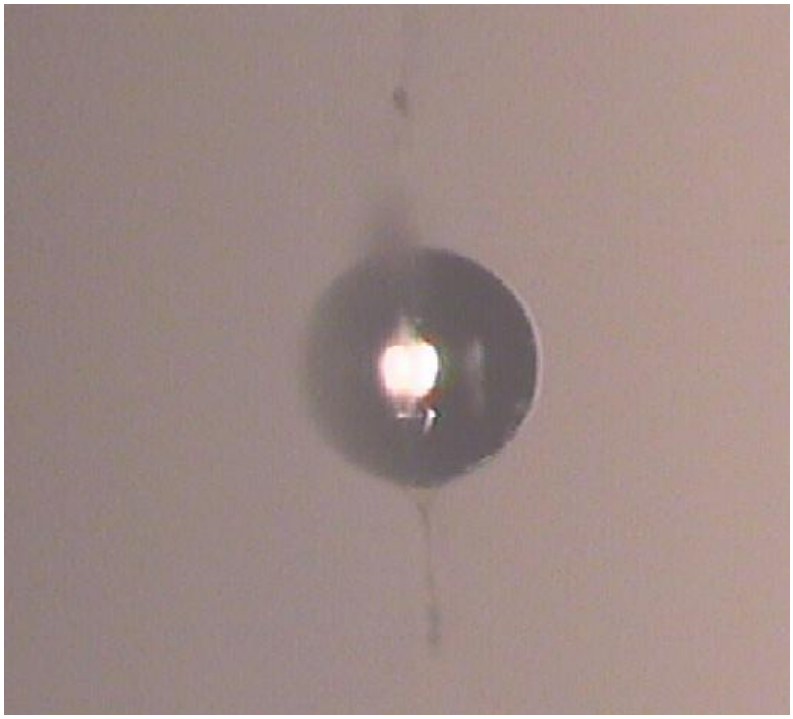


Figure 5.2: *Image of the 50 μm radius electrodeposited hemisphere immersed in DMSO.*

The electrochemical characterization of the mercury hemispheres was carried out through analysis of the limiting current chronoamperogram of an aqueous solution containing 2 mM $[CoSep]Cl_3$ and 0.1 M KNO_3, which is given by the following expression in the case of electrodes with spherical geometry [10,11]:

$$I = FADc^* \left(\frac{1}{\sqrt{\pi Dt}} + \frac{1}{r_0} \right) \tag{5.4}$$

The value of the diffusion coefficient of $[CoSep]Cl_3$ employed for the calculations was $D = 6.3 \times 10^{-10}$ m^2 s^{-1}. This was determined from chronoamperograms recorded at

microdisk electrode of known dimensions with Equation 5.3 and it is in close agreement with literature [37,38].

It is found that radii obtained through the analysis of the chronoamperograms coincide with that determined with the optical measurements outlined in the previous section.

Effect of Solvent/Electrolyte

As the current study seeks a rigorous elucidation of the kinetics pertaining to the one-electron reduction of COT, it is imperative that the interference of the second electrochemical step is eliminated with sufficient separation between the first and second reduction potentials. This can be achieved through the use of an appropriate solvent/electrolyte system that maximize the potential spacing through differential solvation of and ion pairing effects [39] which render the reduction of the anion less favorable.

Various literature sources have reported the successful use of several organic solvent/background electrolyte in the separation of the first and second reduction voltammetric waves. These solvent/electrolyte systems include MeCN/TEAP [6], DMF/TBAP [3], DMF/TBAI [1] and DMSO/TEABr [4]. In these studies, dropping mercury electrodes with radii in the order of several millimeters were used. Since we employ hemispherical microelectrodes of considerably smaller size, the appearance of the voltammetry may differ. It was therefore necessary to undertake a systematic study of the solvent/electrolyte combinations to optimize the separation of the two reduction waves. The solvent/electrolyte systems tested in the work reported in this chapter includes MeCN/TEAP, DMF/TEAP, DMF/TBAP, DMF/TBAI and DMSO/TEABr.

It was found that, when cyclic voltammetry is performed for the reduction of COT in MeCN/TEAP, DMF/TEAP, and DMF/TBAP, one single reduction wave corresponding to 2-electron transfer, such as shown in Figure 5.3A, is observed. Distinct peaks are observed for DMF/TBAI (Figure 5.3B) and DMSO/TEABr (Figure 5.3C) with peak separations of approximately 100 and 280 mV, respectively.

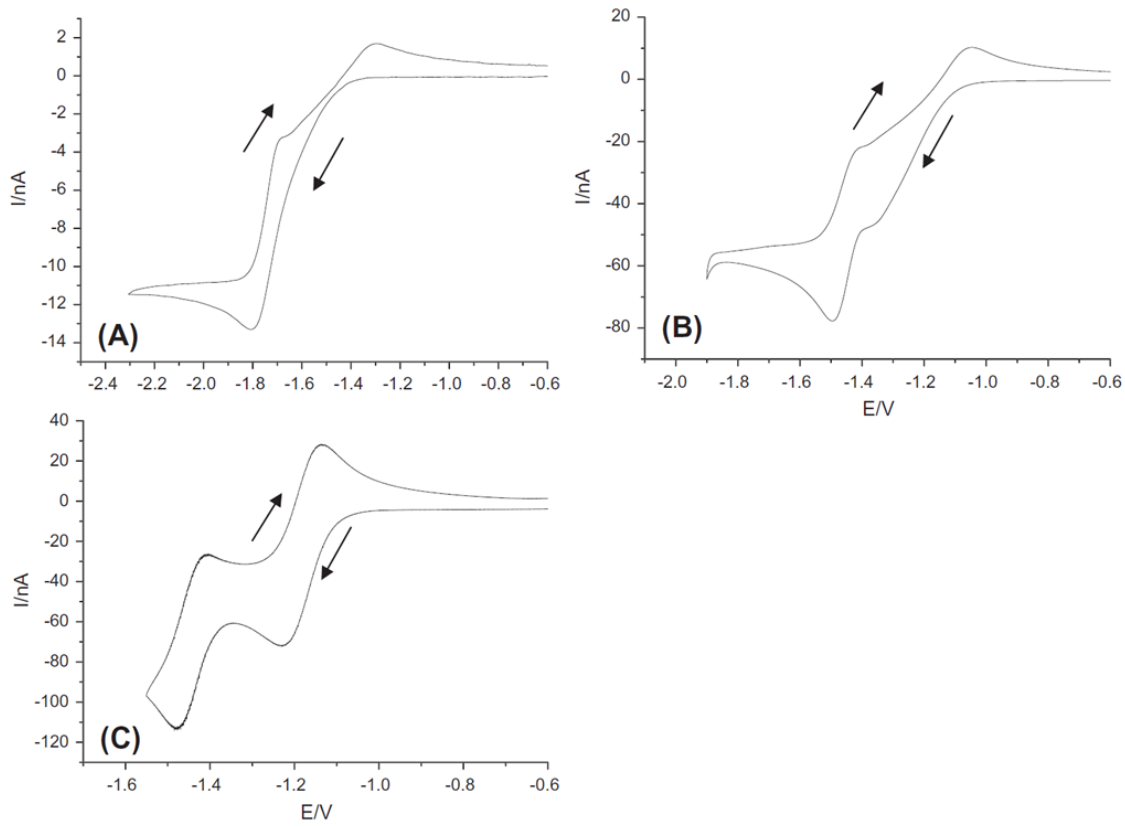


Figure 5.3: *Experimental cyclic voltammograms for the reduction of COT at mercury hemisphere electrodes (A) 2.5 mM COT in DMF/TEAP on 5.5 µm radius hemisphere (scan rate = 5 V s^{-1}) (B) 1.5 mM COT in DMF/TBAI on 50 µm radius hemisphere (scan rate = 0.1 V s^{-1}) (C) 0.9 mM COT in DMSO/TEABr on 50 µm radius hemisphere (scan rate = 0.1 V s^{-1}). An electrolyte concentration of 0.1 M is used in all solutions.*

Accordingly, kinetic study of the first reduction step of COT is performed in DMSO solution with TEABr as background electrolyte since this system is found to yield the optimum separation between the first and the second reductive peaks. The effect of the second electrochemical step on the reverse scan voltammograms of the first one has been evaluated via simulation for the experimental conditions considered. In all cases, the effect on the peak current is smaller than 0.2% such that the first reduction can be analyzed as a pure electron transfer process.

Cyclic and Square Wave Voltammetry Experiments

Cyclic voltammograms were recorded between -0.6 and -1.33 V (vs. Ag wire). The scan rates used ranged from 25 mV s^{-1} to 2.5 V s^{-1}. Square wave voltammograms were recorded between -0.75 and -1.33 V (vs. Ag wire) with a potential step of 10 mV and a potential amplitude of 15 mV. Frequencies used cover the range between 50 and 500 Hz.

All the above measurements were made on 50 μm radius hemisphere electrodes in a solution containing 0.9 mM COT and 0.1 M TEABr electrolyte in DMSO. The solution was degassed with N_2 (BOC Gases) for at least 20 min before each experiment and a positive pressure of N_2 was maintained throughout.

The diffusion coefficient of COT was determined from steadystate linear sweep voltammograms recorded with the 50 μm radius mercury hemispherical electrode according to the equation for the stationary limiting current of a hemispherical electrode [10,11]:

$$I_{ss} = \frac{FADc^*}{r_0} \tag{5.5}$$

The result of $D_{COT} = 7.4 \times 10^{-10}$ m^2 s^{-1} was determined. The diffusion coefficient of the radical anion $COT^{\bullet -}$ was determined from the fitting of the cyclic voltammograms. This gives the value $D_{COT^{\bullet -}} = 6.5 \times 10^{-10}$ m^2 s^{-1}.

Ohmic Drop Effects

The possible occurrence of the uncompensated solution resistance (R_u) on the results in cyclic and square wave voltammetry was evaluated by digital simulation with a program developed in-house [40,41].

The following expression for the value of the uncompensated resistance applies for hemispherical electrodes [42]:

$$R_u = \frac{\rho}{2\pi r_0} \tag{5.6}$$

ρ being the resistivity of the solution.

Under the experimental conditions of this work (0.1 M TEABr electrolyte in DMSO solutions), a value of the resistivity of ρ = 3.4 Ω m can be inferred according to the literature [43]. Assuming this value, simulated CV and SWV curves with and without ohmic drop effects were compared for the range of conditions employed in the experiments. As shown in Figure 5.4, the effect of the uncompensated solution resistance is not significant in any case.

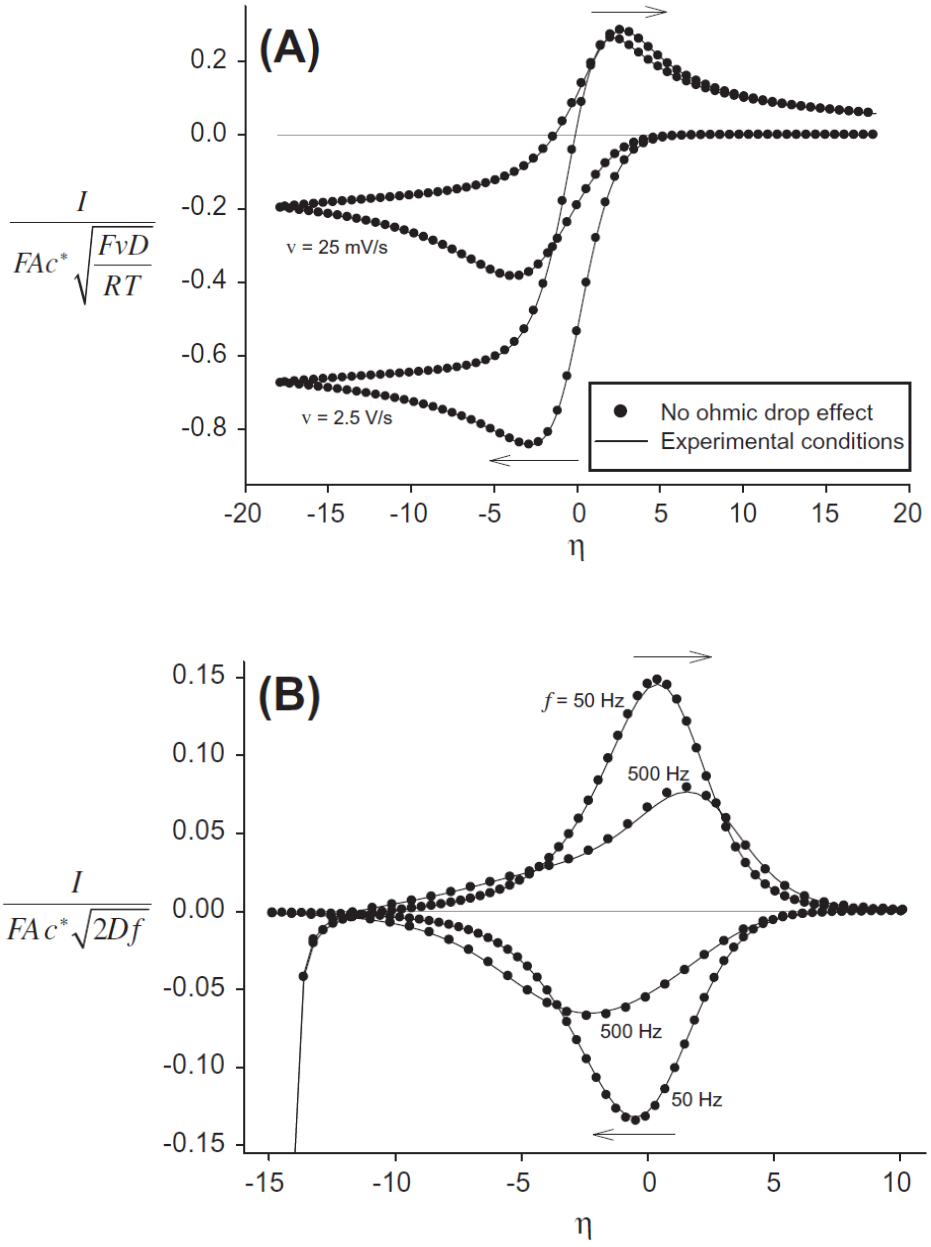


Figure 5.4: *Influence of the uncompensated resistance on the (A) cyclic and (B) square wave voltammograms under the experimental conditions employed for the study of the COT first reduction: r_0 = 50 μm, 1 mM COT, 0.1 M TEABr DMSO solution (resistivity = 3.4 Ω m), $k_0 = 1.0 \times 10^{-2}$ cm s^{-1}, α = 0.40. The values of the scan rate and frequency are shown on the curves, which correspond to the highest and lowest values employed in the experiments.*

5.3 Results and Discussion

Cyclic Voltammetry

Cyclic voltammograms of 0.9 mM COT in 0.1 M TEABr and DMSO solution on 50 μm mercury hemisphere electrode were recorded between -0.6 and -1.33 V (vs. Ag wire), employing scan rates ranging from 25 mV s^{-1} to 2.5 V s^{-1}.

Programs developed in-house by Dr. M. C. Henstridge, which computational details have been described previously [28], was used to simulate cyclic voltammograms based on BV and MH formalisms. This was used, in conjunction with the value of D_{COT} = 7.4 × 10^{-10} m^2 s^{-1} determined through the previous section, to model cyclic voltammograms over the full range of voltage scan rates. Fitting of the experimental voltammograms was carried out by matching the peak potentials, thereby fixing the formal potential ($E_f^{\ominus}$), the standard heterogeneous electron transfer rate constant (k_0) and the transfer coefficient α (in BV formalism) or the reorganization energy λ (in MH formalism).

The quality of the fitting was evaluated from the value of the mean scaled absolute deviation (MSAD). The mathematical expression of %MSAD is given in Equation 4.15 in Chapter 4.

The common set of parameters (including $E_f^{\ominus}$, k_0, α or λ, and D_{COT}•-) giving rise to the ‘‘best fit’’ of theoretical voltammograms to experiment across all scan rates was then determined through the minimization of the MSAD value.

For the fitting with MH formalism, the value of λ was fixed at 1.7 eV in accordance to the estimated inner-sphere reorganization energy from DFT

calculations [8]. Although further contribution from the outer-sphere reorganization energy is expected to be present, it was found that greater λ values do not have a noticeable effect on the simulated voltammograms.

The common set of parameters which provides the minimum MSAD value is listed in Table 5.2. Figure 5.5 shows the results obtained for three representative scan rates.

Table 5.2: *Kinetic parameters for the first reduction of COT at mercury hemispherical electrode in a 0.1 M TEABr DMSO solution determined from cyclic voltammetry at different scan rates in the range: 0.025–2.5 V* s^{-1}.

	Butler-Volmer	**Marcus-Hush-Chidsey**
k_0 (cm s^{-1})	0.014	0.013
α	0.35	-
λ (eV)	-	1.7
% MSAD	7.61 ± 7.9	9.6 ± 3.1

The result of fitting through BV formalism reveals an α value of 0.35, which suggests a planar structure of the transition state [3,6]. This trend agrees well with those observed in the quantitative kinetics studies in other solvents including MeCN [6] and DMF [3].

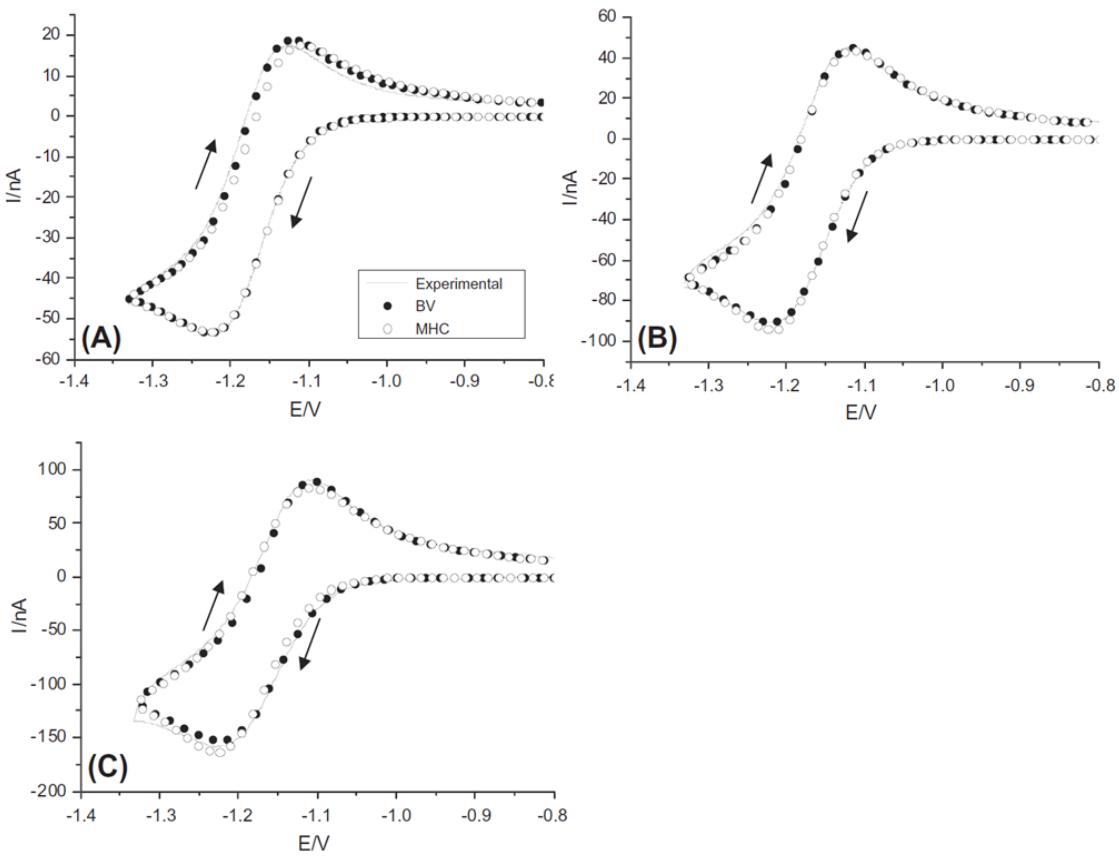


Figure 5.5: *Experimental cyclic voltammograms (solid line) of the first reduction of COT in DMSO/TEABr at a mercury hemispherical electrode of 50 μm radius. The simulated voltammograms correspond to the best fit with BV (black circles) and MH (white circles) are also plotted. (A) Scan rate = 0.05 V* s^{-1}*, (B) Scan rate = 0.25 V* s^{-1} *and (C) Scan rate = 1 V* s^{-1}*. A solution comprising of 1 mM COT and 0.1 M TEABr in DMSO is used in all scans.*

Examination of the MSAD values demonstrates good fits to be obtainable through both formalisms, with BV (% MSAD = 7.6 ± 1.9) resulting in a marginally superior quality of fit over that obtained with MH (% MSAD = 9.6 ± 3.1).

Square Wave Voltammetry

The first reduction of COT was then studied by square wave voltammetry (SWV) under the same experimental conditions. Voltammograms were recorded by scanning the potentials in the negative (forward scan) and positive (backward scan) directions with a pulse amplitude of 15 mV and a step potential of 10 mV. This allows both the reductive and oxidative half-reactions to be examined, which is essential for a sound, critical evaluation of the kinetic model. Otherwise, the voltammogram of a single (forward or backward) scan could be fitted with an inadequate kinetic model by simply adjusting the values of the fitting parameters [24,26]. Moreover, to ensure the soundness of the results, a wide range of frequencies encompassing 50–500 Hz was employed.

The fitting procedure was carried out by minimizing the MSAD value in the region around the peak current, ΔI_{peak}, with $\{k_0, \alpha\}$ or $\{k_0, \lambda\}$ as fitting parameters (only the points with current $\geq 0.7 \times \Delta I_{peak}$ were considered). The imposition of fitting emphasis around the peak region is carried out to focus the analysis on the most informative region and to avoid the distortion of the voltammograms caused by the second electron transfer at the more negative potentials. The mean values of the kinetic parameters obtained from the fitting are shown in Table 5.3 together with the MSAD values. The experimental and theoretical curves are plotted in Figure 5.6. This clearly shows that the quality of the fittings obtained with the BV model is always superior to that corresponding to MH. The differences become greater as the frequency increases, and the kinetic control of the electrochemical response is also more evident.

Table 5.3: *Kinetic parameters for the first reduction of COT at mercury hemispherical electrode in a 0.1 M TEABr DMSO solution determined from square wave voltammetry at different frequencies in the range: 50-500 Hz.*

	Butler-Volmer	**Marcus-Hush-Chidsey**
k_0 (cm s^{-1})	0.011	0.012
α	0.40	-
λ (eV)	-	1.7
% MSAD	3.6 ± 0.7	9.2 ± 3.2

The simulated data obtained with BV simultaneously fit the forward and backward peak heights for a mean value of the standard heterogeneous rate constant and of the transfer coefficient of 1.1×10^{-2} cm s^{-1} and 0.4, respectively. These values are consistent in all the range of frequencies considered. Moreover, they agree well with the values extracted from the fitting of the cyclic voltammograms (Table 5.2).

For the MH fitting, the λ value was fixed at 1.7 eV, as indicated previously, leaving the standard heterogeneous rate constant the only fitting parameter. From the minimization of MSAD, a mean value of $k_0 = 1.2 \times 10^{-2}$ cm s^{-1} was determined. With these k_0 and λ values, the peak heights of both forward and backward peaks can be fitted at low frequencies. However, for higher frequencies, the simultaneous fit of both peaks is not possible with MH: the reductive, forward peak is overestimated whereas the oxidative, backward peak is underestimated.

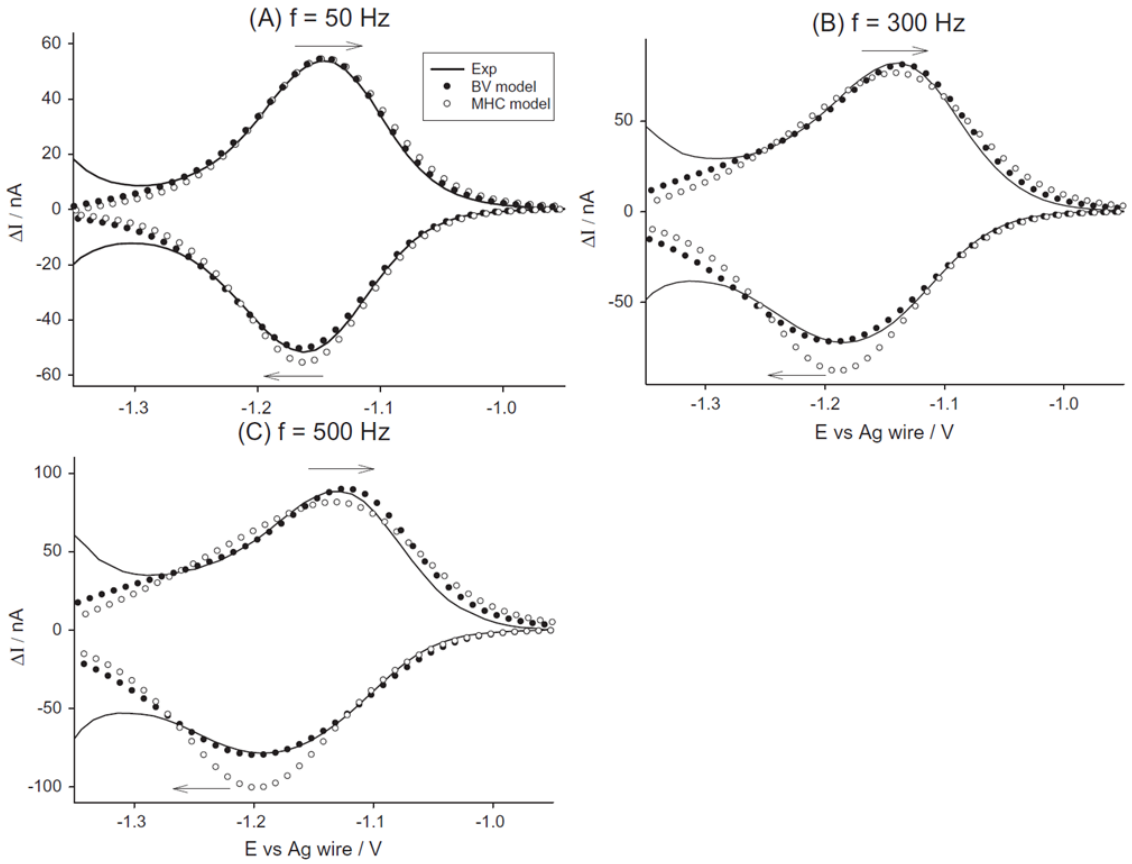


Figure 5.6: *Experimental square wave voltammograms (solid line) with forward and reverse scans corresponding to the first reduction of COT in DMSO/TEABr at a mercury hemispherical electrode of 50μm radius. The simulated voltammograms corresponding to the best fit with BV (black circles) and MHC (white circles) are also plotted. (A) Frequency = 50 Hz, (B) Frequency = 300 Hz and (C) Frequency = 500 Hz. A solution comprising of 1 mM COT and 0.1 M TEABr in DMSO is used in all scans.*

This kinetic model makes use of the symmetric form of Marcus theory where equal reorganization energies for the oxidized and reduced species are assumed. Therefore, the experimental deviations observed may indicate differences in the force constants and the need to use the asymmetric Marcus theory [44].

By comparing the voltammograms and MSAD values obtained from CV and SWV, it can be inferred that the latter technique is more effective in revealing differences and evaluating the suitability of the kinetic models. The greater sensitivity of SWV arises from the position of the voltammograms such that the peak is situated at smaller overpotentials with respect to CV. Accordingly, the voltammetric response is less affected by limitations of mass transport and so it is more sensitive to the electrode kinetics [26].

5.4 Conclusions

The kinetics of the first reduction of cyclooctatetraene in DMSO at mercury hemispherical microelectrodes has been studied by means of cyclic and square wave voltammetries by considering both the Butler–Volmer (BV) and Marcus–Hush–Chidsey (MH) models.

A study of the influence of the solvent/electrolyte combinations on separation of the first and second reduction processes has revealed that two well-resolved waves are obtained for DMSO/TEABr. Under these conditions the examination of the first wave is possible with negligible interference of the second electron transfer. The kinetic analysis confirms a strikingly slow first reduction of COT, with a standard heterogeneous rate constant ca. 10^{-2} cm s^{-1} being determined.

Satisfactory fits of the experimental cyclic voltammograms can be attained through both BV and MH. With the BV formalism, a value of the transfer coefficient significantly smaller than 0.5 ($\alpha = 0.35$) has been determined. This is in agreement with data in the literature and indicates a planar-like transition state.

In the case of square wave voltammetry, significantly better fittings are obtained with the BV model, particularly when high frequencies (f > 100 Hz) are employed. With the MH approach, the forward and backward peak heights cannot be simultaneously fitted. The finding agrees with previous results of our group [25–29] showing that the 3-parameter MH model struggles to describe quantitatively the voltammetric response of solution phase systems whose transfer coefficients display large deviation from 0.5.

These results also support the use of multiple techniques for the quantitative assessment of the kinetic model, SWV being very effective in revealing possible weaknesses.

5.5 References

1. R.D. Allendoerfer, P.H. Rieger, *J. Am. Chem. Soc.* **87** (1965) 2336.
2. L.B. Anderson, J.F. Hanson, T.H. Kakihana, L.A. Paquette, *J. Am. Chem. Soc.* **93** (1971) 161.
3. B.J. Huebert, D.E. Smith, *J. Electroanal. Chem.* **31** (1971) 333.
4. A.J. Fry, C.S. Hutchins, L.L. Chung, *J. Am. Chem. Soc.* **97** (1975) 591.
5. B. Tulyathan, W.E. Geiger, *J. Electroanal. Chem.* **109** (1980) 325.
6. R.A. Petersen, D.H. Evans, *J. Electroanal. Chem.* **222** (1987) 129.
7. G. Grampp, B. Grobmann, J. Heinze, S. Landgraf, K. Rasmussen, *Chem. Phys. Chem.* **9** (2008) 854.
8. A.-M. Kelterer, S. Landgraf, G. Grampp, *Spectrochim. Acta A* **57** (2001) 1959.
9. L.B. Anderson, J.F. Hansen, T. Kakihana, L.A. Paquette, *J. Am. Chem. Soc.* **93** (1971) 161.

10. A.J. Bard, L.R. Faulkner, *Electrochemical Methods, Fundamental and Applications*, Wiley, New York, 2001.
11. R.G. Compton, C.E. Banks, *Understanding Voltammetry, second ed.*, Imperial College Press, United Kingdom, 2010.
12. J.A.V. Butler, *Trans. Faraday Soc.* **19** (1924) 729.
13. T. Erdey-Gruz, M. Volmer, Z. *Physik. Chem.* **150A** (1930) 203.
14. R.A. Marcus, *J. Chem Phys.* **24** (1956) 4966.
15. R.A. Marcus, N. Sutin, *Biochim. Biophys. Acta* **811** (1985) 265.
16. N.S. Hush, *J. Chem. Phys.* **28** (1958) 962.
17. N.S. Hush, *J. Electroanal. Chem.* **470** (1999) 170.
18. C.E.D. Chidsey, *Science* **215** (1991) 919.
19. J.F. Smalley, M.D. Newton, S.W. Feldberg, *J. Electroanal. Chem.* **589** (2006) 1.
20. Q. Chi, J. Zhang, J.E.T. Andersen, J. Ulstrup, *J. Phys. Chem. B.* **105** (2001) 4669.
21. J. Hirst, F.A. Armstrong, *Anal. Chem.* **70** (1998) 5062.
22. H. Finklea, D. Hanshew, *J. Am. Chem. Soc.* **114** (1992) 3173.
23. L. Tender, M.T. Carter, R.W. Murray, *Anal. Chem.* **66** (1994) 3173.
24. S.W. Feldberg, *Anal. Chem.* **82** (2010) 5176.
25. D. Suwatchara, M.C. Henstridge, N.V. Rees, R.G. Compton, *J. Phys. Chem. C* **115** (2011) 14876.
26. E. Laborda, M.C. Henstridge, A. Molina, F. Martinez-Ortiz, R.G. Compton, *J. Electroanal. Chem.* **660** (2011) 169.
27. E. Laborda, Y. Wang, M.C. Henstridge, F. Martinez-Ortiz, A. Molina, R.G. Compton, *Chem. Phys. Lett.* **512** (2011) 133.

28. M.C. Henstridge, Y. Wang, J.G. Limon-Petersen, E. Laborda, R.G. Compton, *Chem. Phys. Lett.* **517** (2011) 29.
29. M.C. Henstridge, E. Laborda, N.V. Rees, R.G. Compton, *Electrochim. Acta*, doi:10.1016/j.electacta.2011.10.026.
30. I. Streeter, R.G. Compton, *J. Phys. Chem. C* **112** (2008) 13716.
31. J.G. Limon-Petersen, I. Streeter, N.V. Rees, R.G. Compton, *J. Phys. Chem. C* **113** (2009) 333.
32. E.J.F. Dickinson, J.G. Limon-Petersen, N.V. Rees, R.G. Compton, *J. Phys. Chem. C* **113** (2009) 11157.
33. C. Amatore, E. Maisonhaute, G. Simonneau, *J. Electroanal. Chem.* **486** (2000) 141.
34. D. Shoup, A. Szabo, *J. Electroanal. Chem.* **237** (1982) 140.
35. K.N. Marsh, A. Deev, A.C.-T. Wu, E. Tran, A. Klamt, Korean *J. Chem. Eng.* **19** (2002) 357.
36. J. Mauzeroll, E.A. Hueske, A.J. Bard, *Anal. Chem.* **75** (2003) 3880.
37. T.J. Davies, B.A. Brookes, A.C. Fisher, K. Yunus, S.J. Wilkins, P.R. Greene, J.D. Wadhawan, R.G. Compton, *J. Phys. Chem.* **107B** (2003) 6431.
38. A. Molina, E. Laborda, E.I. Rogers, F. Martinez-Ortiz, C. Serna, J.G. Limon-Petersen, N.V. Rees, R.G. Compton, *J. Electroanal. Chem.* **634** (2009) 73.
39. B.S. Jensen, A. Ronlan, V.D. Parker, *Acta Chem. Scand. B* **29** (1975) 394.
40. F. Martinez-Ortiz, N. Zoroa, A. Molina, C. Serna, E. Laborda, *Electrochim. Acta* **54** (2009) 1042.
41. E. Laborda, E.I. Rogers, F. Martinez-Ortiz, A. Molina, R.G. Compton, *Electrochim. Acta* **55** (2010) 6577.

42. S.H. Hong, C. Kraiya, M.W. Lehmann, D.H. Evans, *Anal. Chem.* **72** (2000) 454.

43. G. Fuchs, L. Kisova, J. Komenda, G. Gritzner, *J. Electroanal. Chem.* **526** (2002) 107.

44. R.A. Marcus, *J. Chem. Phys.* **43** (1965) 679.

PART III

Experimental Validation of Asymmetric Marcus-Hush-Chidsey Formalism

Following the findings presented in Part II, the asymmetric form of the Marcus-Hush-Chidsey (aMH) model was developed in-house in order to overcome limitations of the Marcus-Hush-Chidsey (MH) formalism. Part III focuses on validation of the aMH model's ability to fit experimental systems. Reagents used include tetraphynylethylene (Chapter 6), 2-methyl-2-nitropropane, cyclooctatetraene and europium(III) (Chapter 7). A comparative study between the aMH and Butler-Volmer (BV) models (Chapter 7) also allows a greater physical insight of the latter to be drawn.

Experiments on 2-methyl-2-nitropropane and europium(III) were carried out by Y. Wang. Programs used for simulation of cyclic voltammetry were developed by Dr. E. Laborda and Dr. M. C. Henstridge, and those for square wave voltammetry by Dr. E. Laborda.

Chapter 6

Comparative Evaluation of the Symmetric and Asymmetric Marcus–Hush-Chidsey Formalisms of Electrode Kinetics – The One-Electron Oxidation of Tetraphenylethylene in Dichloromethane on Platinum Microdisk Electrodes

The work presented in this chapter has been published in

J. Electroanal. Chem. **677** (2012) 120.

This chapter reports an experimental comparative evaluation of the Butler–Volmer (BV), symmetric and asymmetric Marcus-Hush-Chidsey (MH and aMH, respectively) kinetic formalisms. Numerical simulations using these kinetic models are employed to fit experimental cyclic voltammetry of the one-electron oxidation of tetraphenylethylene in dichloromethane under conditions of full electrolyte support at a platinum microdisk electrode. When compared with the BV formalism, the MH model is seen to give rise to an inferior quality of fit determined by calculating the mean scaled absolute deviation (MSAD) between theory and experiment. This can be traced to its inherent assumption of identical force constants of the reagent and product, rendering it unable to address the asymmetry that exists between the forward and reverse sweeps of the cyclic voltammetry due to the difference in force constants. Where the aMH formalism is used, cyclic voltammograms with comparable quality of fit to that of BV are obtained.

Programs used for simulation work in this chapter were written by Dr. M. C. Henstridge.

6.1 Introduction

The electrochemical behavior of tetraphenylethylene (TPE) has been well studied [1–8] mainly for the elucidation of the effect on electrode kinetics which arises from inferred twisting of the central double bond accompanying the transformation of the neutral reagent into the ionic or di-ionic species. In particular, it is found that, for the reduction reactions, the formation of anion involves a large degree of twisting around the double bond while that which accompanies the subsequent di-anion formation is relatively limited [9,10]. The reverse trend is true for the step-wise formation of cation and di-cation [9,10]. The sequential reduction of TPE to form the radical anion ($TPE^{\bullet-}$) and (TPE^{2-}) gives rise to merged voltammetric waves [1–6]. However, the oxidation of TPE has been shown to produce two separate anodic peaks [7,8], each corresponding to a single electron transfer step:

$$TPE \leftrightarrow TPE^{+} + e^{-} \quad (6.1)$$

$$TPE^{+} \leftrightarrow TPE^{2+} + e^{-} \quad (6.2)$$

The radical cation displays remarkable stability due to steric hindrance arising from the propeller-like geometry of the TPE molecule that features the phenyl groups twisted by 35–42º out of plane of the ethylenic bond [9–11] (Figure 6.1) and the only reported solution reaction involving the cation is the disproportionation reaction [12]:

$$TPE^{+} + TPE^{+} \leftrightarrow TPE + TPE^{2+} \quad (6.3)$$

whilst, the di-cation is known to decay through intramolecular cyclization forming 9,10-diphenylphenanthrene (DPP) [7]:

$$TPE^{2+} \rightarrow DPP \qquad (6.4)$$

The work presented in this chapter focuses solely on the first oxidation of TPE in order to compare different models for heterogeneous electron transfer and avoid the complications of subsequent homogeneous chemical steps.

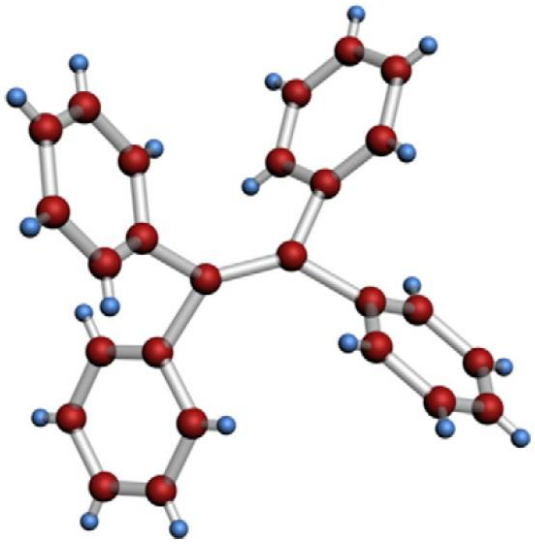


Figure 6.1: *Propeller-like molecular structure of tetraphenylethylene deduced from electronic absorption spectrometry and molecular orbital calculation studies of Suzuki et al.* [9,10]*. Carbon and hydrogen atoms are represented by large and small spheres, respectively.*

Findings from the work presented in Chapters 4 and 5, and recent work performed in the group [13–19] emphasize the inadequacy of the MH model in describing voltammetric response of electrochemical systems where satisfactory parameterization can be obtained with the BV model employing a value of α different from 0.5. This

inadequacy may be due to differences between the reorganization energies of the reduction and oxidation processes. The asymmetric Marcus theory enables the consideration of these differences in the inner-sphere contribution to the reorganization energy. Hence, different force constants in the inner-shell of reactants and products are considered within this model, allowing for the analysis of asymmetric effects in a general and analytical manner.

Accordingly, Laborda and co-workers have developed a kinetic model for heterogeneous electrochemical reactions based on the asymmetric form of Marcus theory which allows different values of reorganization energies between the forward and reverse reactions to be considered [20]. The resulting model (hereafter referred to as the asymmetric Marcus-Hush-Chidsey (aMH) model) can be parameterized in terms of four parameters: the formal potential ($E_f^{\ominus}$), the standard heterogeneous rate constant (k_0), the reorganization energy (λ), and the asymmetric parameter γ. A detailed mathematical treatment of this model is described in Chapter 2.4.

Based on this theory, the symmetric MH model can be considered a particular case of this model for which γ = 0. This is because, for the value of γ = 0, the activation Gibbs energy of the system collapses to that of the symmetric MH form.

This chapter presents an assessment of the BV, MH and aMH models applied to the description of voltammetric response of the first oxidation of TPE in dichloromethane (DCM) on a 25 μm radius platinum microdisk electrode. Kinetics of the reaction is measured through the use of cyclic voltammetry at high scan rates. Fitting of experimental data is then carried out with BV, symmetric and asymmetric MH models using programmes written in-house by M. C. Henstridge. The optimum fit

of each kinetic model is determined through the minimization of the mean-scaled absolute deviation (MSAD) value of the fits.

6.2 Experimental

Chemical Reagents

Tetraphenylethylene (TPE, Sigma–Aldrich, 98%), ferrocene (Aldrich, 98%), tetrabutylammonium hexafluorophosphate ($TBAPF_6$, Fluka, >99%), tetra-n-butylammonium perchlorate (TBAP, Fluka, Puriss. grade), acetonitrile (MeCN, Fisher Scientific, HPLC grade), dimethylsulfoxide (DMSO, Alfa Aesar, >99%) and dichloromethane (DCM, Sigma–Aldrich, HPLC grade) were all used as received without further purification.

Instrumentation

All electrochemical measurements were carried out employing a computer-controlled μAutolab Type2 (Metrohm-Autolab BV, Utrecht, Netherlands).

Microdisk working electrodes of radii 25 and 50 μm were fabricated in-house by sealing Pt wire (Goodfellow Cambridge Ltd., U.K.) into glass capillary according to a published method [23]. The platinum disk was polished prior to each experiment using 1.0, 0.3 and 0.05 μm alumina-water slurry on soft lapping pads (Buehler, Illinois). The disk size was calibrated by numerical fitting of the chronoamperometric response of the 1 mM ferrocene solution in acetronitrile supported by 0.1 M TBAP using the Shoup and Szabo expression [24–26] given in Equation 5.3 in Chapter 5. A widely adopted literature diffusion coefficient for ferrocene of $D = 2.3 \times 10^{-9}$ m^2 s^{-1} at 25 ºC [27] was employed for the calculations.

A platinum mesh counter electrode was employed for all measurements while a silver wire was used as the reference electrode. Stringent thermal control of the electrochemical cell was achieved through the use of an air heater-controller system fabricated in-house. With this system, all measurements reported below were carried out at 25 ± 0.2 ºC.

Cyclic Voltammetry and Double Potential Step Chronoamperometry Measurements

Cyclic voltammograms were recorded between +1.10 and +1.41 V (vs. Ag wire) on 25 and 50 μm radii platinum microdisk electrodes in 1.1 and 2.0 mM TPE solutions containing 0.15 M $TBAPF_6$ supporting electrolyte in DCM.

Double potential step chronoamperometry was recorded in 1.1 mM TPE solution containing 0.15 M $TBAPF_6$ supporting electrolyte in DCM on the 25 μm platinum microdisk electrode. The potential was stepped from +1.15 V where there is no faradaic current to +1.4 V (vs. Ag wire) where the oxidation is fully controlled by diffusion and is held for 0.5 s and then abruptly stepped back to +1.15 V for further 0.5 s. The resulting chronoamperometric response is simultaneously fitted for both the diffusion coefficients and concentration using previously reported method [28–30].

Fitting Methodology

Simulation programs written in-house by Dr. M. C. Henstridge were used to simulate cyclic voltammograms on a microdisk based on the BV, MH and aMH formalisms. These were used, in conjunction with the value of diffusion coefficients determined from double potential step chronoamperometry to model cyclic voltammograms over the full range of experimental conditions. Fitting of the electrochemical reduction processes was carried out by matching the peak potentials,

thereby fixing the formal potential (E_f^{o}), which over the course of the experiment is found to shift within ±50 mV range due to the use of Ag wire pseudo reference electrode), the standard electrochemical rate constant (k_0) and the transfer coefficient (α) (for BV formalism), the reorganization energy (λ) (for MH formalism) or the asymmetric parameter (γ) and reorganization energy (λ) (for aMH formalism). The quality of the fitting was evaluated from the value of the mean scaled absolute deviation (MSAD). The mathematical expression of %MSAD is given in Equation 4.15 in Chapter 4.

In order to avoid large contributions to the MSAD as a consequence of very small signal values, only the points where experimental current is at least 10% of the peak current were considered. The common set of parameters (E_f^{o}, k_0, and α for BV, E_f^{o}, k_0, and λ for MH, and E_f^{o}, k_0, γ and λ for the aMH formalism) giving rise to the ‘‘best fit’’ of theoretical voltammograms to experiment obtained for 1 mM TPE solution on 25 μm radius electrode across all scan rates were then determined through the minimization of the MSAD value.

6.3 Results and Discussion

Characterization of the Voltammograms

In order to study the first oxidation of TPE with negligible interference from subsequent reaction steps, the oxidation reaction is explored in different solvents (dimethylsulfoxide, acetronitrile and DCM) so as to achieve adequate potential separation between the first and second electron transfer waves. First, cyclic voltammetry was performed with the 25 μm radius platinum microdisk electrode from 0 V to the solvent breakdown potential at +2 V (vs. Ag wire pseudo reference

electrode) at a scan rate of 1 V s^{-1} in the solution of 1 mM TPE with 0.15 M $TBAPF_6$ electrolyte in dimethylsulfoxide. The voltammogram obtained showed no oxidation wave within the potential window (Figure 6.2A). It is speculated that, in dimethylsulfoxide, the anodic processes may have been pushed to a further positive potential beyond that which the solvent breakdown occurs, hence, rendering this solvent unsuitable for the study of electro-oxidation of TPE.

Next, cyclic voltammetry was then performed in a solution containing 1.4 mM TPE with 0.15 M $TBAPF_6$ electrolyte in acetonitrile from +0.8 to +1.8 V (vs. Ag wire pseudo reference electrode) at a scan rate of 1 V s^{-1} on the same electrode. The resulting voltammogram features 3 separate oxidation waves positioned in close proximity to one another (Figure 6.2B). This system does not yield sufficient potential separation between the first and second waves as the first oxidation step (peak potential ca. 1.5 V) is seen to be partially merged with the second (peak potential ca. 1.6 V).

Further cyclic voltammetry was then performed at a scan rate of 0.3 V s^{-1} from +0.9 to +1.8 V(vs. Ag wire pseudo reference electrode) with the same electrode in the solution containing 1.1 mM TPE with 0.15 M $TBAPF_6$ electrolyte in DCM. This resulted in a transient voltammogram (Figure 6.2C) which reveals two successive oxidation waves (first peak potential at ca. +1.37 V and second, ca. +1.60 V, vs. Ag wire pseudo reference electrode) corresponding to sequential electron transfers. The first oxidation wave is seen to characterize a reversible single electron transfer whereas, the second wave features enhanced peak height (number of electrons transferred >1) with complete irreversibility. These observations are consistent with the mechanism described previously in the introduction section of this chapter which includes a reversible first oxidation step and a second oxidation coupled with irreversible chemical

step. Furthermore, the enhanced current of the second oxidation wave also suggests electroactivity of the chemical products. This system is chosen for the current study as it gives rise to adequate separation between the first and second oxidation of TPE, rendering the first electron transfer step to be studied without the influence of subsequent oxidation steps.

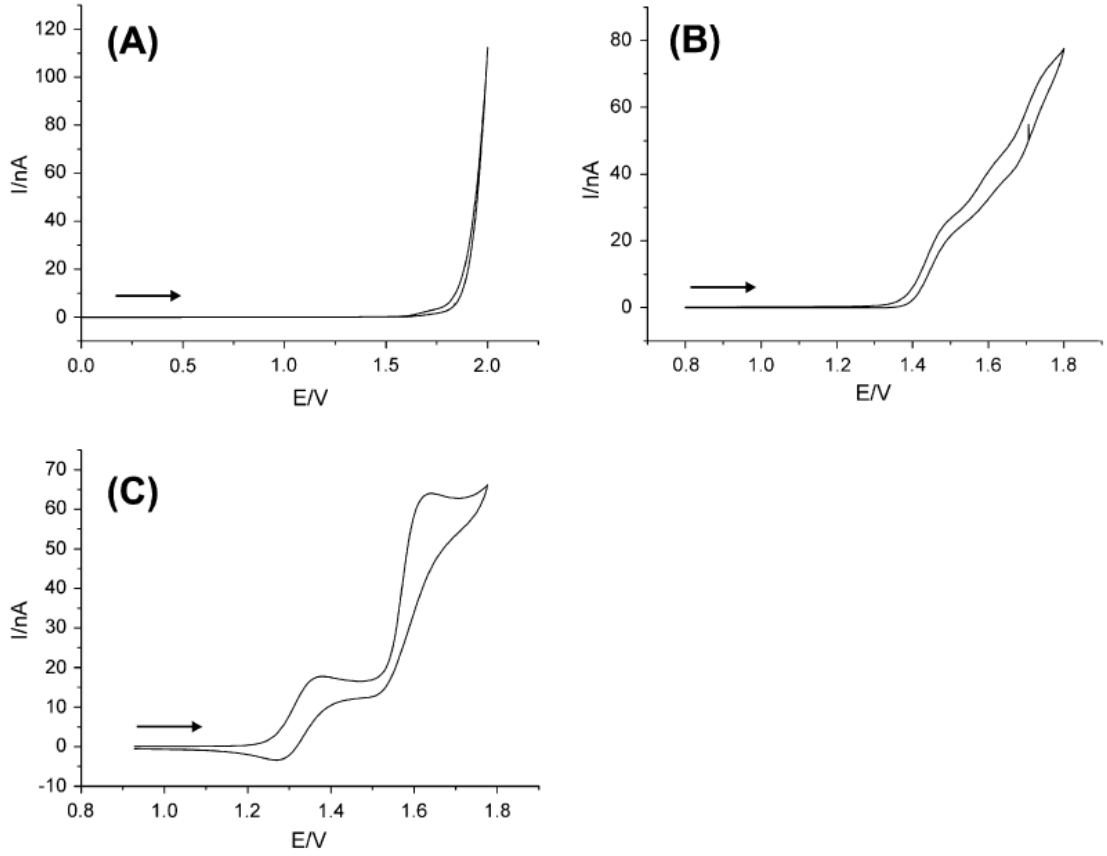


Figure 6.2: *Cyclic voltammograms of the oxidation of TPE in different organic solvents. (A) 1 mM TPE with 0.15 M $TBAPF_6$ in dimethylsulfoxide measured at scan rate = 1 V s^{-1} (B) 1.4 mM TPE with 0.15 M $TBAPF_6$ in acetonitrile measured at scan rate = 1 V s^{-1} (C) 1.1 mM TPE with 0.15 M $TBAPF_6$ in DCM measured at scan rate = 0.3 V s^{-1}. All measurements are made on 25 μm radius platinum microdisk electrode.*

In order to focus on the first electron transfer, cyclic voltammograms were then recorded between +1.10 and +1.41 V with varying scan rates from 0.03 V s^{-1} up to 20 V s^{-1} in order to encompass both steady state and transient voltammetric regimes. This set of measurements is used for numerical fitting for the comparison between BV, MH and aMH formalisms kinetic models. Examples of voltammograms obtained are displayed in Figure 6.3.

The voltammetry measured at the 25 μm electrode was consistent with a one-electron process (E reaction) with no observable effects of second order follow-on chemistry of the radical cation across the range of scan rates employed (as verified by varying concentration and noting that the voltammetry scaled exactly linearly). However, this was not found to be the case for experiments performed at the 50 μm microdisk where indications of the disproportionation step are observed at low scan rates. For the purposes of the comparison of the electron transfer models, the analysis and discussion will therefore be limited to experiments at the 25 μm electrode.

Determination of Diffusion Coefficients

Double-potential step transients were performed in 1.1 mMTPE solution containing 0.15 M $TBAPF_6$ supporting electrolyte on the 25 μm platinum microdisk. The resulting chronoamperometric response is simultaneously fitted for both diffusion coefficients and concentration using a previously reported method [28–30]. The diffusion coefficients of both neutral and radical cation are found to be $(0.96 \pm 0.05) \times 10^{-9}$ and $(1.05 \pm 0.05) \times 10^{-9}$ m^2 s^{-1}, respectively.

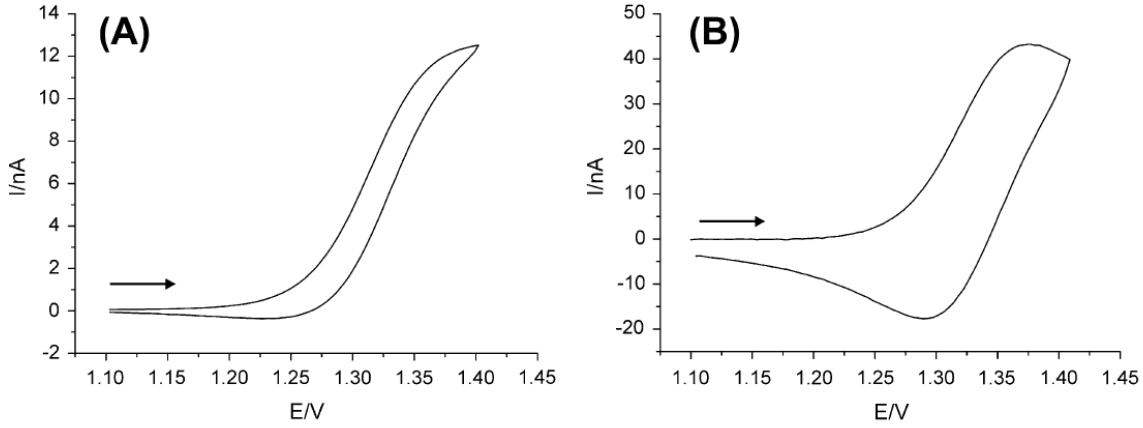


Figure 6.3: *Experimental cyclic voltammograms of the first oxidation of 1.1 mM TPE supported by 0.15 M $TBAPF_6$ in DCM taken at (A) scan rate = 0.03 V s^{-1} and (B) scan rate = 5 V s^{-1}. All measurements are made on a 25 μm radius platinum microdisk electrode.*

Results of Numerical Fitting

The BV, MH and aMH programs were used to systematically simulate cyclic voltammograms of the experimental set obtained in 1.1 mM TPE solution containing 0.15 M $TBAPF_6$ supporting electrolyte in DCM on the 25 μm platinum microdisk electrode across all scan rates ranging from 0.03 to 20 V s^{-1}. For each kinetic model, a common set of parameters that provided the ‘‘best fit’’ between the simulated and experimental voltammograms is determined. These ‘‘best fit’’ parameters are presented in Table 6.1. A comparison between the BV and MH fit is given in Figure 6.4, and between that of MH and aMH in Figure 6.5.

Table 6.1: *Optimum fitting parameters for Butler–Volmer, symmetric and asymmetric Marcus–Hush-Chidsey models.*

	Butler-Volmer	**Marcus-Hush-Chidsey**	**Asymmetric Marcus-Hush-Chidsey**
k_0 (cm s^{-1})	0.17 ± 0.02	0.15 ± 0.02	0.15 ± 0.02
α	0.65 ± 0.05	-	-
λ (eV)	-	≥ 0.53	≥ 0.53
γ/λ $(eV)^{-1}$	-	-	0.55 ± 0.05
$E_f^{\ominus}$ (V)	1.33 ± 0.05	1.33 ± 0.05	1.33 ± 0.05
% MSAD	2.22 ± 0.98	3.30 ± 1.53	2.08 ± 0.74

The simulated voltammograms obtained with the BV model with the optimized value of the standard heterogeneous rate constant and the transfer coefficient of k_0 = 0.17 cm s^{-1} and α = 0.65, respectively, give excellent quality of fit (MSAD value of 2.22 ± 0.98%) across all scan rates. In comparison with an electrochemical system whose heterogeneous reaction is predominantly limited by the change in geometry required in the formation of product (e.g. k_0 = 0.014 cm s^{-1} for cyclooctatetraene in DMSO [15]), the value of k_0 extracted for the current compound is relatively large. This characteristic of fast standard heterogeneous reaction rate is consistent with the finding of an electronic absorption spectroscopic study conducted by Suzuki et al. [10] which states that the geometric change accompanying the first oxidation of TPE is limited and only involves minor rotation around the ethylenic bond and changes in other bond lengths.

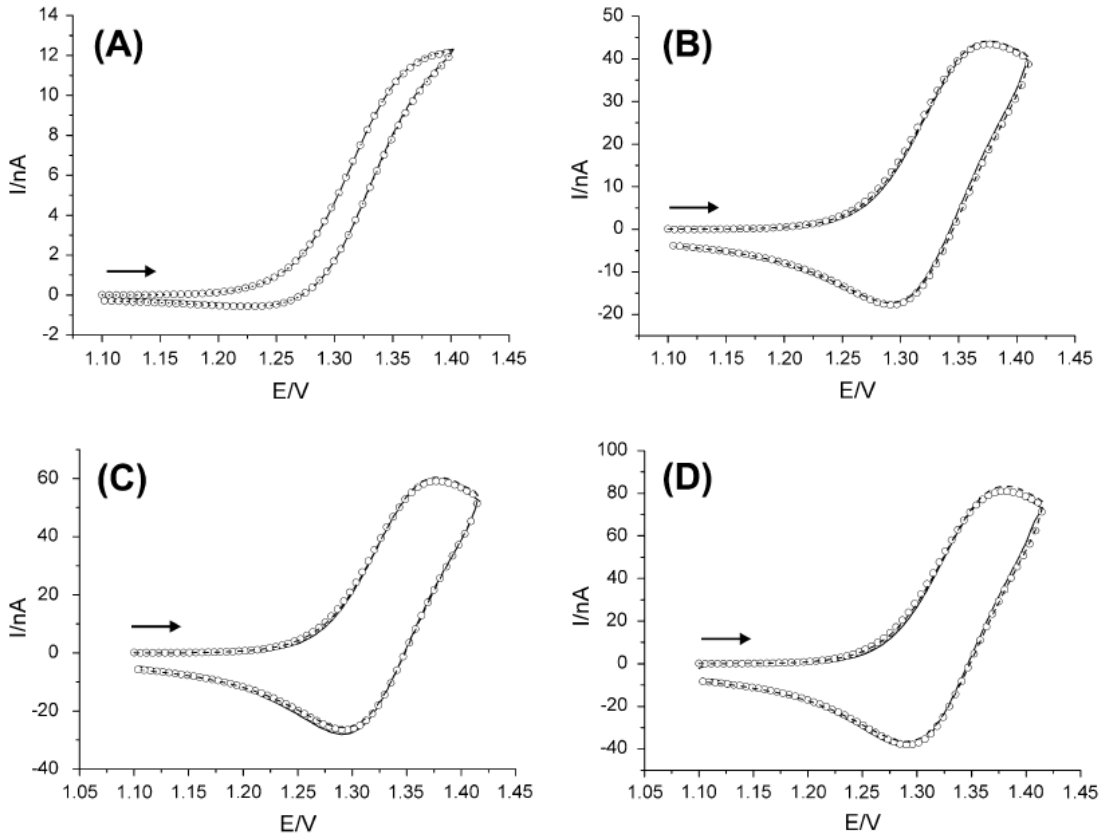


Figure 6.4: *Comparison between experimental voltammogram (solid line), BV (open circles) and MH (dashed line) simulations for voltammograms taken in 1.1 mM TPE solution with 0.15 M TBAPF$_6$ in DCM on 25 μm radius platinum microdisk. (A) Scan rate = 0.03 V s^{-1}, (B) scan rate = 5 V s^{-1}, (C) scan rate = 10 V s^{-1} and (D) scan rate = 20 V s^{-1}.*

For the fitting with the MH model, the value of λ of 0.53 eV used is the outer-sphere reorganization energy calculated from

$$\lambda_{os} = \frac{N_A e^2}{8\pi\varepsilon_0 r}\left(\frac{1}{\varepsilon_{op}} - \frac{1}{\varepsilon_s}\right) \tag{6.5}$$

via the spherical approximation of the Stokes-Einstein equation [31-34]

$$r = \frac{k_B T}{6\pi\eta D} \tag{6.6}$$

where r is the molecular radius here treated as the solvodynamic radius according to Clegg et al. [31], ε_0 is the permittivity of free space, ε_{op} and ε_s are the optical and static frequency components of the dielectric permittivity of the solvent, η is the solvent viscosity, and D is the diffusion coefficient. N_A, e, k_B and T have their usual meanings.

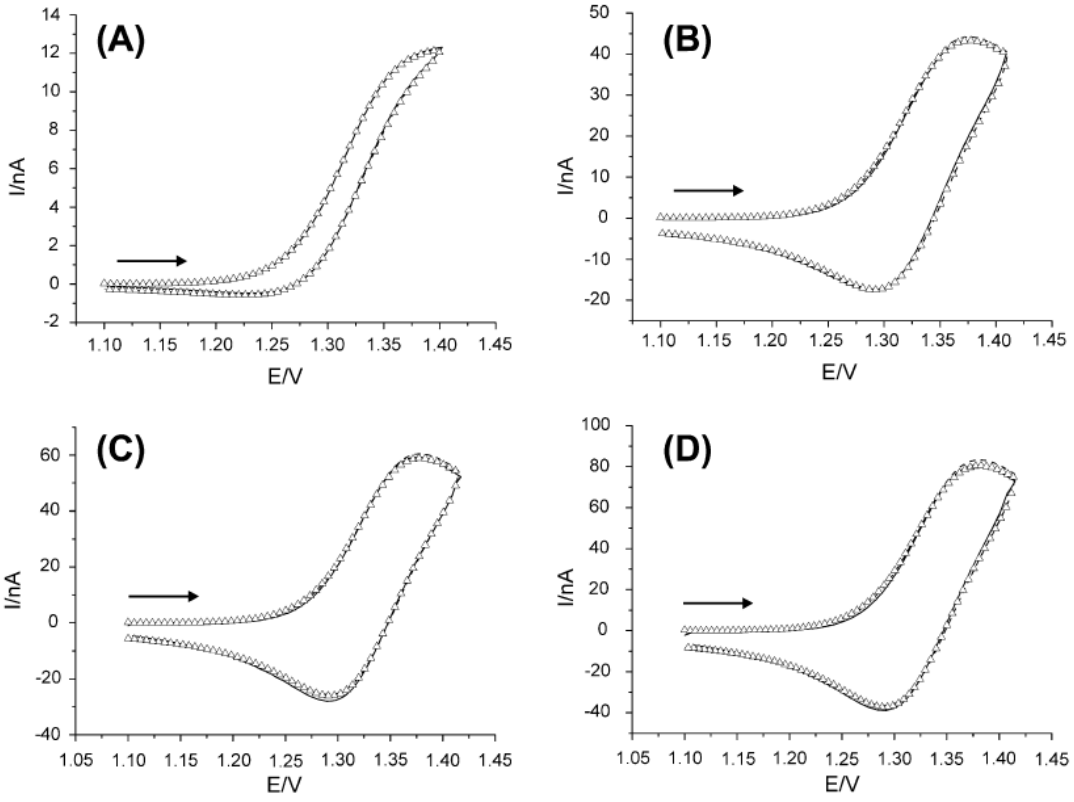


Figure 6.5: *Comparison between experimental voltammogram (solid line), MH (dashed line) and aMH (open triangles) simulations for voltammograms taken in 1.1 mM TPE solution with 0.15 M $TBAPF_6$ in DCM on 25 μm radius platinum microdisk. (A) Scan rate = 0.03 V s^{-1}, (B) scan rate = 5 V s^{-1}, (C) scan rate = 10 V s^{-1} and (D) scan rate = 20 V s^{-1}.*

The use of the outer-sphere reorganization energy of 0.53 eV for the current fitting is appropriate as this presents the minimum reorganization energy for a chemical system in solution and the simulated voltammograms for the current system are extremely insensitive to any increase in the value of λ beyond a threshold value of 0.3 eV. With this minimum value of λ, the optimum k_0 extracted from the fitting with the MH model is 0.15 cm s^{-1}. The corresponding MSAD value is 3.30 ± 1.53% presenting a poorer fit compared with the BV model.

The aMH simulations were carried out with fixed value of λ of 0.53 eV for the same reasons described previously. Optimum fits were obtained with the following set of parameters: k_0 = 0.15 cm s^{-1}, λ = 0.53 eV and γ/λ = 0.53 eV^{-1}, with excellent quality of fit (MSAD = 2.08 ± 0.74%) comparable to that obtained with the BV formalism.

As can be seen from the results of fitting displayed in Table 6.1, the quality of the fittings is similar for the BV and aMH models whereas the MSAD value is greater for the MH model. Hence, we conclude that under our experimental conditions, the parameterization of the voltammetry by BV and aMH models are analogous. Greater differences between these two models are expected for faster scan rates and/or smaller electrodes such that the electrochemical response shifts to greater overpotentials.

The values of α and γ/λ obtained from the fitting indicates that the reduction/oxidation processes arise from a tighter Gibbs energy curve in the case of the oxidized species. In the context of the Marcus model, this is explained by greater average inner-shell force constants present in TPE^+. Asymmetric effects may also arise from the significant increase in degree of interaction with the solvent molecules accompanying the transformation from the neutral molecule to the charged cation. In any case, the MH model which assumes equal Gibbs energy curves for the reactant and

product is not able to address the asymmetry that arises between the forward and reverse reactions, which is manifested in the overestimation of the forward peak current and underestimation of the reverse. While this deviation is insignificant at the slowest scan rates, it becomes more apparent scan rate increases.

6.4 Conclusions

The BV, MH and aMH formalisms for electrode kinetics have been compared via fitting of cyclic voltammetry of the one-electron oxidation of TPE in DCM. The quality of fit, as indicated by the value of MSAD, is found to be comparable in the BV and aMH models, whereas the MH model gives an inferior quality of fit. This is due to asymmetric effects from greater force constants present in the product compared to the reagent species. The BV and aMH models are able to address this asymmetry with an α value of >0.5 ($\alpha = 0.65 \pm 0.05$), for the case of BV, and a positive value of γ/λ ($\gamma/\lambda = 0.55 \pm 0.05$), for the case of aMH formalism. The MH model is unable to address the asymmetry due to its inherent assumption of equal reorganization energies for oxidation and reduction, giving rise to fittings of poorer quality that tends to overestimate the forward peak current and underestimate the reverse. Therefore, we advocate the use of BV and aMH formalisms over the MH for predicting voltammetric responses of heterogeneous electrochemical systems where reactive species diffuse in solution.

6.5 References

1. M. Grzeszczuk, D.E. Smith, *J. Electroanal. Chem.* **162** (1984) 189.
2. M.D. Geraldo, M.I. Montenegro, L. Slevin, D. Pletcher, *J. Phys. Chem. B* **105** (2001) 3182.
3. T. Troll, M.M. Baizer, *Electrochim. Acta* **19** (1974) 951.
4. B.L. Funt, D.G. Gray, *J. Electrochem. Soc.* **117** (1970) 1020.
5. S. Wawzonek, E.W. Blaha, R. Berkey, M.E. Runner, *J. Electrochem. Soc.* **102** (1955) 235.
6. P.G. Grodzka, P.J. Elving, *J. Electrochem. Soc.* **110** (1963) 231.
7. J.D. Stuart, W.E. Ohnesorge, *J. Am. Chem. Soc.* **93** (1971) 4531.
8. V.S. Vyas, R. Rathore, *Chem. Commun.* **46** (2010) 1065.
9. H. Suzuki, K. Koyano, T. Shida, A. Kira, *Bull. Chem. Soc. Jpn.* **52** (1979) 2794.
10. H. Suzuki, *Bull. Chem. Soc. Jpn.* **33** (1960) 389.
11. O. Brede, E. Müller, W. Naumann, *J. Radioanal. Nucl. Chem. Lett.* **105** (1986) 37.
12. E. Steckhan, *Electrochim. Acta* **22** (1977) 395.
13. M.C. Henstridge, E. Laborda, N.V. Rees, R.G. Compton, *Electrochim. Acta*, doi:10.1016/j.electra.2011.10.026.
14. D. Suwatchara, M.C. Henstridge, N.V. Rees, R.G. Compton, *J. Phys. Chem. C* **115** (2011) 14876.
15. D. Suwatchara, N.V. Rees, M.C. Henstridge, E. Laborda, R.G. Compton, *J. Electroanal. Chem.* **665** (2012) 38.
16. M.C. Henstridge, Y. Wang, J.G. Limon-Petersen, E. Laborda, R.G. Compton, *Chem. Phys. Lett.* **517** (2011) 29.

17. E. Laborda, Y. Wang, M. Henstridge, F. Martinez-Ortiz, A. Molina, R.G. Compton, *Chem. Phys. Lett.* **512** (2011) 133.

18. M.C. Henstridge, E. Laborda, E.J.F. Dickinson, R.G. Compton, *J. Electroanal. Chem.* **664** (2012) 73.

19. Y. Wang, E. Laborda, M. Henstridge, F. Martinez-Ortiz, A. Molina, R.G. Compton, *J. Electroanal. Chem.* **668** (2012) 7.

20. E. Laborda, M.C. Henstridge, R.G. Compton, *J. Electroanal. Chem.* **667** (2012) 48.

21. M.C. Henstridge, E. Laborda, Y. Wang, D. Suwatchara, N. Rees, A. Molina, F. Martinez-Ortiz, R.G. Compton, *J. Electroanal. Chem.* **672** (2012) 45.

22. D. Britz, *Digital Simulation in Electrochemistry, third ed.*, Springer, 2005.

23. C. Amatore, E. Maisonhaute, G. Simonneau, *J. Electroanal. Chem.* **486** (2000) 141.

24. R.G. Compton, C.E. Banks, *Understanding Voltammetry, second ed.*, Imperial College Press, Singapore, 2011.

25. A.J. Bard, L.R. Faulkner (Eds.), *Electrochemical Methods Fundamental and Applications*, Wiley, New York, 2001.

26. D. Shoup, A. Szabo, *J. Electroanal. Chem.* **237** (1982) 140.

27. K.N. Marsh, A. Deev, A.C.-T. Wu, E. Tran, A. Klamt, Kor. *J. Chem. Eng.* **19** (2002) 357.

28. Y. Wang, J.G. Limon-Petersen, R.G. Compton, *J. Electroanal. Chem.* **652** (2011) 13.

29. O.V. Klymenko, R.G. Evans, C. Hardacre, I.B. Svir, R.G. Compton, *J. Electroanal. Chem* **571** (2004) 211.

30. C.A. Paddon, D.S. Silvester, F.L. Bhatti, T.J. Donohoe, R.G. Compton, *Electroanalysis* **19** (2007) 11.

31. A.D. Clegg, N.V. Rees, O.V. Klymenko, B.A. Coles, R.G. Compton, *J. Am. Chem. Soc.* **126** (2004) 6185.

32. A.D. Clegg, N.V. Rees, O.V. Klymenko, B.A. Coles, R.G. Compton, *J. Electroanal. Chem.* **580** (2005) 78.

33. A.D. Clegg, N.V. Rees, O.V. Klymenko, B.A. Coles, R.G. Compton, *ChemPhysChem* **5** (2004) 1234.

34. N.V. Rees, A.D. Clegg, O.V. Klymenko, B.A. Coles, R.G. Compton, *J. Phys. Chem. B* **108** (2004) 13047.

Chapter 7

Giving Physical Insight to the Butler–Volmer Model of Electrode Kinetics: Application of Asymmetric Marcus–Hush-Chidsey Theory to the Study of the Electro-reductions of 2-Methyl-2-Nitropropane, Cyclooctatetraene and Europium(III) on Mercury Microelectrodes

The work presented in this chapter has been published in

J. Electroanal. Chem. **672** (2012) 45.

The asymmetric Marcus-Hush-Chidsey (aMH) model for electrode kinetics is applied to the kinetic study of the electro-reduction of 2-methyl-2-nitropropane in acetonitrile, cyclooctatetraene in dimethylsulfoxide and europium(III) in aqueous solution, using mercury microhemispheres as working electrodes. This kinetic model includes the possibility of the oxidative and reductive processes having different reorganization energies due to differences between the force constants of the electroactive species.

For each redox couple, the response obtained in cyclic and square wave voltammetries can be fitted satisfactorily with the four-parameter aMH model. From the fitting of the voltammograms the values of the kinetic parameters are extracted and analyzed in terms of physical properties of the electroactive species. A comparison of

the asymmetric model against the simpler, phenomenological Butler–Volmer (BV) approach is discussed, as well as a possible physical interpretation for the BV transfer coefficient.

Programs used for simulations in this chapter were developed by Dr. E. Laborda and Dr. M. C. Henstridge. Experiments on 2-methyl-2-nitropropane and europium(III) systems were carried out by Y. Wang.

7.1 Introduction

Based on the work described in Chapters 4-6, and other work performed within [1-7] and outside [8-14] of the group, evaluation of the Marcus-Hush-Chidsey (MH) model of electrode kinetics applied to systems where electroactive species diffuse in solution reveals its inadequacy in fitting systems where the Butler-Volmer (BV) transfer coefficient differs from 0.5. Marcus [15] and other authors [8,9] have pointed out that these deviations may be due to differences between the force constants of the reactants and products, which are assumed equal in the MH model. However, as a consequence of the electron transfer, reactant and product species may carry differing charges. This may render the vibrational modes and interactions with the solvent to differ significantly, resulting in differences in the reorganization energies of the oxidative and reductive processes. For homogeneous electron transfer processes, different oxidative and reductive reorganization energies in one of the participating redox couples may be compensated by a corresponding difference in the other. By contrast, for reactions occurring at an electrode there is only one participating redox couple and so such compensation is less likely.

In order to address this inadequacy, further work have been performed in the group by Larborda and co-workers [16] making use of the asymmetric form of the Marcus theory [15] to derive the asymmetric Marcus-Hush-Chidsey (aMH) model which can be parameterized in terms of four parameters: the formal potential (E_f^{θ}), the standard heterogeneous rate constant (k_0), the reorganization energy (λ), and the asymmetric parameter (γ) which is defined as:

$$\gamma = \lambda_i \langle l_s \rangle = \lambda_i \frac{\sum_s k_s (\Delta q_s^0)^2 l_s}{\sum_s k_s (\Delta q_s^0)^2} \tag{7.1}$$

where Δq_s^0 is the difference of the equilibrium values for the s-th normal mode coordinate of reactants and products, and k_s and l_s symmetric and antisymmetric combinations of the force constants of the s-th mode of reactants and products, f_s^{ox} and f_s^{red} respectively:

$$k_s = \frac{2 f_s^{red} f_s^{ox}}{f_s^{red} + f_s^{ox}} \tag{7.2}$$

$$l_s = \frac{f_s^{ox} - f_s^{red}}{f_s^{ox} + f_s^{red}} \tag{7.3}$$

A detailed mathematical treatment of this model is described in Chapter 2.4.

Based on this theory, the symmetric MH model can be considered a particular case of this model for which γ = 0. This is because, for the value of γ = 0, the activation Gibbs energy of the system collapses to that of the symmetric MH form.

This chapter further examines the ability of the aMH model to fit voltammetric responses of systems where α value differs from 0.5. Experimental systems used include the electro-reductions of 2-methyl-2-nitropropane(MeNP) in acetonitrile, cyclooctatetraene(COT) in dimethylsulfoxide and europium(III)(Eu^{3+}) in aqueous solution using mercury microhemisphere working electrodes:

$$MeNP + e^- \rightleftharpoons MeNP^{\bullet -} \quad (7.4)$$

$$COT + e^- \rightleftharpoons COT^{\bullet -} \quad (7.5)$$

$$Eu^{3+} + e^- \rightleftharpoons Eu^{2+} \quad (7.6)$$

The quality of fitting and the uniqueness of the kinetic parameters extracted from cyclic and square wave voltammograms are discussed. Further, an approximate relationship is derived between the transfer coefficient α from Butler–Volmer and the ratio γ/λ from the asymmetric Marcus-Hush-Chidsey model, suggesting the possibility of gaining physical insight into an electrochemical system using the phenomenological Butler–Volmer model.

7.2 Experimental

Chemical Reagents

Cyclooctatetraene (COT, Aldrich, 98%), 2-methyl-2-nitropropane (MeNP, Aldrich, 99%), europium(III) chloride hexahydrate ($EuCl_3 \cdot 6H_2O$, Aldrich, 99.99%), mercury(I) nitrate dehydrate ($Hg_2(NO_3)_2 \cdot 2H_2O$, Aldrich, >97%), nitric acid (HNO_3, Fisher scientific, 70%), ferrocene ($Fe(C_5H_5)_2$, Aldrich, 98%), cobalt(III) sepulchrate

trichloride ([CoSep]Cl_3, Aldrich, 95%), potassium nitrate (KNO_3, Aldrich, >99%), potassium chloride (KCl, Aldrich, >99%), acetonitrile (MeCN, Fisher Scientific, HPLC grade), N,N-dimethylformamide (DMF, Aldrich, anhydrous grade) and dimethylsulfoxide (DMSO, Alfa Aesar, >99%) were all used as received without further purification.

Background electrolytes including tetraethylammonium perchlorate (TEAP, Fluka, Puriss. grade), tetraethylammonium bromide (TEABr, BDH Chemicals, 98%), tetrabutylammonium perchlorate (TBAP, Fluka, Puriss grade) and tetrabutylammonium iodide (TBAI, Aldrich, >98%) were recrystallized from ethanol and dried in a dessicator for 48 h prior to use in order to remove adsorbed moisture and trace electroactive species.

Instrumentation

All electrochemical measurements were performed with a computer-controlled Autolab PGSTAT12 (Metrohm-Autolab BV, Utrecht, Netherlands).

Mercury hemispherical electrodes electrodeposited on platinum disks were used as working electrodes. A silver wire was employed as reference electrode for organic solvents and a saturated calomel electrode (SCE) for aqueous solutions. A platinum foil was used as counter electrode.

Microdisk electrodes of radii 25 and 50 μm were fabricated in-house by sealing Pt wire (Goodfellow Cambridge Ltd., UK) into a soda glass capillary. The platinum disk was polished prior to hemisphere deposition using 1.0, 0.3 and 0.05 μm alumina-water slurry on soft lapping pads (Buehler, Illinois). The disk size was calibrated from chronoamperometry of 1 mM ferrocene solution in acetronitrile supported by 0.1 M

TBAP using the Shoup and Szabo expression [17–19] (see Equation 5.3 in Chapter 5). A value of the diffusion coefficient for ferrocene of $D = 2.3 \times 10^{-9}$ m^2 s^{-1} at 25 ºC was assumed according to literature [20].

Mercury hemispheres were electrochemically deposited onto each microdisk by stepping to –0.25 V vs. Ag wire in a 5 mM $Hg_2(NO_3)_2$ solution containing 0.1 M KNO_3 and acidified to 0.5% with HNO_3 [21].

The size of the hemispherical drop was initially controlled by the amount of charge passed, and then confirmed by both optical and electrochemical methods. Thus, visual measurement of the hemispheres was obtained through the use of a JVC digital video camera TK-C921EG. In all cases, the mercury droplet was found to adopt the radius of its respective microdisk. The electrochemical characterization of the mercury hemispheres was also carried out through analysis of the limiting current chronoamperogram of an aqueous solution containing 2 mM [CoSep]Cl_3 and 0.1 M KNO_3 through the use of Equation 5.4 in Chapter 5. The value of the diffusion coefficient of [CoSep]Cl_3 employed for the calculations was 6.3×10^{-10} m^2 s^{-1} [3,22,23].

Cyclic and Square Wave Voltammetry Experiments

The specific conditions for cyclic voltammetry (CV) and square wave voltammetry (SWV) experiments are given in each figure presented in this chapter.

In all cases, the working solution was degassed with N_2 (BOC Gases) for at least 20 min before each experiment and a positive pressure of N_2 was maintained throughout. Measurements were carried out at 25 ± 0.2 ºC with stringent thermal control of the electrochemical cell through the use of an air heater-controller system.

The diffusion coefficients of the electroactive species were determined separately via double potential step chronoamperometry [19] in the case of MeNP and Eu(III). In the case of COT, the use of double step chronoamperometry was not feasible due to interference by a second reduction wave [3,24]. The diffusion coefficient of the oxidized species (COT) was extracted via single pulse chronoamperograms and that of the reduced species (radical anion $COT^{\bullet-}$) was determined from the fitting of the cyclic voltammograms. The results obtained are included in Table 7.1.

Table 7.1: *Values of the diffusion coefficients obtained for the electroactive species of each redox system under the experimental working conditions for cyclic and square wave voltammetry experiments.*

Redox Couple	**Medium**	**D_{ox} (m^2 s^{-1})**	**D_{red} (m^2 s^{-1})**
$MeNP/MeNP^{\bullet-}$	0.1 M TBAP, MeCN	2.7×10^{-9}	2.7×10^{-9}
$COT/COT^{\bullet-}$	0.1 M TEABr, DMSO	7.4×10^{-10}	6.5×10^{-10}
Eu(III)/Eu(II)	0.4 M KCl, H_2O	6.5×10^{-10}	9.0×10^{-10}

The occurrence of ohmic drop or migration effects are not considered following simulation [25–27] of the influence of the uncompensated resistance for the conditions of the working solutions.

Fitting Methodology

The theoretical results corresponding to the Butler–Volmer and Marcus–Hush models were obtained by means of finite difference numerical methods using programs developed in-house by Dr. M. C. Henstridge and Dr. E. Laborda.

Best fit parameters were sought for each model, $\{E_f^{\Theta}, k_0, \alpha\}$ for BV and $\{E_f^{\Theta}, k_0, \lambda, \gamma\}$ for aMH, via minimization of the mean scaled absolute deviation (MSAD) for each voltammogram. The mathematical expression for %MSAD is given in Equation 4.15 in Chapter 4. In order to avoid large contributions to the MSAD as a consequence of a very small signal value, only the points where experimental current is, at least, 10% of the peak current have been considered in the calculations. In the case of the electro-reduction of COT in SWV, only the points around the SWV peak (experimental current of at least 70% of the peak current) were considered to avoid any distortion by the second wave.

7.3 Results and Discussion

Experimental cyclic (CV) and square-wave (SWV) voltammetries for the electro-reduction of systems (7.4)–(7.6) were fitted using both the aMH and BV models. Voltammetry for each of the three redox systems is shown, along with the best fit of each kinetic model, in Figures 7.1–7.6.

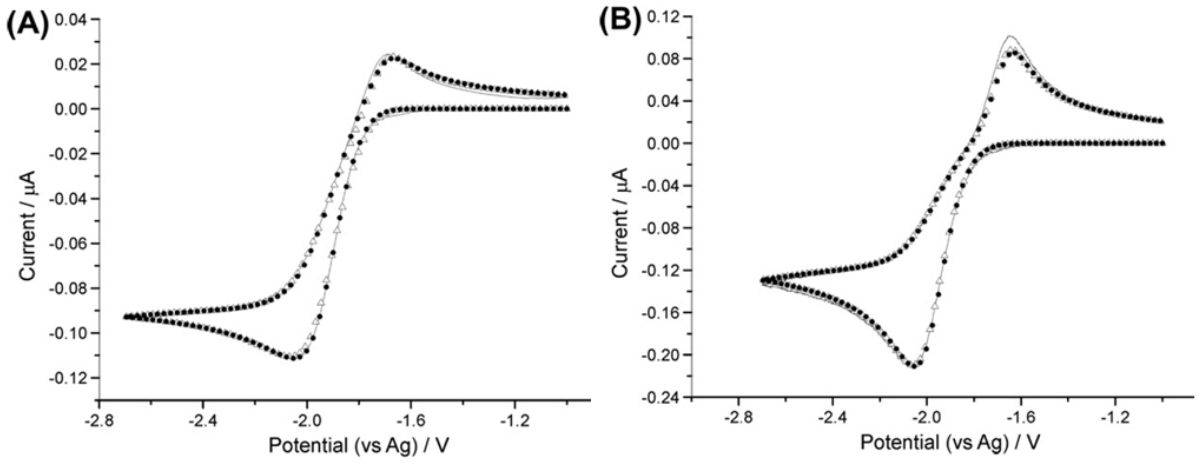


Figure 7.1: *Experimental (solid line) and theoretical CV voltammograms obtained with the aMH (solid circles) and BV (open triangles) models for the electro-reduction of 2-methyl-2-nitropropane with a scan rate: (A) 500 and (B) 5000 mV* s^{-1}*. The values of the kinetic parameters considered for simulated results are given in Table 7.2. Working solution: 2 mM MeNP, 0.1 M TBAP in MeCN. A 25 µm radius mercury hemisphere was employed as working electrode.*

It can be seen in Figures 7.1–7.6 that both CV and SWV can be parameterized satisfactorily by using the classical BV model with $\alpha < 0.5$ for COT and MeNP, and $\alpha > 0.5$ for Eu(III). The best fit kinetic parameters obtained from the BV model, together with the average MSAD values, are given in Table 7.2.

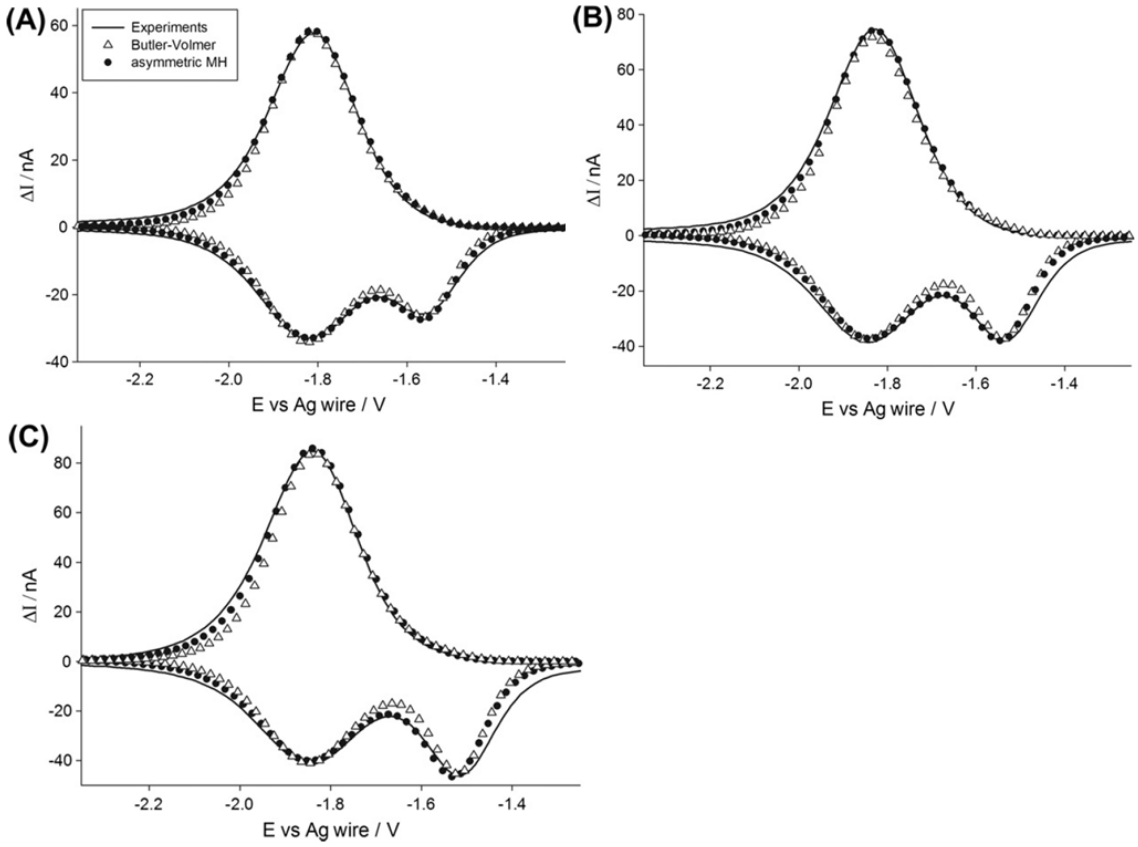


Figure 7.2: *Experimental (solid line) and theoretical SWV voltammograms obtained with the aMH (solid circles) and BV (open triangles) models for the electro-reduction of 2-methyl-2-nitropropane at different frequencies: (A) 100, (B) 200 and (C) 300 Hz. amplitude = 25 mV, and pulse height = 10 mV. The values of the kinetic parameters considered for simulated results are given in Table7.2. Working solution: 2 mM MeNP, 0.1 M TBAP in MeCN. A 25 μm radius mercury hemisphere was employed as working electrode.*

Figures 7.1–7.6 also show that satisfactory fitting of the experimental voltammetry is possible when using the aMH model, with $\{E_f^{\ominus}, k_0, \lambda, \gamma\}$ as adjustable parameters. The quality of the fittings is seen to be comparable or, in some cases, superior to that obtained with the BV model. The aMH approach, however, carries the

additional benefit of enabling rationalization of the kinetic parameters in terms of microscopic properties of the system, as will be discussed below.

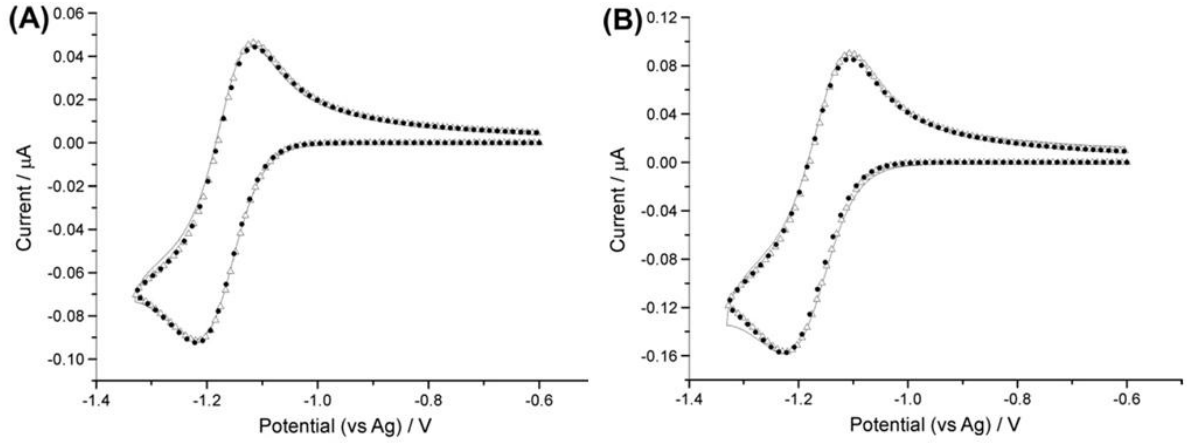


Figure 7.3: *Experimental (solid line) and theoretical CV voltammograms obtained with the aMH (solid circles) and BV (open triangles) models for the electro-reduction of cyclooctatetraene with a scan rate: (A) 250 and (B) 1000 mV* s^{-1}*. The values of the kinetic parameters considered for simulated results are given in Table 7.2. Working solution: 1 mM COT, 0.1 M TEABr in DMSO. A 50 µm radius mercury hemisphere was employed as working electrode.*

Given that four parameters are adjusted in the fitting procedure with the aMH model, the uniqueness of the best-fit set of data may be questioned. In Figure 7.7, this is analyzed via representative MSAD surfaces obtained as a function of the parameters λ and γ/λ, with the k_0 value fixed at the best-fit value (see Table 7.2). For the electro-reduction of MeNP (Figure 7.7A), a minimum in the MSAD surface is observed which enables the unambiguous definition of best-fit kinetic parameters. By contrast, for the

cases of COT and Eu(III) a ‘‘valley’’, rather than a minimum, is obtained. Thus, the MSAD is effectively the same (within 0.5%) in a region defined mainly by the ratio γ/λ (see Figure 7.7B and C). In this situation, from the fitting of the voltammograms only an estimation of the optimum γ/λ value can be extracted.

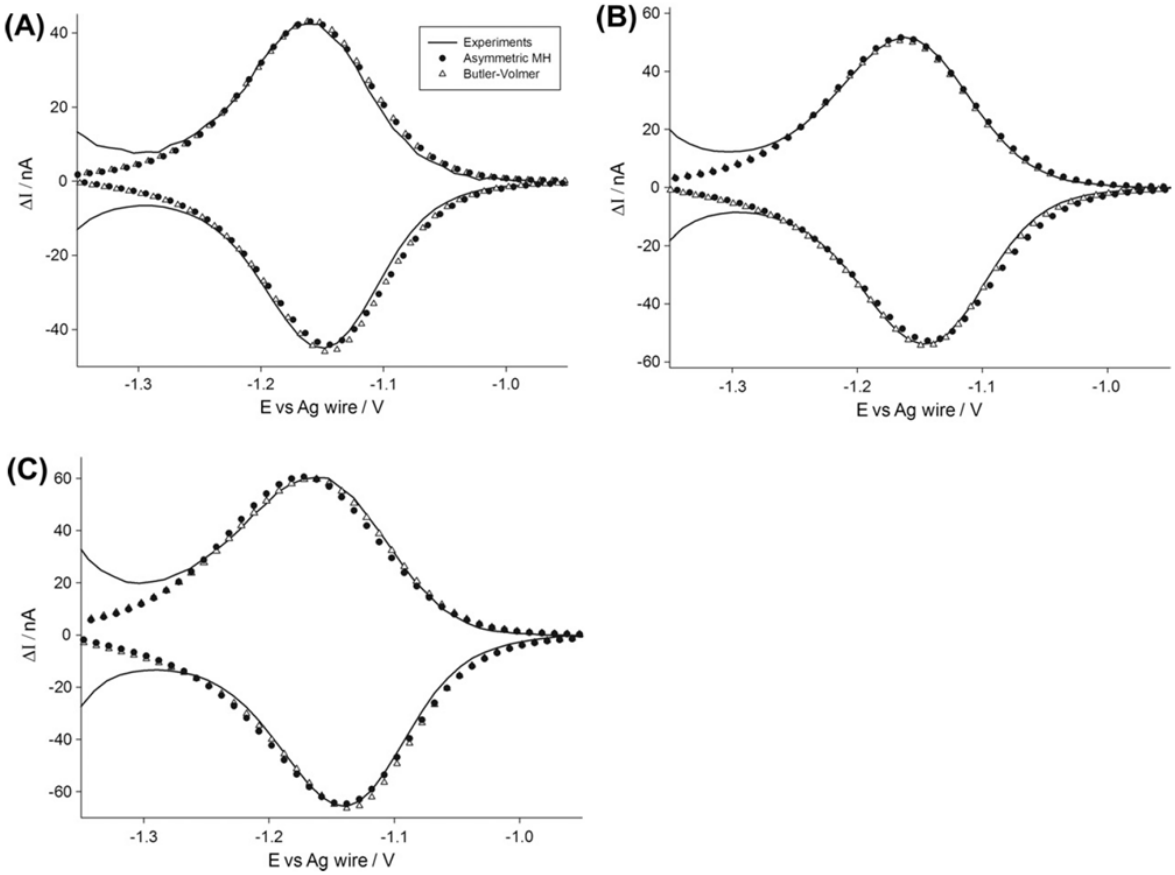


Figure 7.4: *Experimental (solid line) and theoretical SWV voltammograms obtained with the aMH (solid circles) and BV (open triangles) models for the electro-reduction of cyclooctatetraene at different frequencies: (A) 25, (B) 50 and (C) 100 Hz. ESW = 15 mV, ES = 10 mV. The values of the kinetic parameters considered for simulated results are given in Table 7. 2. Working solution: 1 mM COT, 0.1 M TEABr in DMSO. A 50 μm radius mercury hemisphere was employed as working electrode.*

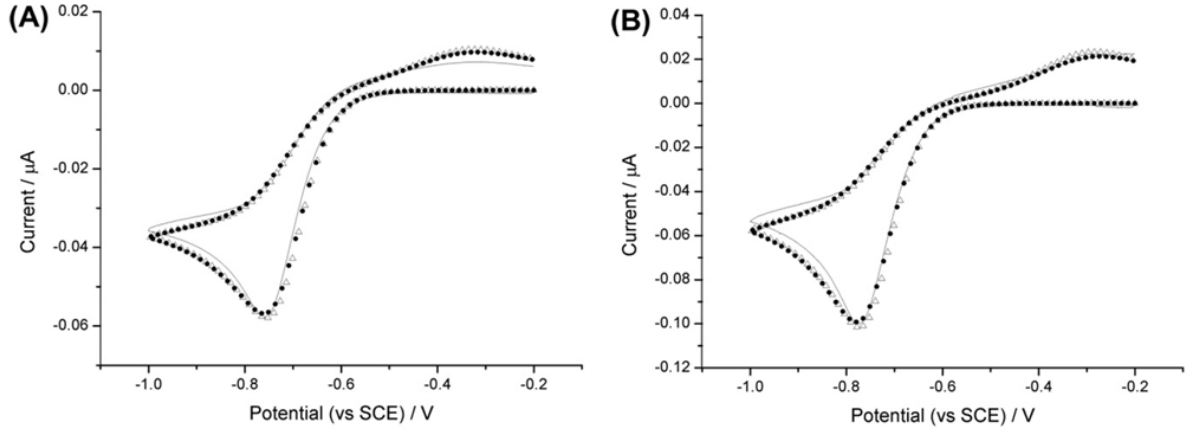


Figure 7.5: *Experimental (solid line) and theoretical CV voltammograms obtained with the aMH (solid circles) and BV (open triangles) models for the electro-reduction of Eu(III) with a scan rate: (A) 250 and (B) 1000 mV* s^{-1}*. The values of the kinetic parameters considered for simulated results are given in Table 7.2. Working solution: 1 mM* $EuCl_3$*, 0.4 M KCl in water. A 50 µm radius mercury hemisphere was employed as working electrode.*

The results obtained from electrochemical methods can be complemented with those from theoretical calculations to gain further information. For example, for the electro-reduction of MeNP, the theoretical estimation of the inner-sphere reorganization energy yields a value of 0.84 eV [28]. Combined with the value γ = -0.31 extracted from the voltammograms, one finds that $\langle l_s \rangle$ = -0.37, which involves that the average ratio of the force constants of the oxidized and reduced species is f_s^{Ox}/f_s^{Red} =0.46 (see Equation 7.3). From the definition of γ (Equation 7.1), the ratio γ/λ is seen to be directly related to the differences between the force constants through $\langle l_s \rangle$. According to the discussion above, this ratio is the key parameter defining the symmetry of the redox process, and so the voltammetric waveshape. Thus, a positive γ/λ value indicates

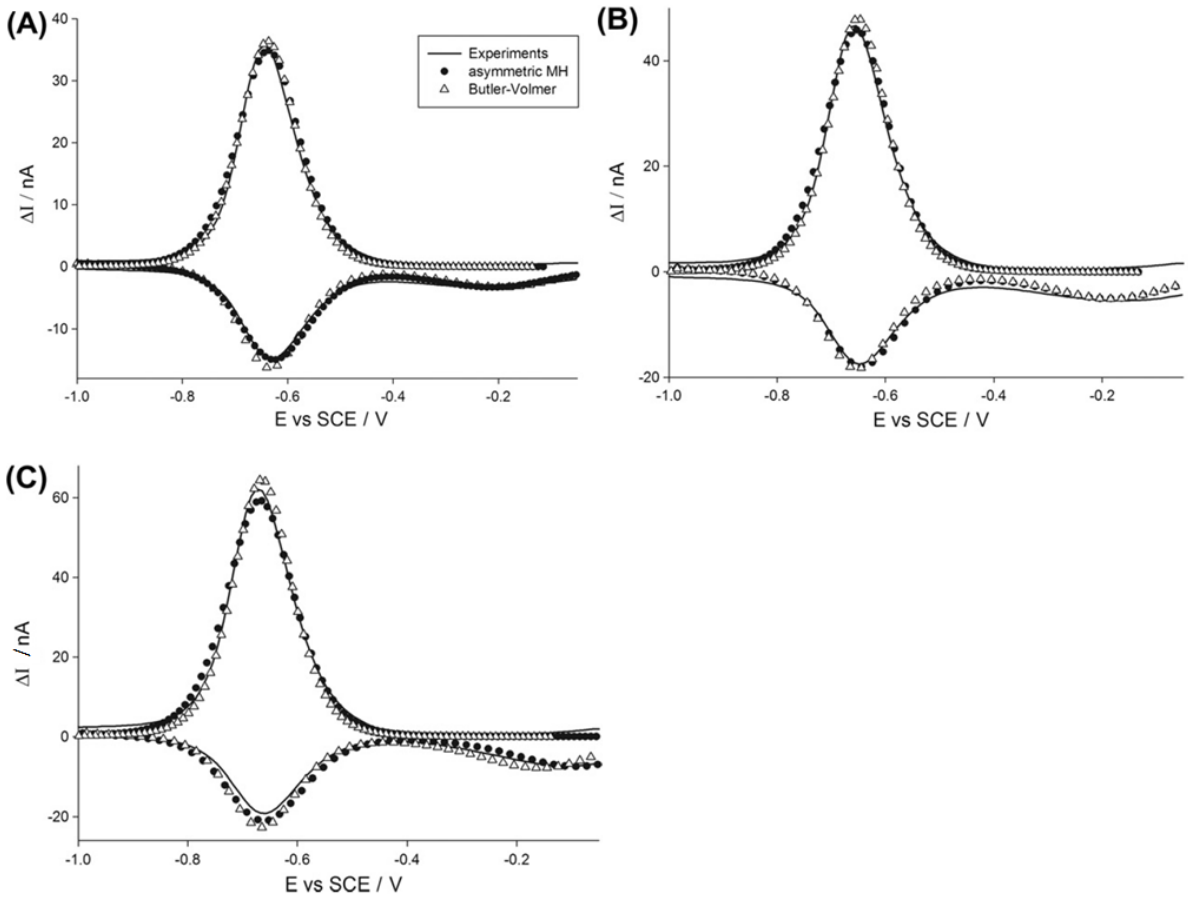


Figure 7.6: *Experimental (solid line) and theoretical SWV voltammograms obtained with the aMH (solid circles) and BV (open triangles) models for the electro-reduction of Eu(III) at different frequencies: (A) 25, (B) 50 and (C) 100 Hz. ESW = 25 mV, ES = 10 mV. The values of the kinetic parameters considered for simulated redults are given in Table 7.2. Working solution: 1 mM $EuCl_3$, 0.4 M KCl in water. A 50 μm radius mercury hemisphere was employed as working electrode.*

$f_s^{Ox} > f_s^{Red}$ and hence a tighter Gibbs energy curve for the oxidized species. This gives rise to an increase of the reductive signal with respect to the oxidative signal [16]. The opposite effect is observed for negative γ/λ values, which are associated with greater force constants of the reduced species. Clearly, the greater the absolute value of γ/λ, the

greater the differences in the force constants and then the greater the effects described above.

Table 7.2: *Kinetic parameters obtained from the fitting of cyclic and square wave voltammograms with the asymmetric Marcus–Hush (aMH) and Butler–Volmer (BV) models.*

Redox Couple	Model	Kinetic Parameters	% MSAD	
			CV	SWV
MeNP/MeNP$^{\bullet-}$	BV	$k_0 = (3.0 \pm 0.2)\times10^{-3}$ cm s^{-1} $\alpha = 0.38 \pm 0.01$	4 ± 2	9.6 ± 0.6
	aMH	$k_0 = (3.0 \pm 0.2)\times10^{-3}$ cm s^{-1} $\gamma/\lambda = -0.31 \pm 0.04$ $\lambda = 1.0 \pm 0.2$ eV	3 ± 1	5 ± 1
COT/COT$^{\bullet-}$	BV	$k_0 = (1.2 \pm 0.2)\times10^{-2}$ cm s^{-1} $\alpha = 0.38 \pm 0.02$	7 ± 2	3.6 ± 0.7
	aMH	$k_0 = (1.1 \pm 0.3)\times10^{-2}$ cm s^{-1} $\gamma/\lambda = -0.22 \pm 0.07$	7 ± 2	4.3 ± 0.6
Eu(III)/Eu(II)	BV	$k_0 = (1.7 \pm 0.7)\times10^{-4}$ cm s^{-1} $\alpha = 0.66 \pm 0.02$	9 ± 2	12 ± 4
	aMH	$k_0 = (1.7 \pm 0.5)\times10^{-4}$ cm s^{-1} $\gamma/\lambda = +0.55 \pm 0.04$	8 ± 3	10 ± 4

Applying this interpretation of the γ/λ value to the experimental results, we observe that negative γ/λ values are obtained for the electro-reduction of COT and MeNP. In both cases the oxidized species is neutral and the reduced species is a radical anion. One would therefore expect the reduced species to interact more strongly with the solvent than the oxidized species and consequently the Gibbs energy curve is tighter for the reduced species [8]. By contrast, for the reduction of Eu(III), a positive γ/λ value is

determined. This can be understood taking into account that in this case the oxidized species carries a larger charge (+3) than the reduced one (+2).

The analysis of the MSAD in Figure 7.7 revealed some correlation between the ratio γ/λ and the transfer coefficient in the BV model. Consequently, it is of interest to analyze the possible connection between these parameters in order to assign a physical interpretation to α. Figure 7.8 shows the variation of both oxidative and reductive rate constants with overpotential for a range of reorganisation energies with a constant ratio $\gamma/\lambda = +0.4$. The value of λ can be seen to affect only the range of potentials over which the ‘‘Tafel’’ plot is approximately linear. Thus, it is principally the ratio γ/λ which determines the rate of variation of the rate constants with overpotential. In this way, the ratio γ/λ acts in a similar fashion within the aMH model as does the transfer coefficient a in the BV model.

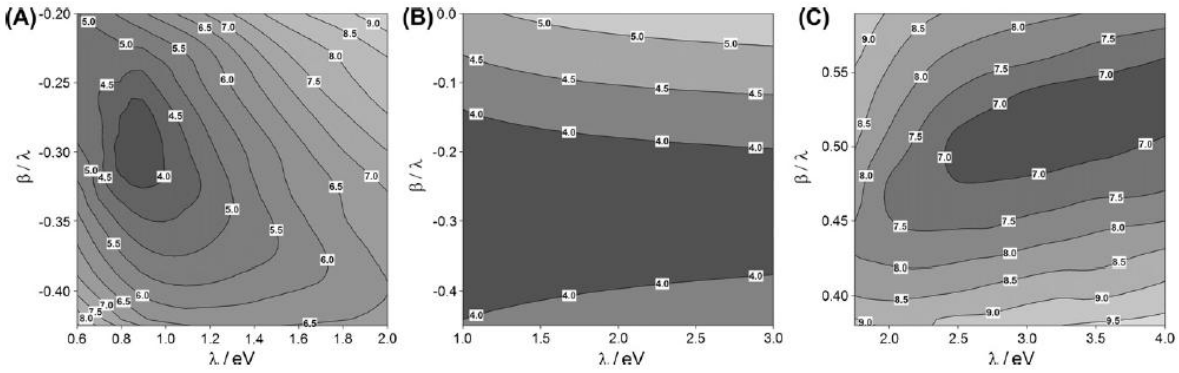


Figure 7.7: *Representative MSAD surfaces corresponding to the fitting of the SWV voltammograms of the electro-reduction of (A) MeNP, (B) COT and (C) Eu(III). Other conditions as described in Figures 7.1–7.6.*

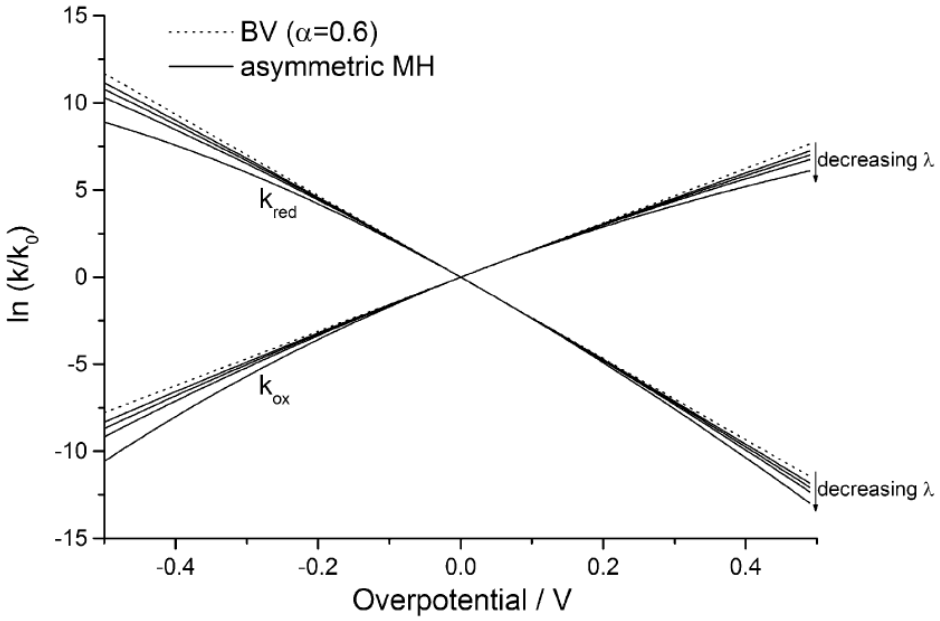


Figure 7.8: *Effect of the reorganization energy (λ) on the evolution of the electrochemical rate constants with the applied overpotential according to the aMH model (solid line) for γ/λ = +0.4. The results corresponding to the BV model for α = 0.6 are also plotted (dotted line).*

Within the symmetric MH model (i.e., $\gamma = 0$) the rate constants have been shown [29] to tend towards those given by the BV model for $\alpha = 0.5$ as $\Lambda \rightarrow \infty$, where Λ is dimensionless reorganization energy, defined thus

$$\Lambda = \frac{F}{RT}\lambda \tag{7.7}$$

The aMH model similarly shows that as $\Lambda \rightarrow \infty$, the rate constants tend towards those given by the BV model for $\alpha = \frac{1}{2} + \frac{1}{4}\frac{\gamma}{\Lambda}$. Accordingly, for the case considered in

Figure 7.8 (i.e., $\gamma/\lambda = +0.4$), we see that the MH curves tend to that for BV with $\alpha = 0.6$ as the reorganization energy increases.

While this relationship between a and γ/λ is exact only in the limit $\Lambda \rightarrow \infty$, the following relationship holds at the formal potential for all values of reorganization energy:

$$(\alpha)_{E=E_f^{\theta}} = \frac{1}{2} + \chi\frac{\gamma}{\lambda} \tag{7.8}$$

Figure 7.9 shows the variation of the parameter χ with λ. While the value of χ deviates markedly from 0.25 for very small reorganization energies, taking a typical experimental reorganisation energy of 2 eV yields $\chi = 0.234$. Empirical fitting of the curve in Figure 7.9 yields the following relationship:

$$\chi = \frac{1}{4} - \frac{1.267}{\Lambda + 3.353} \tag{7.9}$$

which is accurate to within 0.1% for reorganisation energies greater than 0.5 eV.

The above expressions permit a precise estimation of γ/λ once the value of the transfer coefficient at the formal potential is known. This is of importance since it permits an approximate physical interpretation for the great number of experimental systems for which the transfer coefficient is already known. In the same way, it justifies

the use of a simpler Butler–Volmer like analysis of the electrode kinetics, complemented with the physical insights derived from the aMH model.

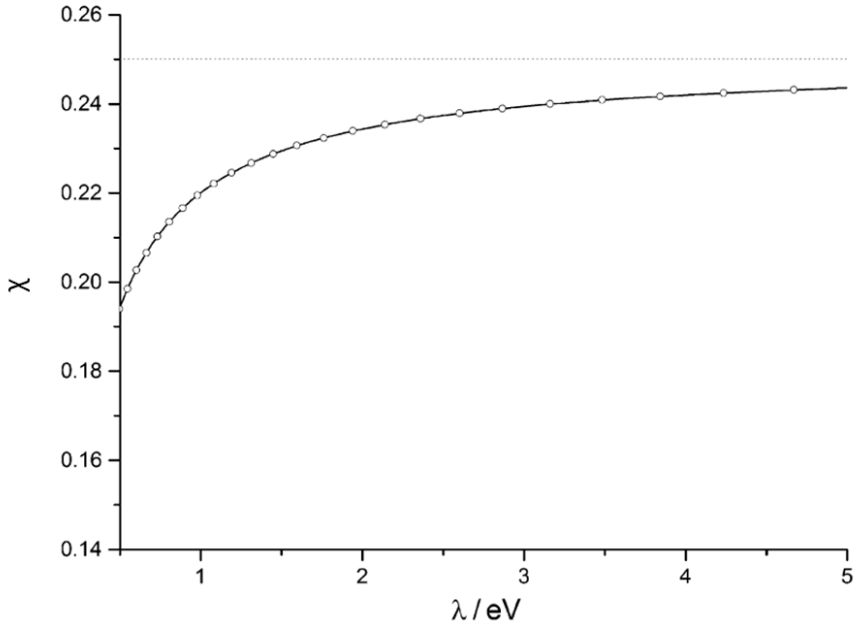


Figure 7.9: *Variation of the parameter χ in Equation 7.8 with the value of the reorganization energy, λ.*

To conclude, α values different from 0.5 can be indicative of asymmetries of the reduction–oxidation processes. According to the aMH model, these are related to differences between the inner-shell force constants of the electroactive species, and they can be treated in a simple, general and analytical way. Nevertheless, asymmetric effects may be described by other theories [30] and they may also arise from interactions outside the coordination shell (e.g., with the solvent), although their treatment can be more complex and needs computer simulations.

7.4 Conclusions

The asymmetric Marcus-Hush-Chidsey model has been applied to the quantitative study of three reduction processes on mercury hemispherical microelectrodes: electro-reduction of 2-methyl-2-nitropropane (MeNP) in acetonitrile, cyclooctatetraene (COT) in dimethylsulfoxide and europium(III) in water solution. The experimental voltammograms recorded in cyclic and square wave voltammetry for all these systems can be fitted satisfactorily using the Butler-Volmer (BV) model, as well as the asymmetric Marcus-Hush-Chidsey (aMH) model.

Through the fitting of experimental data using the aMH model, values of the standard heterogeneous rate constant and the ratio γ/λ are extracted, the latter being related to the differences between the force constants of the oxidized and reduced species. Thus, a positive value of γ/λ is found for the redox couple Eu(III)/Eu(II), which indicates greater force constants in average for the oxidized species. By contrast, for the reductions of the neutral species MeNP and COT into their corresponding radical anions we obtain negative values of γ/λ.

The effect of the ratio γ/λ on the voltammograms has been shown to be analogous to that of the transfer coefficient (α) within the Butler-Volmer formalism. This enables the use of the α value of a given redox couple as an indicator of the differences between the oxidized and reduced species. Thus, the case $\alpha < 0.5$ is related to force constants of the reduced species greater than those of the oxidized one; the opposite situation applies for $\alpha > 0.5$. Moreover, simple relationships have been established to connect the parameters $(\alpha)_{E=E_f^o}$ and γ/λ. This enables a revision of the vast number of α data in terms of this physical interpretation, as well as the use of a

simpler BV-like analysis of electrode kinetics while preserving the physical insights available from Marcus theory.

7.5 References

1. M.C. Henstridge, E. Laborda, N.V. Rees, R.G. Compton, *Electrochim. Acta*, http://dx.doi.org/10.1016/j.electacta.2011.10.026.
2. D. Suwatchara, M.C. Henstridge, N.V. Rees, R.G. Compton, *J. Phys. Chem. C* **115** (2011) 14876.
3. D. Suwatchara, N.V. Rees, M.C. Henstridge, E. Laborda, R.G. Compton, *J. Electroanal. Chem.* **665** (2012) 38.
4. M.C. Henstridge, Y. Wang, J.G. Limon-Petersen, E. Laborda, R.G. Compton, *Chem. Phys. Lett.* **517** (2011) 29.
5. E. Laborda, Y. Wang, M. Henstridge, F. Martinez-Ortiz, A. Molina, R.G. Compton, *Chem. Phys. Lett.* **512** (2011) 133.
6. M.C. Henstridge, E. Laborda, E.J.F. Dickinson, R.G. Compton, *J. Electroanal. Chem.* **664** (2012) 73.
7. Y. Wang, E. Laborda, M. Henstridge, F. Martinez-Ortiz, A. Molina, R.G. Compton, *J. Electroanal. Chem.* **668** (2012) 7.
8. J.-M. Savéant, D. Tessier, *Faraday Discuss. Chem. Soc.* **74** (1982) 57.
9. J.T. Hupp, M.J. Weaver, *J. Phys. Chem.* **88** (1984) 6128.
10. R.M. Haddox, H.O. Finklea, *J. Phys. Chem. B* **108** (2004) 1694.
11. N. Madhiri, H.O. Finklea, *Langmuir* **22** (2006) 10643.
12. A.L. Eckermann, J.A. Shaw, T.J. Meade, *Langmuir* **26** (2010) 2904.
13. G.A. Orlowski, H.-B. Kraatz, *Electrochim. Acta* **51** (2006) 2934.
14. G.A. Orlowski, S. Chowdhury, H.-B. Kraatz, *Langmuir* **23** (2007) 12765.

15. R.A. Marcus, *J. Chem. Phys.* **43** (1965) 679.

16. E. Laborda, M. Henstridge, R.G. Compton, *J. Electroanal. Chem.* **667** (2012) 48.

17. D. Shoup, A. Szabo, *J. Electroanal. Chem.* **237** (1982) 140.

18. A.J. Bard, L.R. Faulkner, *Electrochemical Methods, Fundamentals and Applications*, Wiley, New York, 2001.

19. R.G. Compton, C.E. Banks, *Understanding Voltammetry, second ed.*, Imperial College Press, United Kingdom, 2010.

20. K.N. Marsh, A. Deev, A.C.-T. Wu, E. Tran, A. Klamt, Kor. *J. Chem. Eng.* **19** (2002) 357.

21. J. Mauzeroll, E.A. Hueske, A.J. Bard, *Anal. Chem.* **75** (2003) 3880.

22. T.J. Davies, B.A. Brookes, A.C. Fisher, K. Yunus, S.J. Wilkins, P.R. Greene, J.D. Wadhawan, R.G. Compton, *J. Phys. Chem. B* **107** (2003) 6431.

23. A. Molina, E. Laborda, E.I. Rogers, F. Martinez-Ortiz, C. Serna, J.G. Limon-Petersen, N.V. Rees, R.G. Compton, *J. Electroanal. Chem.* **634** (2009) 73.

24. R.D. Allendoerfer, P.H. Rieger, *J. Amer. Chem. Soc.* **87** (1965) 2336.

25. J.G. Limon-Petersen, I. Streeter, N.V. Rees, R.G. Compton, *J. Phys. Chem. C* **113** (2009) 333.

26. E.J.F. Dickinson, J.G. Limon-Petersen, N.V. Rees, R.G. Compton, *J. Phys. Chem. C* **113** (2009) 11157.

27. C. Amatore, E. Maisonhaute, G. Simonneau, *J. Electroanal. Chem.* **486** (2000) 141.

28. C. Kraiya, P. Singh, D.H. Evans, *J. Electroanal. Chem.* **563** (2004) 203.

29. C.E.D. Chidsey, *Science* **215** (1991) 919.

30. S. Fletcher, *J. Solid State Electrochem.* **14** (2010) 705.

PART IV

Developing Further Physical Insights Based on the Asymmetric Marcus-Hush-Chidsey Model of Electrode Kinetics

Part 4 presents further development of physical insights into microscopic processes of heterogeneous electron transfer based on the asymmetric Marcus-Hush-Chidsey model. Cyclic voltammetry carried out at variable temperature has been applied to 1-Nitropentane (Chapter 8) and 3-Nitrophenolate (Chapter 9) as a method for the appraisal of the value of reorganization energy of the reactive species. Furthermore, the ability of the model to correlate the variation of electron transfer rate to the degree of adiabaticity was also evaluated using 3-Nitrophenolate reagent (Chapter 10) with the distance of approach augmented through variation in size of supporting electrolyte cations. Chapter 11 extends the study on adiabaticity to a system with a lesser degree of adiabaticity, namely 2-Nitropropane. Here, the cyclic voltammograms were fitted with the asymmetric Marcus-Hush-Chidsey model and the adiabaticity of the system is studied with the potential energy curve model developed by Waldeck and Mishra (*J. Phys. Chem. C* **113** (2009) 17904).

Programs used for simulations were written by Dr. E. Laborda.

Chapter 8

Molecular Insights into Electron Transfer Processes via Cyclic Voltammetry at Variable Temperature: Application of the Asymmetric Marcus-Hush-Chidsey Model

The work presented in this chapter has been published in

J. Electroanal. Chem. **685** (2012) 53.

This chapter describes the study of the variation of the kinetics of electrode processes with temperature based on the asymmetric version of the Marcus theory. This kinetic model introduces a new symmetry parameter that takes into account possible differences between the inner-sphere force constants of the oxidized and reduced electroactive species. Variable temperature measurements in fast-scan cyclic voltammetry are employed to gain further insights into the molecular properties of the electro-reduction of 1-nitropentane in acetonitrile on mercury hemispherical microelectrodes of 28.5 μm radius. Thus, the values of the reorganization energy of the electron transfer process and the symmetry parameter as well as the degree of adiabaticity of the electron transfer reaction are evaluated.

The results are also analyzed in terms of the ability of the different kinetic models employed in Electrochemistry, namely: Butler–Volmer (BV), and symmetric and asymmetric Marcus-Hush-Chidsey (MH and aMH, respectively) to fit the experimental voltammograms with consistent values for the kinetic parameters in a range of temperatures and scan rates.

Programs used for simulations were written by Dr. E. Laborda.

8.1 Introduction

The application of microscopic models of electron transfer processes to electrode reactions potentially enables the use of electrochemical measurements to gain information about the molecular characteristics of the electron transfer reaction [1–5]. Through these models the electrode kinetics can be related to the molecular properties of the electroactive species in a particular medium as well as to the electronic characteristics of the electrode material. Among them, the Marcus theory is the most widely used [6,7]. In this model, the reorganization energy, λ, is related to the energy required to modify the inner (angles and bonds) and outer (solvent) configurations of the reagent species into those of the product. However, several experimental discrepancies from the symmetric version of the Marcus theory (known as the Marcus-Hush-Chidsey (MH) model for electrode processes) [6–9] has been reported in the literature for both diffusional and surface-bound electrode processes [10–25].

Differences between the inner-sphere and outer-sphere force constants of the reduced and oxidized species can be responsible for the deviations mentioned above. Thus, the asymmetric form of the Marcus theory (referred as asymmetric Marcus-Hush-Chidsey (aMH) model) has been applied to the study of electrode reactions [23–25]. Results of the study have been presented in Part III of this thesis. The asymmetric version of the model introduces the symmetry parameter γ which is associated with the difference between the vibrational modes of the electroactive species. The mathematical treatment of the aMH model is described in detail in Chapter 2.4.

In this chapter the aMH model is used in kinetic studies at variable temperaature. Electrochemical measurements at different temperatures are very

valuable in order to obtain microscopic information about a given electrode reaction. Whereas the symmetry parameter can be determined with satisfactory accuracy from voltammetric measurements at constant temperature, this may not be the case of the value of the reorganization energy [24]. Voltammetric experiments at different temperatures enable more accurate determination of the λ value as well as estimation of the degree of adiabaticity of the electrode reaction [26,27]. This information is of interest in the understanding of the fundamental factors determining electron transfers which are key processes in chemistry and biology. Moreover, it offers a more thorough evaluation of the soundness of the different kinetic models employed in Electrochemistry.

The electro-reduction of 1-nitropentane in acetonitrile is studied experimentally by using hemispherical mercury microelectrodes and fast scan cyclic voltammetry. Cyclic voltammograms have been recorded at several temperatures in the range of 26-37 ºC and fitted considering different kinetic approaches: Butler-Volmer (BV), symmetric Marcus-Hush-Chidsey (MH) and asymmetric Marcus-Hush-Chidsey (aMH) models. The kinetic parameters and the quality of the fittings obtained from each model are quantified and compared. Finally, the value of the reorganization energy and the degree of adiabaticity are determined from the variation of the standard electrochemical rate constant with temperature.

8.2 Experimental

Chemical Reagents

1-Nitropentane ($CH_3(CH_2)_3CH_2NO_2$, Aldrich, 97%), tetra-nbutylammonium perchlorate (TBAP, Fluka, Puriss. grade), mercury(I) nitrate dihydrate ($Hg_2(NO_3)_2 \cdot 2H_2O$, Aldrich, >97%), nitric acid (HNO_3, Fisher scientific, 70%),

ferrocene ($Fe(C_5H_5)_2$, Aldrich, 98%), cobalt(III) sepulchrate trichloride ($[CoSep]Cl_3$, Aldrich, 95%), potassium nitrate (KNO_3, Aldrich, >99%), acetonitrile (MeCN, Fisher Scientific, HPLC grade), were all used as received without further purification.

Instrumentation

Cyclic voltammetry with a scan rate range between 30 mV s^{-1} and 5 V s^{-1} and potential step chronoamperometry were performed with a computer-controlled Autolab PGSTAT12 (Metrohm-Autolab BV, Utrecht, Netherlands). Fast-scan cyclic voltmmograms encompassing scan rates between 180 and 1844 V s^{-1} were recorded with a fast-scan potentiostat constructed in-house conforming to the design developed by Amatore et al. [28]. This potentiostat is capable of ohmic drop compensation by means of an internal positive feedback circuit. Microdisk working electrodes of 28.5 μm radius was fabricated in-house by sealing Pt wire (Goodfellow Cambridge Ltd., UK) into soda glass capillary according to the published method [29]. The platinum disk was polished prior to hemisphere deposition using 1.0, 0.3 and 0.05 μm alumina-water slurry on soft lapping pads (Buehler, Illinois). The disk size was calibrated by numerical fitting of the chronoamperometric response of the 1.0 mM ferrocene solution in acetonitrile supported by 0.1 M TBAP using the Shoup and Szabo expression [1,2,30] (see Equation 5.3 in Chapter 5). A widely adopted literature diffusion coefficient for ferrocene of $D = 2.3 \times 10^{-9}$ m^2 s^{-1} at 25 ºC [31] was employed for the calculations.

A mercury hemisphere was then electrochemically deposited onto the microdisk from a 50 mM $Hg_2(NO_3)_2$ solution containing 0.1 M KNO_3 and acidified to 0.5% with HNO_3 following the method laid out by Bard et al. [32]. For deposition, the potential was stepped to -0.25 V vs. Ag wire. The size of the hemispherical drop was controlled by the amount of charge passed.

A platinum foil counter electrode was employed for all electrochemical measurements while a silver wire was used as the reference electrode. Stringent thermal control of the electrochemical cell was achieved through the use of an air heater-controller system fabricated in-house. With this system, temperature control was achieved within the precision of ±0.1 ºC.

Characterization of the Hemispherical Mercury Electrode

The size and shape of the mercury deposit was characterized by optical and electrochemical methods.

Visual measurement of the hemisphere was obtained through the use of a JVC digital video camera TK-C921EG. To allow the appraisal of size and shape of the hemisphere in the environment of the reagent solution, the working electrode was submerged in the solution sealed within a UV/vis cuvette, and visual image taken. It was found that the mercury droplet formed a hemisphere which adopted the radius of the microdisk. An image of the 28.5 μm hemisphere is shown in Figure 8.1.

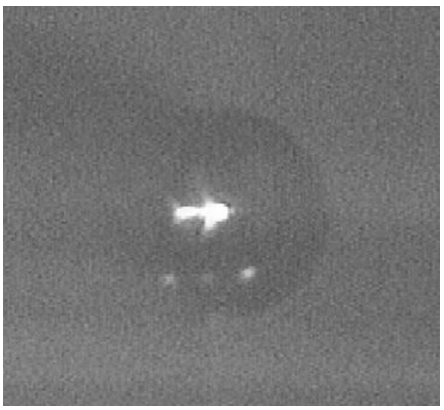


Figure 8.1: *Image of the 28.5 μm radius electrodeposited hemisphere immersed in acetonitrile.*

The electrochemical characterization of the mercury hemispheres was carried out through analysis of the limiting current chronoamperogram of an aqueous solution containing 2 mM $[CoSep]Cl_3$ and 0.1 M KNO_3, which is given by the expression shown in Equation 5.4 of Chapter 5 for the case of electrodes with spherical geometry[1,2]. The value of the diffusion coefficient of $[CoSep]Cl_3$ employed for the calculations was $D = 6.3 \times 10^{-10}$ m^2 s^{-1}. This was determined from chronoamperograms recorded at microdisk electrode of known dimensions from the Shoup and Szabo expression and it is in close agreement with literature [33,34].

The radius obtained through the analysis of the chronoamperogram was found to be 28.5 μm. This coincides with that determined with the optical measurements outlined previously.

Cyclic Voltammetry and Potential Step Chronoamperometry Measurements

Cyclic voltammograms at typical scan rates (within the range of 30 mV s^{-1} to 5 V s^{-1}) were recorded between -1.00 and -1.90 V (vs. Ag wire) on 28.5 μm radius mercury hemispherical electrode in 1.5, 0.5 and 0.073 mM 1-nitropentane solution containing 0.1 M TBAP supporting electrolyte in MeCN.

Fast-scan cyclic voltammograms encompassing the scan rates of 180–1844 V s^{-1} were recorded between -1.00 and -2.10 V (vs. Ag wire) on 28.5 μm radius mercury hemispherical electrode. Ohmic drop compensation was set by the on-screen adjustment relative to the onset of observed oscillations as described in [35]. Care was taken to ensure that the circuit was not over-compensated to avoid large amplitude oscillations which often have deleterious effects on the electrode surface.

Six sets of voltammograms, each recorded at a different temperature, were obtained with fast-scan cyclic voltammetry: (1) T = 26 ºC, scan rates: 187–1844 V s^{-1}; (2) T = 27.5 ºC, scan rates: 142–1300 V s^{-1}; (3) T = 30 ºC, scan rates: 180–1495 V s^{-1}; (4) T = 32 ºC, scan rates: 180–1494 V s^{-1}; (5) T = 35 ºC, scan rates: 145–1337 V s^{-1}; and (6) T = 37 ºC, scan rates: 182–1491 V s^{-1}. All the solutions contained 0.1 M TBAP background electrolyte in MeCN solvent.

Potential step chronoamperometry was recorded for each experimental set conducted in the current study. The potential was stepped from -1.30 V where there is no faradaic current to -1.80 V (vs. Ag wire) where the reduction current is fully controlled by diffusion and was held for 0.5 s. The resulting chronoamperometric response was simultaneously fitted for both the diffusion coefficient and concentration of the electroactive species using a previously reported method [36–38].

Fitting Methodology

Simulation programs written in-house were used to simulate cyclic voltammograms on a hemispherical electrode based on the BV, MH and aMH formalisms. These were used, in conjunction with the value of diffusion coefficients determined through numerical fitting of chronoamperometric responses, to model cyclic voltammograms over the full range of experimental conditions. Fitting of the electrochemical reduction processes was carried out by matching the peak potentials, thereby fixing the formal potential (E_f^{Θ}), which over the course of our experiment is found to shift within ±30 mV range due to the use of Ag wire pseudo reference electrode), the standard electrochemical rate constant (k_0) and the transfer coefficient (a) (for BV formalism), the reorganization energy (λ) (for MH formalism), or the asymmetric parameter (γ) and reorganization energy (λ) (for aMH formalism).

The quality of the fitting was evaluated from the value of the mean scaled absolute deviation (MSAD). The mathematical expression of %MSAD has been given in Equation 4.15 in Chapter 4.

Large contributions to the MSAD as a consequence of very small signal values were avoided by considering only the points where i_{exp} is at least 10% of the peak current. In order to maintain a consistent physical plausibility, a given set of fitting is carried out with the parameters α (for the BV model), λ (for the MH and aMH models), and γ (for the aMH model) kept as a global constant across all four experimental sets. Next, the optimum value of the standard electrochemical rate constant (k_0) was determined for the fitting within each experimental set. The (E_f^{Θ}) value is considered as a floating variable that is allowed to vary from one voltammogram to the other due to actual shift that accompanies the use of the Ag wire pseudo-reference electrode. Coupled with the use of this fitting methodology, the 'best fit' parameters are determined through the minimization of the MSAD value.

8.3 Theory

We consider the one-electron reduction of a solution-phase species Ox at the surface of an electrode:

$$Ox + e^- \rightleftharpoons Red \qquad (8.1)$$

Adopting a transition-state model the electrochemical rate constants of thermally activated electron transfers can be expressed as [27,39,40]:

$$k_{red/ox} = \upsilon_n \kappa_{el} \kappa_n \tag{8.2}$$

where υ_n is the nuclear vibration frequency factor, κ_{el} the electronic transmission coefficient and κ_n the nuclear reorganization factor. The κ_{el} value is related to the electronic coupling between the electroactive species and the energy levels of the electrode, thus defining the adiabaticity character of the electron transfer process. Thus, $\kappa_{el} \rightarrow 1$ for adiabatic processes and $\kappa_{el} << 1$ in the non-adiabatic limit.

The nuclear reorganization factor, κ_n, considering the continuum of electronic levels of the metallic electrode is given by:

$$\kappa_n = \int_{-\infty}^{\infty} \frac{\exp\left[-\Delta G^{\neq}_{red/ox}(x)\right]}{1 + \exp(\mp x)} dx \tag{8.3}$$

with $x = F(\varepsilon - E)/RT$ being an integral variable. Where two signs appear, the upper sign refers to the reductive process; the lower one to the oxidative reaction. The nuclear factor introduces the dependence of the rate constants with the applied potential, *E*, such that the standard rate constant, k_0, corresponds to the value of the reduction and oxidation rate constants at the formal potential: $k_{red}\left(E - E_f^{\ominus}\right) = k_{ox}\left(E - E_f^{\ominus}\right) = k_0$.

To evaluate the activation energy of the electro-reduction and electro-oxidation processes we will make use of the aMH model [7,23,24]. Accordingly, $\Delta G^{\neq}_{red/ox}(x)$ is given by:

$$\Delta G^{\neq}_{red/ox}(x) = \frac{\lambda^*}{4}\left[1 \pm \frac{\eta + x}{\lambda^*}\right]^2 + \gamma\left[\frac{\eta + x}{4\lambda^*}\right]\left[1 - \left(\frac{\eta + x}{\lambda^*}\right)^2\right] + \frac{\gamma^2 \lambda^*}{16} \tag{8.4}$$

where $\lambda^* = F\lambda/RT$ is the dimensionless reorganization energy, $\eta = F(E - E_f^{\ominus})/RT$ the dimensionless overpotential and γ the symmetry parameter. The latter accounts for the differences between the inner-shell force constants of oxidized and reduced species such that the c absolute value increases with the disparity between the force constants. Note that when γ = 0 the above equation reproduces the activation energy predicted by the symmetric version of Marcus theory, the most widely used so far.

Assuming that only the value of the nuclear factor κ_n varies significantly with temperature under the experimental conditions, one can infer that the natural logarithm of the standard rate constant ln(k_0) has a linear dependence with the inverse of temperature (1/T). The slope of which is mainly defined by the reorganization energy, whereas the intercept relates to the degree of adiabaticity of the process. On the other hand, the numerical evaluation of the temperature behaviour of k_0 shows that the symmetry parameter does not have a significant effect on the values of the slope and intercept except for very extreme values where $|\gamma| > 1/3$.

8.4 Results and Discussion

First, cyclic voltammetry was carried out at typical scan rates (0.03, 0.1, 0.3 and 5 V s^{-1}) with a mercury hemispherical electrode as working electrode immersed in a solution containing 1.5 mM 1-nitropentane and 0.1 M TBAP in MeCN from -1.0 to -1.9 V (vs. Ag wire reference electrode) at 26 ºC. Voltammograms obtained are displayed in Figure 8.2.

The voltammograms obtained reveal a single reduction wave with the reversibility of the process in the reverse scan being dependent on the value of the scan

rate. In particular, the reverse scan does not show any oxidative peak at 0.1 V s^{-1}, it displays a modest peak at 0.3 V s^{-1}, and finally the oxidation counterpart is clearly observed at 5 V s^{-1}. This indicates the presence of a follow-up chemistry of the radical anion whose contribution becomes negligible when a scan rate beyond 5 V s^{-1} is applied.

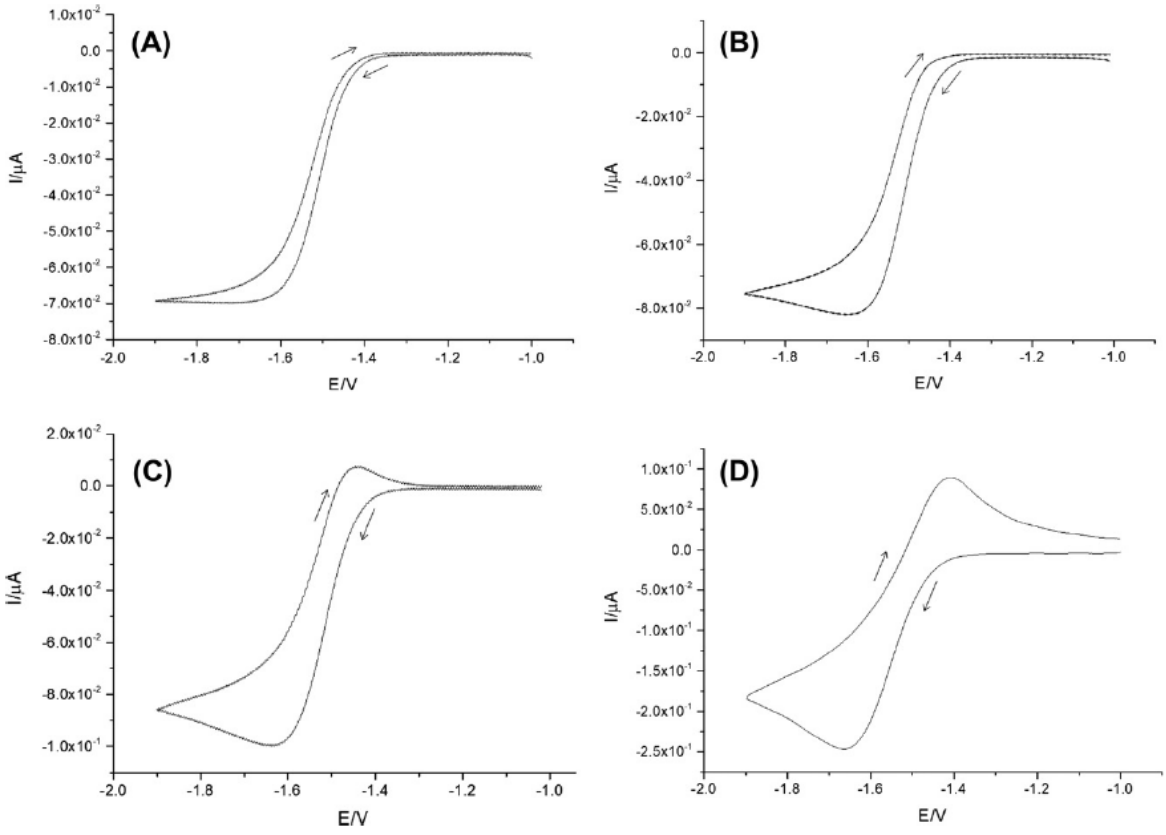


Figure 8.2: *Experimental cyclic voltammograms for the reduction of 1.5 mM 1-nitropentane in acetonitrile at mercury hemisphere electrode. The solution is thermostated at 26 ºC and supported by 0.1 M TBAP. Scan rate (V s^{-1}): (A) 0.03, (B) 0.1, (C) 0.3, and (D) 5.*

The fitting of chronoamperometric response of the system simultaneously for the number of electrons transferred and the diffusion coefficient of 1-nitropentane, $D_{\text{Nitropentane}}$, yields the value of 1 electron transferred and $D_{\text{Nitropentane}} = (2.5 \pm 0.1) \times 10^{-9}$ $m^2\ s^{-1}$.

In order to eliminate the contribution of the follow-up chemistry of the radical anion, fast-scan cyclic voltammetry was used to collect 6 sets of voltammograms, each taken at a different temperature. The specific experimental conditions are described in Section 8.2. All the voltammograms are recorded on a 28.5 μm radius Hg hemispherical electrode from -1.00 to -2.10 V (vs. Ag wire) (representative fast-scan voltammograms are shown in Figure 8.3). All solutions contain 0.1 M TBAP background electrolyte in MeCN solvent.

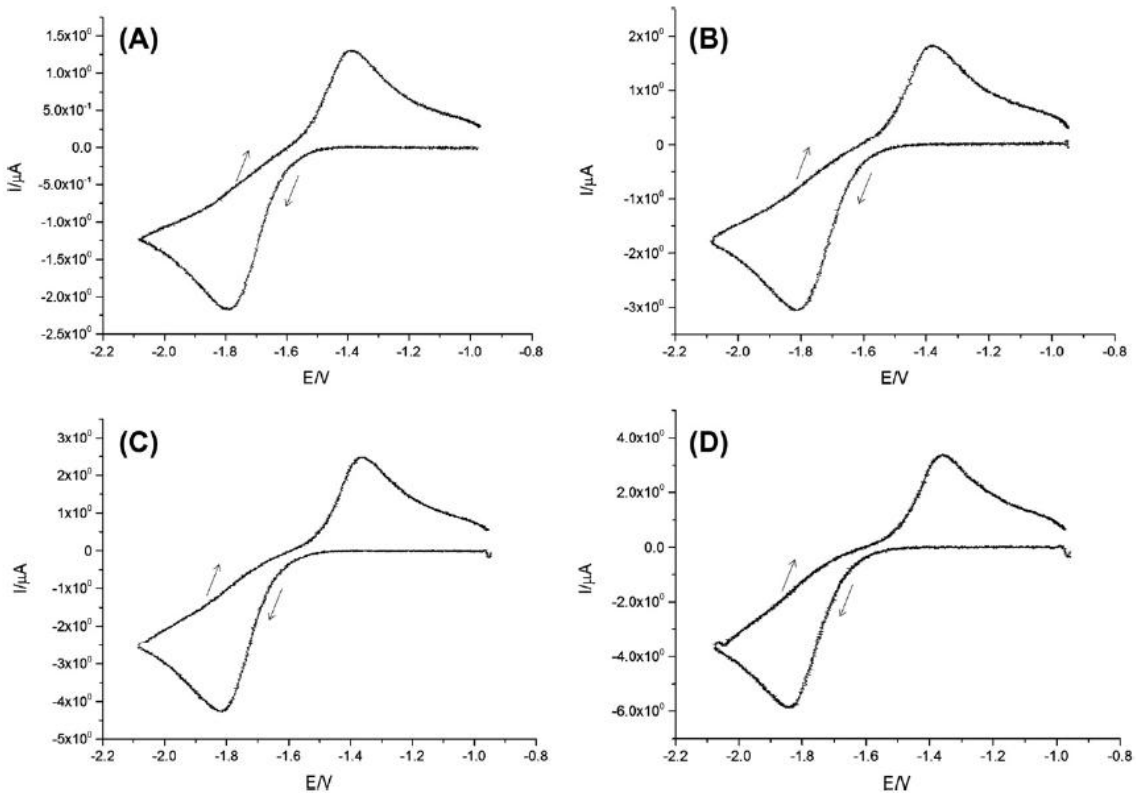


Figure 8.3: *Experimental fast-scan cyclic voltammograms for the electro-reduction of 2.97 mM 1-nitropentane in acetonitrile at 28.5 μm radius mercury hemisphere*

electrode. The solution is thermostated at 32 ºC and is supported by 0.1 M TBAP. Scan rate (V s^{-1}): (A) 180, (B) 380 (C) 762, and (D) 1494.

Determination of the Concentration and Diffusion Coefficient

Under the experimental conditions of each of the 6 fast-scan experiments described in the previous section, potential step chronoamperometry was employed to determine both the concentration and diffusion coefficient of 1-nitropentane simultaneously using a previously reported method [36–38]. This is necessary as heating of the original solution prepared at room temperature up to the desired experimental temperature results in the decrease of concentration due to solvent expansion, and the increase of diffusion rates. The results from the fitting of chronoamperometric responses are presented in Table 8.1.

Table 8.1: *Diffusion coefficients of 1-nitropentane at various temperatures*

	Temperature(ºC)	**Concentration(mM)**	$D_{nitropentane}$**(m^2 s^{-1})**
Fast-scan Experiment 1	26.0	3.13±0.05	(2.53±0.03) × 10^{-9}
Fast-scan Experiment 2	27.5	1.89±0.02	(2.67±0.02) × 10^{-9}
Fast-scan Experiment 3	30.0	3.25±0.06	(2.78±0.03) × 10^{-9}
Fast-scan Experiment 4	32.0	2.97±0.02	(2.90±0.02) × 10^{-9}
Fast-scan Experiment 5	35.0	1.89±0.02	(3.00±0.03) × 10^{-9}
Fast-scan Experiment 6	37.0	3.00±0.06	(3.14±0.05) × 10^{-9}

From the values of the diffusion coefficient obtained at different temperatures the diffusional activation energy, $E_{a,d}$, can be calculated according to the following Arrhenius-like equation:

$$D = D_{\infty} \exp\left(\frac{-E_{a,d}}{RT}\right) \tag{8.5}$$

where D_{∞} is the hypothetical diffusion coefficient at infinite temperature. Note that the ability to obtain of the $E_{a,d}$ value is benefitial since it enables the determination of the diffusion coefficient of a species for any given temperature. Figure 8.4 shows that the experimental points are consistent with Equation 8.5 such that the *D* value decreases linearly with temperature in the range under study. From the bestfit linear regression a value for $E_{a,d}$ of 14 ± 1 kJ mol^{-1} was obtained.

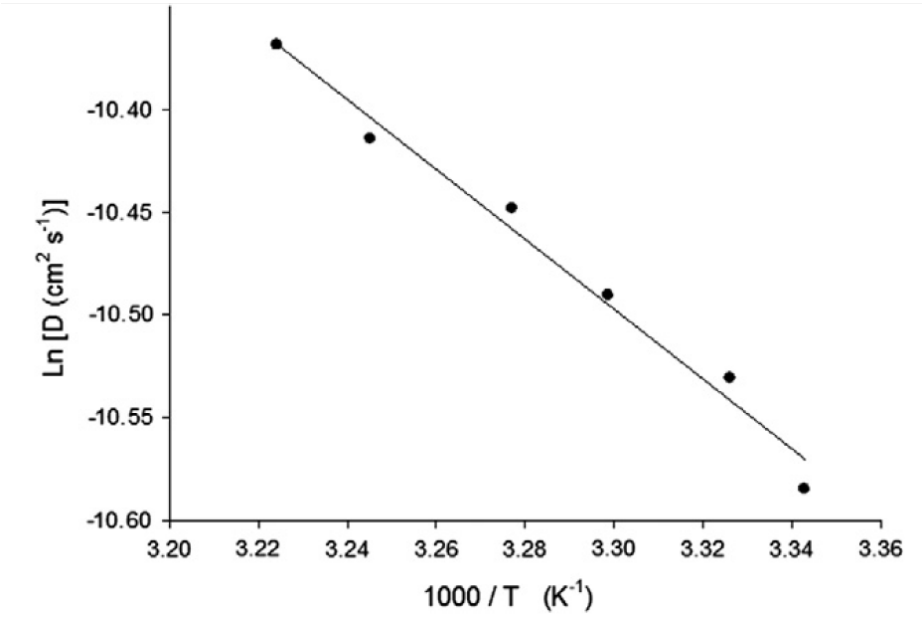


Figure 8.4: *Arrhenius plots of ln D vs. 1000 × T^{-1} for 1-nitropentane in acetonitrile containing 0.1 M TBAP.*

Determination of Kinetic Parameters

The study of the kinetics of the electro-reduction of 1-nitropentane in acetonitrile on a mercury microelectrode was first carried out employing the aMH model. The determination of the kinetic parameters $\{E_f^{\Theta}, k_0, \lambda, \gamma\}$ was performed following an iterative procedure. Thus, given that the voltammograms were remarkably insensitive to changes in λ above 1 eV, a hypothetical value of λ = 1 eV was initially assumed and the results from fastscan experiments 1–6 were fitted by minimization of the MSAD value with γ and k_0 as fitting parameters. The symmetry of the oxidative and reductive peak is mainly dependent on the γ value whereas the peak-to-peak separation of the voltammograms is established almost exclusively by the rate constant. Once the k_0 value for each temperature was known, a value of the reorganization energy of 1.7 ± 0.1 eV was extracted from the slope of the bestfit linear regression of ln(k_0) vs. 1/T (see Figure 8.5). Accordingly, the fitting procedure was repeated with λ = 1.7 eV confirming that it is consistent with the experimental results and can be accepted as the ‘‘true’’ value of the reorganization energy. The ‘‘best-fit’’ kinetic parameters are shown in Table 8.2 and some of the fittings are displayed in Figure 8.6.

As can be observed in Figure 8.6, the values of the kinetic parameters obtained give rise to a very satisfactory agreement of the theoretical and experimental results (MSAD < 5%) in a wide range of scan rates (between 180 and 1844 V s^{-1}) and at the different temperatures considered. Whereas the value of the standard rate constant increases with temperature, the temperature-independent values for the reorganization energy (1.7 eV) and the symmetry parameter (-0.14) are physically consistent.

Table 8.2: *Kinetic parameters obtained with the aMH model.*

	Fast-scan Experiment 1 (26ºC)	**Fast-scan Experiment 2 (27.5ºC)**	**Fast-scan Experiment 3 (30ºC)**
k_0 **(cm s^{-1})**	0.013	0.0135	0.017
λ (eV)	1.7	1.7	1.7
γ	-0.14	-0.14	-0.14
E_f^{θ} **(V)**	-1.61 ± 0.03	-1.41 ± 0.02	-1.57 ± 0.01
%MSAD	5 ± 1	4 ± 1	4 ± 1
	Fast-scan Experiment 4 (32ºC)	**Fast-scan Experiment 5 (35ºC)**	**Fast-scan Experiment 6 (37ºC)**
k_0 **(cm s^{-1})**	0.019	0.021	0.025
λ (eV)	1.7	1.7	1.7
γ	-0.14	-0.14	-0.14
E_f^{θ} **(V)**	-1.580 ± 0.002	-1.475 ± 0.007	-1.58 ± 0.01
%MSAD	2.9 ± 0.8	5 ± 1	3 ± 1

According to the physical meaning of the parameter γ, the negative value -0.14 obtained indicates that the force constants of the reduced species are (in average) greater than those of the oxidized species. We have also reported this behaviour for the electro-reductions of 2-methyl-2-nitropropane and cyclooctatetraene in Chapter 7 where neutral species are reduced into radical anions. The likely stronger interactions of the anion with the solvent as compared with the neutral parent molecule can justify the negative γ values obtained for all these redox systems.

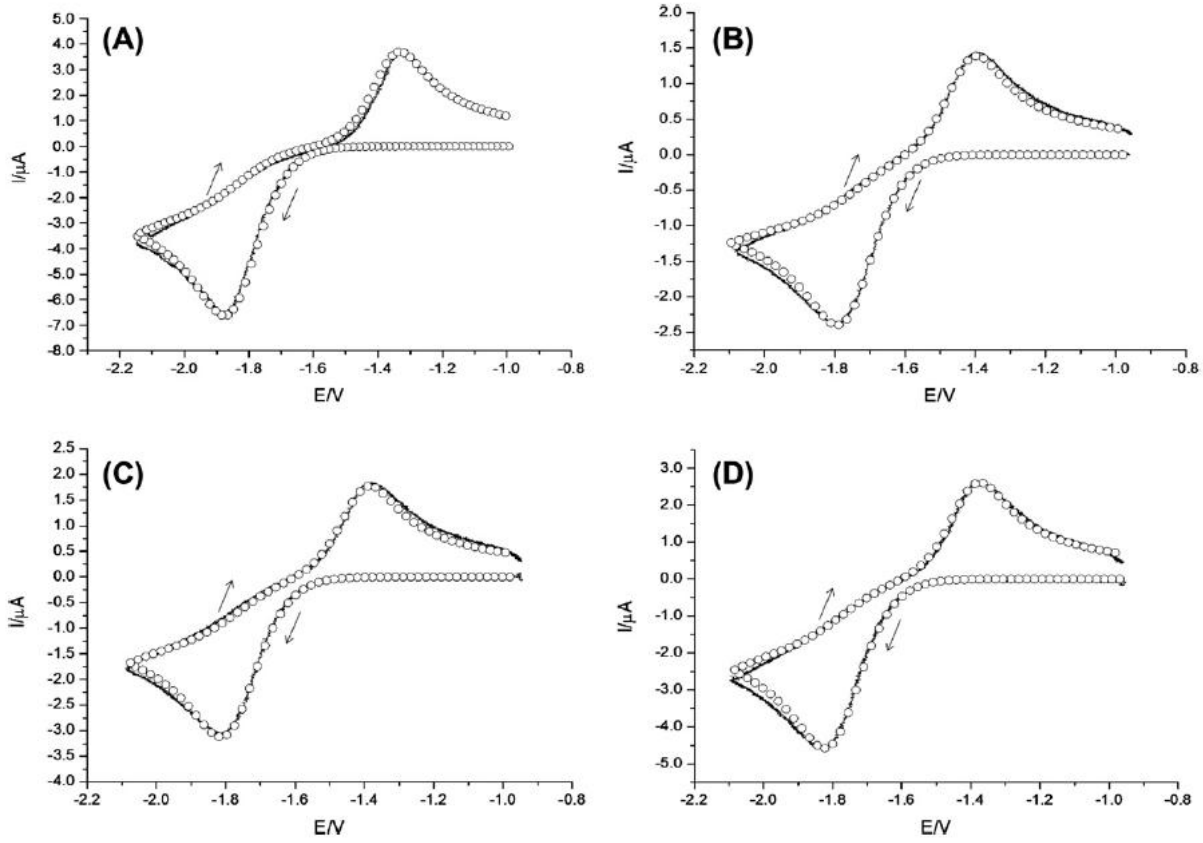


Figure 8.6: *Experimental (solid line) and simulated (open circles) cyclic voltammograms for the reduction of 1-nitropentane in acetonitrile at 28.5 μm radius mercury hemisphere electrode: (A) 3.13 mM 1-nitropentane at 26 ºC (scan rate = 1844 V s^{-1}); (B) 3.25 mM 1-nitropentane at 30 ºC (scan rate = 180 V s^{-1}); (C) 2.97 mM 1-nitropentane at 32 ºC (scan rate = 380 V s^{-1}); and (D) 3.00 mM 1-nitropentane at 37 ºC (scan rate = 760 V s^{-1}). All solutions are supported with 0.1 M TBAP.*

Degree of Adiabaticity

Variable temperature experiments also enable us to estimate the degree of adiabaticity of the electron transfer process. This is of fundamental interest since it informs about the magnitude of the electronic interaction between the reactant species

and the electrode, which is a major question for the understanding of electrode reactions [41–44].

As can be deduced from Equation 8.2, the degree of adiabaticity of the process is accessible from the value of the pre-exponential constant that increases with the electronic coupling between the electroactive species and the electrode. In order to gain information about the magnitude of this coupling we will make use of the approximate expression for the electronic transmission coefficient reported by Feldberg and Sutin for heterogeneous electron transfers [39]:

$$\kappa_{el} \approx \frac{1}{\beta} \ln\left(1 + \frac{4\pi^2 \rho_M H_{0,AB}^2}{\upsilon_n h \sqrt{4\pi\lambda^*}}\right) \tag{8.6}$$

where β is the tunnelling factor, ρ_M the density of electronic levels in the electrode, $H_{0,AB}$ electronic coupling element at the plane of closest approach and *h* the Planck's constant. From Equations 8.3 and 8.4, we obtain that for our system (λ and γ values given in Table 8.2) the nuclear reorganization factor at the formal potential can be approximated as:

$$\kappa_n(E = E_f^{\ominus}) \approx 2.9 \times \exp\left(-\frac{\lambda F}{4RT}\left(1 + \frac{\gamma^2}{4}\right)\right) \tag{8.7}$$

Note that the lowering of the energy barrier as a consequence of the electronic coupling is not considered in the present study.

Considering reasonable values for the tunnelling factor $\beta = 10^8$ cm^{-1} [39], the density of states of s-band metals $\rho_M \approx 0.3$ eV^{-1} [45] and the nuclear vibration frequency factor of the system $\upsilon_n = 10^{13}$ s^{-1} [46,47], we have calculated the variation of the intercept (Z) of the plot ln(k_0) vs. 1/T with the coupling constant ($H_{0,AB}$) from Equations 8.2, 8.6 and 8.7 (see Figure 8.7). The linear domain at small $H_{0,AB}$ values corresponds to a non-adiabatic behaviour (weak electronic coupling) whereas the adiabatic region (strong electronic coupling) corresponds to the plateau observed at large $H_{0,AB}$values.

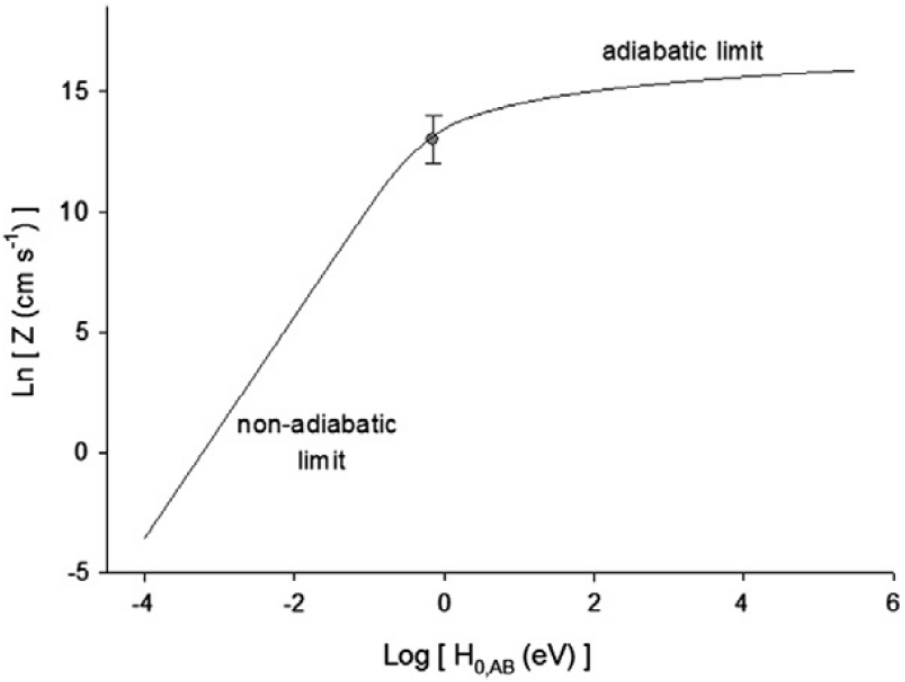


Figure 8.7: *Variation of the intercept (Z) of the plot ln(k_0) vs. 1/T with the electronic coupling element ($H_{0,AB}$). The grey dot corresponds to the Z value obtained in this work for the electro-reduction of 1-nitropropane in acetonitrile/TBAP solution on a mercury microhemisphere.*

From the best-fit linear regression shown in Figure 5, a value for the intercept of $\ln[Z(\text{cm s}^{-1})] = 13 \pm 1$ is obtained. As can be seen in Figure 8.7, this value lies in the transition region between the nonadiabatic and the adiabatic domains. This suggests a moderate adiabatic character for the electron transfer process considered here and it can ask for the use of quantum–mechanical models [48–50] that take into account the effect of the resonance energy on the activation energy.

Comparison Between BV, MH, and aMH Models

As shown in Chapters 4-7, the weaknesses of the symmetric MH model in the description of several electrode processes have been pointed out via cyclic and square wave voltammetry at constant temperature. Here, the consistency of the different kinetic models will be further examined from the experimental results obtained in fast-scan cyclic voltammetry at different temperatures.

The BV, MH and aMH kinetic approaches were used to systematically simulate cyclic voltammograms of the experimental set obtained through fast-scan experiments 1–6. The ‘‘true’’ value of λ determined in the previous section was used in conjunction with the MH aMH models. A common set of parameters that provided the ‘‘best fit’’ between the simulated and experimental voltammograms is then determined for each model. These ‘‘best fit’’ parameters are presented in Tables 8.2–8.4. A comparison between the BV and MH fits is given in Figure 8.8, and between that of the MH and aMH in Figure 8.9.

The optimized simulated voltammograms obtained with the BV model give excellent quality of fit across all experimental sets. At 26 ºC, the value of $k_0 = 0.011$ cm s^{-1} is extracted for the current compound. In comparison with an electrochemical system whose heterogeneous reaction is predominantly limited by the change in

geometry required in the formation of the product species (e.g. k_0 = 0.014 cm s^{-1} for cyclooctatetraene in DMSO at 25 ºC (see Chapter 5)), the value of k_0 extracted for the current compound is within a similar order. This relatively slow standard heterogeneous reaction rate is consistent with the findings of Peover and Powell [51] which concluded that the concentration of negative charge on the nitro group of aliphatic nitro compounds is responsible for a high value of outer-sphere reorganization energy.

Table 8.3: *Kinetic parameters obtained with the BV model.*

	Fast-scan Experiment 1 (26ºC)	**Fast-scan Experiment 2 (27.5ºC)**	**Fast-scan Experiment 3 (30ºC)**
k_0 (cm s^{-1})	0.011	0.012	0.015
α	0.42	0.42	0.42
E_f^{θ} (V)	-1.59 ± 0.03	-1.41 ± 0.02	-1.567 ± 0.003
%MSAD	5 ± 1	4.3 ± 0.5	4 ± 1
	Fast-scan Experiment 4 (32ºC)	**Fast-scan Experiment 5 (35ºC)**	**Fast-scan Experiment 6 (37ºC)**
k_0 (cm s^{-1})	0.017	0.022	0.022
λ (eV)	0.42	0.42	0.42
E_f^{θ} (V)	-1.566 ± 0.005	-1.47 ± 0.01	-1.571 ± 0.006
%MSAD	3.9 ± 0.1	7 ± 1	4.4 ± 0.5

Table 8.4: *Kinetic parameters obtained with the MH model.*

	Fast-scan Experiment 1 (26ºC)	**Fast-scan Experiment 2 (27.5ºC)**	**Fast-scan Experiment 3 (30ºC)**
k_0 **(cm s^{-1})**	0.0135	0.0135	0.017
λ (eV)	1.7	1.7	1.7
E_f^o **(V)**	-1.63 ± 0.03	-1.42 ± 0.02	-1.59 ± 0.01
%MSAD	8 ± 1	5.2 ± 0.7	6 ± 1
	Fast-scan Experiment 4 (32ºC)	**Fast-scan Experiment 5 (35ºC)**	**Fast-scan Experiment 6 (37ºC)**
k_0 **(cm s^{-1})**	0.019	0.021	0.025
λ (eV)	1.7	1.7	1.7
E_f^o **(V)**	-1.589 ± 0.006	-1.490 ± 0.007	-1.59 ± 0.01
%MSAD	4.9 ± 0.6	6 ± 1	6 ± 1

With the value of λ obtained in the previous section (λ = 1.7 eV), the optimum k_0 extracted from the fitting with the MH model (see Table 8.4) gives rise to an average MSAD value of 6% which is poorer than with the BV model. The aMH simulations were carried out with fixed values of λ = 1.7 eV and γ = -0.14 with excellent quality of fit (average MSAD = 4%) comparable to that obtained with the BV formalism. The optimum k_0 value is identical to that of the MH fitting as the peak-topeak separation between the forward and reverse scan is almost exclusively fixed by k_0 whereas the effect exerted by the parameter γ is negligible under these conditions.

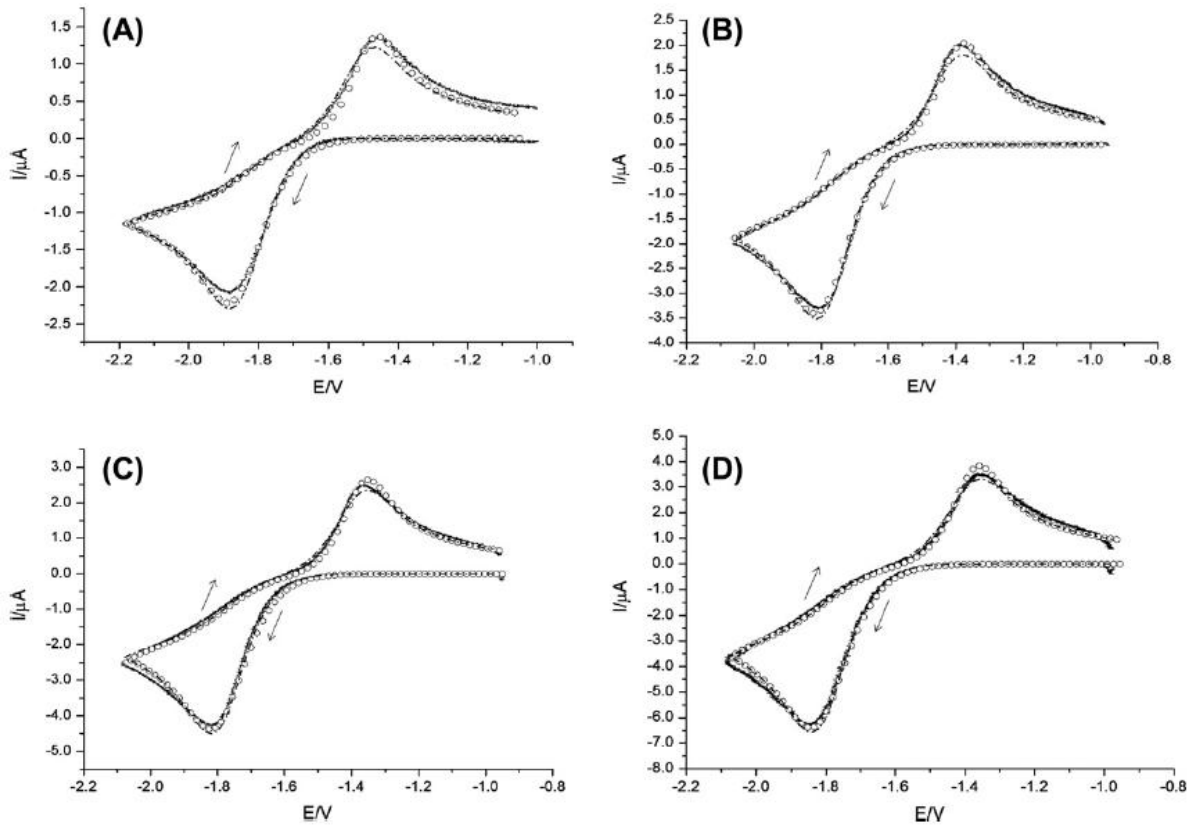


Figure 8.8: *Experimental (solid line) and simulated cyclic voltammograms with Butler-Volmer (open circles) and Marcus-Hush-Chidsey (dashed line) models for the reduction of 1-nitropentane in acetonitrile at 28.5 μm radius mercury hemisphere electrode: (A) 3.13 mM 1-nitropentane at 26 ºC (scan rate = 187 V s^{-1}); (B) 3.25 mM 1-nitropentane at 30 ºC (scan rate = 377 V s^{-1}); (C) 2.97 mM 1-nitropentane at 32 ºC (scan rate = 762 V s^{-1}); and (D) 3.00 mM 1-nitropentane at 37 ºC (scan rate = 1491 V s^{-1}). All solutions are supported with 0.1 M TBAP.*

According to the above results, the quality of the fittings with the BV and aMH models are comparable but superior to that obtained with the symmetric version of the MH model. This highlights the inability of the symmetric MH approach to describe properly the voltammetry of different solution-phase redox couples.

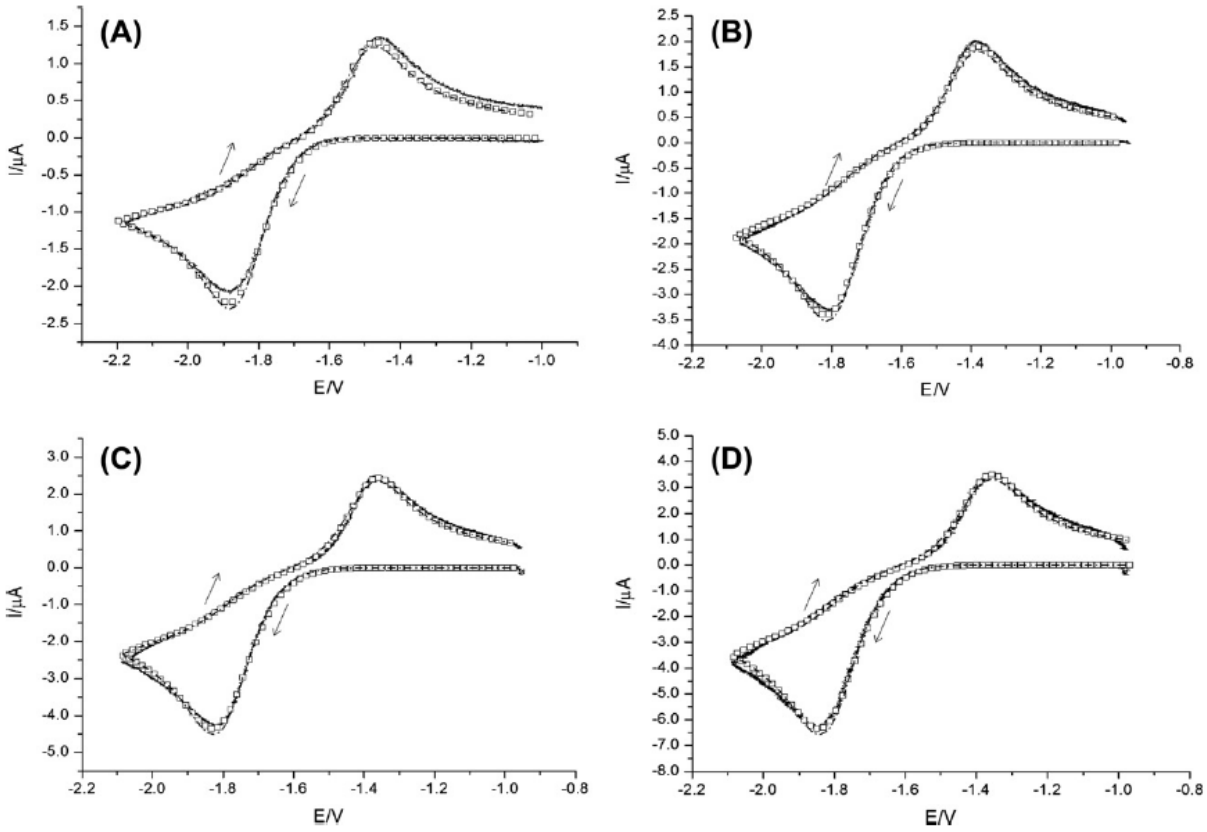


Figure 8.9: *Experimental (solid line) and simulated cyclic voltammograms with asymmetric Marcus-Hush-Chidsey (open squares) and symmetric Marcus-Hush-Chidsey (dashed line) models for the reduction of 1-nitropentane in acetonitrile at 28.5 μm radius mercury hemisphere electrode: (A) 3.13 mM 1-nitropentane at 26 ºC (scan rate = 187 V s^{-1}); (B) 3.25 mM 1-nitropentane at 30 ºC (scan rate = 377 V s^{-1}); (C) 2.97 mM 1-nitropentane at 32 ºC (scan rate = 762 V s^{-1}); and (D) 3.00 mM 1-nitropentane at 37 ºC (scan rate = 1491 V s^{-1}). All solutions are supported with 0.1 M TBAP.*

8.5 Conclusions

The asymmetric Marcus-Hush-Chidsey (aMH) model has been employed in variable temperature voltammetry in order to extend the physical insights into electron transfer processes available via electrochemical measurements. With this aim, the electro-reduction of 1-nitropentane in acetonitrile has been investigated through fast-scan cyclic voltammetry and using mercury microhemispheres as working electrodes.

From the fitting of the voltammograms at different temperatures with the aMH model, the values of the reorganization energy (λ = 1.7 eV) and the symmetry parameter (γ = -0.14) have been extracted. The negative γ value indicates greater force constants for the radical anion electrogenerated than for the initial neutral species. The above λ and γ values lead to very satisfactory agreement of simulated and experimental results in all the range of temperatures and scan rates considered. The variation of the standard rate constant with the temperature also informs that the system has an intermediate behaviour between the adiabatic and non-adiabatic limits.

The comparison of the different kinetic models has been carried out obtaining comparable fit qualities for the Butler-Volmer (with α = 0.42) and aMH models, whereas the symmetric MH approach gives rise to worse description of the voltammograms.

8.6 References

1. A.J. Bard, L. Faulkner, *Electrochemical Methods: Fundamentals and Applications, second ed.*, Wiley & Sons, New York, 2001.
2. R.G. Compton, C.E. Banks, *Understanding Voltammetry, second ed.*, Imperial College Press, London, 2011.
3. R.A. Marcus, N. Sutin, *Biophys. Chim. Acta* **265** (1985) 811.

4. S. Fletcher, *J. Solid State Electrochem*. **14** (2010) 705.
5. A.M. Kuznetsov, J. Ulstrup, *Electron Transfer in Chemistry and Biology: An Introduction to the Theory*, Wiley and Sons, Chichester, 1999.
6. R.A. Marcus, *J. Chem. Phys.* **24** (1956) 966.
7. R.A. Marcus, *J. Chem. Phys.* **43** (1965) 679.
8. C.E.D. Chidsey, *Science* **215** (1991) 919.
9. S.W. Feldberg, *Anal. Chem.* **82** (2010) 5176.
10. J.T. Hupp, M.J. Weaver, *J. Phys. Chem.* **88** (1984) 6128.
11. R.M. Haddox, H.O. Finklea, *J. Phys. Chem. B* **108** (2004) 1694.
12. N. Madhiri, H.O. Finklea, *Langmuir* **22** (2006) 10643.
13. G.A. Orlowski, H.-B. Kraatz, *Electrochim. Acta* **51** (2006) 2934.
14. G.A. Orlowski, S. Chowdhury, H.-B. Kraatz, *Langmuir* **23** (2007) 12765.
15. A.L. Eckermann, J.A. Shaw, T.J. Meade, *Langmuir* **26** (2010) 2904.
16. D. Suwatchara, M.C. Henstridge, N.V. Rees, R.G. Compton, *J. Phys. Chem. C* **115** (2011) 14876.
17. M.C. Henstridge, Y. Wang, J.G. Limon-Petersen, E. Laborda, R.G. Compton, *Chem. Phys. Lett.* **517** (2011) 29.
18. E. Laborda, Y. Wang, M. Henstridge, F. Martinez-Ortiz, A. Molina, R.G. Compton, *Chem. Phys. Lett.* **512** (2011) 133.
19. D. Suwatchara, N.V. Rees, M.C. Henstridge, E. Laborda, R.G. Compton, *J. Electroanal. Chem.* **665** (2012) 38.
20. M.C. Henstridge, E. Laborda, E.J.F. Dickinson, R.G. Compton, *J. Electroanal. Chem.* **664** (2012) 73.
21. Y. Wang, E. Laborda, M. Henstridge, F. Martinez-Ortiz, A. Molina, R.G. Compton, *J. Electroanal. Chem.* **668** (2012) 7.

22. M.C. Henstridge, E. Laborda, N.V. Rees, R.G. Compton, *Electrochim. Acta* (2012). doi: j.electacta.2011.10.026.
23. E. Laborda, M.C. Henstridge, R.G. Compton, *J. Electroanal. Chem.* **667** (2012) 48.
24. M.C. Henstridge, E. Laborda, Y. Wang, D. Suwatchara, N. Rees, A. Molina, F. Martinez-Ortiz, R.G. Compton, *J. Electroanal. Chem.* **672** (2012) 45.
25. D. Suwatchara, M.C. Henstridge, N.V. Rees, E. Laborda, R.G. Compton, *J. Electroanal. Chem.* **677** (2012) 120.
26. C. Costentin, C. Louault, M. Robert, V. Rogé, J.M. Savéant, *Phys. Chem. Chem. Phys.* **14** (2012) 1581.
27. J.T. Hupp, M.J. Weaver, *J. Electroanal. Chem.* **152** (1983) 1.
28. C. Amatore, C. Lefrou, F.J. Pflüger, *J. Electroanal. Chem.* **270** (1989) 43.
29. C. Amatore, E. Maisonhaute, G. Simonneau, *J. Electroanal. Chem.* **486** (2000) 141.
30. D. Shoup, A. Szabo, *J. Electroanal. Chem.* **237** (1982) 140.
31. K.N. Marsh, A. Deev, A.C.-T. Wu, E. Tran, A. Klamt, Korean *J. Chem. Eng.* **19** (2002) 357.
32. J. Mauzeroll, E.A. Hueske, A.J. Bard, *Anal. Chem.* **75** (2003) 3880.
33. T.J. Davies, B.A. Brookes, A.C. Fisher, K. Yunus, S.J. Wilkins, P.R. Greene, J.D. Wadhawan, R.G. Compton, *J. Phys. Chem.* **107B** (2003) 6431.
34. A. Molina, E. Laborda, E.I. Rogers, F. Martinez-Ortiz, C. Serna, J.G. Limon-Petersen, N.V. Rees, R.G. Compton, *J. Electroanal. Chem.* **634** (2009) 73.
35. C. Amatore, E. Maisonhaute, G. Simonneau, *Electrochem. Commun.* **2** (2000) 81.

36. Y. Wang, J.G. Limon-Petersen, R.G. Compton, *J. Electroanal. Chem.* **652** (2011) 13.

37. O.V. Klymenko, R.G. Evans, C. Hardacre, I.B. Svir, R.G. Compton, *J. Electroanal. Chem* **571** (2004) 211.

38. C.A. Paddon, D.S. Silvester, F.L. Bhatti, T.J. Donohoe, R.G. Compton, *Electroanalysis* **19** (2007) 11.

39. S.W. Feldberg, N. Sutin, *Chem. Phys.* **324** (2006) 216.

40. J.M. Savéant, *J. Phys. Chem. B* **106** (2002) 9387.

41. W. Schmickler, *J. Electroanal. Chem.* **204** (1986) 31.

42. T. Iwasita, W. Schmickler, J.W. Schultze, *Ber. Bensunges. Phys. Chem.* **89** (1985) 138.

43. S. Gosavi, R.A. Marcus, *J. Phys. Chem. B* **104** (2000) 2067.

44. A.M. Kuznetsov, J. Ulstrup, *Electrochim. Acta* **45** (2000) 2339.

45. R.L. Birke, Q. Huang, T. Spataru, D.K. Gosser, *J. Am. Chem. Soc.* **128** (2006) 1922.

46. W.R. Fawcett, M. Opallo, *Angew. Chem. Int. Ed. Engl.* **33** (1994) 2131.

47. J.T. Hupp, M.J. Weaver, *J. Electroanal. Chem.* **145** (1983) 43.

48. W. Schmickler, *J. Electroanal. Chem.* **204** (1986) 31.

49. A.A. Kokkanen, A.M. Kuznetsov, I.G. Medvedev, *Russ. J. Electrochem.* **44** (2008) 397.

50. A.K. Mishra, D.H. Waldeck, *J. Phys. Chem. C* **115** (2011) 20662.

51. M.E. Peover, J.S. Powell, *J. Electroanal. Chem.* **20** (1969) 427.

Chapter 9

Variable Temperature Study of the Electro-reduction of 3-Nitrophenolate via Cyclic and Square Wave Voltammetry. Molecular Insights into Electron Transfer Processes Based on the Asymmetric Marcus-Hush Model

The work presented in this chapter has been published in

Electrochim. Acta DOI: j.electacta.2012.12.129

In this chapter, variable temperature experiments have been used in conjunction with numerical fitting of cyclic and square wave voltammogram responses via the asymmetric version of Marcus theory to provide molecular insight into the electro-reduction of the 3-nitrophenolate anion in DMSO studied at mercury hemispherical microelectrodes of 23 μm radius. As a result, the reorganization energy, differences between the inner-sphere force constants of the electroactive species, and the degree of adiabaticity of the reaction have been evaluated.

Furthermore, a comparison between the quality of fitting obtained through the Butler-Volmer and asymmetric Marcus-Hush models is also presented to evaluate the relative ability of the kinetic models in predicting voltammetric responses in a range of temperatures and scan rates.

Programs used for the simulations were written by Dr. E. Laborda.

9.1 Introduction

The study of molecular characteristics of electrochemical reactions through electrochemical measurements can be carried out using microscopic models of electron transfer processes [1-5]. The most widely used is the Marcus theory [6,7] that relates the rate of electron transfer to the reorganization energy, λ, which parameterizes the energy required to modify the reagent's inner (bond lengths and angles) and outer (orientation of solvent molecules surrounding the reactive species) configurations. However, weaknesses of the symmetric version of the Marcus theory (referred here as the Marcus-Hush-Chidsey model for electrode processes, MH) [6-9] have been reported in this thesis (Chapters 4-6) and in the literature for the quantitative description of the voltammetry of both diffusional and surface-bound electrode processes [10-26]. A possible explanation for this lies in the validity of the assumption of the inner-sphere and outer-sphere "force constants" of the reduced and oxidized species being equal, which does not necessarily hold true given the structural and charge changes that can take place upon the electron transfer.

In response to this, the asymmetric form of the Marcus theory (referred as asymmetric Marcus-Hush-Chidsey model, aMH) has been applied recently to the study of electrode reactions [23-26] (see Chapters 6-8). This version of the MH model introduces the symmetry parameter, γ, which is associated with the differences between the vibrational modes of the electroactive species.

In this chapter the aMH model is used in variable temperature kinetic studies via cyclic and square wave voltammetry to determine the λ value as well as the degree of adiabaticity of the electro-reduction of the 3-nitrophenolate anion in DMSO on a hemispherical mercury microelectrode (radius = 23 μm). Cyclic voltammetry was

carried out with scan rates between 0.05-2 Vs^{-1} and square wave voltammetry with frequencies ranging between 25 and 200 Hz. Voltammetric measurements were taken within the temperature range of 24-47.5°C and fitted with Butler-Volmer (BV) and aMH kinetic models. The kinetic parameters and the quality of the fittings obtained from the different models are quantified and compared at different temperatures. The results obtained offer an extension to the insight of how the reorganization energy and the standard rate constant are affected as the reagent transits from nitro-aliphatic compounds to nitro-aromatics.

9.2 Experimental

Chemical Reagents

3-Nitrophenol ($Ph(OH)NO_2$, Aldrich, 99%), tetra–n-butylammonium perchlorate (TBAP, Fluka, Puriss grade), tetra–n-butylammonium hydroxide ($TBAOH{\cdot}30H_2O$, Aldrich, >98%), mercury(I) nitrate dihydrate ($Hg_2(NO_3)_2{\cdot}2H_2O$, Aldrich, >97%), nitric acid (HNO_3, Fisher scientific, 70%), ferrocene ($Fe(C_5H_5)_2$, Aldrich, 98%), cobalt(III) sepulchrate trichloride ($[CoSep]Cl_3$, Aldrich, 95%), potassium nitrate (KNO_3, Aldrich, >99%), dimethylsulfoxide (DMSO, Alfa Aesar, >99%), acetonitrile (MeCN, Fisher Scientific, HPLC grade), were all used as received without further purification.

The 3-nitrophenolate anion solutions were prepared by adding an excess of base ($TBAOH{\cdot}30H_2O$) to the corresponding 3-nitrophenol solutions in the molar ratio of 1.2:1 [27].

Instrumentation

Cyclic voltammetry with a scan rate range between 50 mVs^{-1} and 2 Vs^{-1} and potential step chronoamperometry were performed with a computer-controlled Autolab PGSTAT12 (Metrohm-Autolab BV, Utrecht, Netherlands). Microdisk working

electrodes of 23 µm radius was fabricated in-house by sealing Pt wire (Goodfellow Cambridge Ltd., UK) into soda glass capillary according to the published method [28]. The platinum disk was polished prior to hemisphere deposition using 1.0, 0.3 and 0.05 µm alumina-water slurry on soft lapping pads (Buehler, Illinois). The disk size was calibrated by numerical fitting of the chronoamperometric response of the 1.0 mM ferrocene solution in acetonitrile supported by 0.1 M TBAP using the Shoup and Szabo expression [1,2,29] (see Equation 5.3 in Chapter 5). A widely adopted literature diffusion coefficient for ferrocene of $D = 2.3 \times 10^{-9}$ m^2 s^{-1} at 25 ºC [30] was employed for the calculations.

A mercury hemisphere was then electrochemically deposited onto the microdisk from a 50 mM $Hg_2(NO_3)_2$ solution containing 0.1 M KNO_3 and acidified to 0.5% with HNO_3 following the method laid out by Bard *et al.* [31]. For deposition, the potential was stepped to -0.25 V *vs* Ag wire. The size of the hemispherical drop was controlled by the amount of charge passed.

A platinum mesh counter electrode was employed for all electrochemical measurements while a silver wire was used as the reference electrode. Stringent thermal control of the electrochemical cell was achieved through the use of an air heater-controller system fabricated in-house. With this system, temperature control was achieved within the precision of ± 0.1 °C.

Characterization of the Hemispherical Mercury Electrode

The size and shape of the mercury electrode was characterized by optical and electrochemical methods.

Visual measurement of the hemisphere was obtained through the use of JVC digital video camera TK-C921EG. To allow the appraisal of size and shape of the hemisphere in the environment of the reagent solution, the working electrode was

submerged in the solution sealed within a UV/vis cuvette, and visual image taken. It was found that the mercury droplet formed a hemisphere which adopted the radius of the microdisk. An image of the 23 μm hemisphere is shown in Figure 9.1.



Figure 9.1: *Image of the 23 μm radius electrodeposited hemisphere immersed in DMSO.*

The electrochemical characterization of the mercury hemispheres was carried out through analysis of the limiting current chronoamperogram of an aqueous solution containing 2 mM $[CoSep]Cl_3$ and 0.1 M KNO_3 using Equation 5.4 given in Chapter 5.

The value of the diffusion coefficient of $[CoSep]Cl_3$ employed for the calculations was $D=6.3\times10^{-10}m^2s^{-1}$. This was determined from chronoamperograms recorded at microdisk electrode of known dimensions and it is in close agreement with literature [32, 33].

The radius obtained through the analysis of the chronoamperogram was found to be 28.5 µm. This coincides with that determined with the optical measurements outlined previously.

Cyclic voltammetry, square wave voltammetry and potential step chronoamperometry measurements

Cyclic voltammograms within the scan rate range of 50 mVs^{-1} to 2 Vs^{-1} were recorded between -0.35 and -0.90 V (*vs* Ag wire) on 23 µm radius mercury hemispherical electrode. Four sets of voltammograms, each recorded at a different temperature (24, 30.8, 39 and 47.5 °C), were obtained. All the solutions contained 0.1 M TBAP background electrolyte in DMSO solvent.

Square wave voltammograms were recorded between -0.48 and -0.95 V (vs. Ag wire) with a potential step and amplitude of 15 mV. Frequencies used cover the range between 25 and 200 Hz.

Double potential step chronoamperometry was recorded for each experimental set conducted in the current study. The potential was stepped from -0.45 V where there is no faradaic current to -0.85 V (*vs* Ag wire) where the reduction current is fully controlled by diffusion and was held for 0.5 s and then abruptly stepped back to -0.45V for further 0.5 s.. The resulting chronoamperometric response was simultaneously fitted for both the diffusion coefficients and concentration of the electroactive species using the previously reported method [34-36].

Fitting Methodology

Simulation programs developed in-house by Dr. E. Laborda were used to simulate cyclic and square wave voltammograms on a hemispherical electrode based on the BV and aMH formalisms. These were used, in conjunction with the value of diffusion coefficients determined through numerical fitting of chronoamperometric responses, to model cyclic voltammograms over the full range of experimental conditions. Fitting of the electrochemical reduction processes was carried out by matching the peak potentials, thereby fixing the formal potential ($E_f^{\ominus}$, which over the course of our experiment is found to shift within ±50 mV range due to the use of Ag wire pseudo reference electrode), the standard electrochemical rate constant (k_0) and the transfer coefficient (α) (for BV formalism), or the asymmetric parameter (γ) and reorganization energy (λ) (for aMH formalism).

The quality of the fitting was evaluated from the value of the mean scaled absolute deviation (MSAD). The mathematical expression for %MSAD is given in Equation 4.15 in Chapter 4. Large contributions to the MSAD as a consequence of very small signal values were avoided by considering only the points where i_{exp} is at least 10% of the peak current. In order to maintain a consistent physical plausibility, a given set of fitting is carried out with the parameters α (for the BV model), and λ and γ (for the aMH model) kept as a global constant across all four experimental sets. Next, the optimum value of the standard electrochemical rate constant (k_0) was determined for the fitting within each experimental set. The $E_f^{\ominus}$ value is considered as a floating variable that is allowed to vary from one voltammogram to the other due to actual shift that accompanies the use of the Ag wire pseudo-reference electrode. Over the course of our experiment is found to shift within ±50 mV range. Coupled with the use of this

fitting methodology, the 'best fit' parameters are determined through the minimization of the MSAD value.

9.3 Results and Discussion

Determination of Concentration and Diffusion Coefficient

For each temperature at which voltammetric data sets were obtained, double potential step chronoamperometry was also employed to determine both the concentration and diffusion coefficients of the electroactive species simultaneously using a previously reported method [34-36]. The results are presented in Table 9.1.

Table 9.1: *Diffusion coefficients of 3-Nitrophenolate $^{-/\bullet 2-}$ at different temperatures*

Temperature (°C)	**Concentration (mM)**	$D_{\text{Nitrophenolate}^-}$ **(m^2/s)**	$D_{\text{Nitrophenolate}^{\bullet 2-}}$ **(m^2/s)**
24	0.9	4.58×10^{-10}	4.00×10^{-10}
30.8	0.85	5.52×10^{-10}	4.82×10^{-10}
39	0.84	6.80×10^{-10}	6.00×10^{-10}
47.5	0.84	8.1×10^{-10}	7.1×10^{-10}

From the results obtained, the diffusional activation energy, $-E_{a,d}$, can be calculated from the following Arrhenius-like equation:

$$D = D_{\infty} \exp\left(\frac{-E_{a,d}}{RT}\right) \tag{9.1}$$

where D_{∞} is the hypothetical diffusion coefficient at infinite temperature. From the best-fit linear regression (see Figure 9.2) values for $-E_{a,d}$ of 19 ± 1 and 20 ± 1 kJ mol^{-1} were obtained for the nitrophenolate anion and nitrophenolate dianion, respectively.

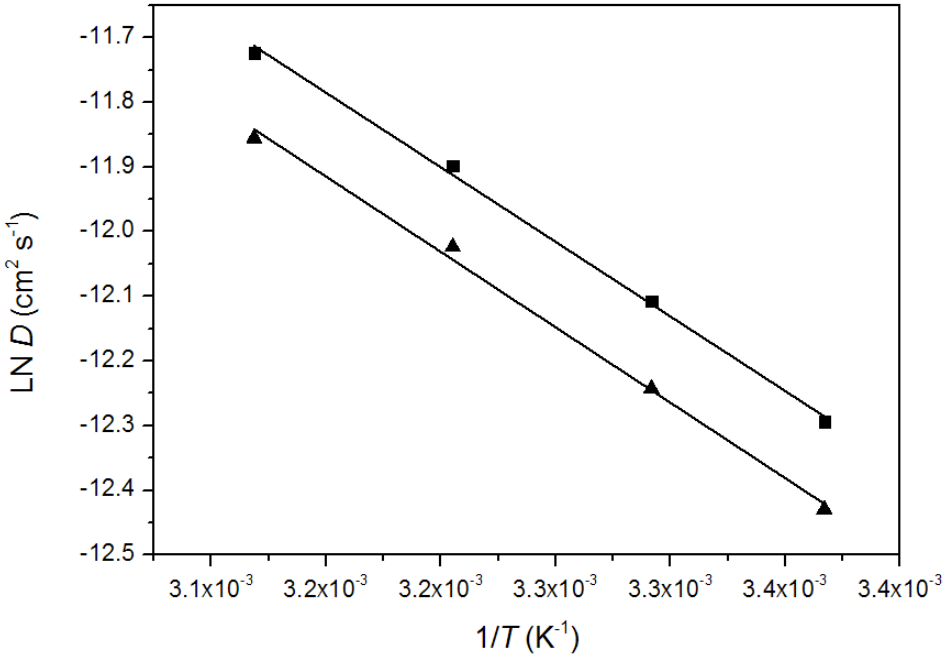


Figure 9.2: *Arrhenius plots of ln D vs T^{-1} for 3-Nitrophenolate$^{\cdot-}$ (solid squares) and 3-Nitrophenolate$^{2-\cdot}$ in DMSO containing 0.1 M TBAP.*

Cyclic Voltammetry

Cyclic voltammetry measurements of the electro-reduction of the 3-nitrophenolate anion in DMSO supported by 0.1 M TBAP on mercury hemispherical

microelectrodes of 23 μm radius was made within the scan rate range of 0.05-2 Vs^{-1} In this study, 4 sets of voltammograms, each recorded at a different temperature (24, 30.8, 39 and 47.5 °C) were obtained.

Theoretical fittings of the voltammograms were carried out using the BV and aMH formalisms. For the aMH formalism, the "true" reorganization energy of $\lambda = 0.6$ eV was extracted from the slope of the best-fit linear regression of the $\ln(k_0)$ *vs* $1/T$ plot (see Figure 9.3). Both kinetic approaches were seen to give rise to excellent quality of fit (MSAD value of 3.8 ± 1.6% for BV, and 5.6 ± 2.4% for aMH formalism). The "best fit" parameters are presented in Tables 9.2 and 9.3. A comparison between the simulated and experimental voltammograms is given in Figure 9.4.

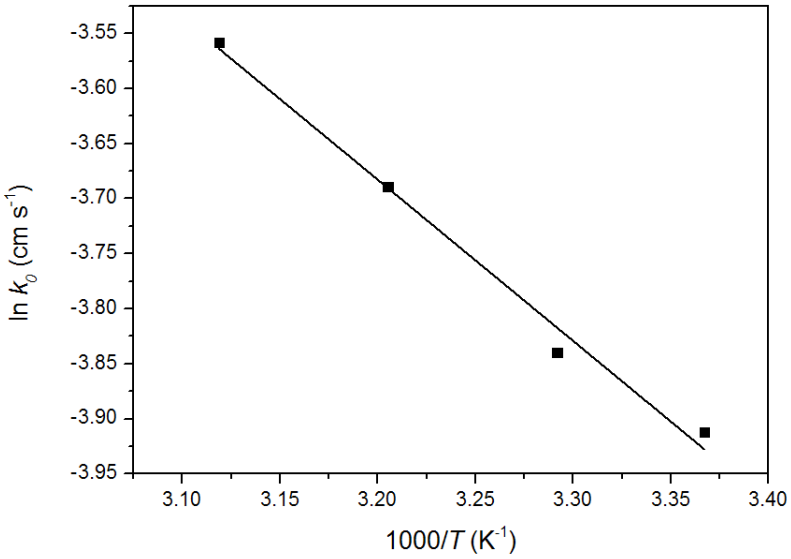


Figure 9.3: *Arrhenius plot of ln k_0 vs. 1000 × T^{-1} for 3-Nitrophenolate in DMSO containing 0.1 M TBAP k_0 values obtained through the fitting of cyclic voltammograms.*

Table 9.2: *Kinetic parameters obtained through the fitting of cyclic voltammograms with the Butler-Volmer model.*

	24.0°C	**30.8°C**	**39.0°C**	**47.5°C**
k_0 **(cm s^{-1})**	0.021	0.023	0.028	0.031
α	0.42	0.42	0.42	0.42
E_f^{θ} **(V)**	-0.71±0.015	-0.67±0.005	-0.66±0.003	-0.66±0.005
MSAD (%)	2.2±0.4	5.1±2.3	3.9±0.7	3.9±0.8

Table 9.3: *Kinetic parameters obtained through the fitting of cyclic voltammograms with the asymmetric Marcus-Hush model.*

	24.0°C	**30.8°C**	**39.0°C**	**47.5°C**
k_0 **(cm s^{-1})**	0.020	0.021	0.025	0.028
λ (eV)	0.52	0.52	0.52	0.52
γ	-0.42	-0.42	-0.42	-0.42
E_f^{θ} **(V)**	-0.71±0.01	-0.670±0.005	-0.66±0.003	-0.660±0.005
MSAD (%)	1.9±0.5	8±1	6.1±0.3	7±1

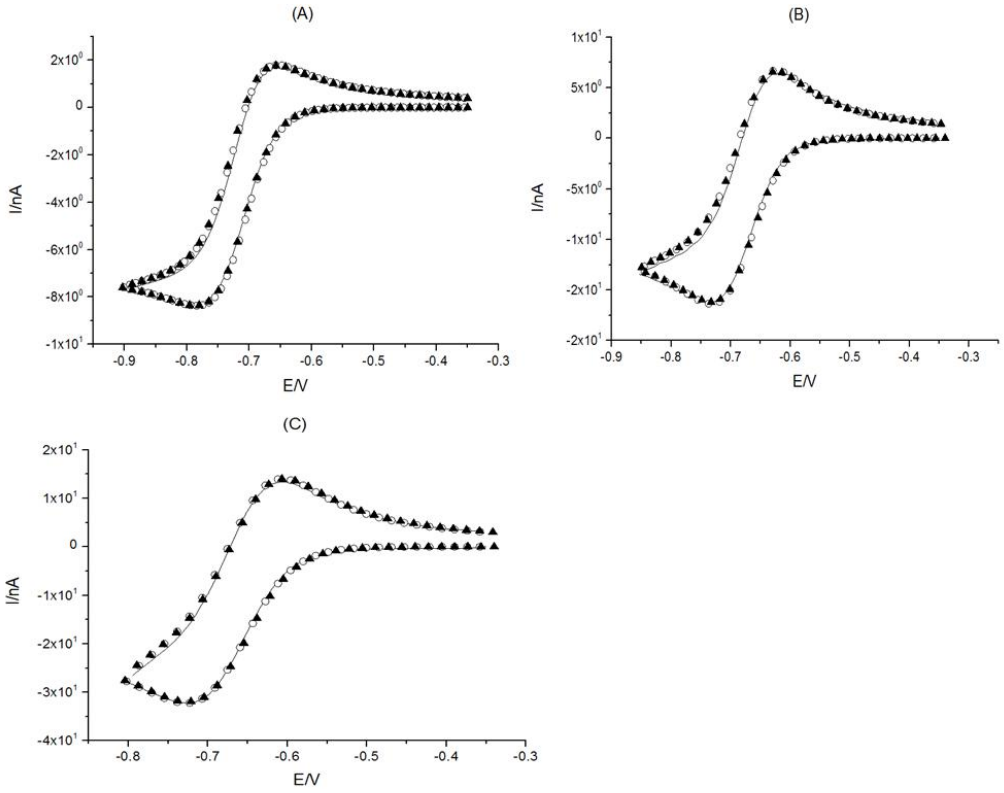


Figure 9.4: *Experimental (solid line) and simulated (open circles for BV and solid triangles for aMH) cyclic voltammograms for the reduction of 3-Nitropephenolate in DMSO at 23 μm radius mercury hemisphere electrode. (A) scan rate = 0.05 Vs^{-1}, temperature = 24 °C; (B) scan rate = 0.5 Vs^{-1}, temperature = 30.8 °C; (C) scan rate = 2 Vs^{-1}, temperature = 47.5 °C. All solutions are supported with 0.1 M TBAP.*

Square Wave Voltammetry

The kinetics of the electro-reduction of 3-nitrophenolate has also been studied via square wave voltammetry (SWV). Advantages of this technique are two-fold. First, as a pulse technique it enables the reduction of charging current effects. Second, as a differential technique it provides well-defined peaks with high sensitivity to the electrode kinetics. Moreover, the profound shape of the peaks makes their analysis easier and more accurate.

For each temperature square wave voltammograms were recorded towards negative (forward mode) and positive (reverse mode) potentials at different frequencies, keeping constant the pulse amplitude (E_{SWV} = 15 mV) and step potential (E_s = 15 mV). The reductive and oxidative peaks obtained in the forward and reverse scans, respectively, for each frequency were analyzed simultaneously according to the aMH formalism with k_0 and γ as fitting parameters. The value for the reorganization energy, λ, was determined iteratively from the concurrent analysis of the SWV peaks and ln(k_0) *vs* 1/*T* plots. The values of the kinetic parameters corresponding to the best fit (i.e., minimum MSAD value) of the whole series of square wave voltammograms at each temperature are given in Table 9.4. Note that the k_0, λ and γ values obtained give rise to very good fittings of the square wave peaks at all frequencies and temperatures (Figure 9.5) with consistent values for the reorganization energy (λ = 0.6 eV) and the symmetry parameter (γ = -0.42). Moreover, the values compare well with those obtained via cyclic voltammetry (see Table 9.3).

Molecular Insights

Relative force constants of electroactive species

From the fitting of the cyclic and square wave voltammograms for the electro-reduction of the 3-nitrophenolate anion negative γ value has been determined (Tables 3 and 4). The asymmetric Marcus-Hush formalism employed [7] rationalizes the deviations from γ = 0 in terms of differences between the elastic force constants of the electroactive species. Thus, the situation γ < 0 corresponds to force constants of the reduced species greater, in average, than those of the oxidized one. On the other hand, a positive γ value points out greater force constants for the oxidized species. In the

context of the Butler-Volmer formalism, these two cases corresponds to $\alpha < 0.5$ and $\alpha > 0.5$, respectively.

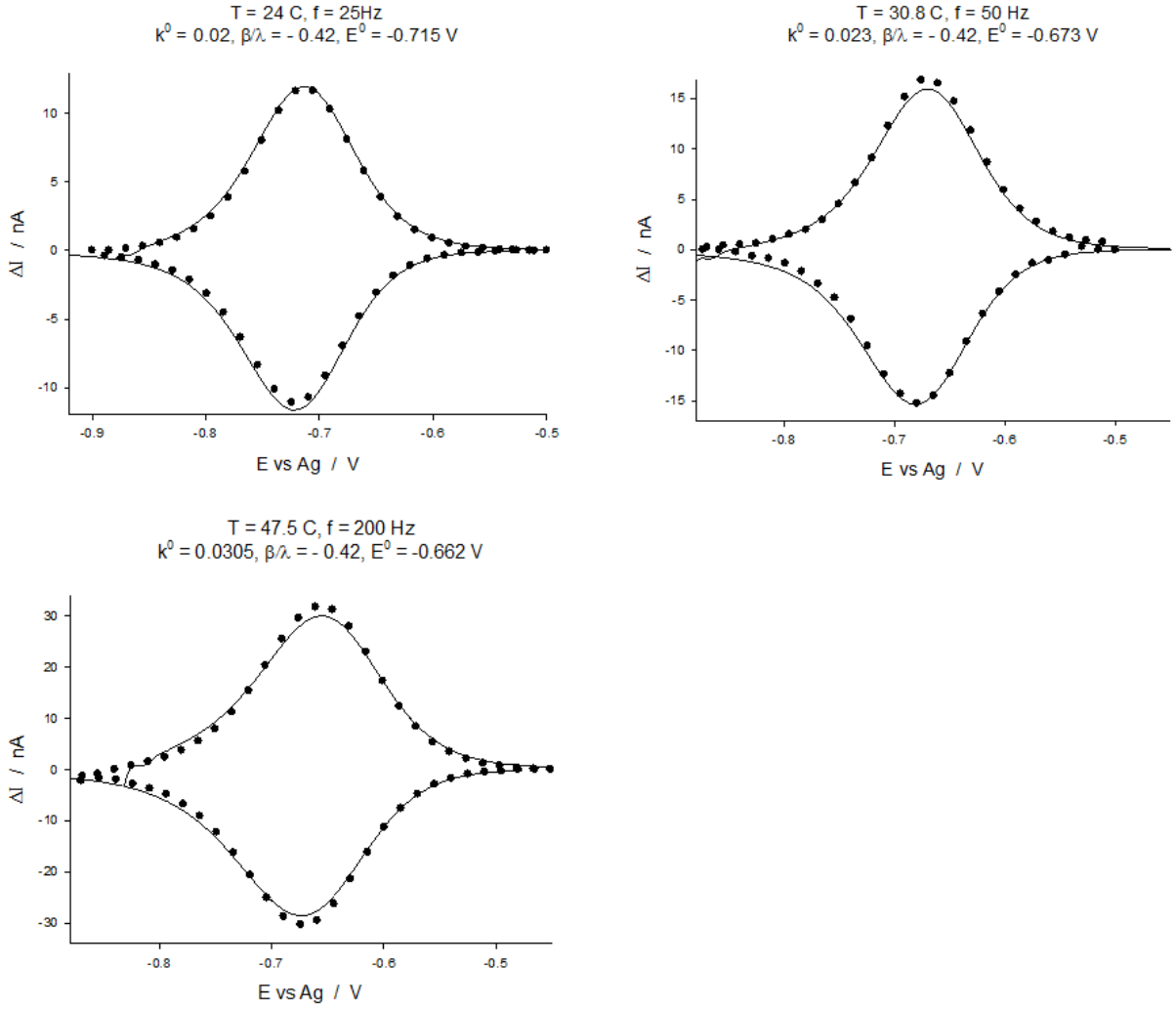


Figure 9.5: *Experimental (solid line) and simulated (solid circles) square wave voltammograms for the reduction of 3-Nitropephenolate in DMSO at 23 µm radius mercury hemisphere electrode.*

Table 9.4: *Kinetic parameters obtained with the asymmetric Marcus-Hush model from the fitting of experimental square wave voltammograms.*

	24.0°C	**30.8°C**	**39.0°C**	**47.5°C**
k_0 **(cm s^{-1})**	0.0200	0.0235	0.0270	0.0305
λ (eV)	0.6	0.6	0.6	0.6
γ	-0.42	-0.42	-0.42	-0.42
E_f^{θ} **(V)**	-0.715	-0.673	-0.665	-0.662
MSAD (%)	3±1	4±1	5±1	5±1

The value γ = -0.42 obtained for the electro-reduction of 3-nitrophenolate on mercury in DMSO indicates greater force constants for the reduced species. This can be explained by the higher charge of the radical dianion which can lead to stronger interactions with the solvent.

Reorganization energy

As discussed in Chapter 8.3, the slope of the plot ln(k_0) *vs* 1/*T* enables the extraction of the reorganization energy whereas the intercept (*Z)* value is directly related to the degree of adiabaticity of the electron transfer according to the relationship:

$$\ln(k_0) = \ln(z) - \frac{\lambda F}{4R}\left(1 + \frac{\gamma^2}{4}\right)\frac{1}{T} \tag{9.2}$$

Figure 9.6 shows the variation of k_0 with the inverse of temperature for the electro-reduction of 3-nitrophenolate according to the results obtained here from CV

(solid squares and solid line) and SWV (open circles and dotted line). In both cases, the experimental points show good linearity which confirms the Arrhenius-like dependence of the standard rate constant with temperature. From the slope of the regression line a value for the reorganization energy of λ = 0.6 eV (SWV) is extracted.

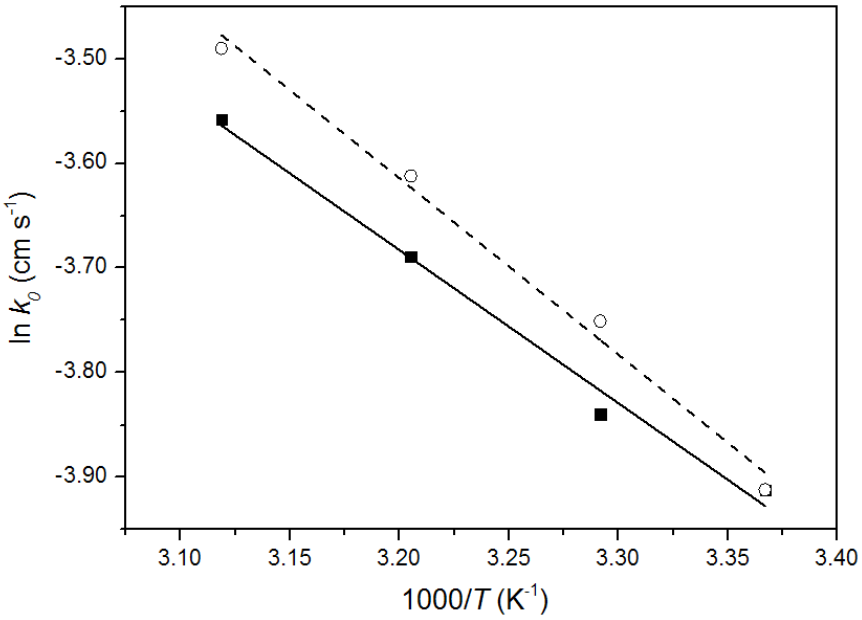


Figure 9.6: *Arrhenius plot of ln (k_0) vs. 1000 × T^{-1} for 3-Nitrophenolate in DMSO containing 0.1 M TBAP k_0 values obtained through the fitting of cyclic (solid squares) and square wave voltammograms (open circles).*

The above λ value is significantly smaller than those obtained for aliphatic nitrocompounds by similar temperature-variable voltammetric studies. Thus, λ = 1.74 eV has been obtained for the electro-reduction of 2-methyl-2-nitropropane in *N*,*N*-dimethylformamide [37] and λ = 1.7 eV for the electrochemical reduction of 1-nitropentane in acetonitrile [26].

According to the interpretation given by Peover and Powell [38] this difference between the reorganization energies can be explained by calculating the outer sphere component (λ_o) of the overall reorganization energy. The λ_o value accounts for the energy required for the reorientation of the solvent molecules around the electroactive species. Due to the partial delocalization of the negative charge in the aromatic ring [39], the λ_o value for aromatic compounds are partially smaller than those of the aliphatic species [38,40]. However, Kraiya *et al.* [41] questioned this conclusion and pointed out that the major difference between the λ values of aliphatic and aromatic nitrocompounds are due to the inner-sphere component (λ_i). This argument is based on the structural changes that take place upon the electron transfer. Whereas the main contribution for nitroaliphatics comes from the nitrogen pyramidalization, the turning of the nitro group out of the plane of the aromatic ring is the major change for nitroaromatics. From DFT calculations these authors showed that the differences in the λ_i values can be very significant. For example, the λ_i value predicted for 2-nitropropane is 2.7 eV greater than for nitrobenzene.

Degree of adiabaticity

The difference between the standard rate constants of 3-nitrophenolate (λ = 0.6 eV, γ = -0.42) and 1-nitropentane (λ = 1.7 eV, γ = -0.14) is not as large as expected from the magnitude of the difference between the reorganization energies. Thus, assuming the same pre-exponential factor for both processes in Equation 9.2, the standard rate constants at 25 ºC for 3-nitrophenolate should be more than four orders of magnitude greater than for 1-nitropentane. However, the k_0 value reported for 1-nitropentane for 26 ºC (k_0 = 0.013 cm s^{-1}) is only slightly smaller than that obtained for 3-nitrophenolate at 24 ºC (k_0 = 0.02 cm s^{-1}).

To understand this behaviour, the degree of adiabaticity of the electron transfer will be analyzed in this section. This is associated with the strength of the electronic interaction between the electroactive species and the electrode electronic levels. Thus, the adiabatic regime (strong interaction) corresponds to $\kappa_{el} \to 1$ and the non-adiabatic one (weak coupling) to $\kappa_{el} << 1$.

The degree of adiabaticity of the process can be evaluated from the pre-exponential constant *Z* in Equation 9.2. Making use of the approximate expression for the electronic transmission coefficient reported by Feldberg and Sutin for heterogeneous electron transfers the following expression is obtained for the intercept *Z* [42]:

$$Z = 3.0\,\nu_n \kappa_{el} \approx \frac{3.0\,\nu_n}{\beta}\,\mathrm{Ln}\left(1 + \frac{4\pi^2 \rho_M H_{0,AB}^2}{\nu_n h\sqrt{4\pi\lambda^*}}\right) \tag{9.3}$$

where β is the tunnelling factor, ρ_M the density of electronic levels in the electrode, $H_{0,AB}$ electronic coupling element at the plane of closest approach and h the Planck's constant.

Considering appropriate values for the tunnelling factor $\beta = 10^8$ cm^{-1} [42], the density of states of s-band metals $\rho_M \approx 0.3$ eV^{-1} [43] and the nuclear vibration frequency factor of the system $\upsilon_n = 10^{12}$ s^{-1} [44], the variation of the intercept (*Z*) of the plot ln(k_0) *vs* 1/*T* with the coupling constant ($H_{0,AB}$) have been calculated. As can be seen in Figure 9.7, the experimental value obtained from square wave voltammetry for 3-nitrophenolate ln[*Z*(cm s^{-1})] = 1.8 ± 0.4 (circle point) lies in the non-adiabatic linear domain

corresponding to small $H_{0,AB}$ values and therefore to weak electronic coupling. This value also compares well with that measured through cyclic voltammetry experiments ($\ln[Z(\text{cm s}^{-1})] = 1.0 \pm 0.3$). This contrasts with the much larger value obtained for the electro-reduction of 1-nitropentane in acetonitrile from Chapter 8 ($\ln[Z(\text{cm s}^{-1})] = 13 \pm 1$, triangular point in Figure 7.7) and it explains the negligible difference between the rate constants in spite of the large discrepancy of the values of the reorganization energy. Given that the same electrode material (mercury) and supporting electrolyte (TBAP) were used in both studies, the difference between the strengths of the electronic coupling may be related to different steric hindrance and electronic structure of 1-nitropentane and 3-nitrophenolate molecules.

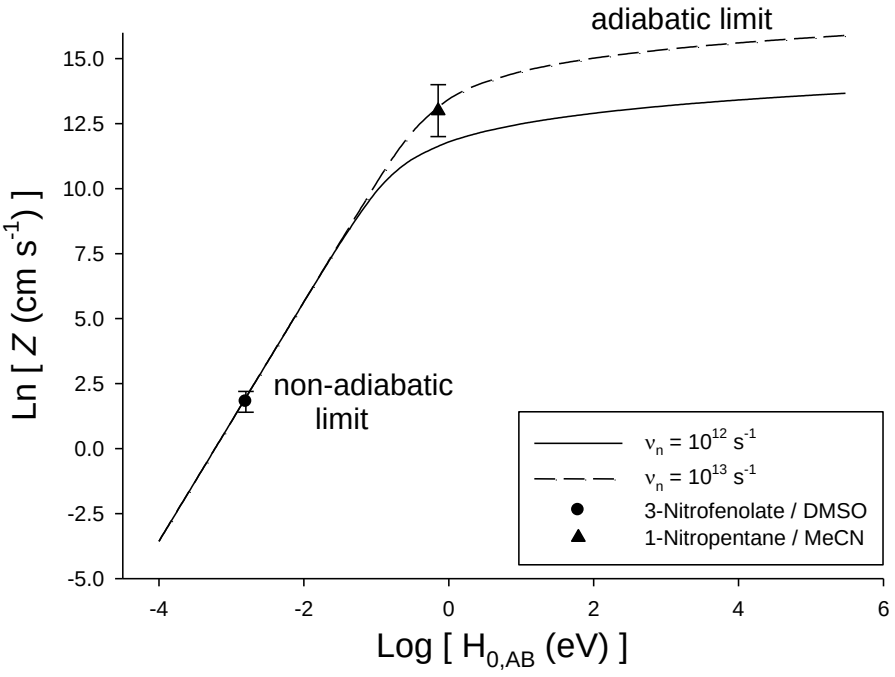


Figure 9.7: *Variation of the intercept (Z) of the plot Ln(k_0) vs 1/T with the coupling constant ($H_{0,AB}$).*

These results signal the need for taking into account both factors, reorganization energy and degree of adiabaticity, when carrying out comparative analysis of electrode kinetics. Temperature-variable cyclic and square wave voltammetry are adequate procedures to evaluate these two characteristics of electrode reactions in diffusional systems.

9.4 Conclusions

The kinetic analysis of temperature-variable voltammetry in combination with the asymmetric Marcus theory provides significant insights into heterogeneous electron transfer processes. The occurrence of changes in bond lengths, angles and force constants can be inferred as well as the electronic coupling between the electroactive species and the electrode.

In this chapter, this methodology has been applied to the study of the electro-reduction of 3-nitrophenolate on mercury hemispherical microelectrodes in DMSO. From the fitting of cyclic and square wave voltammograms recorded at different temperatures in the range between 24 and 47.5 ºC the reorganization energy is determined to be λ = 0.6 eV, and the symmetry parameter γ = 0.42. The negative γ value indicates that the force constants of the electrogenerated species (radical dianion) are greater than for the monoanion. The λ value is strikingly smaller than those documented for aliphatic nitrocompounds. This can be attributed to different structural changes upon the electron transfer. On the other hand, the electronic coupling with the mercury electrode is much smaller in the case of 3-nitrophenolate, being situated in the non-adiabatic regime.

Chapter 10 extends on the study described in this chapter to cover an aliphatic nitrocompound reagent, namely 2-nitropropane.

9.5 References

1. A.J. Bard, L. Faulkner, *Electrochemical Methods: Fundamentals and Applications, 2nd Ed.*, Wiley & Sons, New York, 2001.
2. R.G. Compton, C.E. Banks, *Understanding Voltammetry, 2nd Ed*., Imperial College Press, London, 2011.
3. R.A. Marcus, N. Sutin, *Biophys. Chim. Acta* **265** (1985) 811.
4. S. Fletcher, *J. Solid State Electrochem.* **14** (2010) 705.
5. A.M. Kuznetsov, J. Ulstrup, *Electron transfer in chemistry and Biology: An Introduction to the Theory*, Wiley and Sons, Chichester, 1999.
6. R.A. Marcus, *J. Chem Phys.* **24** (1956) 966.
7. R.A. Marcus, *J. Chem. Phys.* **43** (1965) 679.
8. C.E.D. Chidsey, *Science* **215** (1991) 919.
9. S.W. Feldberg, *Anal. Chem.* **82** (2010) 5176.
10. J.T. Hupp, M.J. Weaver, *J. Phys. Chem.* **88** (1984) 6128.
11. R.M. Haddox, H.O. Finklea, *J. Phys. Chem. B* **108** (2004) 1694.
12. N. Madhiri, H.O. Finklea, *Langmuir* **22** (2006) 10643.
13. G.A. Orlowski, H.-B. Kraatz, *Electrochim. Acta* **51** (2006) 2934.
14. G.A. Orlowski, S. Chowdhury, H.-B. Kraatz, *Langmuir* **23**, (2007) 12765.
15. A.L. Eckermann, J.A. Shaw, T.J. Meade, *Langmuir* **26** (2010) 2904.
16. D. Suwatchara, M.C. Henstridge, N.V. Rees, R.G. Compton, *J. Phys. Chem. C* **115** (2011) 14876.

17. M.C. Henstridge, Y. Wang, J.G. Limon-Petersen, E. Laborda, R.G. Compton, *Chem. Phys. Lett.* **517** (2011) 29.
18. E. Laborda, Y. Wang, M. Henstridge, F. Martinez-Ortiz, A. Molina, R.G. Compton, *Chem. Phys. Lett.* **512** (2011) 133.
19. D. Suwatchara, N.V. Rees, M.C. Henstridge, E. Laborda, R.G. Compton, *J. Electroanal. Chem.* **665** (2012) 38.
20. M.C. Henstridge, E. Laborda, E.J.F. Dickinson, R.G. Compton, *J. Electroanal. Chem.* **664** (2012) 73.
21. Y. Wang, E. Laborda, M. Henstridge, F. Martinez-Ortiz, A. Molina, R. G. Compton, *J. Electroanal. Chem.* **668** (2012) 7.
22. M.C. Henstridge, E. Laborda, N.V. Rees, R.G. Compton, *Electrochim. Acta*, DOI: j.electacta.2011.10.026 (2012).
23. E. Laborda, M.C. Henstridge, R.G. Compton, *J. Electroanal. Chem.* **667** (2012) 48.
24. M.C. Henstridge, E. Laborda, Y. Wang, D. Suwatchara, N. Rees, A. Molina, F. Martínez-Ortiz, R.G. Compton, *J. Electroanal. Chem.* **672** (2012) 45.
25. D. Suwatchara, M.C. Henstridge, N.V. Rees, E. Laborda, R.G. Compton, *J. Electroanal. Chem.* **677** (2012) 120.
26. D. Suwatchara, N.V. Rees, M.C. Henstridge, E. Laborda, R.G. Compton, *J. Electroanal. Chem.* **685** (2012) 53.
27. N. G. Tsierkezos, U. Ritter, *J. Appl. Electrochem.* **40** (2010) 409.
28. C. Amatore, E. Maisonhaute, G. Simonneau, *J. Electroanal. Chem.* **486** (2000) 141.
29. D. Shoup, A. Szabo, *J. Electroanal. Chem.* **237** (1982) 140.

30. K.N. Marsh, A. Deev, A.C.-T. Wu, E. Tran, A. Klamt, Korean *J. Chem. Eng.* **19** (2002) 357.

31. J. Mauzeroll, E.A. Hueske, A.J. Bard, *Anal. Chem.* **75** (2003) 3880.

32. T.J. Davies, B.A. Brookes, A.C. Fisher, K. Yunus, S.J. Wilkins, P.R. Greene, J.D. Wadhawan, R.G. Compton, *J. Phys. Chem.* **107B** (2003) 6431.

33. A. Molina, E. Laborda, E.I. Rogers, F. Martínez-Ortiz, C. Serna, J.G. Limon-Petersen, N.V. Rees, R.G. Compton, *J. Electroanal. Chem.* **634** (2009) 73.

34. Y. Wang, J.G. Limon-Petersen, R.G. Compton, *J. Electroanal. Chem.* **652** (2011) 13.

35. O.V. Klymenko, R.G. Evans, C. Hardacre, I.B. Svir, R.G. Compton, *J. Electroanal. Chem.* **571** (2004) 211.

36. C.A. Paddon, D.S. Silvester, F.L. Bhatti, T.J. Donohoe, R.G. Compton, *Electroanalysis* **19** (2007) 11.

37. C. Costentin, C. Louault, M. Robert, V. Rogé, J.M. Savéant, *Phys. Chem. Chem. Phys.* **14** (2012) 1581.

38. M.E. Peover, J.S. Powell, *J. Electroanal. Chem.* **20** (1969) 427.

39. M.H. Baik, C.K. Schauer, T. Ziegler, *J. Am. Chem. Soc.* **124** (2002) *11167*.

40. W.R. Fawcett, Y.I. Kharkats, *J. Electroanal. Chem.* **47** (1973) 413.

41. C. Kraiya, P. Singh, D.H. Evans, *J. Electroanal. Chem.* **563** (2004) 203.

42. S. W. Feldberg, N. Sutin, *Chem. Phys.* **324** (2006) 216.

43. R.L. Birke, Q. Huang, T. Spataru, D.K. Gosser, *J. Am. Chem. Soc.* **128** (2006) 1922.

44. M. Opallo, *J. Chem. Soc. Faraday Trans.* **82** (1986) 339.

Chapter 10

On the Adiabaticity of Electrode Processes: Effect of the Supporting Electrolyte Cation on the Kinetics of Electro-reduction of 3-Nitrophenolate

The work presented in this chapter has been published in

J. Electroanal. Chem., (2013), doi: j.jelechem.2013.02.010

As shown in the previous chapter, comparative analysis of voltammetric responses at different temperatures through the asymmetric Marcus-Hush-Chidsey theory provides physical insight into the changes upon the electron transfer mechanism and the electronic interaction between the electrode and the electroactive species. In this chapter, this approach is applied to the assessment of the influence of the nature of the supporting electrolyte on the kinetics of electrode processes.

In particular, the electro-reduction of the 3-nitrophenolate anion is studied in dimethylsulfoxide solutions via the use of a mercury hemispherical working microelectrode. Three different tetra-alkyl-ammonium perchlorates are employed as supporting electrolyte: tetraethylammonium, tetrabutylammonium and tetrahexylammonium. From these kinetic studies undertaken at different temperatures the reorganization energy, force constant symmetry and the strength of the electronic coupling are determined and analyzed for the different conditions. The results presented show a significant effect of the identity of the supporting electrolyte cation on the

electrode kinetics that can be attributed to the change of the distance of closest approach between the electroactive species and the electrode as well as to ion-pairing effects. The experimental behaviour observed suggests that the process has a non-adiabatic character.

Programs used for simulations are written by Dr. E. Laborda.

10.1 Introduction

As demonstrated through the work described in Chapter 9, kinetic studies at different temperatures offers insight into physical phenomena of electrode processes. Microscopic kinetic models, and particularly the asymmetric Marcus-Hush (aMH) model [1,2], enable one to rationalize the kinetics of heterogeneous electron transfers in terms of the difference between the configurations of the reactant and product species (reorganization energy), the difference between their vibrational force constants, and the strength of the electronic interaction between the electrode and the electroactive species (adiabaticity).

In the literature, various theoretical approaches to the adiabatic character of outersphere electrode processes have been described [3-5]. Herein, there is a need for new experimental investigations to assist the development of suitable holistic models. Usually, the sensitivity of the electrode kinetics to the electronic density of the electrode material and the solution viscosity has been criteria to examine the degree of adiabaticity of a given process [6-8]. The first approach [6] is based on the simplifying idea that the rate constant of the processes increases with the density of states up to a limit value corresponding to the adiabatic regime. Therefore, the kinetics of non-adiabatic processes is expected to scale with the electrode density of states whereas adiabatic reactions should be independent of this parameter and therefore independent of the

electrode material. Schmickler *et al*. found the latter behaviour when studying the electro-reduction of several ions in *aqueous* solutions under turbulent flow and, consequently, these reactions were classified as adiabatic [6,7].

This strategy requires a precise knowledge of the density and nature of electronic states of the electrode material [3].

With respect to the study of the electronic coupling through viscosity variable studies [8], the rate constant of a non-adiabatic process is expected to be independent of the solution viscosity, whereas for adiabatic processes the electron transfer rate should be enhanced as the solution viscosity decreases. This simplifying criterion does not reflect the complexity of the effect of viscosity on the electrode kinetics and can lead to misinterpretation [8].

The study of the variation of the standard heterogeneous rate constant (k_0) with temperature is an interesting and valuable alternative that has been applied to the study of several electrode reactions [9-13]. Apart from enabling the evaluation of the degree of adiabaticity, the value of the reorganization energy can also be better estimated with superior accuracy compared to voltammetry at constant temperature.

In the present work, this methodology is applied to explore the effect of the size of the supporting electrolyte cation on the kinetics of electro-reduction of 3-nitrophenolate anion at the interface between a mercury microelectrode and a dimethylsulfoxide solution. As has been reported for other nitrocompounds [9,14], at the negative potentials where the electrode process takes place the size of the cation is expected to establish the distance of closest approach between the electroactive species and the electrode. The resulting effect on the rate constants is predicted to be significant for non-adiabatic processes and to decrease as the reaction is more adiabatic [15].

10.2 Experimental

Chemical Reagents

3-Nitrophenol ($Ph(OH)NO_2$, Aldrich, 99%), tetra–n-ethylammonium perchlorate (TEAP, Fluka, Puriss grade), tetra–n-butylammonium perchlorate (TBAP, Fluka, Puriss grade), tetra–n-hexylammonium perchlorate (THAP, Alfa Aesar), tetra–n-butylammonium hydroxide ($TBAOH \cdot 30H_2O$, Aldrich, >98%), mercury(I) nitrate dihydrate ($Hg_2(NO_3)_2 \cdot 2H_2O$, Aldrich, >97%), nitric acid (HNO_3, Fisher scientific, 70%), ferrocene ($Fe(C_5H_5)_2$, Aldrich, 98%), cobalt(III) sepulchrate trichloride ($[CoSep]Cl_3$, Aldrich, 95%), potassium nitrate (KNO3, Aldrich, >99%), dimethylsulfoxide (DMSO, Alfa Aesar, >99%), acetonitrile (MeCN, Fisher Scientific, HPLC grade), were all used as received without further purification.

A 20% excess of TBAOH was added to the corresponding 3-nitrophenol solution in order to generate the 3-nitrophenolate monoanion [16].

Instrumentation

All the electrochemical experiments were carried out with a computer-controlled Autolab PGSTAT12 (Metrohm-Autolab BV, Utrecht, Netherlands) and a three-electrode setup where a platinum mesh acted as the counter electrode and a silver wire as the reference electrode.

A mercury hemisphere was employed as the working electrode. This was electrodeposited onto a microdisk electrode of 23 μm radius by applying a potential pulse at -0.25 V (vs Ag wire) in a 50 mM $Hg_2(NO_3)_2$ and 0.1 M KNO_3 solution acidified to 0.5% with HNO_3 [17].

The amount of charge passed enabled a first control of the size of the hemisphere. After deposition, the size and shape of the mercury deposit were confirmed by both electrochemical and optical methods as detailed in previous works [12,13]. The results confirmed the deposition of a 23 μm radius mercury drop with hemispherical shape.

An air heater-controller system fabricated in-house was used for thermal control of the electrochemical experiments within a precision of ± 0.2 °C.

Determination of Reactant Concentration and Diffusion Coefficients

For this work, DMSO solutions containing *ca*. 1 mM of 3-nitrophenolate monoanion and *ca*. 0.1 M of a different background electrolyte (TEAP, TBAP or THAP) were used for electrochemical measurements at different temperatures in the ranges: 24-49°C for TEAP; 24-47.5°C for TBAP; and 23-53°C for THAP.

The diffusion coefficient of the electroactive species and the concentration of the 3-nitrophenolate anion were determined at each temperature through independent measurements prior to the kinetic study in order to reduce the number of unknown variables. Note that these magnitudes vary with temperature given the temperature dependent nature of diffusion coefficients and solvent thermal expansion.

Double potential step chronoamperommetry [18] was carried out at each temperature. The potential was initially set at -0.25 V (*vs* Ag wire) where no faradaic process takes place. Then, the potential value was stepped to a potential corresponding to diffusion limited conditions for the electro-reduction of the 3-nitrophenolate monoanion for 0.5 s. In the second pulse the potential was stepped back to -0.25 V for

0.5 s such that the radical dianion electrogenerated during the first pulse is oxidized under limiting current conditions.

The analysis of the first step chronoamperogram yields the diffusion coefficient and bulk concentration of the 3-nitrophenolate monoanion and, once this is known, the diffusion coefficient of the radical dianion is obtained from the second step chronoamperogram. The reactant concentrations studied ranged between 0.84 and 1.13 mM, and the results for the diffusion coefficients (D) are shown in Figure 10.1 in the form of Arrhenius plots of ln(D) vs 1/ T.

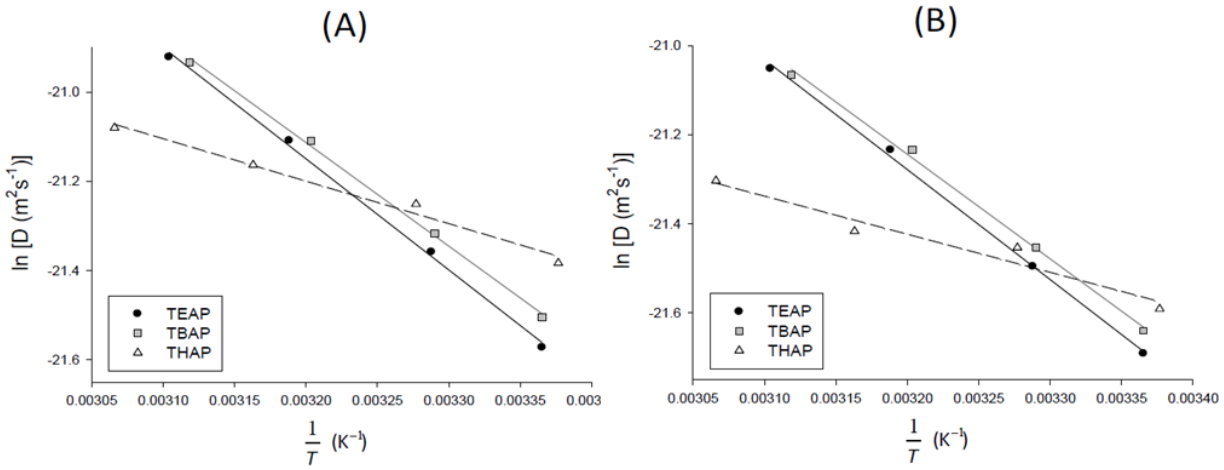


Figure 10.1: *Arrhenius plots of ln D vs T^{-1} for 3-nitrophenolate^{-} (A) and 3-nitrophenolate2^{-} (B) in DMSO containing 0.1 M supporting electrolyte.*

Cyclic Voltametry at Variable Temperature

Cyclic voltammograms within the scan rate range of 50 mV s^{-1} to 2 V s^{-1} were recorded between -0.2 and -0.92 V (*vs* Ag wire) on 23 µm radius mercury hemispherical electrode. Thus, the electrode kinetics was investigated in a very wide

experimental time scale from a nearly purely linear diffusional regime at high scan rates to a nearly purely convergent diffusion at low scan rates. For each solution, four sets of voltammograms each recorded at a different temperature (24-49°C for TEAP; 24-47.5°C for TBAP; and 23-53°C for THAP), were obtained.

10.3 Simulation and Fitting Methodology

The program used for simulation work in this chapter was developed in-house by Dr. E. Laborda. The mathematical treatment of the asymmetric Marcus-Hush-Chidsey formalism used in the program is described in Chapter 2.4.

The quality of the fitting of the experimental cyclic voltammograms was evaluated through the value of the mean scaled absolute deviation (MSAD); the smaller the MSAD value, the better the quality of the fitting. The mathematical expression of %MSAD is given in Equation 4.15 in Chapter 4. In order to avoid large contributions to the MSAD of very small signal values only the points where i_{exp} is at least 10% of the peak current have been considered.

Given that the concentration and diffusion coefficients of the electroactive species are known, the fitting parameters are reduced to four: $\{E_f^{\Theta}, k_0, \lambda, \gamma\}$ (the formal potential, standard heterogeneous rate constant, reorganization energy, and asymmetry parameter, respectively. For the sake of consistency, the activation parameters λ and γ were kept constant for a given solution (i.e., a given supporting electrolyte) across all the temperature range. For a given temperature, the voltammograms are relatively insensitive to the λ-value, and so the effective fitting parameters are $\{E_f^{\Theta}, k_0, \gamma\}$, the optimum values of which were determined from minimization of the MSAD value for each experimental set.

However, as shown in Section 10.4, the λ-value can be accurately obtained from the variation of k_0 with temperature. The $E_f^{\ominus}$, value is considered as a floating variable due to the actual shift that accompanies the use of the Ag wire pseudo-reference electrode. The results are shown in Figures 10.2-10.4 and Tables 10.2-10.4, and in all cases the agreement between theory and experiments is good (average MSAD < 4%).

10.3 Results and Discussion

Activation Energy for Diffusion

The activation energy for diffusion, $-E_{a,d}$, of the electroactive species was calculated from the Arrhenius-like variation of the *D*-value with temperature (see Equation 9.1 in Chapter 9).

The $E_{a,d}$ values obtained are given in Table 10.1, showing significantly larger activation energy for both electroactive species in presence of TEA^+ and TBA^+ compared to those obtained when using THAP as supporting electrolyte. Given that the smaller cations (TEA^+ and TBA^+) are expected to have stronger coulombic interactions with the negatively charged electroactive species, these results can be assigned to larger effective molecular volume [19] due to ion-pairing in the case of TEA^+ and TBA^+ but not in the case of THA^+. Indeed, as a result of these interactions the $E_{a,d}$ value in presence of TEA^+ and TBA^+ is larger than the activation energy of viscosity for DMSO, $E_{a,\eta}$, = 14.1 kJ mol^{-1} [20]. Given that the $E_{a,d}$, and the hypothetical diffusion coefficient at infinite temperature (D_∞) values (dependent on the molecule size [19]) for the oxidized and reduced species are very similar, we can conclude that there is no change of the ion-pair stoichiometry after the electron transfer and so the process can be modelled as a single electron transfer mechanism.

Table 10.1: *Diffusion activation energy and diffusion coefficient at infinite temperature of 3-nitrophenolate^{-} ($3NP^{-}$) and 3-nitrophenolate^{2-} ($3NP^{2-}$) in 0.1 M TXAP, DMSO solutions obtained from the variation of the D-value with temperature. D_{∞} is the hypothetical diffusion coefficient at infinite temperature*

Supporting Electrolyte	**$E_{a,d}$ (kJ mol^{-1})**		**ln[D_{∞} (m^2 s^{-1})]**	
	$3NP^{-}$	$3NP^{2-}$	$3NP^{-}$	$3NP^{2-}$
TEAP	20.7 ± 0.6	20.5 ± 0.6	-13.2 ± 0.3	-13.4 ± 0.2
TBAP	19.3 ± 0.6	19.5 ± 0.8	-13.7 ± 0.2	-13.7 ± 0.3
THAP	7.9 ± 0.7	7 ± 1	-18.1 ± 0.3	-18.7 ± 0.5

The activation energy for diffusion of the electroactive species in THAP solutions is approximately half of the $E_{a,\eta}$ value, which indicates that the electroactive molecules deviate significantly from macroscopic hydrodynamic theory in this medium. Assuming that there is no ion-pairing between the electroactive species and THA^{+}, this behaviour can be ascribed to the more planar shape and smaller size of 3-nitrophenolate with respect to the ion pairs with TEA^{+} and TBA^{+}, such that its diffusion is less affected by the solvent viscosity [21].

The above possibility was investigated by UV-visible spectroscopy of 3-nitrophenolate solutions in presence and absence of supporting electrolyte with a U-2001 spectrophotometer (HITACHI, UK). The spectra obtained (not shown) show two peaks at 291nm (with an extinction coefficient, ε = 4380 M^{-1} cm^{-1}) and 496nm (ε = 1380 M^{-1} cm^{-1}), the heights of which do not change significantly when varying the concentration of TXAP between 0 and 100 mM. However, the study of ion-pairing through UV-vis spectroscopy has been reported to be inconclusive, especially for non-

contact ion pairs [22]. Therefore, in spite of the UV-vis results and on the basis of the values obtained for the activation energy for diffusion, the possible incidence of ion-pairing on the kinetics will be present in the following discussions.

Reorganization Energy and Symmetry Parameters

The fitting of the cyclic voltammograms at different scan rates (50-2000 mV s^{-1}) yielded the best-fit set of parameters $\{E_f^{o}, k_0, \lambda, \gamma\}$ reported in Tables 10.2-10.4. As discussed in Section 10.3, the E_f^{o}, k_0 and γ values were determined from the fitting of the voltammogram position, peak-to-peak separation and peak heights at each scan rate and temperature.

A negative γ value is obtained in all cases which indicates greater vibrational force constants of the reduced form (i.e. dianion) than for the oxidized form (i.e., monoanion), which follows the behaviour reported for the electro-reduction of other nitrocompounds [2,23]. The correlation between the size of the supporting electrolyte cation and the value of the symmetry parameter γ is not clear, γ being effectively in TEA^+ and THA^+ solution, and greater (in absolute value) for TBA^+.

Table 10.2: *Kinetic parameters for the electro-reduction of 3-nitrophenolate in 0.1 M TEAP, DMSO solution on a mercury hemispherical microelectrode. Values obtained through the fitting of cyclic voltammograms with the asymmetric Marcus-Hush model.*

	Experiment 1 (24.0 ºC)	**Experiment 2 (31.0 ºC)**	**Experiment 3 (40.5 ºC)**	**Experiment 4 (49.0 ºC)**
k_0 (cm s^{-1})	0.025	0.031	0.039	0.049
λ (eV)	0.88 ± 0.02	0.88 ± 0.02	0.88 ± 0.02	0.88 ± 0.02
γ	-0.26	-0.26	-0.26	-0.26
% MSAD	4.3 ± 0.5	4 ± 1	4 ± 1	4 ± 1

Table 10.3: *Kinetic parameters for the electro-reduction of 3-nitrophenolate in 0.1 M TBAP, DMSO solution on a mercury hemispherical microelectrode. Values obtained through the fitting of cyclic voltammograms with the asymmetric Marcus-Hush model.*

	Experiment 1 (24.0 ºC)	**Experiment 2 (30.8 ºC)**	**Experiment 3 (39.0 ºC)**	**Experiment 4 (47.5 ºC)**
k_0 **(cm s^{-1})**	0.020	0.021	0.025	0.028
λ (eV)	0.52 ± 0.03	0.52 ± 0.03	0.52 ± 0.03	0.52 ± 0.03
γ	-0.42	-0.42	-0.42	-0.42
% MSAD	1.9 ± 0.5	8 ± 1	6.1 ± 0.3	7 ± 1

Table 10.4: *Kinetic parameters for the electro-reduction of 3-nitrophenolate in 0.1 M THAP, DMSO solution on a mercury hemispherical microelectrode. Values obtained through the fitting of cyclic voltammograms with the asymmetric Marcus-Hush model.*

	Experiment 1 (23.0 ºC)	**Experiment 2 (32.0 ºC)**	**Experiment 3 (43.0 ºC)**	**Experiment 4 (53.0 ºC)**
k_0 **(cm s^{-1})**	0.0040	0.0048	0.0058	0.0064
λ (eV)	0.53 ± 0.04	0.53 ± 0.04	0.53 ± 0.04	0.53 ± 0.04
γ	-0.25	-0.25	-0.25	-0.25
% MSAD	2.9 ± 0.9	3 ± 1	2 ± 1	3 ± 1

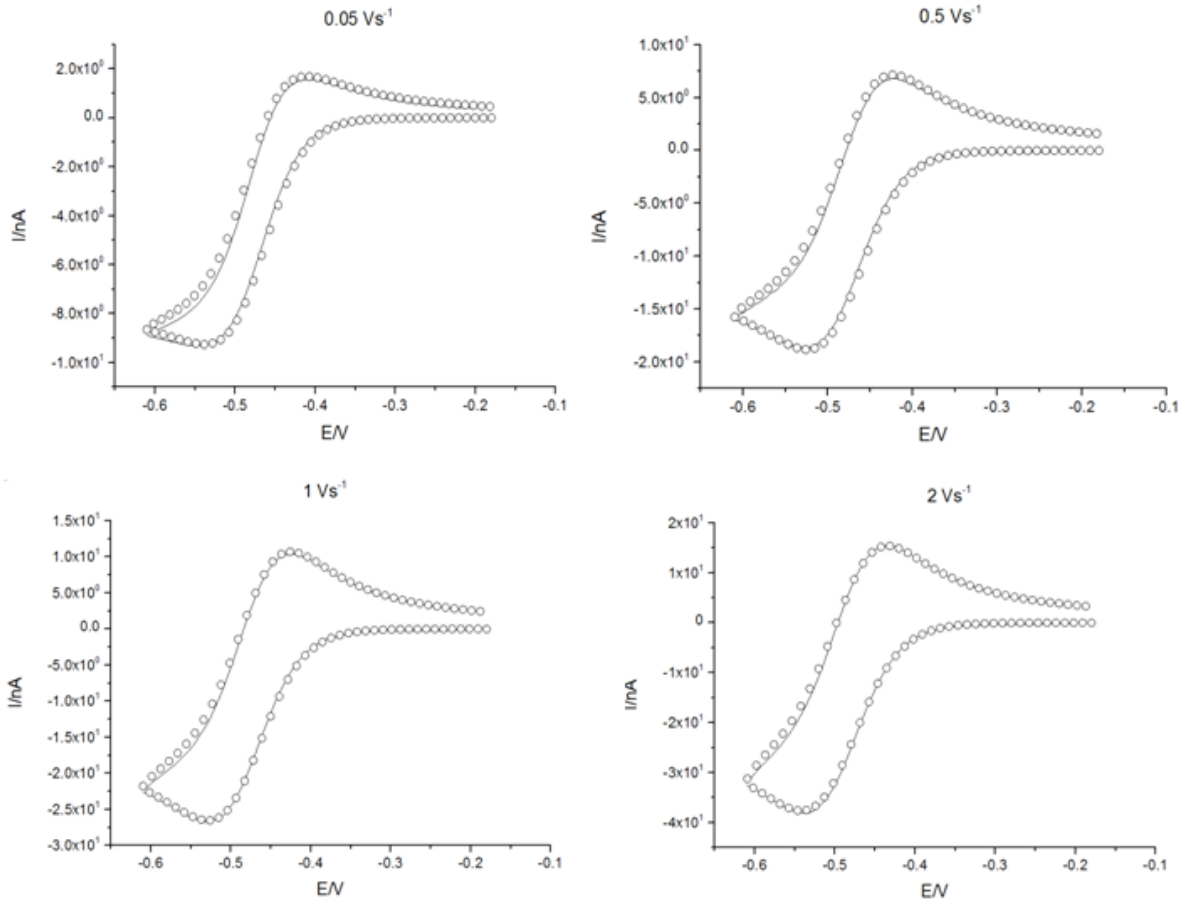


***Figure 10.2**: Fittings of experimental voltammograms obtained from 3-nitrophenolate solution in DMSO with 0.1 M TEAP as supporting electrolyte. A) Scan rate = 0.05 Vs^{-1}, T = 24ºC; B) Scan rate = 0.5 Vs^{-1}, T = 31ºC; C) Scan rate = 1Vs^{-1}, T = 40.5ºC; D) Scan rate = 2 Vs^{-1}; T = 49ºC.*

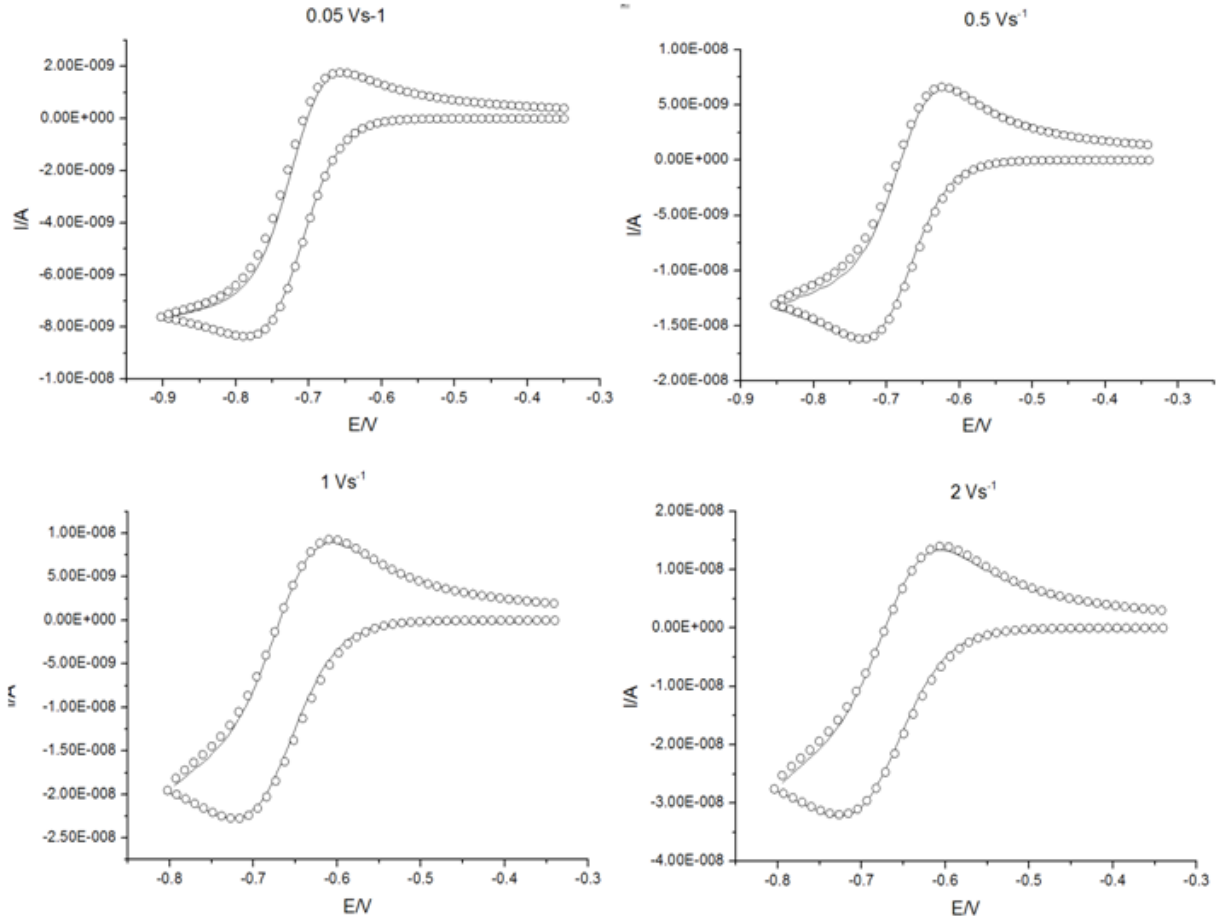


Figure 10.3: *Fittings of experimental voltammograms obtained from 3-nitrophenolate solution in DMSO with 0.1 M TBAP as supporting electrolyte. A)Scan rate = 0.05 Vs-^{1}, T = 24ºC; B) Scan rate = 0.5 Vs^{-1}, T = 30.8ºC; C) Scan rate = 1Vs^{-1}, T = 39ºC; D) Scan rate = 2 Vs^{-1}; T = 47.5ºC.*

Once k_0 is known, the value of the reorganization energy was determined from the slope of the variation of ln(k_0) value with T^{-1} (Figure 10.5):

$$\ln(k_0) = \ln(z) - \frac{\lambda F}{4R}\left(1 + \frac{\gamma^2}{4}\right)\frac{1}{T} \qquad (10.2)$$

where *Z* is given by:

$$Z = \frac{C\nu_n}{\beta} \ln\left(1 + \frac{4\pi^2 \rho_M H_{0,AB}^2}{\nu_n h\sqrt{4\pi\lambda^*}}\right) \tag{10.3}$$

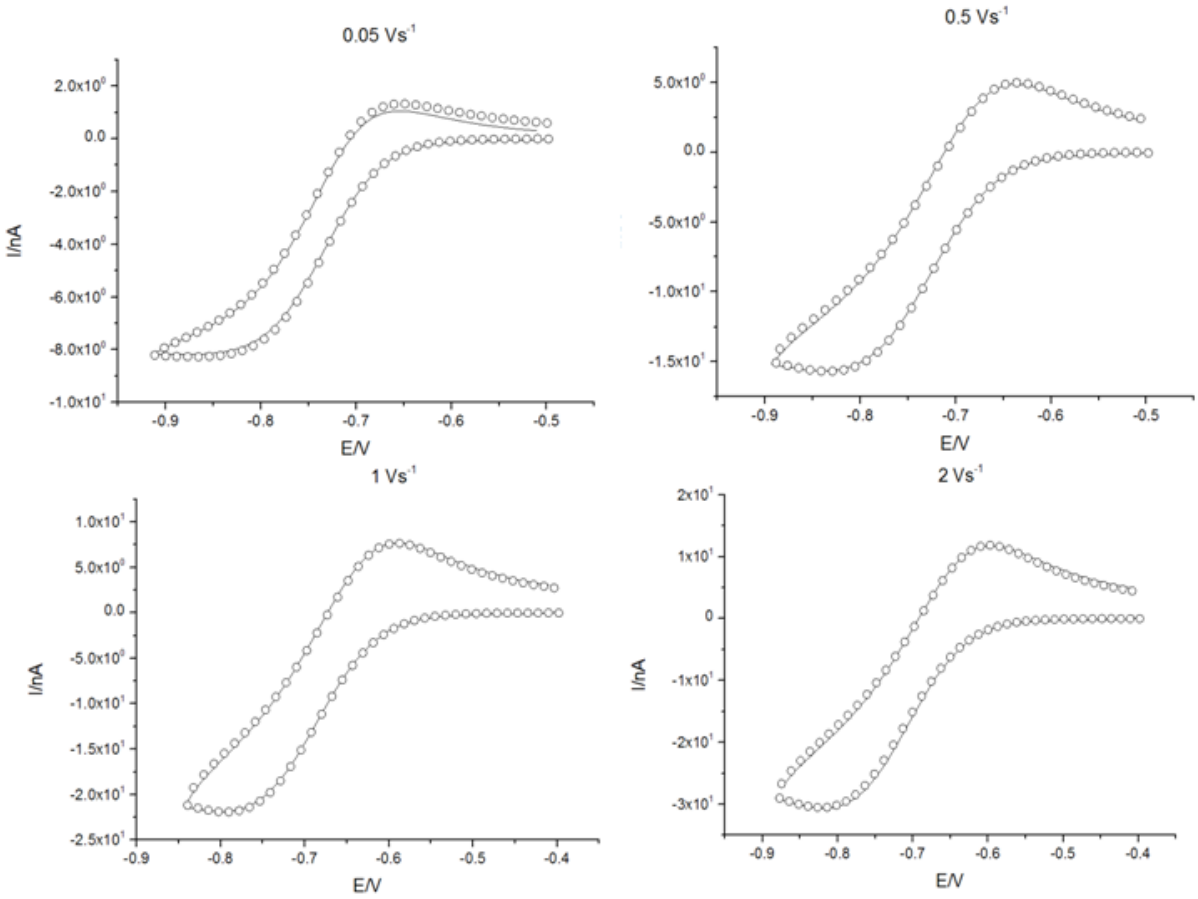


***Figure 10.4**: Fittings of experimental voltammograms obtained from 3-nitrophenolate solution in DMSO with 0.1 M THAP as supporting electrolyte. A) Scan rate = 0.05 Vs-1, T = 23ºC; B) Scan rate = 0.5 Vs-1, T = 32ºC; C) Scan rate = 1Vs-1, T = 43ºC; D) Scan rate = 2 Vs-1; T = 53ºC.*

where C is approximately constant for the temperature range here considered, and it is calculated from Equation 10.3 and the λ and γ values of each redox couple. As can be seen in Figure 10.5, the experimental results follow the linear behaviour indicated by Equation 10.2 and the value of the reorganization energy is calculated from the slope according to Equation 10.2.

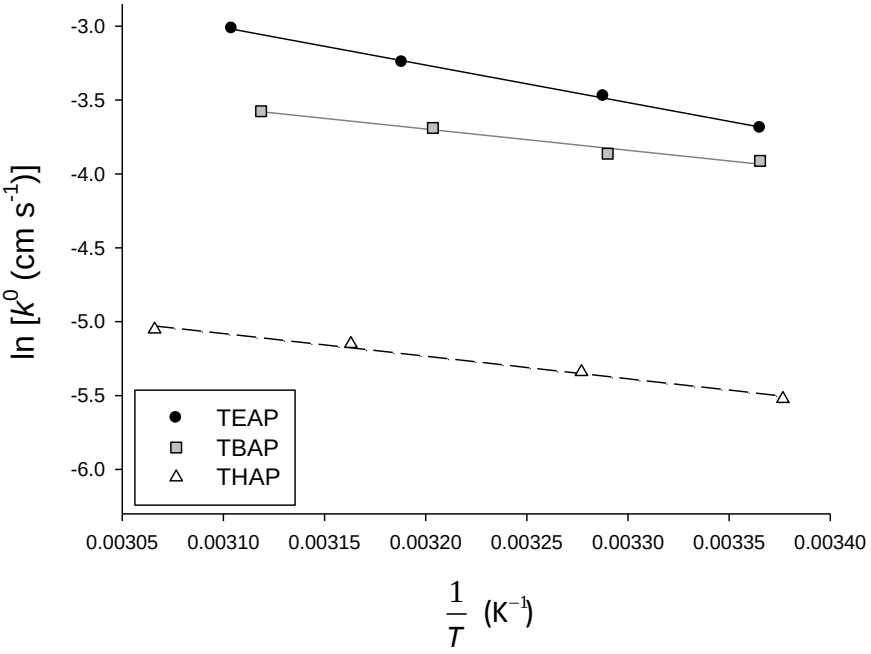


FIGURE 5. *Arrhenius plot of ln(k_0) vs T^{-1} for 3-nitrophenolate electro-reduction on mercury in DMSO containing 0.1 M TXAP. k_0 values obtained through the fitting of experimental cyclic voltammograms.*

The λ values obtained are shown in Tables 10.2-10.4. In all cases the reorganization energy is significantly smaller than that determined for the electro-reduction of nitroaliphatics such as 2-methyl-2-nitropropane (λ =1.74eV [10]) and 1-nitropentane (λ =1.7eV [12]). According to the conclusions reached by Kraiya *et al.* [24],

this difference is due to the different origin of the inner-sphere changes upon the electron transfer process, which is the nitrogen pyramidalization for nitroaliphatics and the turning of the nitro group out of the aromatic ring plane for nitroaromatics.

The influence of the size of the supporting electrolyte cation on the λ value is quite significant, the reorganization energy of the smaller cation, TEA^+, being larger than that for TBA^+ and THA^+. Given that no change of ion-pair stoichiometry is expected either for TEA^+ or TBA^+, the difference between the corresponding λ values may be ascribed to the stronger coulombic interactions of TEA^+, resulting in the reorganization of the ion-pair being energetically more expensive.

Degree of Adiabaticity

The intercept of the linear regressions (*Z*) in Figure 10.5 is closely related to the magnitude of the electronic coupling between the electrode and the electroactive molecules. According to Feldberg and Sutin's approximate treatment [15], the *Z* value increases as the electronic interaction is stronger until reaching a limit value corresponding to the adiabatic regime (see solid line in Figure 10.6).

Making use of Equation 10.3 and considering adequate values for the different variables ($\beta = 10^8$ cm^{-1} [15], $\rho_M \approx 0.3$ eV^{-1} [25], $\upsilon_n = 10^{12}$ s^{-1} [26]), the theoretical and experimental values for the pre-exponential factor are compared in Figure 10.6, in the three cases the electrode reaction lying in the non-adiabatic regime. Accordingly, the effect of the size of the supporting electrolyte cation on the *Z* value is remarkable such that *Z* increases as the cation is smaller and then the distance of closest approach to the electrode surface diminishes and $H_{0,AB}$ increases. This experimental behaviour reinforces the idea of adiabaticity as a gradual property of the electrode reaction that

can be "modulated" through, for example, the electron-tunnelling distance [27]. Therefore, the degree of adiabaticity must not be ascribed only to the processes itself but also to the medium (including the supporting electrolyte) and electrode material.

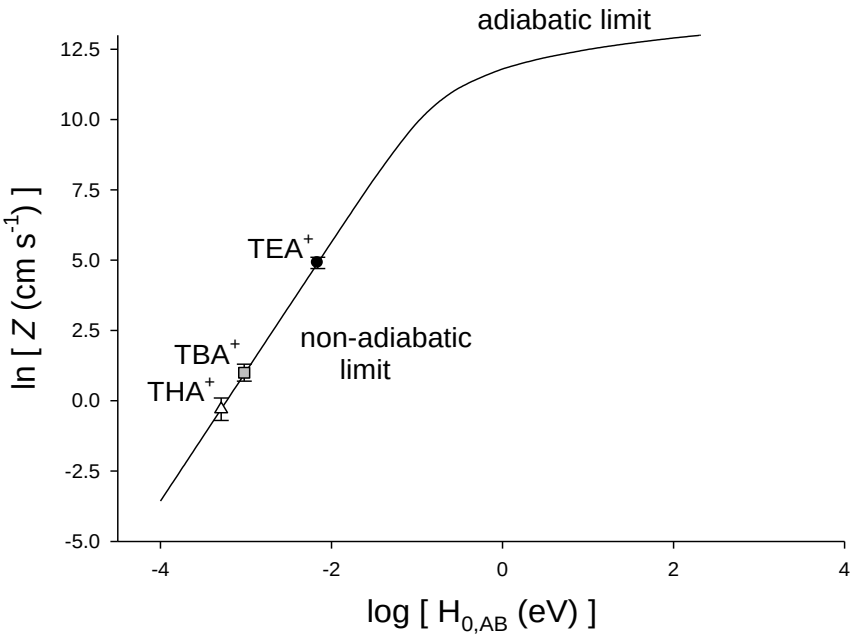


Figure 10.6: *Variation of the intercept (Z) of the plot ln(k_0) vs 1/T with the coupling constant ($H_{0,AB}$).*

As shown in this work, this can be carried out easily by varying the nature of the supporting electrolyte such that the subsequent variation of the kinetic parameters informs about the degree of adiabaticity of the process. In the future it is of interest to extent this methodology to the study of nitroaliphatics (such as 1-nitropentane) for which a more adiabatic character has been reported [13].

10.4 Conclusions

Kinetic study of electrode processes through temperature-variable cyclic voltammetry is a valuable alternative for the estimation of the reorganization energy and degree of adiabaticity of the process. In this paper, this approach has been applied to study the effect of the size of the supporting electrolyte cation on the kinetics of electro-reduction of 3-nitrophenolate on a mercury hemispherical microelectrode in DMSO. Thus, the kinetics of this reaction has been investigated with the asymmetric Marcus-Hush-Chidsey model and three different supporting electrolytes: tetra-n-ethylammonium perchlorate, tetra-n-butylammonium perchlorate and tetra-n-hexylammonium perchlorate.

The results obtained show a significant effect on the electrode kinetics: the smaller the cation, the faster the process. Considering that the size of the cation establishes the minimum distance for electronic interaction between the molecules and the electrode, this behaviour confirms that the reaction has a non-adiabatic character given that the influence is predicted to be very small for adiabatic processes.

The experimental behaviour is also consistent with the idea stated by Batchelor-McAuley *et al.* [5] according to which electrode processes are reported to be more adiabatic in aqueous solutions due to the smaller size of the supporting electrolyte ions employed in this medium. On the other hand, larger ions are usually employed in organic solvents (such as those considered in the present study) in such a way that the minimum electron tunneling distance is longer and the electronic coupling weaker.

10.5 References

1. E. Laborda, M.C. Henstridge, R.G. Compton, *J. Electroanal. Chem.* **667** (2012) 48.
2. M.C. Henstridge, E. Laborda, Y. Wang, D. Suwatchara, N. Rees, A. Molina, F. Martínez-Ortiz, R.G. Compton, *J. Electroanal. Chem.* **672** (2012) 45.
3. S. Gosavi, R. A. Marcus, *J. Phys. Chem. B* **104** (2000) 2067.
4. N.B. Luque, W. Schmickler, *Electrochim. Acta* (2012) doi: j.electacta.2012.07.135.
5. C. Batchelor-McAuley, E. Laborda, M. C. Henstridge, R. Nissim, R. G. Compton, *Electrochim. Acta* (2012) doi: j.electacta.2012.09.123.
6. T. Iwasita, W. Schmickler, J.W. Schultze, *Berichte der Bunsengesellschaft für Physikalische Chemie* **89** (1985) 138.
7. W. Schmickler, *J. Electroanal. Chem.* **204** (1986) 31.
8. R.R. Nazmutdinov, G.A. Tsirlina, I.R. Manyurov, M.D. Bronshtein, N.V. Titova, Z.V. Kuzminova, *Chem. Phys.* **326** (2006) 123.
9. C. Costentin, M. Robert, J.M. Savéant, *Phys. Chem. Chem. Phys.* **12** (2010) 13061.
10. C. Costentin, C. Louault, M. Robert, V. Rogé, J.M. Savéant, *Phys. Chem. Chem. Phys.* **14** (2012) 1581.
11. J.T. Hupp, M.J. Weaver, *J. Electroanal. Chem.* **152** (1983) 1.
12. D. Suwatchara, N.V. Rees, M.C. Henstridge, E. Laborda, R.G. Compton, *J. Electroanal. Chem.* **685** (2012) 53.
13. E. Laborda, D. Suwatchara, N. V. Rees, M.C. Henstridge, A. Molina, R.G. Compton, *Electrochim. Acta* DOI: j.electacta.2012.12.129 (2013).
14. D.H. Evans, *Chem. Rev.* **108** (2008) 2113.

15. S. W. Feldberg, N. Sutin, *Chem. Phys.* **324** (2006) 216.

16. H. Wang, O. Hammerich, *Acta Chem. Scan.* **46** (1992) 563.

17. J. Mauzeroll, E.A. Hueske, A.J. Bard, *Anal. Chem.* **75** (2003) 3880.

18. Y. Wang, E.I. Rogers, R.G. Compton, *J. Electroanal. Chem.* **648** (2010) 15.

19. K. Okamoto, M. Terazima, N. Hirota, *J. Chem. Phys.* **103** (1995) 10445.

20. M.D.C. Grande, M. Garcia, C.M. Marschoff, *J. Chem. Eng. Data* **54** (2009) 652.

21. Q. Li, C. Batchelor-McAuley, N.S. Lawrence, R.S. Hartshorne, R.G. Compton, *J. Electroanal. Chem.* DOI: j.jelechem.2012.07.039 (2012).

22. G. Hefter, *Pure Appl. Chem.* **78** (2006) 1571.

23. D. Suwatchara, M.C. Henstridge, N.V. Rees, R.G. Compton, *J. Phys. Chem. C* **115** (2011) 14876.

24. C. Kraiya, P. Singh, D.H. Evans, *J. Electroanal. Chem.* **563** (2004) 203.

25. R.L. Birke, Q. Huang, T. Spataru, D.K. Gosser, *J. Am. Chem. Soc.* **128** (2006) 1922.

26. M. Opallo, *J. Chem. Soc. Faraday Trans.* **82** (1986) 339.

27. S. Fletcher, V.J. Black, I. Kirkpatric, T.S. Varley, *J. Solid State Electrochem.* **17** (2013) 327.

Chapter 11

Theoretical and Experimental Approach to the Adiabaticity of Diffusional Electron Transfer Processes. Electro-reduction of 2-Nitropropane on Mercury Microelectroelectrodes

The work presented in this chapter is currently in press in *J. Electroanal. Chem.*

In this chapter, a theoretical and experimental approach to the degree of adiabaticity of electrode processes is considered for the case where the electroactive species of the redox couple diffuse freely in solution. The theoretical treatment considers a transition state-like framework which incorporates the influence of activation energy of electron transfer and the probability of electron tunnelling on the degree of adiabaticity.

The theory is applied to the study of the electro-reduction kinetics of 2-nitropropane in fully-supported DMSO solutions on mercury hemispherical microelectrodes of 23 μm radius. By fitting of experimental cyclic voltammetry, the standard rate constant (k_0) is determined at different temperatures and for different supporting electrolytes. The reorganization energy and degree of adiabaticity are determined from the variation of k_0 with temperature.

Programs used for simulations were developed and written by Dr. E. Laborda.

11.1 Introduction

The work described in Chapters 8-10 makes use of the variation of the standard heterogeneous rate constant (k_0) with temperature to provide molecular insight into the electro-reduction of aliphatic and aromatic nitrocompounds [1-3]. The results obtained highlights the need for evaluation of not only the reorganization energy (λ) but also the electronic interaction between the electroactive species and the electrode (i.e., the degree of adiabaticity) in order to fully understand the electron transfer kinetics. Thus, the variation of the experimental k_0 values with temperature indicates a higher adiabaticity and greater reorganization energy for 1-nitropentane (Chapter 8) than for 3-nitrophenolate (Chapters 9 and 10), the difference in λ being connected to different structural changes taking place upon the electron transfer process [4].

Within a transition state-like framework, the higher degree of adiabaticity of the electro-reduction of nitroaliphatics (within fully adiabatic limit or transition region between non-adiabatic and adiabatic behaviour) may require a lowering of the energy barrier in the kinetic model. In order to examine this, this chapter considers the effect of the electronic interaction not only on the probability of electron tunnelling, but also on the energy barrier. Consequently, and given that the electron transfer involving a species in solution occurs over a solution region next to the electrode surface [5], the activation energy depends on the distance of electron transfer as will be shown in the formulation of the kinetics.

For the modelling of the potential energy curve of the system, the generalization of the Anderson-Newns model developed by Schmickler [6-8] will be used. Next, the theory will be assessed by investigating the kinetics of electro-reduction of 2-nitropropane on mercury microelectrodes in fully-supported dimethylsulfoxide

solutions. The k_0 value of the reaction is determined at different temperatures (between 22.0 °C and 44.5 °C) from the fitting of cyclic voltammetry. The values and temperature dependence of k_0 enables the estimation of the degree of adiabaticity of the process. The procedure is applied in different media, with different supporting electrolyte cations, with the aim of analyzing the effect of the electron transfer distance on the kinetics of the process. This methodology provides further insight into the adiabatic character of diffusional, heterogeneous electron transfer processes and it contributes to the development of models and experimental strategies for more realistic description and analysis.

11.2 Experimental

Chemical Reagents

2-Nitropropane ($CH_3CH(NO_2)CH_3$, Aldrich, >96%), tetra-n-methylammonium perchlorate (TMAP, Fluka, Puriss grade), tetra-n-ethylammonium perchlorate (TEAP, Fluka, Puriss grade), tetra–n-butylammonium perchlorate (TBAP, Fluka, Puriss grade), mercury(I) nitrate dihydrate ($Hg_2(NO_3)_2 \cdot 2H_2O$, Aldrich, >97%), nitric acid (HNO_3, Fisher scientific, 70%), ferrocene ($Fe(C_5H_5)_2$, Aldrich, 98%), cobalt(III) sepulchrate trichloride ($[CoSep]Cl_3$, Aldrich, 95%), potassium nitrate (KNO_3, Aldrich, >99%), dimethylsulfoxide (DMSO, Alfa Aesar, >99%), acetonitrile (MeCN, Fisher Scientific, HPLC grade), were all used as received without further purification.

Instrumentation

Cyclic voltammetry and potential step chronoamperometry were performed with a computer-controlled Autolab PGSTAT12 (Metrohm-Autolab BV, Utrecht, Netherlands). Microdisk working electrode of 23 μm radius was fabricated in-house by

sealing Pt wire (Goodfellow Cambridge Ltd., UK) into soda glass capillary according to the method laid out by Amatore *et al.* [9]. The microdisk was polished prior to hemisphere deposition using 1.0, 0.3 and 0.05 μm alumina-water slurry on soft lapping pads (Buehler, Illinois). The disk size was calibrated by numerical fitting of the chronoamperometric response of the 1.0 mM ferrocene solution in acetonitrile supported by 0.1 M TBAP using the Shoup and Szabo expression [10-12]. A widely adopted literature diffusion coefficient for ferrocene of $D = 2.3 \times 10^{9}$ m^2s^{-1} at 25 °C [13] was used for the calculations.

A mercury hemisphere was then electrochemically deposited onto the microdisk from an aqueous solution of 50 mM $Hg_2(NO_3)_2$ containing 0.1 M KNO_3 acidified to 0.5% with HNO_3 following the method described by Bard *et al.* [14]. During the deposition, the potential was stepped to -0.25 V *vs* Ag wire. The size of the hemispherical drop was controlled by the amount of charge passed.

For all electrochemical measurements, a platinum mesh counter electrode was used, whereas a silver wire was employed as the reference electrode. Thermal control of the electrochemical cell with accuracy within the range of ± 0.2 °C was achieved through the use of an air heater-controller system fabricated in-house.

Characterization of the Hemispherical Mercury Electrode

The size and shape of the mercury electrode was characterized by optical and electrochemical methods.

For the optical characterization, visual measurement of the hemisphere was obtained through the use of JVC digital video camera TK-C921EG. To allow the appraisal of size and shape of the hemisphere in the environment of the reagent

solution, the working electrode was submerged in the solution sealed within a UV/vis cuvette and visual image was taken. It was found that the mercury droplet formed a hemisphere which adopted the radius of the microdisk.

The electrochemical characterization of the mercury hemispheres was carried out through analysis of the limiting current chronoamperogram of an aqueous solution containing 1 mM $[CoSep]Cl_3$ and 0.1 M KNO_3 (see Equation 5.4 in Chapter 5).

The value of the diffusion coefficient of $[CoSep]Cl_3$ employed for the calculations was $D=6.3\times10^{-10}m^2s^{-1}$. This was determined from chronoamperograms recorded at microdisk electrode of known dimensions and it is in close agreement with literature [15,16].

Both characterization techniques confirmed that the mercury hemisphere adopted the radius of the platinum microdisk on which it is deposited.

Determination of reagent concentration and diffusion coefficients

For the current study, the concentration of the 2-nitropropane reagent, its diffusion coefficient and the diffusion coefficient of the radical anions in the working solutions (consisting of DMSO solvent and 0.1M background electrolyte in the form of TMAP, TEAP or TBAP) are simultaneously evaluated through numerical fitting of the double potential step chronoamperometric responses [17]. During the chronoamperometric measurement, the potential was initially set at -1.0 V (*vs* Ag wire) where no faradaic process takes place. This is followed by an abrupt step in potential to the value of -1.7 V, corresponding to diffusion-limited conditions for the electro-reduction, and it is held for 0.5 s. The potential is then stepped back to -1.0 V and held

for further 0.5 s such that the radical anion is oxidized under diffusion-limited conditions. The results obtained are displayed in Tables 11.1-11.3.

Table 11.1: *Concentration and diffusion coefficients of the electroactive species in 0.1 M TMAP DMSO solution at the different temperatures examined determined by double potential step chronoamperometry.*

T (°C)	Concentration (mM)	$D_{\text{2-nitropropane}}$ (m^2s^{-1})	$D_{\text{2-nitropropane}^{\bullet-}}$ (m^2s^{-1})
22.0	1.9	5.4×10^{-10}	6.0×10^{-10}
29.5	1.9	6.3×10^{-10}	7.0×10^{-10}
34.8	1.9	6.7×10^{-10}	7.5×10^{-10}
41.0	1.8	7.6×10^{-10}	8.5×10^{-10}

Table 11.2: *Concentration and diffusion coefficients of the electroactive species in 0.1 M TEAP DMSO solution at the different temperatures examined determined by double potential step chronoamperometry.*

T (°C)	Concentration (mM)	$D_{\text{2-nitropropane}}$ (m^2s^{-1})	$D_{\text{2-nitropropane}^{\bullet-}}$ (m^2s^{-1})
23.0	1.6	5.5×10^{-10}	6.2×10^{-10}
29.0	1.5	6.3×10^{-10}	7.0×10^{-10}
35.0	1.4	6.8×10^{-10}	7.7×10^{-10}
42.0	1.5	7.7×10^{-10}	8.6×10^{-10}

Table 11.3: *Concentration and diffusion coefficients of the electroactive species in 0.1 M TBAP DMSO solution at the different temperatures examined determined by double potential step chronoamperometry.*

T (°C)	Concentration (mM)	$D_{\text{2-nitropropane}}$ (m^2s^{-1})	$D_{\text{2-nitropropane}^{\bullet-}}$ (m^2s^{-1})
23.0	1.5	5.6×10^{-10}	6.2×10^{-10}
28.5	1.4	6.4×10^{-10}	7.1×10^{-10}
34.0	1.5	6.9×10^{-10}	7.8×10^{-10}
44.5	0.8	8.0×10^{-10}	8.9×10^{-10}

From the experimental data, the diffusional activation energy of the electroactive species, $E_{a,d}$, in the different media are extracted according to the Arrhenius-like relationship given in Equation 9.1 in Chapter 9. The $E_{a,d}$ values obtained are included in Table 11.4 and they are statistically equivalent for all the different supporting electrolytes and species, being very similar to the activation energy of viscosity for DMSO: $E_{a,\eta}$ = 14.1kJ mol^{-1}.

Table 11.4: *Diffusion activation energy ($E_{a,d}$) and diffusion coefficients at infinite temperature (D_∞) of the electroactive species in 0.1 M TXAP, DMSO solutions obtained from the variation of the D-value with temperature.*

Supporting electrolyte	$E_{a,d}$ (kJ mol^{-1})		$\ln\left[D_\infty\left(\text{cm}^2\,\text{s}^{-1}\right)\right]$	
	2NPr	$2NPr^{-\bullet}$	2NPr	$2NPr^{-\bullet}$
TMAP	13.3 ± 0.8	13.8 ± 0.7	-6.7 ± 0.3	-6.4 ± 0.3
TEAP	13.2 ± 0.6	13.2 ± 0.6	-6.7 ± 0.2	-6.6 ± 0.3
TBAP	12.6 ± 0.9	13 ± 1	-6.9 ± 0.4	-6.8 ± 0.5

Cyclic Voltammetry

Cyclic voltammetry is performed in various working solutions encompassing three different systems differentiated through the use of different supported electrolytes: TMAP, TEAP and TBAP. Cyclic voltammograms within the scan rate range of 0.3 Vs^{-1} to 5.0 Vs^{-1} were recorded between -0.10 and -1.75 V (*vs* Ag wire) on a 23 μm radius mercury hemispherical electrode. For each system, four sets of voltammograms each recorded at a different temperature (22.0-41.0°C for TMAP; 23.0-42.0°C for TEAP; 23.0-44.5°C for TBAP) were obtained.

11.3: Theory

In this chapter, the potential energy curve model [8] developed by Waldeck and Mishra is used to model the experimental response. This model is discussed in more detail in Chapter 2.5.

Through this model, the potential energy curve is generated (through Equation 11.2), and the corresponding energy barrier is calculated (through Equation 11.3), at each energy level of the electrode:

$$G(q,x) = \frac{q^2}{4\lambda} + [\theta + x + \lambda(1-2z) + q]\langle n_r(q)\rangle - zq + \frac{\Delta}{2\pi}\ln[[\theta + x + \lambda(1-2z) + q]^2 + \Delta^2 + C] \tag{11.2}$$

$$\begin{aligned} &\Delta G^{\ddagger}_{red}(x) = G\left(q_{\dagger}, x\right) - G(q_{ox}, x) \qquad \text{for } x > x_{cr}^{red} \\ &\Delta G^{\ddagger}_{red}(x) = 0 \qquad \text{for } x_{cr}^{red} \geq x \geq -(\lambda + \theta) \\ &\Delta G^{\ddagger}_{red}(x) = \Delta G^{\ddagger}_{red}(-2(\lambda + \theta) - x) \qquad \text{for } x < -(\lambda + \theta) \end{aligned} \tag{11.3}$$

Where θ is the overpotential, q is an effective reaction coordinate and C a constant. The parameter Δ is associated with the strength of the electronic interaction between the electrode and reactant electronic states that decays exponentially with the distance from the electrode, r. x_{cr}^{red} is the critical value from which an activationless situation is attained and so the energy curve does not show two minima and a maximum but only one minimum. From Equation 11.3, the activation energies of reduction plotted in

Figure 11.1B are obtained for different degrees of adiabaticity. For small Δ values, $\Delta G_{red}^{\ddagger}$ is equivalent to that predicted by the Marcus theory. As the electronic coupling is stronger, the $\Delta G_{red}^{\ddagger}(x)$ level *x* decreases.

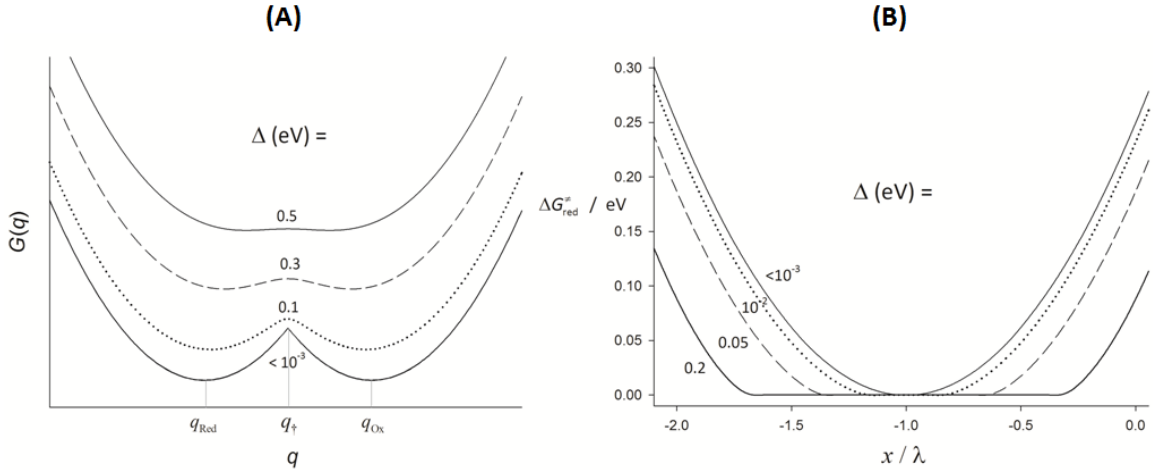


Figure 11.1: *(A) Potential energy curves corresponding to the redox couple* Ox^0 / Red^{-1} *for different degrees of adiabaticity ((Δ values indicated on the graph) for λ = 1 eV, η + x = 0, T = 298 K. (B) Activation energy for the energy levels at the electrode, x, corresponding to the one-electron reduction of species* Ox^0 *for different degrees of adiabaticity (Δ values indicated on the graph) calculated from Equation 11.3 with λ = 1 eV, η = 0, T = 298 K.*

In the calculation of the heterogeneous rate constant, this approach makes use of a transition-state treatment, taking into account the continuum of electronic energy levels in the metal electrode. Hence, the heterogeneous rate constant of reduction is given by [18]:

$$k_{red} = \frac{\upsilon_n}{\omega}\int_0^{\infty}\kappa_{el}\int_{-\infty}^{\infty}\frac{\exp\left[-\frac{G_{red}(x,r)}{RT}\right]}{1+\exp(-x^*)}dx^*d\omega(r-r_0) \tag{11.4}$$

where υ_n is the effective nuclear frequency, ω the spatial decay constant, r_0 the distance of closest approach, x^* the integral defined by x^* = F*x*/RT = F(ε-*E*)/RT with *F*ε being the energy of given electronic level and *E* the applied potentialand the effect of the degree of adiabaticity on the electronic transmission coefficient (κ_{el}) can be estimated through the Landau-Zener expression [12,15]:

$$\kappa_{el} = \frac{2\left[1-\exp\left(-\frac{\upsilon_{el}}{2\upsilon_n}\right)\right]}{2-\exp\left(-\frac{\upsilon_{el}}{2\upsilon_n}\right)} \tag{11.5}$$

where υ_{el} is the electron tunnelling frequency:

$$\upsilon_{el} = \frac{4\pi^2\rho_M}{h\sqrt{4\pi\frac{\lambda F}{RT}}}H_{AB}^2 \tag{11.6}$$

where ρ_M is the density of electronic levels of the electrode, *h* Planck's constant and H_{AB} is an effective average of the electronic coupling element at a given electron transfer distance, which is calculated from the corresponding energy barrier [19,20].

It is worth mentioning that, as can be seen in Figure 11.1A, the formalism considered here for the potential energy curve of the system considers that this is symmetrical in contrast with the more general picture provided by the asymmetric Marcus-Hush-Chidsey model employed in previously in Chapters 9 and 10. However, for the sake of simplicity and given that the asymmetric effects are moderate for this system, this formulation will be employed as a first approach. When necessary, the simultaneous evaluation of adiabatic and asymmetric can be included through the two-dimensional model formulated by Schmickler and Koper [21].

Figure 11.2A shows the variation of k_0 with the strength of the electronic coupling (parameterized through Δ_0 which is defined as the Δ value at distance r_0) for typical values of the reorganization energy (λ = 1-2 e V) and the nuclear frequency factor ($\upsilon_n = 10^{10}$-10^{14} s^{-1}). In order to assess the importance of the lowering of the energy barrier, the simulated results when this is ignored are also plotted in Figure 11.2B.

As can be observed, the value of the rate constant is independent of the nuclear frequency in the non-adiabatic regime (i.e., small Δ_0 values) where the transfer rate is determined by the strength of the electronic coupling: the stronger the interaction, the faster the electrode reaction. For weakly adiabatic systems, the increase of the rate constant starts levelling off, tending to a *plateau* value for adiabatic processes if the lowering of the energy barrier is ignored (Figure 11.2B). Under this simplification, the electron transfer rate is predicted to be independent of the electronic coupling in the adiabatic regime and limited by the effective nuclear frequency, υ_n [1-3,18]. However, when the decrease of the activation energy due to electronic coupling is taken into account, the k_0 value further increases with Δ_0. Note that this result implies that, even

for a high adiabatic character, the rate constant is predicted to be dependent on the electronic coupling and all the factors that affect it such as the electron transfer distance, tunnelling medium and electronic structure of electrode and species. A region of intermediate Δ_0 values where this dependence is much weaker can be found for very low υ_n values (for example, limited by the solvent dynamical properties [7,19,22,23]) as can be inferred from the curves for $\upsilon_n = 10^{10}$ s^{-1} in Figure 11.2A.

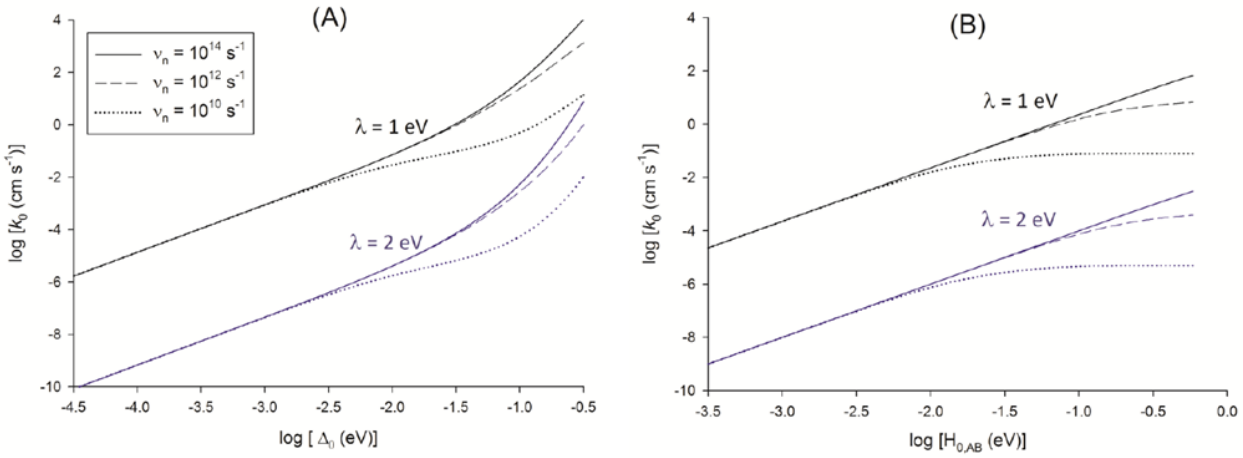


Figure 11.2: *(A)Standard heterogeneous rate constant, k_0, for a redox system Ox^0/Red^{-1} calculated from Equation 11.4 for different υ_n and λ values (indicated on the graphs); (B)k_0 values when the effect of the electronic coupling on the activation energy is ignored. In this case, $H_{AB} = H_{0,AB}\exp[-\omega(r - r_0)]$ where $H_{0,AB}$ is the electronic coupling element at the distance of closest approach, r_0. $\omega = 10^8$ cm^{-1}, $\rho_M = 0.3$ eV^{-1}, $T = 298$ K.*

11.4 Results and Discussion

Next, the formalism discussed in the previous section will be applied to the study of the electro-reduction of 2-nitropropane on mercury microhemispheres (r_0 = 23μm) in DMSO solutions. The adiabatic character of the reaction will be examined in presence of cations of different size: tetramethylammonium (TMA^+), tetraethylammonium (TEA^+) and tetra-n-butylammonium (TBA^+). Recognising the negative potential values where the electro-reduction takes place, the supporting electrolyte cation is expected to define the distance of closest approach to the electrode and so affect the electronic coupling and rate constant.

The k_0 value of the reaction is determined at different temperatures via fitting of the experimental cyclic voltammetry in a wide range of scan rates (from 0.3 to 5.0Vs^{-1}). For this, the asymmetric Marcus-Hush-Chidsey formulation is employed to describe the potential dependence of the oxidation/reduction rate constants with a fixed, tentative value of the reorganization energy of 1 eV since the cyclic voltammetry has proven to be poorly sensitive to the λ value.

Given that the diffusion coefficients of both electroactive species are known from double potential pulse chronoamperometry (values given in Tables 11.1-11.3), the fitting of the experimental voltammograms is carried out with the standard electrochemical rate constant (k_0), the asymmetric parameter (γ, which accounts for the difference between the force constants of the oxidized and reduced species) and the formal potential (E_f^o) as fitting parameters (the E_f^o value varies between experiments due to the use of an Ag wire pseudo reference electrode). The values corresponding to the best fitting over the range of scan rates are shown in Tables 11.5-11.7. The best fitting is established by minimization of the mean scaled absolute deviation (MSAD).

Table 11.5: *Kinetic parameters obtained for the electro-reduction of 2-nitropropane on a mercury hemispherical microelectrode in 0.1 M TMAP DMSO solution at different temperatures through the fitting of cyclic voltammograms with the asymmetric Marcus-Hush-Chidsey model.* $E_f^{\circ} = -1.38 \pm 0.02$ *V.*

	22.0°C	**29.5°C**	**34.8°C**	**41.0°C**
k_0 **(cm s^{-1})**	0.18	0.24	0.30	0.42
γ	-0.10	-0.10	-0.10	-0.10
%MSAD	2.6±0.5	3.7±0.4	4±1	4.5±0.4

Table 11.6: *Kinetic parameters obtained for the electro-reduction of 2-nitropropane on a mercury hemispherical microelectrode in 0.1 M TEAP DMSO solution at different temperatures through the fitting of cyclic voltammograms with the asymmetric Marcus-Hush-Chidsey model.* $E_f^{\circ} = -1.39 \pm 0.06$ *V.*

	23.0°C	**29.0°C**	**35.0°C**	**42.0°C**
k_0 **(cm s^{-1})**	0.017	0.023	0.029	0.041
γ	-0.10	-0.10	-0.10	-0.10
%MSAD	3.5±0.5	3.1±0.7	3.1±0.7	4.2±0.6

Table 11.7: *Kinetic parameters obtained for the electro-reduction of 2-nitropropane on a mercury hemispherical microelectrode in 0.1 M TBAP DMSO solution at different temperatures through the fitting of cyclic voltammograms with the asymmetric Marcus-Hush-Chidsey model.* $E_f^{\circ} = -1.41 \pm 0.07$ *V.*

	23.0°C	**28.5°C**	**34.0°C**	**44.5°C**
k_0 **(cm s^{-1})**	0.0075	0.0090	0.0110	0.0150
γ	-0.10	-0.10	-0.10	-0.10
%MSAD	3±1	3.1±0.5	4.0±0.7	4±1

As can be seen in Figures 11.3-11.5, in all cases a very satisfactory agreement between simulated and experimental voltammograms is obtained with the values included in Tables 11.5-11.7 (MSAD $\leq$ 4.5%). A negative γ value of -0.1 is determined, which indicates moderately larger force constants (on average) for the radical monoanion. This is explained by its higher charge that can lead to stronger interactions with the solvent [1-3].

Next, following the methodology employed in previous works (Chapters 8-10), the k_0 value of the reaction is determined and their variation with temperature are analyzed through Equation 11.6 with the aim of obtaining information about the reorganization energy and the degree of adiabaticity of the electron transfer. Thus, the variation of k_0 with temperature in the different media is fitted with λ and Δ_0 as variables.

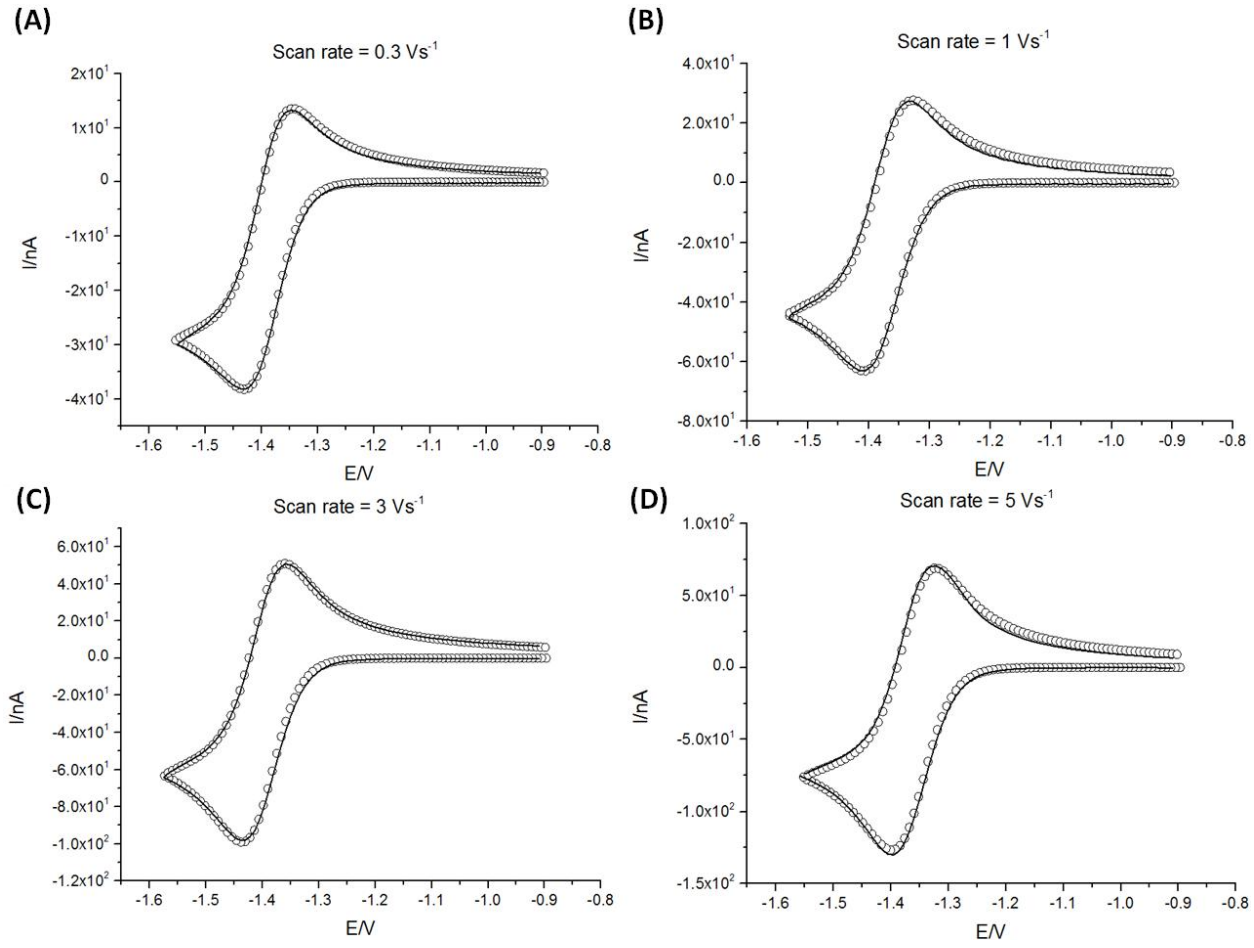


Figure 11.3: *Fittings of experimental voltammograms of 2-nitropropane in DMSO supported by 0.1 M TMAP electrolyte on a 23 μm radius mercury hemisphere electrode. A) Scan rate = 0.3 Vs^{-1}, T = 22.0°C; B) Scan rate = 1 Vs^{-1}, T = 29.5°C; C) Scan rate = 3 Vs^{-1}, T = 34.8°C; D) Scan rate = 5 Vs^{-1}, T = 41.0°C. Experiments (solid line); simulation (open circles).*

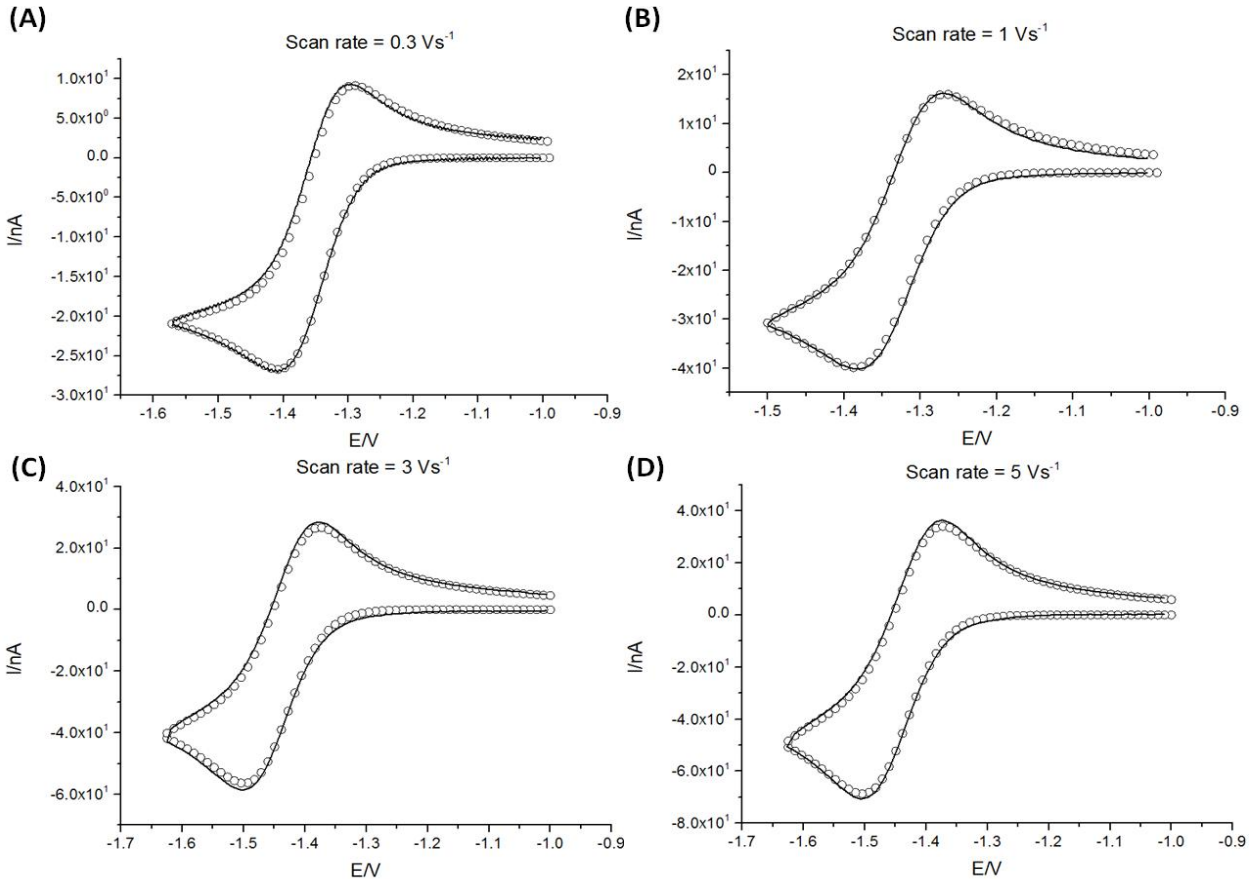


Figure 11.4: *Fittings of experimental voltammograms of 2-nitropropane in DMSO supported by 0.1 M TEAP electrolyte on a 23 μm radius mercury hemisphere electrode. A) Scan rate = 0.3 Vs^{-1}, T = 23.0°C; B) Scan rate = 1 Vs^{-1}, T = 29.0°C; C) Scan rate = 3 Vs^{-1}, T = 35.0°C; D) Scan rate = 5 Vs^{-1}, T = 42.0°C. Experiments (solid line); simulation (open circles).*

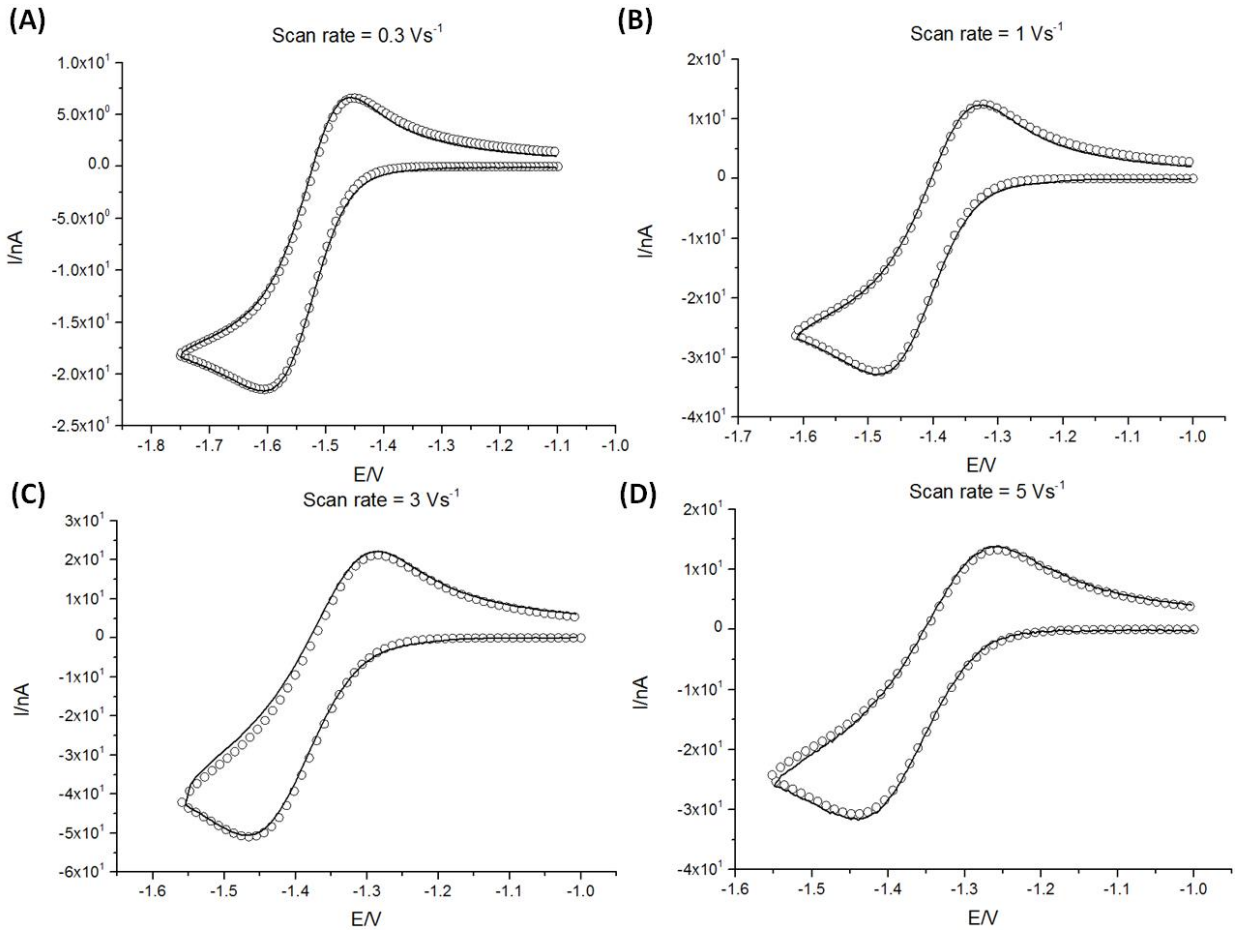


Figure 11.5: *Fittings of experimental voltammograms of 2-nitropropane in DMSO supported by 0.1 M TBAP electrolyte on a 23 μm radius mercury hemisphere electrode. A) Scan rate = 0.3 Vs^{-1}, T = 23.0°C; B) Scan rate = 1 Vs^{-1}, T = 28.5°C; C) Scan rate = 3 Vs^{-1}, T = 34.0°C; D) Scan rate = 5 Vs^{-1}, T = 44.5°C. Experiments (solid line); simulation (open circles).*

From theoretical calculations the value of the reorganization energy for the electro-reduction of 2-nitropropane is estimated to lie in 2.4-3.0 eV attending to the values calculated for the inner-sphere component (λ_i = 0.3 eV [4]) and the outer-sphere contribution assuming the solvent as a dielectric continuum (as detailed in Chapter 2.2 and ref. [24]). Typical values of the nuclear frequency are in the range $\upsilon_n = 10^{10}$ to 10^{14} s^{-1} so that the fitting analysis was carried out for the above λ and υ_n values. The best simultaneous fitting of the three different media was obtained with $\upsilon_n = 10^{14}$ s^{-1} and the corresponding parameters are reported in Table 11.8. For the TMAP and TEAP salts, multiple $\{\lambda , \Delta_0\}$ pairs were found to yield fittings of similar quality such that precise, unique values for these two parameters could not be extracted. Instead, the range of Δ_0/λ values obtained for $2.4 \leq \lambda(eV) \leq 3.0$ is given in Table 11.8. The results indicate that they both lie in the weakly adiabatic region ($0.09 \leq \Delta_0/\lambda \leq 0.16$), the electronic interaction being stronger in presence of TMAP given that the cation is smaller and so the electron transfer distance is shorter. Under these conditions, the correction due to the lowering of the activation barrier starts being significant and it must be included in the modelling.

Table 11.8: *Value of the reorganization energy (λ) and degree of adiabaticity (through Δ_0/λ) for the electro-reduction of 2-nitropropane on a mercury hemispherical microelectrode in 0.1 M TXAP DMSO solutions obtained from the analysis of the variation of k_0 with temperature. $\upsilon_n = 10^{14}$ s^{-1}, $\omega = 10^8$ cm^{-1}, ρ_M = 0.3 eV^{-1}. [a]Values corresponding to theoretical calculations.*

	TMAP	**TEAP**	**TBAP**
λ (eV)	3.0-2.4[a]	3.0-2.4[a]	1.0
Δ_0/λ	0.16-0.13	0.13-0.09	9×10^{-3}
MSAD (%)	3.0	2.5	0.25

With respect to the study in the TBAP solution, it was not possible to obtain a satisfactory fitting of the k_0 variation with temperature for λ values in the range 2.4-3.0 eV as can be seen in Figure 11.6B. In fact, a significantly smaller value of 1.0 eV is required for the proper description of the k_0 temperature-dependence (Figure 11.6C), from which it is concluded that the reaction in TBAP solution is non-adiabatic. Therefore, as expected, the strength of the electronic coupling is directly related to the size of the supporting electrolyte cation and it increases in the order TBAP<TEAP<TMAP, as illustrated in Figure 11.6A.

In Figure 11.7 we revisit the results obtained in previous works for the electro-reduction of 2-methyl-2-nitropropane (2Me2NP) on mercury in 0.1 M TBAP *N*,*N*'-dimethylformamide [25], 3-nitrophenolate ($3NPh^-$) on a mercury microelectrode in DMSO solutions with different supporting electrolytes (see figure caption) [1] and *p*-benzoquinone (BQ) and dichloro-*p*-benzoquinone (DCQ) on carbon fibre microelectrode in 0.1M TBAP acetonitrile solutions [26]. λ values calculated according to the considerations discussed above are employed for 2Me2NP (2.7 eV) and $3NPh^-$ (2.0 eV) and a value of 1.24 eV for the benzoquinones [26].

From the value of the standard rate constants at 25ºC, a weakly adiabatic character can be assigned to the electro-reduction of 2Me2NP, DCQ and 3NPh in TEAP and TBAP solutions. Significantly weaker interactions are obtained for the electro-reduction of BQ in TBAP and $3NPh^-$ in tetra-n-hexylammonium perchlorate (THAP) solutions that are situated in the non-adiabatic region.

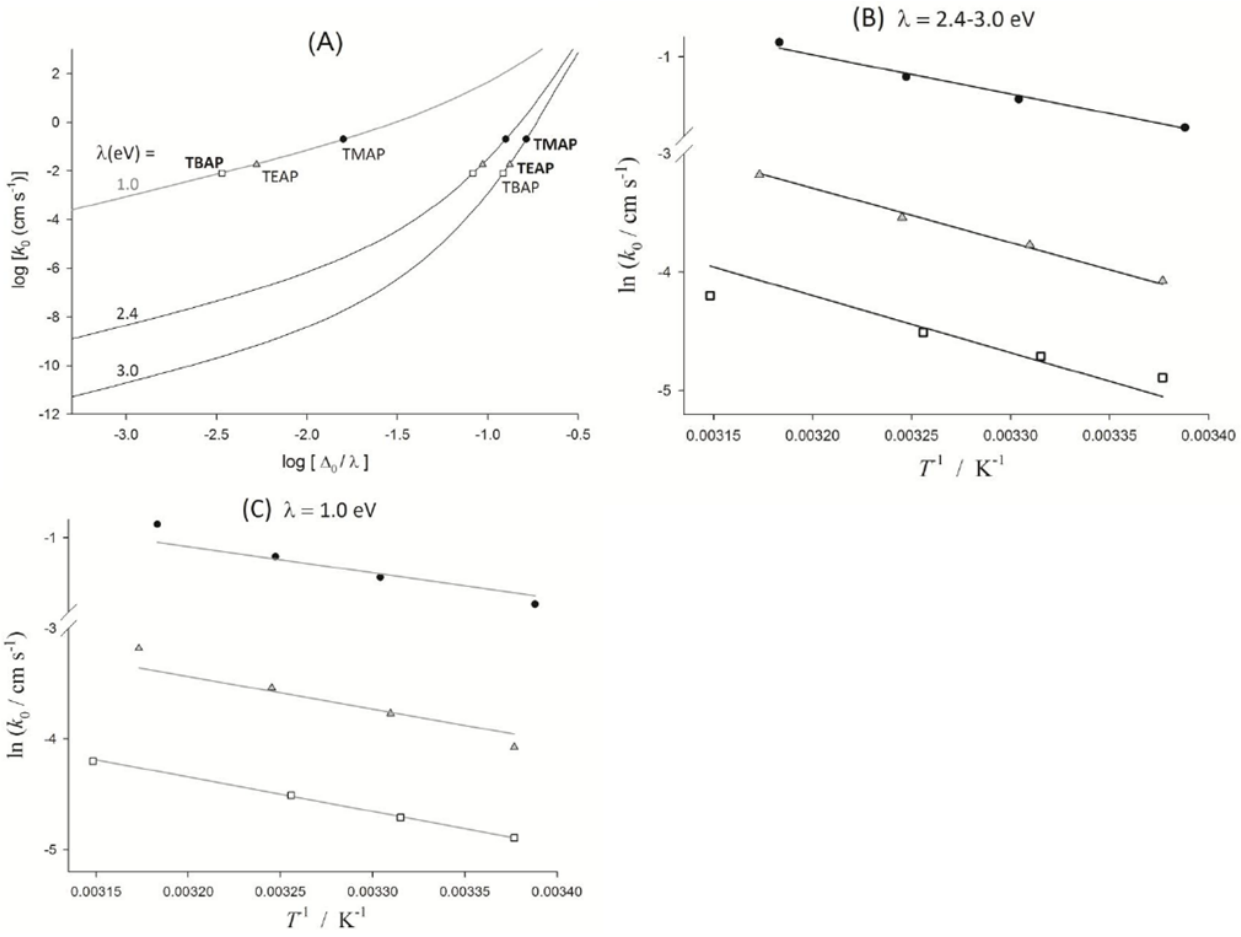


Figure 11.6: *(A) Experimental values of the standard rate constant at 25ºC for the electro-reduction of 2-nitropropane on a 23 μm radius mercury hemisphere electrode in DMSO containing 0.1 M TMAP (black circle), TEAP (grey triangle) and TBAP (open square). The solid lines correspond to the theoretical curves calculated from Equation 11.4 for the λ values indicated on the graph. (B)/(C) Experimental (points) and simulated (solid line) Arrhenius-like plots ln(k_0) vs T^{-1} for the Δ_0 / λ values included in Table 11.8 and the λ values indicated on the graph. $\upsilon_n = 10^{14}\ s^{-1}$, $\omega = 10^8\ cm^{-1}$, $\rho_M = 0.3\ eV^{-1}$.*

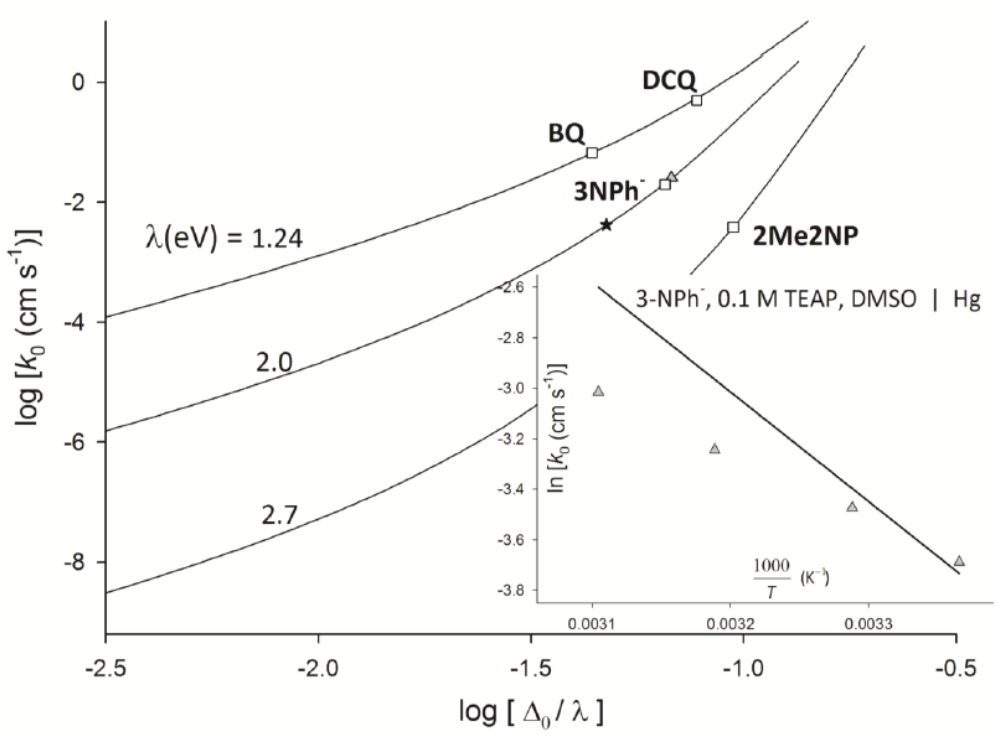


Figure 11.7: *(A) Experimental values of the standard rate constant at 25ºC for the electro-reduction of 2-methyl-2-nitropropane (2Me2NP) on mercury electrode in 0.1 M TBAP N,N'-dimethylformamide solution [25], p-benzoquinone (BQ) and dichloro-pbenzoquinone (DCQ) on carbon fibre microelectrode in 0.1M TBAP acetonitrile solution [26], and 3-nitrophenolate ($3NPh^-$) on mercury microelectrode in DMSO solutions with different supporting electrolytes: TEAP (grey triangle), TBAP (open square) and tetra-n-hexylammonium perchlorate (THAP, star) [1]. The solid lines correspond to the theoretical curves calculated from Equation 11.4 for the λ values indicated on the graph.* ***Inset:*** *Corresponding experimental (points) and simulated (solid line) Arrhenius-like plots ln(k_0) vs T^{-1} for $3NPh^-$ /$3NPh^{2-}$ in TEAP DMSO solution. $\upsilon_n = 10^{14}\ s^{-1}$, $\omega = 10^8\ cm^{-1}$, $\rho_M = 0.3\ eV^{-1}$ (Hg), $\rho_M = 0.035\ eV^{-1}$ (C).*

Although the k_0 values at one temperature in conjunction with the corresponding theoretical λ allows for estimation of the electronic interaction, this may not provide a satisfactory fitting of the k_0 temperature-dependence as discussed above for $2NP/2NP^-$ in TBAP DMSO solutions Figure 11.6B. As can be seen in the inset of Figure 11.7, this is also the case of $3NPh^-$ /$3NPh^{2-}$ in DMSO solutions. In both cases, the λ value extracted from the ln (k_0) *vs* 1/*T* plot is significantly smaller than the theoretical one. With the caveats about the accuracy of the latter, the disagreement may point to the need for a critical reassessment of the model employed.

11.5 Conclusions

The description of the adiabaticity of diffusional heterogeneous electron transfer processes has been developed making use of Schmickler's potential energy curve model [6] and the Landau-Zener formalism [18]. Our approach considers that the electron transfer takes place not only at a fixed distance from the electrode but over a range of distances, the probability of tunnelling decreasing exponentially with the latter.

The theoretical results show the importance of a full description of the adiabatic effects at the weakly and strongly adiabatic regimes. Thus, when the lowering of the energy barrier is ignored a maximum value of the rate constant is predicted, which is exceeded when including the adiabatic effects on the transition region.

The feasibility of the determination of the adiabatic character and reorganization energy of electrode process via voltammetric experiments at different temperatures has been examined. The model has been applied to the kinetic study of electro-reduction of 2-nitropropane on mercury microhemispheres of 23 μm radius in DMSO solutions fully supported with different electrolytes. Although the degree of adiabaticity could be estimated in all cases, theoretical values for the reorganization energy (2.4-3.0 eV) have

been necessary for those systems where the electronic interaction is significant, that is, in tetramethylammonium and tetraethylammonium perchlorate solutions. The process was found to be more adiabatic in the presence of TMA^+ since the electroactive species approaches more to the electrode surface. For the same reason, a much weaker electronic coupling has been obtained in tetra-n-butylammonium perchlorate solutions, together with a value for the reorganization energy significantly smaller than the theoretical predictions: $\lambda = 1.0$ eV. The difficulties of extracting a λ value consistent with the theoretical calculations and for the different supporting electrolytes may point to the need for revision of the approach employed here to model adiabaticity.

11.6: References

1. E. Laborda, C. Batchelor-McAuley, D. Suwatchara, M.C. Henstridge, R.G. Compton, *J. Electroanal. Chem.* **694** (2013) 30.
2. D. Suwatchara, N.V. Rees, M.C. Henstridge, E. Laborda, R.G. Compton, *J. Electroanal. Chem.* **685** (2012) 53.
3. E. Laborda, D. Suwatchara, N.V. Rees, M.C. Henstridge, A. Molina, R.G. Compton, *Electrochim. Acta* DOI: j.electacta.2012.12.129 (2013).
4. C. Kraiya, P. Singh, D.H. Evans, *J. Electroanal. Chem.* **563** (2004) 203.
5. D.J. Gavaghan, S.W. Feldberg, *J. Electroanal. Chem.* **491** (2000) 103.
6. W. Schmickler, *J. Electroanal. Chem.* **204** (1986) 31.
7. W. Schmickler, J. Mohr, *J. Chem. Phys.* **117** (2002) 2867.
8. A.K. Mishra, D.H. Waldeck, *J. Phys. Chem. C* **113** (2009) 17904.
9. C. Amatore, E. Maisonhaute, G. Simonneau, *J. Electroanal. Chem.* **486** (2000) 141.

10. A.J. Bard, L. Faulkner, *Electrochemical Methods: Fundamentals and Applications*, 2nd Ed., Wiley & Sons, New York, 2001.
11. R.G. Compton, C.E. Banks, *Understanding Voltammetry, 2nd Ed.*, Imperial College Press, London, 2011.
12. D. Shoup, A. Szabo, *J. Electroanal. Chem.* **140** (1982) 237.
13. K.N. Marsh, A. Deev, A.C.-T. Wu, E. Tran, A. Klamt, *Korean J. Chem. Eng.* **19** (2002) 357.
14. J. Mauzeroll, E.A. Hueske, A.J. Bard, *Anal. Chem.* **75** (2003) 3880.
15. T.J. Davies, B.A. Brookes, A.C. Fisher, K. Yunus, S.J. Wilkins, P.R. Greene, J.D. Wadhawan, R.G. Compton, *J. Phys. Chem. B* **107** (2003) 6431.
16. A. Molina, E. Laborda, E.I. Rogers, F. Martínez-Ortiz, C. Serna, J.G. Limon-Petersen, N.V. Rees, R.G. Compton, *J. Electroanal. Chem.* **634** (2009) 73.
17. E. Laborda, Y. Wang, M. Henstridge, F. Martinez-Ortiz, A. Molina, R.G. Compton, *Chem. Phys. Lett.* **512** (2011) 133.
18. S.W. Feldberg, N. Sutin, *Chem. Phys.* **324** (2006) 216.
19. A.K. Mishra, D.H. Waldeck, *J. Phys. Chem. C* **115** (2011) 20662.
20. B.S. Brunschwig, N. Sutin, *Coord. Chem. Rev.* **187** (1999) 233.
21. W. Schmickler, M.T.M. Koper, *Electrochem. Commun.* **1** (1999) 402.
22. G.E. McManis, A.K. Mishra, M.J. Weaver, *J. Chem. Phys.* **86** (1987) 5550.
23. W.R. Fawcett, M. Opallo, *Angew. Chem. Int. Ed. Engl.* **33** (1994) 2131.
24. D. Suwatchara, M.C. Henstridge, N.V. Rees, R.G. Compton, *J. Phys. Chem. C* **115** (2011) 14876.
25. C. Costentin, C. Louault, M. Robert, V. Rogéa, J-M Savéant, P*hys. Chem. Chem. Phys.* **14** (2012) 1581.

26. R. Nissim, C. Batchelor-McAuley, M.C. Henstridge, R.G. Compton, *Chem. Commun.* **48** (2012) 3294.

APPENDIX

Fast Scan Potentiostat

This appendix presents the circuit details of the fast scan potentiostat used for fast scan cyclic voltammetry experiments described in Chapters 4 and 8 of this thesis. The potentiostat is constructed and maintained by Mr. P. Hurst, Electronics Workshop, PTCL, Oxford University.

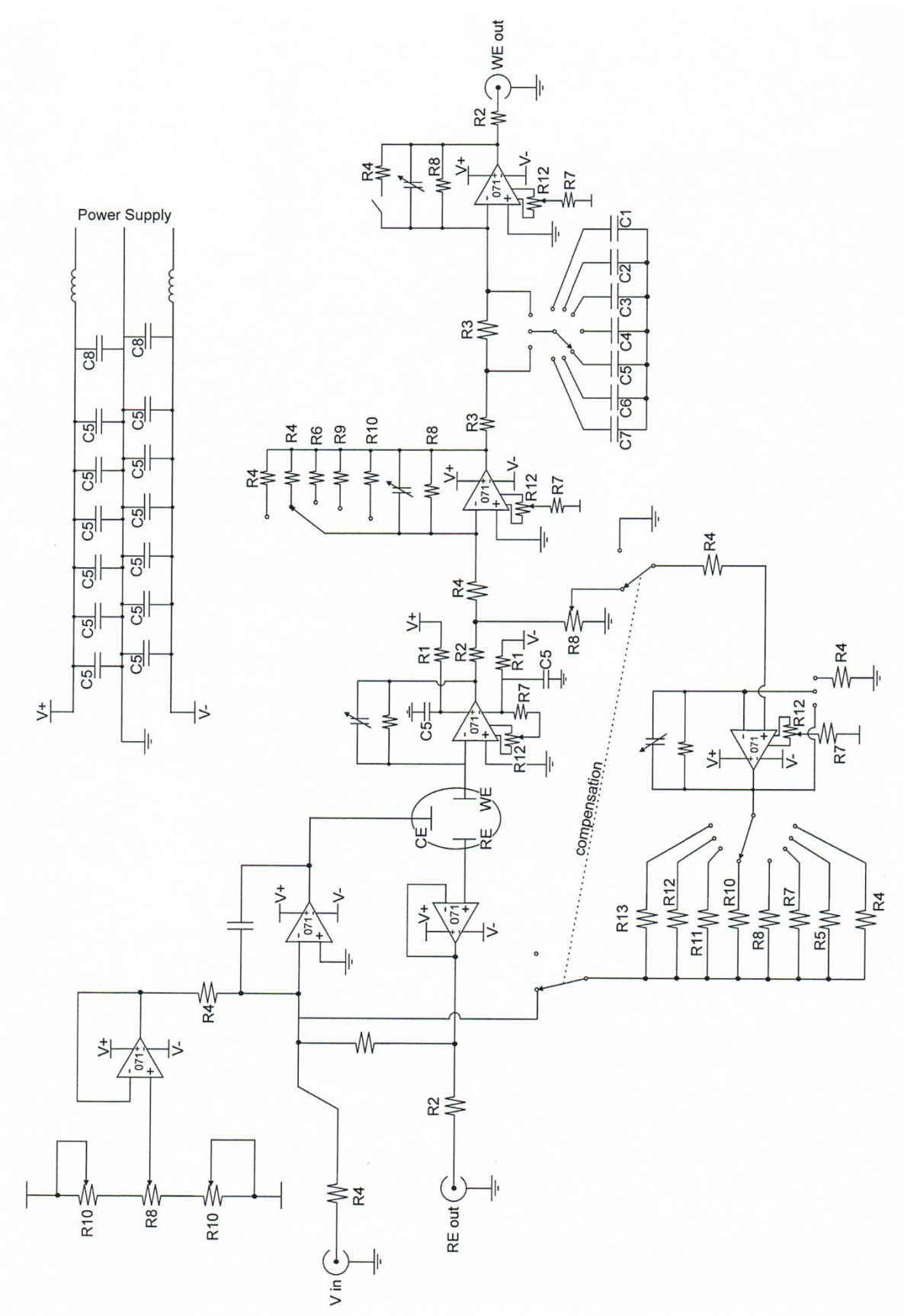


Figure A.1: *Circuit diagram of the fast scan potentiostat*

Table A.1: *Labels for Figure A.1*

Resistor	Resistance (Ω)	Capacitor	Capacitance (nF)
R1	10	C1	0.1
R2	51	C2	1
R3	500	C3	10
R4	1.0×10^3	C4	22
R5	2.0×10^3	C5	100
R6	4.7×10^3	C6	220
R7	5.0×10^3	C7	470
R8	1.0×10^4	C8	1.0×10^5
R9	1.5×10^4		
R10	2.0×10^4		
R11	5.0×10^4		
R12	1.0×10^5		
R13	2.0×10^5		